

## **ULTRACAM observations of interacting binaries**

by

**Susana Cristina Cabral de Barros**

**Thesis**

Submitted to the University of Warwick

for the degree of

**Doctor of Philosophy**

**Physics Department**

April 2008

THE UNIVERSITY OF  
**WARWICK**

# Contents

<b>List of Tables</b>	vii
<b>List of Figures</b>	ix
<b>Acknowledgments</b>	xii
<b>Declarations</b>	xiii
<b>Abstract</b>	xiv
<b>Chapter 1 Introduction</b>	1
1.1 Motivation . . . . .	1
1.2 Variable Stars . . . . .	2
1.3 Close Binary Stars . . . . .	3
1.4 The Formation of CVs . . . . .	5
1.5 Angular momentum loss mechanisms . . . . .	6
1.6 Secular evolution of CVs . . . . .	8
1.7 Accretion discs . . . . .	12
1.7.1 Formation of an accretion disc . . . . .	12
1.7.2 Accretion disc viscosity . . . . .	14
1.8 Types of Cataclysmic Variables . . . . .	17
1.8.1 Nova-like variables . . . . .	18

1.8.2	Dwarf Novae (DN) . . . . .	19
1.8.3	Magnetic CVs: AM Her . . . . .	20
1.8.4	Magnetic CVs: DQ Her . . . . .	23
1.8.5	AM Canum Venaticorum Stars . . . . .	24
1.9	X-ray binaries . . . . .	27
1.10	Stochastic Variability in Accreting Objects . . . . .	28
1.10.1	Flickering in low mass X-rays binaries . . . . .	28
1.10.2	Flickering in other objects . . . . .	31
1.10.3	Flares in M stars . . . . .	32
<b>Chapter 2</b>	<b>Observation and Analysis</b>	<b>35</b>
2.1	Observations and reduction <sup>1</sup> . . . . .	35
2.1.1	CCDs . . . . .	35
2.1.2	CCD Data reduction . . . . .	38
2.1.3	Differential Photometry . . . . .	44
2.1.4	Flux calibration . . . . .	47
2.2	ULTRACAM . . . . .	50
2.2.1	Introduction . . . . .	50
2.2.2	ULTRACAM reading modes . . . . .	50
2.2.3	Design . . . . .	52
2.2.4	Science with ULTRACAM . . . . .	53
2.3	Conversion of systems of time . . . . .	56
<b>Chapter 3</b>	<b>Time series methods<sup>2</sup></b>	<b>59</b>
3.1	Fourier transform . . . . .	61
3.2	Discrete Fourier transform . . . . .	62
3.3	Power Spectra . . . . .	63
3.3.1	Window function . . . . .	66

3.4	Lomb Scargle Periodogram . . . . .	67
3.4.1	White noise level . . . . .	70
3.5	Correlation Function . . . . .	71
3.6	Simulation of power law light curves . . . . .	72
3.6.1	Power spectral index . . . . .	73
3.6.2	Frequency break . . . . .	77
3.6.3	Length of the light curve . . . . .	78
3.6.4	High frequency pass filter . . . . .	81
<b>Chapter 4</b>	<b>Constraints upon the unipolar model of V407 Vul and HM Cnc<sup>3</sup></b>	<b>86</b>
4.1	Introduction . . . . .	86
4.2	Observational Constraints . . . . .	88
4.3	The Geometric Model . . . . .	89
4.3.1	Computations . . . . .	93
4.4	Results . . . . .	95
4.4.1	Detailed analysis of the phase constraint . . . . .	98
4.5	Discussion . . . . .	101
4.5.1	Effects of different masses . . . . .	101
4.5.2	Spot Size . . . . .	102
4.6	Conclusion . . . . .	103
<b>Chapter 5</b>	<b>ULTRACAM Photometry of the ultracompact binaries V407 Vul and HM Cnc<sup>4</sup></b>	<b>106</b>
5.1	Introduction . . . . .	106
5.2	Observations and reduction . . . . .	107
5.3	Results . . . . .	110
5.3.1	Ephemerides . . . . .	110
5.3.2	V407 Vul . . . . .	111

5.3.3	Pulsation astrometry of V407 Vul . . . . .	113
5.3.4	HM Cnc . . . . .	118
5.3.5	The Optical/X-Ray phase shift of HM Cnc . . . . .	121
5.3.6	Flickering . . . . .	122
5.4	Discussion . . . . .	124
5.4.1	The X-ray versus optical phases . . . . .	124
5.4.2	A limit on the bolometric luminosity of HM Cnc . . . . .	128
5.4.3	Direct impact or polar? . . . . .	134
5.4.4	Period changes in V407 Vul and the G star . . . . .	134
5.5	Conclusion . . . . .	135
<b>Chapter 6</b>	<b>Flickering of Cataclysmic Variables</b>	<b>137</b>
6.1	Introduction . . . . .	137
6.2	Observations and reduction . . . . .	143
6.3	Results . . . . .	147
6.3.1	Light Curves . . . . .	147
6.3.2	Cross Correlation . . . . .	154
6.3.3	Flickering Colour . . . . .	154
6.3.4	Intrinsic Variability and sources of noise . . . . .	159
6.3.5	Power spectrum analysis . . . . .	161
6.3.6	Simulations . . . . .	169
6.3.7	Comparison of power spectra . . . . .	172
6.3.8	Variability throughout the eclipses of RW Tri and V345 Pav . .	176
6.4	Discussion . . . . .	181
6.4.1	Periodicities in the presence of red noise . . . . .	181
6.4.2	The steepness of the power spectrum . . . . .	186
6.4.3	Timescales of the flickering . . . . .	187

6.4.4	Comparison with Soft X-ray Transients . . . . .	190
6.4.5	Flares in M stars . . . . .	197
6.5	Conclusion . . . . .	202
<b>Chapter 7</b>	<b>Conclusion and Future Work</b>	<b>204</b>
7.1	The nature of V407 Vul and HM Cnc . . . . .	204
7.2	Stochastic variability in CVs . . . . .	207
7.3	Future work . . . . .	209
<b>Appendix A</b>	<b>Ephemeris of V407 Vul and HM Cnc</b>	<b>211</b>
A.1	. . . . .	211
<b>Appendix B</b>	<b>Normalisation of the simulated light curves</b>	<b>219</b>
B.1	Introduction . . . . .	219
B.2	Normalisation . . . . .	220

# List of Tables

2.1	Mean and RMS of a typical typical bias frame . . . . .	40
3.1	Fitted parameters of the LSP of the simulated light curves with steep power spectrum . . . . .	74
3.2	Fitted parameters of the LSP of the simulated light curves with different length . . . . .	80
3.3	Fitted parameters of the LSP of the simulated light curves with different length, fitting only the lowest frequencies . . . . .	80
3.4	Fitted parameters of the LSP of the simulated filtered light curves for increasing values of $\alpha$ . . . . .	82
5.1	Observation log . . . . .	108
5.2	Positions relative to the target and magnitude of the comparison stars used to flux calibrate the data . . . . .	110
5.3	Measured magnitudes for V407 Vul and HM Cnc . . . . .	110
5.4	First and second harmonic decomposition of the optical light curves for V407 Vul and HM Cnc. . . . .	112
5.5	Results of single harmonic sinusoid fit to V407 Vul's data . . . . .	112
5.6	Results of single harmonic sinusoid fits to the HM Cnc data . . . . .	119

5.7	The best fit, minimum and maximum allowed temperatures of the primary star as a function of reddening . . . . .	131
6.1	Types and periods of the CVs in our sample . . . . .	144
6.2	Observation log . . . . .	145
6.3	Mean apparent magnitudes of the CVs observed . . . . .	147
6.4	Dominant source of flickering for each CV . . . . .	159
6.5	Fitted parameters of the power law model for the $r'$ filter LSP . . . . .	169
6.6	Fitted parameters of the power law model for the $g'$ filter LSP . . . . .	170
6.7	Fitted parameters of the power law model for the $u'$ filter LSP . . . . .	170
6.8	Fitted parameters of the Lorentzian model for the peaks of RW Tri in the $g'$ filter . . . . .	186
6.9	Fitted parameters for power law model for the LSP of V404 Cyg . . . . .	194
6.10	Variability characteristics of SXTs in quiescence . . . . .	197
A.1	Ephemeris of V407 Vul derived from Ramsay et al. (2006a) . . . . .	212
A.2	Times of the rise to maximum for V407 Vul . . . . .	215
A.3	Ephemeris of HM Cnc derived from Strohmayer (2005) . . . . .	215
A.4	Times of mid “eclipse” for HM Cnc . . . . .	216

# List of Figures

1.1	Roche equipotentials . . . . .	5
1.2	Period distribution of CVs . . . . .	9
1.3	Particle path after living $L_1$ . . . . .	14
1.4	Decomposition of the light curve of ?? . . . . .	15
1.5	Artist's impression of a Non-magnetic CV . . . . .	17
1.6	Artist's impression of a AM Her star . . . . .	21
1.7	Artist's impression of a DQ Her star . . . . .	22
1.8	Structure of a flare in the Martens and Kuin two-ribbon flare mode . . . . .	33
2.1	ULTRACAM left bias frame . . . . .	39
2.2	ULTRACAM right bias frame . . . . .	39
2.3	ULTRACAM dark frame . . . . .	39
2.4	Peppering in the g' CCD of ULTRACAM . . . . .	42
2.5	ULTRACAM flat frame . . . . .	42
2.6	Noise analysis for ULTRACAM . . . . .	43
2.7	ULTRACAM object frame; V407 Vul . . . . .	48
2.8	ULTRACAM readout modes . . . . .	52
2.9	ULTRACAM optical components . . . . .	54
2.10	ULTRACAM schematics . . . . .	55
2.11	ULTRACAM mounted in the WHT . . . . .	55

3.1	Simulated light curves for steep power spectra . . . . .	75
3.2	LSP of the simulated light curves for steep power spectra . . . . .	76
3.3	Simulated light curves for $\alpha = 2$ and different frequency breaks . . . . .	78
3.4	LSP of simulated light curves for different light curve lenghts . . . . .	79
3.5	LSP of the simulated filtered light curves for steep power spectrum . . .	83
4.1	Definition of the geometric model . . . . .	90
4.2	Geometric constraints for the unipolar model of V407 Vul and HM Cnc	94
4.3	Track of the heated spot upon the primary star. . . . .	95
4.4	Examples of the simulated X-ray phase light curves for V407 Vul . . . .	96
4.5	The parameter space ruled out by the combination of all the constraints for V407 Vul and HM Cnc . . . . .	98
4.6	The minimum phase shift relative to a quadratic ephemeris as a function of the degree of spin/orbit asynchronism . . . . .	100
4.7	Dependence of the allowed parameter space upon the spot size . . . . .	104
5.1	Phase-folded light curves of V407 Vul and HM Cnc . . . . .	111
5.2	Amplitude spectra of the variation of the position of V407 Vul . . . . .	114
5.3	Phase-folded position variation for V407 Vul . . . . .	116
5.4	Dependence of the amplitude of the variation of the position upon the width of the Gaussian used to calculate the position . . . . .	117
5.5	X-Ray/optical phase-folded light curves of V407 Vul and HM Cnc . . .	121
5.6	Absence of flickering in V407 Vul and HM Cnc . . . . .	123
5.7	Possible emission sites of the X-ray and optical that reproduce the ob- served X-ray/optical relative phase . . . . .	126
5.8	The system mass constraints for V407 Vul and HM Cnc . . . . .	128
5.9	Mean fluxes and pulsation amplitudes for HM Cnc . . . . .	129
5.10	$\chi^2$ map for the primary star temperature and extinction parameter space	132

6.1	Light curves of the CVs observed . . . . .	149
6.2	Eclipse light curves of RW Tri and V345 Pav . . . . .	153
6.3	Full resolution $g'$ filter light curves of KR Aur expanded . . . . .	154
6.4	Flux ratio diagram for the observed CVs . . . . .	156
6.5	Zoom of the flux ratio diagram for the observed CVs . . . . .	157
6.6	Lomb Scargle Periodogram of the $g'$ filter light curves of the CVs . . . . .	162
6.7	Comparison of the $g'$ filter LSP of non-variable stars with the LSP of KR Aur . . . . .	165
6.8	Lomb Scargle Periodogram of the $g'$ filter light curves of the CVs . . . . .	168
6.9	Simulated light curves in the $g'$ filter . . . . .	173
6.10	LSPs of the light curves in the $r'$ , $g'$ and $u'$ filters . . . . .	177
6.11	Residual variability of the light curve of RW Tri . . . . .	179
6.12	Residual variability of the light curve of V345 Pav . . . . .	180
6.13	Low frequency LSP of the observation of LS Peg . . . . .	182
6.14	Low frequency LSP of the observation of LS Peg and significance levels for the false alarm probability. . . . .	184
6.15	Significance of the peaks of RW Tri . . . . .	185
6.16	Dynamical frequency at the radius of the white dwarf versus white dwarf mass . . . . .	190
6.17	Light curves of V404 Cyg . . . . .	193
6.18	Comparison of the LSPs of V404 Cyg and SS Cyg . . . . .	196
6.19	Light curve of EQ Peg B . . . . .	198
6.20	Flux ratio diagram for EQ Peg B . . . . .	199
6.21	Zoom of the flux ratio diagram for EQ Peg B . . . . .	200
A.1	Phase residuals of V407 Vul and HM Cnc after subtraction of constant frequency models . . . . .	214

# Acknowledgments

I am grateful to my supervisor Professor Tom Marsh for all his help, guidance and encouragement during my PhD. To him I also own the ULTRACAM reduction packages, without which the data reduction procedure would have been a nightmare. I am also thankful for the opportunity to work with the William Hershel Telescope.

I would also like to thank my collaborators for their useful suggestions, comments and kindness: Vik Dhillon, Paul Groot, Gijs Nelemans, Gavin Ramsay, Gijs Roelofs, Danny Steeghs, Joern Wilms, Peter Wheatley and Stuart Littlefair. I am specially thankful to Joern Wilms for always helping me with IDL, to Gijs Roelofs for letting me use his data on V407 Vul and to Boris Gaensicke for his help during my PhD.

I am also grateful to Dr. Kieran O'Brien for giving me the opportunity to work on Cygnus X-2, in European Southern Observatory and to visit the Very Large Telescope.

I am thankful to all the ULTRACAM team, to them I own the unique quality of my data.

I am profoundly grateful to Fundação para a Ciência e Tecnologia e Fundo Social Europeu no âmbito do III Quadro Comunitário de Apoio who supported in full this PhD.

I was very lucky to have met wonderful people during my PhD who made happier my time at Warwick: Amornrat Aungwerojwit, Daniela Floro, Carlos Barros, Carla Gil, Luisa Coelho, David Collins, Cristiana Lages, Marta Ferreira Dias and Monihar Dhillon. I also thank my parents and my sister for their love and support.

# **Declarations**

I declare that this thesis has not been submitted for a degree at another university. The material of this thesis is my own work although it contains help from my collaborators. Specifically the author of appendix B is Professor Tom Marsh.

The following chapters are based on refereed publications that were submitted during the course of my studies:

Chapter 4: S. C. C. Barros, T. R. Marsh, P. Groot, G. Nelemans, G. Ramsay, G. Roelofs, D. Steeghs, J. Wilms, "Geometrical constraints upon the unipolar model of V407 Vul and RXJ0806.3+1527", Monthly Notices of the Royal Astronomy Society, 357,1306,(2005).

Chapter 5: S. C. C. Barros, T. R. Marsh, V. S. Dhillon, P. Groot, S. Littlefair, G. Nelemans, G. Roelofs, D. Steeghs, P. J. Wheatley, "ULTRACAM photometry of the ultracompact binaries V407 Vul and HM Cnc", Monthly Notices of the Royal Astronomy Society, 374,1334 (2007).

# Abstract

This thesis focuses upon two different aspects of interacting binary stars, the study of the shortest period binary stars known V407 Vul and HM Cnc and the study of stochastic variability in cataclysmic variable stars.

V407 Vul and HM Cnc are X-ray emitting stars with X-ray and optical light curves that are modulated on periods of 569 and 321 s, respectively.

In chapter 4 we consider geometrical constraints upon the unipolar inductor model for these stars, in particular what parameter values (component masses, orbital inclination and magnetic colatitude) can describe the X-ray and optical light curves. We find that for a dipole field on the primary star, the unipolar inductor model fails to match the data on V407 Vul for any combination of parameters, and can only match HM Cnc if the sparser set of observations of this star have been unlucky timed.

In chapter 5 we present optical light curves of V407 Vul and HM Cnc. The optical and X-ray light curves of HM Cnc have been reported as being in antiphase, but we find that in fact the X-rays peak around 0.2 cycles after the maximum of the optical light, as seen also in V407 Vul. The X-ray/optical phase shifts are well explained under the accreting models of the systems if most of the optical modulation comes from the heated faces of the mass donors and if the X-ray emitting spots are positioned in advance of the mass donors, as is expected given the angular momentum of the accreting

material. Some optical emission may also come from the vicinity of the X-ray spot, and we further show that this can explain the non-sinusoidal light curves of HM Cnc. The only significant difference between the two stars is that V407 Vul is observed to have the spectrum of a G star. The variation in position on the sky of a blend of a variable and a constant star can be used as a measure of their separation, and is sensitive to values well below the limit set by seeing. We apply this “pulsation astrometry” to deduce that the G star is separated from the variable by about 0.027 arcsec and hence plays no role in the variability of V407 Vul. We show that light travel time variations could influence the period change in V407 Vul if it forms a triple system with the G star.

In chapter 6 we present the study of flickering. Flickering is a characteristic of accreting systems. It is thought that the maximum frequency present in an accretion disc is the dynamic frequency at the inner accretion disc radius. In cataclysmic variable stars this would appear as a break in the power spectrum on frequencies 0.01 – 3 Hz. We use the high speed CCD Camera ULTRACAM to obtain high time resolution data on 14 cataclysmic variables in the hope of seeing the expected break in their power spectrum. We did not find such a break because the power spectra of the cataclysmic variable stars observed was steeper than was expected. We measure a power spectrum proportional to  $f^{-2.5}$  while previous studies reported it to be proportional to  $f^{-2}$ . We compared flickering in cataclysmic variable stars with stellar flares and concluded that they have the same colour behaviour so they have could the same origin i.e. magnetic reconnection. We also compare the power spectra of cataclysmic variable stars and of X-ray binaries in the optical and concluded that the latter are much shallower than cataclysmic variable stars. We argue that this implies that flickering in X-ray transients comes from the inner accretion disc in both systems since their outer discs are thought to be similar.



# Chapter 1

## Introduction

### 1.1 Motivation

This thesis is divided into two areas: the study of the shortest period binaries known, V407 Vul and HM Cnc, and the study of accretion discs in binaries through the study of stochastic variability.

V407 Vul and HM Cnc show special properties hence our difficulty in classifying them. Moreover regardless of what is the correct model for these systems their unique nature will bring insight to their class of objects. We initially study these systems to determine if they flicker. Flickering has been used in the past to prove the existence of accretion and is the object of study of the second part of this thesis. We studied flickering in several cataclysmic variable stars (CVs) taking advantage of the high time resolution of ULTRACAM. Our data is one of the highest time resolution optical data of cataclysmic variables. Our aim was to probe the inner accretion discs in these systems which is where the high frequency variability is thought to come from.

In this chapter I will give an introduction to CVs, discussing how they are formed, how they evolve and review the different types of CVs and related objects. I will also give an overview of the accretion discs in CVs. I will finish with a summary about stochastic

variability in interacting binaries. I will start with a broad overview of the variability of stars.

## 1.2 Variable Stars

Stars show variability that can be seen with the naked eye. However, due to Aristotle's dogma of the immutability of the sky, in the West the first reference to variability of stars dates only from 1572 when Tycho Brahe observed a supernova in Cassiopeia. In the East there are references in Chinese astronomical records to the supernova explosion that created the Crab nebula in 1054 AD. Besides supernovae, which are extreme events, stars show variability with many different timescales and amplitudes. Variability can be periodic or not and it can be intrinsic to the system or due to geometric effects like, for example, eclipses. Some examples of intrinsic variability of a star are: rotation of a non-homogeneous atmosphere, magnetic-flares, instabilities of stellar structure or mass transfer in an interacting binary.

Variable stars are classified in groups and sub-groups that have similar properties. This thesis focuses upon interacting binaries, specifically cataclysmic variable stars and related objects. In interacting binaries the stars are so close that mass is transferred from one star to the other. They show continuous variability due to their binary nature (showing different perspectives of the system as it rotates) and due to the mass-transferring process which is turbulent by nature. Furthermore, some types of interacting binaries develop instabilities and show different types of recurrent eruptions, such as dwarf novae and novae and others might even end as a type Ia supernovae. Cataclysmic variable stars are a type of interacting binary where the accretor is a white dwarf. The name comes from the Greek word "Kataklýsmos" which means flood, deluge, catastrophe. The transfer of matter from one star to the other is seen as a flood that in some rare cases (like novae) can have a catastrophic effect on the star, although in many cases it

can be relatively calm!

### 1.3 Close Binary Stars

More than half of stars are binaries or multiple systems (Duquennoy & Mayor 1991; Halbwachs et al. 2003). In a binary, the stars are gravitationally bound and affect each other's motion. Assume that the stars have masses  $M_1$  and  $M_2$ . In general the relative motion of the two stars is an ellipse with semi major axis  $a$ . According to Kepler's third law the period of the orbit is:

$$P = 2\pi \sqrt{\frac{a^3}{G(M_1 + M_2)}} \quad (1.1)$$

where  $G$  is the gravitation constant. In a close binary tidal forces are strong and tend to circularise the orbits and synchronise the rotation period of the star with the orbital period of the binary (Zahn 1977). The timescale for synchronisation is proportional to  $(a/R)^6$  and the timescale for circularisation is proportional to  $(a/R)^8$ . We will restrict our discussion to interacting binaries, where the accretor is a compact degenerate star. In interacting binaries the accretor is called the primary star and it accretes matter from the mass donor star or secondary star. Since the primary star is an evolved star we can assume that the tidal forces have had time to circularise the orbit and at least the secondary star (which usually is a main sequence star or a sub-giant so it has a relatively large radius) is synchronously rotating. Therefore hereafter we assume circular orbits and synchronous rotation of the secondary star.

To compute the potential of the two stars in the rotating frame we use the Roche approximation in which the stars are approximated as point masses. Consider a Cartesian coordinate system  $(x,y,z)$ , where the origin is in the centre of star 1, the  $x$ -axis is in the direction of the centre of star 2, the  $z$ -axis is along the rotation axis and the  $y$ -axis is given by right-hand rule. In this coordinate system star 2 is at  $(a,0,0)$  and the centre of

mass is at  $(\mu a, 0, 0)$  with  $\mu=M_2/(M_1 + M_2)$ . The total potential of the system is equal to the sum of the gravitational potentials of each star plus the centrifugal potential and is given by:

$$\Phi = -\frac{GM_1}{\sqrt{x^2 + y^2 + z^2}} - \frac{GM_2}{\sqrt{(x - a)^2 + y^2 + z^2}} - \frac{\Omega^2}{2} \cdot [(x - \mu a)^2 + y^2] \quad (1.2)$$

The level surfaces of this potential ( $\Phi=\text{constant}$ ) are called the Roche equipotentials. In Fig. 1.1 we show a plot of the equipotentials in the plane  $z = 0$  for  $M_2 = 0.4 M_1$ . The equipotential surfaces are almost spherical near the centre of the stars. Further out the gravitational influence of the companion distorts the equipotential surfaces that become elongated in the direction of the other star due to gravity, and flattened in the  $z$  direction due to rotation. The surface of the stars is an equipotential surface because these have zero tangential force. Due to its larger radius the secondary star is the most affected by the presence of the companion and it has a spherical shape elongated in the  $x$  direction. The primary star is compact so it preserves its spherical shape.

If we compute the derivative of the potential we can find extremes of the potential - equilibrium points (Lagrangian points). At the Lagrangian points the net force of the binary upon a test particle is zero. There are five Lagrangian points which are plotted in Fig. 1.1.

From the second derivative of the potential we conclude that at  $L_1$ ,  $L_2$  and  $L_3$  the equilibrium is unstable in the  $x$  direction and that  $L_4$  and  $L_5$  are also unstable except for extreme mass ratios  $q < 1/24.96$ , where  $q = M_2/M_1$ .  $L_1$  is called the inner Lagrangian point and is specially important. The critical potential that passes through this point, has a figure-eight shape with two “Roche Lobes”. An approximate formula (Eggleton 1983) for the  $L_1$  point is:

$$\frac{R_{L_1}}{a} = \frac{0.49 q^{2/3}}{0.6 q^{2/3} + \ln(1 + q^{1/3})} \quad (1.3)$$

According to whether the component stars fill their Roche Lobes, the binaries are classified as:

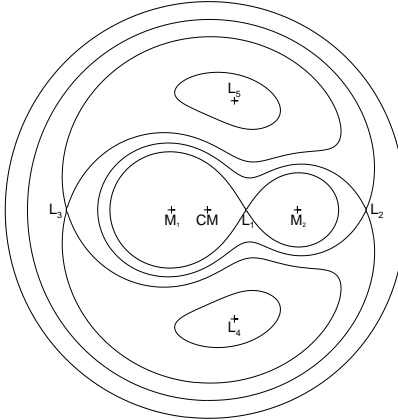


Figure 1.1: Roche equipotentials in the plane  $z = 0$ , for  $M_2/M_1 = 0.4$ , the position of the Lagrangian points is plotted. (Wilms, priv. comm.)

- Detached, when both stars are smaller than their respective Roche Lobes.
- Semi-detached, if the secondary star overfills its Roche Lobe. This is the case of interacting binaries, where as mentioned above, there is mass transfer from the secondary star to the primary star through the  $L_1$  point.
- Contact binaries, if the two stars overfill their Roche Lobe. In this case a common envelope forms around the two stars. W UMa stars are examples of these.

Cataclysmic variables are semi-detached binaries where the primary star is a white dwarf. If the primary star is a neutron star or a black-hole, the systems are called X-ray binaries.

## 1.4 The Formation of CVs

Most binary stars are detached systems but some of them can evolve to become semi-detached either by expansion of one of the stars or by shrinking of the Roche-Lobe.

In a binary, the heavier star evolves off the main sequence first and becomes a red giant. If the original period of the system is less than 10 years then the star will

overfill its Roche Lobe and transfer matter to its companion. When mass is transferred from the heavier star to its companion, the mass moves away from the centre of mass and gains angular momentum. To conserve angular momentum the binary must shrink. If in response to mass transfer the binary shrinks, the overfilling factor of Roche Lobe of the donor star increases enhancing mass transfer in a runaway process. Therefore, this configuration is unstable. In the opposite case when the primary star is lighter than the secondary star, the binary separation increases and the system is stable to mass transfer. In the unstable configuration the mass transfer process continues rapidly until at some point the primary star also overfills its Roche lobe and the system becomes a contact binary sharing a common envelope. The drag force due to the movement of the stars inside the common envelope will shrink the period of the binary further and it acts as a propeller of the outer layers (Paczynski 1976; Iben & Livio 1993; Iben & Tutukov 1993). Eventually, the envelope is expelled forming a planetary nebula and leaving a binary composed of a white dwarf (remnant of the heavier star) and a red dwarf in its centre. If after the common envelope phase the system is semi-detached and stable, we have a cataclysmic variable. If the white dwarf is lighter than its companion, mass transfer is unstable and the binary will merge. However, if the binary is detached it might be brought into contact by angular momentum loss and become a cataclysmic variable. When this happens in less than the Hubble time the binary is called a pre-CV.

## 1.5 Angular momentum loss mechanisms

Since CVs are stable to mass transfer, they have to lose angular momentum so that the secondary star is kept in contact with its Roche lobe and the mass transfer processes continues. In CVs and pre-CVs there are two processes that cause the loss of angular momentum in a binary and decrease the binary separation, driving their evolution. These are: gravitational radiation and magnetic braking.

**Gravitational Radiation** The general theory of relativity states that a binary system loses angular momentum by emission of gravitational waves. This was first suggested by Kraft et al. (1962). Using weak-field general relativity, for example Landau & Lifshitz (1958), proved that the variation of angular momentum due to gravitational radiation is given by:

$$\frac{\dot{J}_{GR}}{J_{GR}} = -\frac{32}{5} \frac{G^3}{c^5} \frac{M_1 M_2 M}{a^4} \quad (1.4)$$

where  $c$  is the speed of light and  $M = M_1 + M_2$ . From equation 1.4 we can see that gravitational radiation is only important when  $a$  is small, i.e. in short period systems. King (1988) derives an estimate of the mass transfer rate given by gravitational wave emission.

$$-\dot{M}_2 = \dot{M}_{GR} \approx 10^{-10} \left( \frac{P_h}{2} \right)^{-\frac{2}{3}} M_\odot \text{yr}^{-1} \quad (1.5)$$

This mass-transfer rate is in agreement with the observed mass transfer rates below a period of 2 hours. For long period systems angular momentum loss due to gravitational radiation is very small and other mechanisms are needed to explained the observed mass-transfer rates. The best candidate is magnetic braking.

**Magnetic Braking** In a magnetic rotating star, stellar wind is forced to follow magnetic field lines and co-rotate with the star to large distances. The resulting lever arm creates a torque that spins down the star's rotation. In a close binary the rotation period of the secondary star is locked to the orbital period, which also decreases. Therefore the binary shrinks due to angular momentum loss to the stellar wind. This process was first suggested by Huang (1966), Mestel (1968) and Eggleton (1976) and applied to binaries by Verbunt & Zwaan (1981). Although the exact theory for magnetic braking is still under discussion, King (1988) gives an estimate

of the mass transfer rate due magnetic braking:

$$-\dot{M}_2 = \dot{M}_{MB} \approx 6 \times 10^{-10} \left(\frac{P_h}{3}\right)^{\frac{5}{3}} M_{\odot} \text{yr}^{-1} \quad (1.6)$$

This is in agreement with estimated mass-transfer rates of CVs with periods longer than 3 hours.

In summary angular momentum loss drives the evolution of CVs and secular changes the orbital parameters.

## 1.6 Secular evolution of CVs

As explained above, CVs evolve to shorter periods due loss of angular momentum, so the period distribution of these systems is similar to a distribution of ages (secular evolution). The period distribution of CVs is shown in Figure 1.2. There are three striking features in the period distribution of CVs:

- Long Period Cutoff – The majority of the systems have periods shorter than 12 hours.
- Minimum Period – There are very few systems that have periods shorter than 80 minutes.
- Period Gap – There are very few systems with periods between 2 and 3 hours.

Selection effects can distort the observed period distribution. For example, we expect a decrease in the number of long period CVs because their periods are longer than the typical observation time (one night  $\sim 12$  hours). However, it is generally agreed that these three features are real and are not produced by selection effects. They can be understood under the standard theory of CV evolution which was reviewed by King (1988). A more recent review can be found in Hellier (2001).

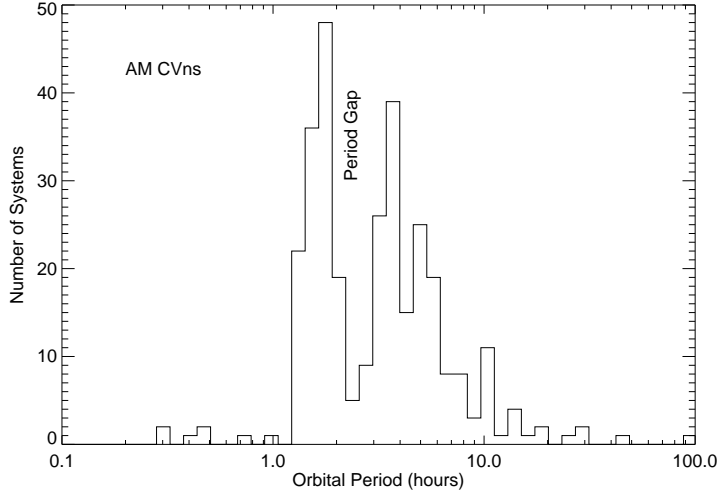


Figure 1.2: Period distribution of CVs, periods taken from the Ritter and Kolb Catalogue.

The long period cut off can be well explained by the standard evolution theory.

As mentioned above, to have stable mass transfer, the mass of secondary star has to be smaller than the mass of the primary star. In CVs since the primary star is a white dwarf it can not exceed Chandrasekhar's limit of  $1.4 M_{\odot}$ , so the mass of the secondary star also has to be less than  $1.4 M_{\odot}$ . Using the mass-period relation (equation 1.1) we conclude that the period has to be smaller than 13 hours. Note that other interacting binaries which have different primary stars or with sub-giant secondaries can have longer periods.

The reason of the existence of the period gap is less well understood. As stated above, after starting mass transfer the binary will evolve to shorter periods due to angular momentum loss. The observed mass-transfer rates below the period gap are approximately one tenth of mass-transfer rates above the period gap. As mentioned above this implies that above the period gap CVs lose angular momentum due to magnetic braking and below the gap the evolution of the system is driven by gravitational wave radiation. Therefore magnetic braking appears to stop at orbital periods of 3 hours (Robinson et al. 1981; Spruit & Ritter 1983; Rappaport et al. 1983; Taam & Spruit

1989). Although this was used to explain the existence of the period gap (Verbunt & Zwaan 1981; Spruit & Ritter 1983; Rappaport et al. 1983; Paczynski & Sienkiewicz 1983; Patterson 1984; Howell et al. 2001) it was only recently confirmed in single stars in clusters. Reiners (2007) concluded that magnetic braking appears to stop for stars with spectral type later than M3.5, which is the transition to fully convective stars. He also adds that this is not due to a decrease in magnetic activity but it might be due to a change in field topology. In CVs at a period equal to three hours the secondary star is out of thermal equilibrium because above the period gap the thermal time scale (Kelvin Helmholtz  $t_{\text{KH}} = GM_2^2/R_2L_2$ ) is longer than the mass transfer time scale ( $t_{\dot{M}}$ ). The star does not have time to adjust to the rapid mass loss and becomes over-sized for its mass. When magnetic braking stops, the secondary star has time to shrink to its thermal equilibrium radius (normal main sequence radius), and detaches from the Roche Lobe. Although the magnetic braking stops, the system still loses angular momentum through gravitational wave radiation, whose strength increases at shorter periods ( $\propto a^{-4}$ ). So gravitational radiation continues to bring the stars together until the secondary star fills its Roche lobe again and the mass transfer restarts around  $P = 2$  h on the lower edge of the period gap. This explains the difference in mass transfer rates and the existence of the period gap. The few systems observed in the period gap have probably been born there and their evolution will always be driven by gravitation wave emission.

The existence of the period minimum can be well explained by the standard theory although there is some inconsistency between the observed period minimum and that predicted by theory (Kolb & Baraffe 1999). The period minimum depends on the interplay of two timescales; the mass-transfer timescale  $t_{\dot{M}}$  which always tends to increase the binary orbital period and the thermal timescale  $t_{\text{KH}}$ . Below the period gap  $t_{\dot{M}} > t_{\text{KH}}$ . But as the period decreases  $t_{\dot{M}}$  becomes shorter than  $t_{\text{KH}}$  so the secondary star is driven out of thermal equilibrium and becomes over-sized and over-luminous for its mass. This implies that the secondary star's mass-radius relation changes and the radius

of the star is not longer proportional to the mass. When the radius of the secondary star loses its sensitivity to mass loss, the secondary star behaves like a degenerate star even before it becomes degenerate when  $M \lesssim 0.095 M_{\odot}$ . When mass is transferred from a degenerate star to a higher mass primary star, the binary period increases. In early studies the period minimum was estimated to be at  $\approx 80$  min when  $t_{\text{KH}} = 1.5 t_{\dot{M}}$  (Paczynski 1981; Paczynski & Sienkiewicz 1981; King 1988). As the binary separation increases, the mass transfer rate due to gravitational radiation gradually decreases. The orbital period continues to increase until the mass of the secondary star is so low that the star stops hydrogen burning and becomes a brown dwarf. The systems in the latest stages of evolution are so faint that are very unlikely to be observed. The minimum period depends upon the stellar mass-radius relation. For main-sequence stars it is at 80 min but for helium-rich stars (AM CVn stars) it is at 10 min (Savonije et al. 1986). In the case of the degenerate secondary at the onset of mass transfer the period can be as short as 2 min (Nelemans et al. 2001a).

Later more rigorous calculations predict a theoretical period minimum  $\sim 65$  min (Kolb & Ritter 1992) while the observed period minimum is at 80 min (Kolb & Baraffe 1999). One of the possible explanations for this discrepancy is that besides the gravitational radiation there is additional angular momentum loss. This would increase the period minimum to the observed value. Possible candidates for the extra angular momentum loss are: residual magnetic braking which would continue to operate after the period gap but at a much lower rate (King et al. 2002), or the existence of a circumbinary disc (Willems et al. 2005).

The standard theory of CV evolution has some problems. We only observe 1–10 per cent of the predicted number of CVs (Ritter & Burkert 1986; de Kool 1992; Politano 1996; Schreiber & Gänsicke 2003; Gänsicke et al. 2002). It predicts that the systems below the period gap should be 99 per cent of all CVs (Kolb 1993; Howell et al. 1997) while we observe roughly equal numbers of systems below and above the period

gap. The standard theory also predicts an accumulation of systems near the period minimum (Kolb & Baraffe 1999) which is not seen. Moreover, as mentioned above, the predicted period minimum of 65 min is different from the observed period minimum at 80 min. Furthermore recent observations of single stars suggest that the strength of the magnetic braking is not enough to produce the observed mass transfer rate above the period gap (Andronov et al. 2003). However this is still the best model to explain the period distribution observed.

## 1.7 Accretion discs

### 1.7.1 Formation of an accretion disc

Let us consider what happens when the secondary star fills its Roche lobe and the mass-transfer starts. As mentioned above, the  $L_1$  point is unstable in the direction of the primary star, so a thin stream of matter passes from the sphere of influence of the secondary star to the sphere of influence of the primary star at approximately the sound speed and it soon becomes supersonic (Lubow & Shu 1975). The matter has the same angular velocity as the  $L_1$  point around the centre of mass of the system so instead of free-falling it orbits around the white dwarf (Figure 1.3). Depending upon the system parameters the stream can hit directly the surface of the primary star (direct impact accretion) but in general the stream misses the primary star surface and ends up colliding with itself. The shock is turbulent and the material settles down into a circular orbit at the circularisation radius. The circularisation radius is the radius at which the material has the same angular momentum that it had when it was at the  $L_1$  point.

The ring of material rotates differentially around the star and there is dissipation of shear energy due to viscosity. This means that some particles lose energy and move to smaller orbits and their excess of angular momentum (relative to the Keplerian velocity) is transferred to other particles that move to wider orbits. Therefore material of the ring

is spread into a disc until it reaches the primary star surface and is accreted. Accretion discs are an efficient way of removing angular momentum from the particles so that they can be accreted; while most of the material travels inwards and releases gravitational energy, the rest of the material moves outwards carrying the angular momentum from the system. The inner disc is truncated at the radius of the primary star and outer disc is truncated due to tidal interactions with the secondary star. For a review of accretion discs see Pringle (1981). The disc can fill up to 85 – 90 per cent of the radius of the primary star’s Roche lobe. After the disc is formed the stream hits the disc forming a hot spot. The collision is turbulent so the hot spot is a source of enhanced emission and variability in the system. The hot spot can be seen directly in some light curves. Its relative brightness depends upon the system but it can reach up to 30 per cent of the total light of the system (Warner & Nather 1971; Krzeminski & Smak 1971). If the system is magnetic the accretion disc can be partially or totally disrupted as we will see later.

Most of the interest in CVs is due to the study of accretion discs which are more easily studied in CVs but also exist in other astrophysical objects like proto-stars, other interacting binaries and active galactic nuclei (AGN). Accretion discs are also responsible for most of the variability in these objects.

CVs have small angular dimensions so they cannot be resolved, however their geometry can be studied using several techniques. One of them is known as eclipse mapping (Horne 1985). Using eclipses we can have an idea of the angular dimensions of the different components of the binaries and their relative brightnesses. In Figure 1.4 we show a light curve of Z Cha, which is an eclipsing dwarf nova. The figure is adapted from Hellier (2001) but the analysis was previously performed by Janet Wood (Wood et al. 1986). The authors use eclipse mapping to decompose the light curve into the different components; the white dwarf, the accretion disc and the hot spot, whose light curves are shown at the bottom of Figure 1.4. The size of the components is related to

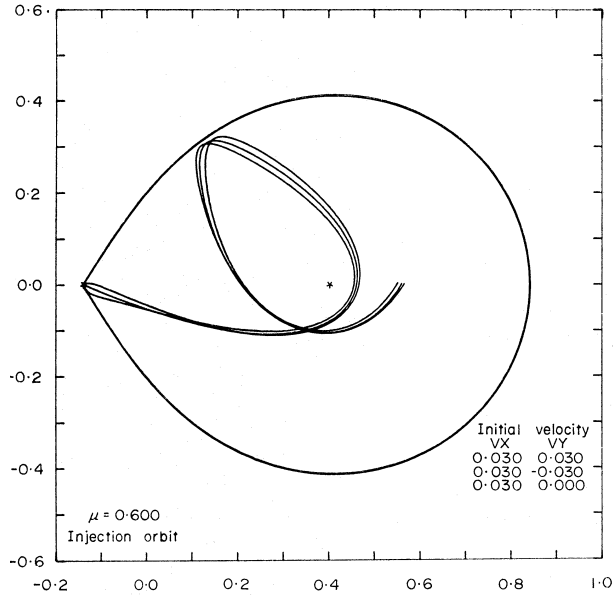


Figure 1.3: Particle path after leaving  $L_1$  for  $M_2/M_1 = 2/3$ . Three initial velocities were considered. Adapted from Flannery (1975).

the steepness of the eclipse. At an orbital phase of 0.65 the hot spot becomes visible and the brightness increases. Around orbital phase 0.96 the accretion disc and the hot spot start to be eclipsed by the secondary star. At this point the light curve is very steep because the hot spot has a small size. An even steeper drop in flux happens when the white dwarf and the inner accretion disc are eclipsed at phase 0.98. The white dwarf egress time is at phase 1.02 but the disc only comes out of eclipse at an orbital phase of 1.1.

### 1.7.2 Accretion disc viscosity

Each annulus of the accretion disc rotates at the local Keplerian velocity. So the accretion disc does not behave as a rigid body but rotates differentially. The different annuli slide by each other which causes shearing. Viscosity of the material opposes the sliding motion and damps out the shearing. Since viscosity tries to make neighbouring annuli co-rotate it speeds up material in the larger radius and slows down material in

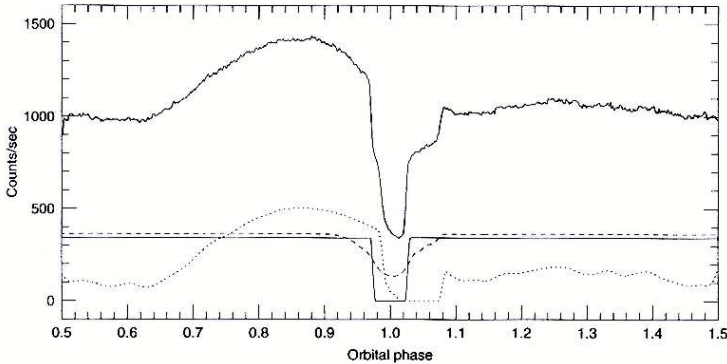


Figure 1.4: The light curve of Z Cha showing the decomposition into the light curve of the white dwarf (solid line), the light curve of the accretion disc (dashed line) and the light curve of hot spot (dotted line). This figure was adapted from Hellier (2001) and the analysis was performed by Janet Wood (Wood et al. 1986).

the smaller radius. So the end result is that angular momentum is transported outwards. The loss of angular momentum allows the material to sink to lower orbits converting gravitational potential energy into radiation, as mention above. Therefore ultimately it is viscosity which drives the accretion discs.

The nature of viscosity was elusive for many years because molecular viscosity is too low to account for the observed mass flow in accretion discs. For several decades it was assumed that the cause of viscosity was turbulence in the accretion disc which mixed material from adjacent annuli (e.g. Crawford & Kraft 1956; Shakura & Syunyaev 1973). This theory assumed that viscosity would adjust to provide a steady mass flow through the disc. Although it was assumed that accretion discs were turbulent, no known instabilities were capable of explaining the viscosity in accretion discs. In fact numerical calculations showed that they are stable and tend to damp out turbulence if it is added to the model (Balbus et al. 1996; Hawley et al. 1999).

An important advance in accretion disc theory was made by Shakura & Syunyaev (1973) who parameterised the viscosity in the alpha prescription. They assumed that the turbulent eddies are smaller than the scale height of the disc  $H$  and that they transfer material up to the sound speed  $c_s$ . So they proposed that the viscosity  $\nu$  can be written

as:

$$\nu = \alpha c_s H \quad (1.7)$$

where  $\alpha$  is less than 1. This parameterisation was important so that the viscosity could be included in the fluid equations for models of the accretion disc, although it did not give physical insight about the cause of viscosity.

The problem of viscosity was solved when Balbus & Hawley (1991) showed that although accretion discs are stable to non-magnetic instabilities, a weak magnetic field renders them unstable to angular velocity gradients. This is called the magneto-rotation instability (MRI) and is the only one known to be capable of explaining the high viscosity observed in accretion discs. The MRI is caused by the stretching of the magnetic field lines between adjacent annuli due to the differential rotation of the accretion disc, so it can be seen as a type of viscosity. The stretching of magnetic field lines amplifies the magnetic field resulting in further stretching and the process runs away. This gives rise to magnetic turbulence which is known as Balbus-Hawley instability. So its the angular momentum transport that is the cause of the instability (Balbus 2003). The MRI depends upon the coupling between the magnetic field and the accretion disc since ionised material is forced to follow magnetic field lines while neutral material is not so affected by magnetic fields. This is the likely reason for the different viscosity of the accretion discs of cold quiescent dwarf novae,  $\alpha \sim 0.01 - 0.05$ , and the hot accretion discs of dwarf novae in outburst and novalike variables,  $\alpha \sim 0.1 - 0.5$ . The cold accretion discs are weakly ionised while in the hot accretion discs most of the hydrogen is ionised, increasing the coupling between matter and magnetic field. 3-dimensional simulations of accretion discs including MRI can reproduce some details of the observations. For example in simulations of AGNs, three components form naturally, an accretion disc, a strongly magnetised corona and a jet.

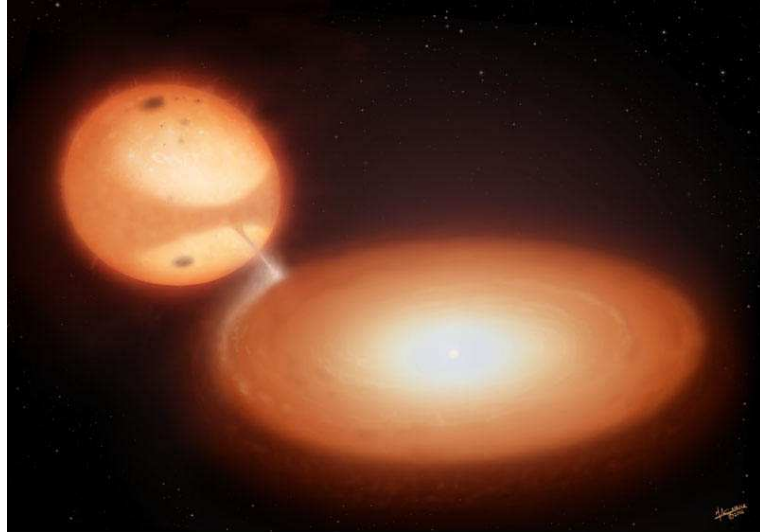


Figure 1.5: Artist's impression of a non-magnetic CV. Note that the inner disc is much brighter than the outer disc. Art by Mark A. Garlick.

## 1.8 Types of Cataclysmic Variables

There are several types of cataclysmic variables grouped according to their characteristics. The magnetic field of the primary star can have profound influence upon the geometry and evolution of the CVs so they are first divided into two groups, magnetic and non-magnetic. An artist's impression of a non-magnetic CV is given in Figure 1.5. As mentioned above the magnetic field can partially (intermediate polars or DQ Her stars) or totally (polars or AM Her stars) disrupt the accretion disc of CVs. In these cases mass is accreted through an accretion stream that is forced to follow the magnetic field lines.

The other important defining characteristic of CVs is their mass-transfer rate. The mass-transfer rate together with the mass ratio, which is related to the period, combine to create the different subclasses of non-magnetic CVs. In systems of high mass-transfer rates (most are above the period gap) the accretion disc is always in the high state and is stable (nova-like variables). In systems with low mass-transfer rates the accretion disc is in a low state and develops instabilities. These systems have occasional

outbursts and are called dwarf novae. These outbursts are responsible for the name cataclysmic for the class of objects.

A more historical division of the CVs is based on whether they had any or even more than one nova eruptions. Nova eruptions are thermonuclear runways in the hydrogen shell of accreted material on the surface of the white dwarf. The system brightness rises by about 14 magnitudes, and the amplitude is strongly correlated with the rate of fading. The classical novae are CVs that have had one recorded nova eruption. When a CV is known to have had more than one nova eruption it is called a recurrent nova. These systems can be identified spectroscopically because of the shells that surrounds classical novae after the eruption.

Any CV can belong to more than one of the classes mentioned above. I will give a brief description of some classes and some of their subclasses below. The classes are named after the first star discovered. A comprehensive review on cataclysmic variables can be found in Warner (1995) and more recent in Hellier (2001).

### 1.8.1 Nova-like variables

Accretion discs of CVs are prone to the thermal-viscous instability (Osaki 1974; Hōshi 1979; Meyer & Meyer-Hofmeister 1981). This instability develops when the mass-transfer rate of the secondary star corresponds to a disc temperature at which the hydrogen is partially ionised. When the temperature of the disc is always higher (high state) or lower (quiescence) than the instability zone, the disc is stable to the thermal-viscous instability. In nova-like variables or novalikes the disc is always ionised, i.e it is always in the high state or we could also say its always in outburst. Most of the novalikes are above the period gap since the evolution of these systems is driven by magnetic braking and their mass-transfer rates are higher.

### 1.8.2 Dwarf Novae (DN)

Dwarf novae undergo recurrent outbursts which can last for several days. This is thought to be due to the thermal-viscous instability (Osaki 1974). The brightness can rise between 2 and 3 magnitudes and in some cases by 8 magnitudes.

In dwarf novae the accretion disc is normally in the low state (quiescence) where the viscosity is low, this means that the transport of angular momentum through the disc is low. In these systems the disc mass flow is lower than the mass transfer rate from the secondary star and the material starts accumulating in the disc. When the density reaches the critical density at some annulus of the disc it sets off the thermal-viscous instability. In other words the material starts to ionise, trapping the energy while at the same time the viscosity increases and produces a runaway rise in temperature. This annulus enters into the outburst state where it has a much higher viscosity and consequently an enhanced angular momentum transport. The instability passes to neighbouring annuli spreading across the disc as a heating wave, giving rise to an outburst. When the density drops below a critical level a cooling wave is sent through the disc and it returns to quiescence. The outbursts have different light curve shapes depending upon the radius at which the outburst starts and whether only part or the whole disc goes into outburst.

Z Cam stars are a class of stars that are between novalikes and dwarf novae (Smak 1983). For the majority of time, the accretion rate of the secondary star is sufficient to maintain the disc in the high state. However occasionally the mass-transfer rate drops slightly and the disc goes into quiescence. Given that the mass-accretion rate of this system is so high, a series of outbursts follows until the mass-transfer rate rises enough so that the system returns to the high state.

There is a class of dwarf novae that besides normal outbursts also shows super-outbursts. These are called SU UMa stars. The number of normal outbursts between

superoutbursts and the recurrence time of superoutbursts (supercycle) are a characteristic of each star. The superoutbursts are possibly explained by the thermal and tidal instabilities (Osaki 1989). In these systems after a normal outburst there is still some left over material that is not removed. Therefore, material gradually accumulates in the disc which increases in size. In one of the outbursts the outer disc reaches the three-to-one resonance orbit ( $r \sim 0.46a$ ) and the outer disc becomes tidally unstable triggering a superoutburst. The disc becomes elliptical (Vogt 1982; Whitehurst 1988) and precesses creating a superhump which is also a characteristic of this class of objects. The superoutbursts are brighter and last longer than the normal outburst because the tidal stress increases the angular momentum transport in the disc. In superoutburst the mass flow in the disc is now higher than the mass-transfer rate from the secondary star so after removing the accumulated material the disc begins to shrink. When the outer disc gets smaller than  $0.35a$  the disc becomes circular, shutting down the instability. Note that the disc becomes elliptical at a larger radius on the way to outburst than when it returns to circularity; this is due to the difference in the surface density of the disc when jumping to the high state compared to jumping to the low state. The three-to-one resonance can be reached for systems with a mass ratio less than 0.3 so these systems of dwarf novae are all below the period gap. Recent 3 dimensional simulations of superhumps (Smith et al. 2007) have greatly improved our understanding of the disc eccentricity and the energy dissipation. These simulations have shown that all the disc participates in the precession and not only the regions outside the resonances. Smith et al. (2007) showed that 3 dimensional simulations can better match the observed period excess/mass ratio relation (Patterson et al. 2005) than the 2 dimensional simulations.

### 1.8.3 Magnetic CVs: AM Her

In some cataclysmic variable stars the magnetic field of the white dwarf disrupts the accretion disc. There are two subtypes of magnetic systems according to the strength

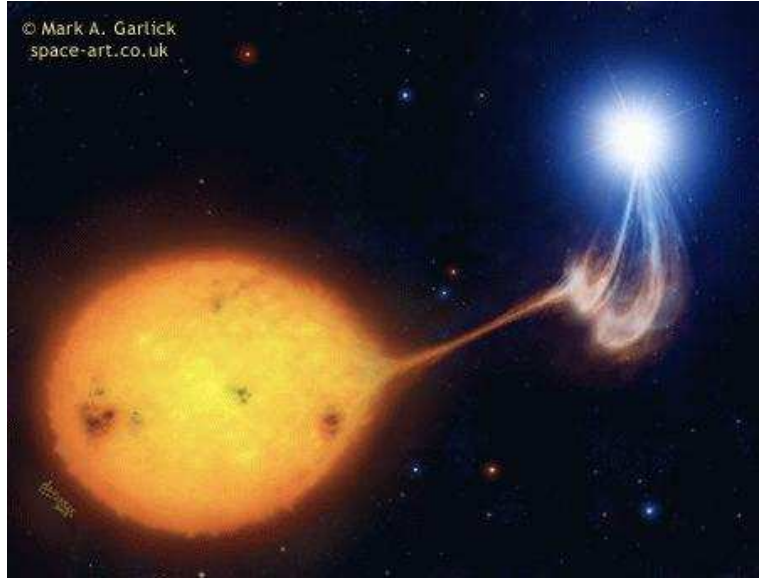


Figure 1.6: Artist's impression of a AM Her star. Art by Mark A. Garlick.

of the magnetic field of the primary star: Polars or AM Her stars ( $B \sim 10 - 230$  MG) (Schmidt et al. 1996) and Intermediate Polars or DQ Her stars ( $B \sim 1 - 10$  MG). In AM Her stars the magnetic field is strong enough to synchronise the spin period of the white dwarf with the orbital period of the binary (Figure 1.6). DQ Her stars (Figure 1.7) have weaker fields and their spin periods are shorter than the orbital period (typically  $P_{\text{spin}} \sim 0.1P$ ).

Magnetic CVs can be divided in two regions; an inner region where the magnetic field dominates the accretion which is called magnetosphere and an outer region where the magnetic field is negligible, so it behaves like the outer regions of non-magnetic CVs. The different geometries of the magnetic CVs depend upon the size of magnetosphere. Inside the magnetosphere the matter is forced to follow magnetic field lines, therefore all the magnetosphere co-rotates with the white dwarf. The spin period of magnetic CVs evolves towards an equilibrium configuration so that the speed at the radius of the magnetosphere is the same as the speed of the material just outside the magnetosphere.

In AM Her stars the radius of the magnetosphere is larger than the circularisation

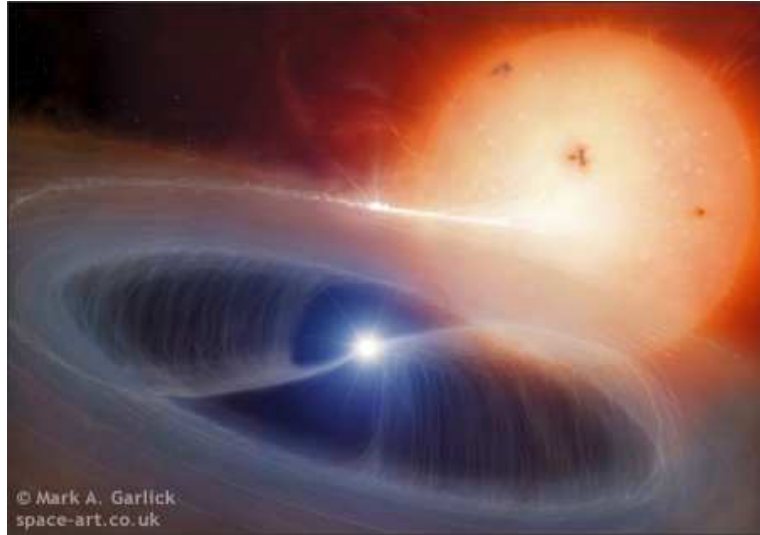


Figure 1.7: Artist's impression of a DQ Her star. Art by Mark A. Garlick.

radius so the disc cannot form. The matter coming out of the  $L_1$  point follows a ballistic trajectory but once it reaches the magnetosphere the matter is forced to follow the field lines and heads towards the magnetic poles almost in free-fall. The stream is broken into blobs surrounded by diffuse material (Wynn 2000). The ionised matter circles around the magnetic field lines emitting cyclotron radiation which is polarised. Cyclotron humps and polarisation in AM Her stars can be used to estimate the geometry and strength of the magnetic field in these systems. AM Her stars are the most polarised objects in the sky and hence the name “Polars” (Tapia 1977). Usually, in these systems, the magnetic field is tilted to minimise energy and the stream flows preferentially to one pole. The accretion spots are tiny, only  $\sim 1/100^{th}$  of the white dwarf radius. For a review on AM Her stars see Cropper (1990).

Diffuse and dense blobs behave differently as they are accreted onto the white dwarf. They create an accretion column above the white dwarf surface due to the magnetic field collimation. The diffuse material shocks the at top of the accretion column and emits hard X-rays by bremsstrahlung as it slows down and eventually settles onto the white dwarf’s surface. The denser blobs do not shock the accretion column

but directly hit the white dwarf surface, forming a buried shock. This implies that their accreting energy is thermalized and emerges as blackbody emission which peaks in the soft X-ray region. In AM Her stars most of the accreted material are dense blobs so they are strong soft X-rays emitters.

#### 1.8.4 Magnetic CVs: DQ Her

DQ Her stars have lower magnetic field strengths and are between Polars and non-magnetic systems, which is why they are also called Intermediate Polars (IPs). DQ Her stars can be stream-fed (no accretion disc) (Hameury et al. 1986) or have an accretion disc which is truncated at an inner radius. The stream-fed accretion is in equilibrium when the circularisation radius is the same as the co-rotational radius. The disc-fed systems are in equilibrium when white dwarf co-rotates with the Keplerian motion at the magnetosphere radius. This is the reason for the observed relation  $P_{\text{spin}} \sim 0.1P$  (Barrett et al. 1988; Warner & Wickramasinghe 1991). For a review on DQ Her stars see Patterson (1994).

In a disc accreting DQ Her star, the disc feeds material onto the field lines over some range of azimuth through an accretion curtain and creates a small ring around the pole where the material hits the white dwarf. Contrary to the AM Her stars, in DQ Her stars normally there is accretion to both poles. This implies that as the star rotates the occultation of one pole is cancelled out by the appearance of the other pole and we have no reason to expect pulsations. However a characteristic of IPs is that they show several periodicities (e.g. Hellier 1993) in their light curves: the orbital period, the spin period of the white dwarf and the beat period between the two. In this case the observed pulsations are thought to be due to veiling of the accretion spot by the accretion curtain (King & Williams 1985). When the upper pole is pointing towards us, the accretion curtain obscures the accretion spot and the X-rays and optical show a minimum of emission. When the upper pole points away from us we can directly see the

accretion spot so the X-rays show a maximum. Moreover at this point, the accretion curtain presents to us its maximum area so also the optical will show a maximum.

Contrary to Polars, in Intermediate polars most of the accreted material consists of diffuse material so they are strong emitters of hard X-rays and show low levels of soft X-rays. Furthermore they have other sources of optical emission apart from cyclotron radiation so due to dilution of the polarised light, very few DQ Her stars show polarisation.

The synchronisation of the spin period of the white dwarf with the orbital period of the magnetic systems depends upon the magnetic field strength but it also depends upon the orbital period of the systems. Therefore we expect that some of the highest field DQ Her stars will become AM Her stars once their orbital period decreases below the period gap.

### 1.8.5 AM Canum Venaticorum Stars

AM Canum Venaticorum (AM CVns) stars are interacting binaries with short orbital periods (3-65 min) and helium rich spectra. They are part of the ultra-compact binary class and have white dwarf primary stars while the other subclass, the ultra-compact X-ray binaries have neutron star primary stars. The secondary stars of AM CVns are helium white dwarfs or helium-rich stars hence their compact nature. AM CVn stars evolution is thought only to be driven by angular momentum loss due to gravitational wave radiation and as a result their mass-transfer rate is a function of the orbital period. According to their orbital period the AM CVns show three different states which are due to the stability of the helium disc. Systems with periods shorter than 20 min are in the high state and show low amplitude photometric variability including distinct orbital and superhump periods. Systems with periods between 20 and 40 min are in the outburst state and are the helium-rich analogues of the dwarf novae. Finally systems with periods longer than 40 min have such low accretion rates that their discs are always in quiescence.

They show no photometric variability and their periods are determined spectroscopically.

The nature and composition of the components of the AM CVn stars depend upon their formation history. There are three formation channels of AM CVns: one for the formation of a white dwarf secondary; the “double degenerate” channel (Paczyński 1967), and two involving the formation of a helium star donor either from a detached white dwarf helium star binary (Iben & Tutukov 1991) or from a CV with an evolved secondary star (Podsiadlowski et al. 2003). In the double degenerate channel a double white dwarf binary which has had two common-envelope phase, evolves to shorter periods by gravitational wave radiation. When the less massive white dwarf fill its Roche lobe, depending upon the system parameters, the binary can either merge or it becomes an AM CVn star evolving to longer periods. In a similar way a detached white dwarf plus a non-degenerate helium-rich star can be brought into contact by gravitational wave emission before helium exhaustion in the stellar core and, if the binary does not merge, it becomes a AM CVn star. Another possible way of producing an AM CVn is if a CV has an evolved secondary. Mass-transfer can remove the outer layers and leave the helium core which will behave as a helium-rich star. A discussion about the formation of AM CVns and the theoretical space density of these systems is given in Nelemans et al. (2001a) and references therein.

As mentioned above, the nature of the secondary star sets the minimum period that the systems can reach which is independent of the primary star mass. For non-degenerate helium star donors, the systems first evolve to short periods, they reach a minimum period at approximately 10 min and then evolve to longer periods. For white dwarf donors the period is minimum at the onset of mass-transfer and they evolve to longer periods (however see D’Antona et al. 2006; DeJonge & Taam 2006). In this double-degenerate configuration the orbital periods can be as short as 3 min and the orbital separation is of the order of  $0.1R_{\odot}$  so it is possible that the accretion stream directly impacts the primary star and no disc is formed (Webbink 1984). This is called

direct impact accretion (Marsh & Steeghs 2002) and may be taking place in the case of the ultra-compact candidates HM Cnc and V407 Vul (Chapter 5) and of the AM CVn star ES Cet (Espaillat et al. 2005).

The relative importance of the formation channels is difficult to establish both observationally and theoretically. The two types of donor have different mass-period relations, so for the same donor mass, systems with helium star donors have lower mass-transfer rates and longer periods due to the larger radius of the donor. But the masses and radii are difficult to measure and often one resorts to spectroscopy to determine the nature of the secondary stars (e.g. (Sion et al. 2006)). Theoretical predictions of the population density of AM CVn stars from each channel depend upon unknown parameters such as the efficiency of the common envelope phase. Therefore more observational constraints are needed to obtain a statistical sample of the number of AM CVns as a function of orbital period. Hence the need to find more AM CVns. Two surveys are currently taking place: Omega White led by Paul Groot and RATs led by Gavin Ramsay and Pasi Hakala (Ramsay & Hakala 2005; Ramsay et al. 2006b).

The study of AM CVns is of great importance since as seen above they can give insight into binary evolution. They also directly probe the cores of stars through the abundances of elements in the accretion disc. Furthermore AM CVns are test sources for the space gravitational wave detector LISA (Laser Interferometer Space Antenna)(Nelemans et al. 2001b). LISA will provide the periods and mass distribution of semi-detached and detached binaries which will revolutionise our understanding of these systems. AM CVns are also astrophysically important since they are potential progenitors of supernovae type Ia, which are used as standard candles (Nelemans et al. 2001b; Solheim & Yungelson 2005).

## 1.9 X-ray binaries

Another type of interacting binary are the X-ray binaries which have late-type star donors and a neutron star or black-hole primary stars. Since neutron stars and black-holes are more compact and more massive than white dwarfs, the accreted matter flows to a deeper potential well than in CVs. Hence X-ray binary discs are hotter and their spectra peak at X-ray wavelengths (van Paradijs & McClintock 1995). According to the secondary star's mass, X-ray binaries can be divided into low-mass X-ray binaries (LMXBs) ( $M_2 < 2 M_\odot$ ), intermediate-mass X-ray binaries ( $2 < M_2 < 10 M_\odot$ ) and high-mass X-ray binaries ( $M > 10 M_\odot$ ). In high-mass X-ray binaries, the primary star accretes from the wind of a massive companion star while low- and intermediate-mass X-ray binaries have Roche-lobe filling secondary stars. Besides the accretion disc, some X-ray binaries also have collimated jets perpendicular to the disc. The jets can be continuous or have intermittent emission and probably form near the compact object. Jet structures are also seen in AGNs. Furthermore X-ray binaries can also have coronae. The geometry of the coronae is not well established. They might lie above and below the disc (sandwich model) (Poutanen et al. 1997; Hua & Titarchuk 1995; Haardt & Maraschi 1993) or be spherically symmetric around the compact object (Dove et al. 1997).

LMXBs are similar to CVs and are also divided into two main classes according to the stability of the discs. Systems with stable discs show persistent emission while systems with unstable discs are called soft X-ray transients because in quiescence few X-rays can be detected from the systems. The outburst shows a rise in the optical and X-ray fluxes; the latter can increase by a factor of 1000. The outburst is thought to be due to the thermal-viscous instability as in dwarf novae outbursts, but in this case the timescales are longer. The outburst can last from weeks to months, but the majority of the time the systems are in quiescence. The recurrence times are variable and in some cases only one outburst has been seen. Most of the persistent sources have neutron star

accretors but the majority of soft X-ray transients accretors are black-holes.

As in CVs, LMXBs are divided into magnetic systems which include strongly magnetic neutron star primaries with magnetic fields  $> 10^{12}$  G and weakly magnetic primaries which include both neutron stars and black-hole primaries with magnetic fields  $< 10^{10}$  G. In the strong magnetic field systems, the accretion disc is disrupted at the magnetospheric radius of 10<sup>8</sup> cm (Lamb et al. 1973).

In LMXBs the optical light comes from the reprocessing of the X-rays in the accretion disc, the companion star and the hot spot. The irradiation of the disc by X-rays might be the reason why the discs of X-ray binaries are warped which makes them look thicker than CV discs.

## 1.10 Stochastic Variability in Accreting Objects

A characteristic property of accreting stellar objects is stochastic magnitude variations also called flickering. Flickering is present in the light curves of cataclysmic variables, X-ray binaries, active galactic nuclei, symbiotic stars and young stellar objects. In this section I will give an overview of flickering in weakly magnetised LMXBs, and also briefly discuss flickering in other objects and stellar flares. These will be used as comparisons to the specific case of flickering in CVs which will be discussed in detail in chapter 6.

### 1.10.1 Flickering in low mass X-rays binaries

Variability in LMXBs can be broadly divided into three types (van der Klis 2006): red power-law noise ( $P \propto f^{-\alpha}$ ), red noise that steepens towards the high frequencies (usually called band-limited noise) and quasi-periodic oscillations (QPOs) which are seen as peaks in the power spectrum. The band-limited noise (BLN) can either have a break or gradually steepen to high frequencies. If the BLN flattens at low frequencies, having  $\alpha = 0$  is called flat-topped BLN.

The low magnetic field LMXBs are divided into different source types which show similar timing and spectral properties. Black-hole binaries form one source type while neutron stars have three different source types which are in order of decreasing X-ray luminosity: Z-sources, atoll sources (Hasinger & van der Klis 1989) and weak LMXBs. There is no difference between source types for persistent and transient systems. Note that some black-hole transients remain in the low/hard state during all the outburst (Nowak 1995; Brocksopp et al. 2004).

The spectral and timing properties of the sources are correlated and they show different states. The division between the source states is qualitative, phenomenological, it makes use of the colour-colour diagram (CD), the hardness-intensity diagram (HDI) as well as the power spectrum shape (Hasinger & van der Klis 1989). The division in source type is also related to the shape that the source tracks in the CD/HDI. It is thought that the different states are due to variations of the mass-transfer rate (e.g. Hasinger et al. 1990) but an extra parameter is needed to explain the source's behaviour.

An extensive description of the different source states and their variability components is beyond the scope of this chapter but can be found in van der Klis (2006). Here I will focus on the time variability of black-hole X-ray binaries as an illustrative example. The power spectral shapes of neutron star binaries are more complex because they have more variability components and because there are more source types to consider.

Black-hole X-ray binaries show three different states according to the X-ray luminosity; low, intermediate and high states. In the low state the spectrum is the sum of a soft thermal component and a hard non-thermal power law. The soft component comes from the accretion disc and the hard component is thought to originate in the hot corona by comptonization (Nowak et al. 1999). In the high state the spectrum is dominated by the soft thermal blackbody radiation coming from the optically thick accretion disc. The unified model for radio jets (Fender et al. 2004) states that in the

high soft state there is no jet but as the system evolves to the low/hard state a jet is launched and the inner accretion disc is truncated.

The power spectrum of black-hole and neutron stars binaries can be very similar in the low state probably because the inner disc is larger so it is further away from the compact object. In the low/hard state the power spectrum shows a flat-topped BLN which can reach 50 per cent RMS variability. The characteristic frequencies are shorter for neutron stars than for black-holes which implies that neutron star systems have much higher noise power at kilohertz frequencies. As the systems move to the intermediate states, the BLN (which might include different components) becomes weaker but more coherent. Moreover the characteristic frequencies increase, which is interpreted as the inner disc getting closer to the compact object. In the high state the BLN disappears and only a power-law noise is left with a few per cent RMS variability and a power spectral index ( $\alpha$ ) of 0.7 – 1.4 (e.g. Wijnands et al. 1996).

Besides the noise components, neutron star systems show double kilohertz QPOs (200 – 1200 Hz) and hectohertz QPOs (100 – 200 Hz) while black-holes show high frequency QPOs (100 – 450 Hz). There are correlations between the frequencies of the different components which suggest that they are caused by physically similar phenomena. Since these happen in both black-hole and neutron star binaries, it suggests that they come from the accretion disc. Warner & Woudt (2002) suggested that this correlation can be extended to include QPOs observed in dwarf novae in outburst. The cause of the noise components is still unknown.

The most famous black-hole X-ray binary is Cygnus X-1. In the high/soft state the power spectrum is a flat-topped power law with a low frequency break at 10 Hz and for frequencies higher than 10 Hz the power spectrum is a power law with  $\alpha \sim 1$  (Belloni & Hasinger 1990; Nowak et al. 1999; Revnivtsev et al. 2000; Churazov et al. 2001). In the low/hard state the spectrum is flat-topped BNL. For  $10^{-3} < f < 0.1$  Hz,  $\alpha = 0$ , for  $0.1 < f < 3$  Hz,  $\alpha = 1$  and for  $3 < f < 10^3$  Hz,  $\alpha = 2$ . The steepness of the power

spectrum at high frequencies suggests that this region can be affected by red noise leak (van der Klis 1997).

Baptista et al. (2002) applied eclipse mapping, in the optical, to the LMXB X1822-317 and concluded that the bright spot does not contribute strongly to the flickering. The dominant source of flickering is the accretion disc as a whole. They also found that the non-eclipsed flickering light has a colder temperature than the outer accretion disc, while the eclipsed flickering light has a higher temperature than the inner parts of the accretion disc.

### 1.10.2 Flickering in other objects

#### AGN

AGNs show similar variability properties to black-hole X-ray binaries and it is thought that the physical processes are the same for both types of objects but the characteristic variability timescales scale with central black-hole mass. Uttley et al. (2002) analysed the power spectra of four Seyfert galaxies (which are a type of AGN) and concluded that three of them show steepening of their power spectra similar to the low state of LMXBs and possibly in the other object the power spectrum is similar to the high state of LMXBs. Their results are consistent with the characteristic timescale of AGN and LMXBs scaling linearly with back hole mass.

#### AM Her stars

Although in AM Her stars the magnetic field prevents formation of an accretion disc, they also show very strong flickering. In this case flickering is thought to be a superposition of individual flares or shots which are produced when an individual dense blob is accreted. The individual optical flares were successfully modelled as shots by Panek (1980). To describe any asymmetry in the flares, the shots were modelled by either an exponential

rise or fall. Panek (1980) concluded that the mean flare duration is 70 – 90 s, which is the time that a blob takes to cross the emission zone and that many pulses overlap at the same time. He estimated the size of the blobs for the case of a hot flow would be  $\sim 4 R_{WD}$  while for the case of a cool flow  $\sim 14 R_{WD}$ . This implies that the blobs are very elongated which can be explained by tidal forces.

### The special case of AE Aqr

AE Aqr is a quite peculiar cataclysmic variable especially due to its flaring activity. There are alternative periods of strong and quiet flickering activity. It also appears that the variability depends upon orbital phase (Bruch & Grutter 1997). These can be explained by the magnetic propeller model for the system (Wynn et al. 1997). Magnetic propellers are AM Her stars whose white dwarfs are rotating faster than the angular velocity of particles outside the magnetosphere. So the particles from the accretion stream cannot enter the magnetosphere and are accelerated by the magnetic field, the majority being expelled from the system. In this type of geometry the flickering is thought to be due to the shock of particles in the accretion stream with the particles that were expelled by the magnetic propeller. The shocks are seen preferentially at a given orbital phase (Eracleous & Horne 1996). So in this case the origin of flickering is very different from a normal CV.

### 1.10.3 Flares in M stars

Flares have been known to occur in the Sun since 1859 when they were discovered independently by two English amateur astronomers (Carrington 1859; Hodgson 1859). Haisch et al. (1991) defines a flare as a “Catastrophic release of magnetic energy leading to particle acceleration and electromagnetic radiation”. Stellar flares have timescales of minutes to more than an hour and release energy between  $10^{29}$  to  $10^{32}$  ergs from gamma rays to radio wavelengths (Strong et al. 1984). This can be directly compared with the

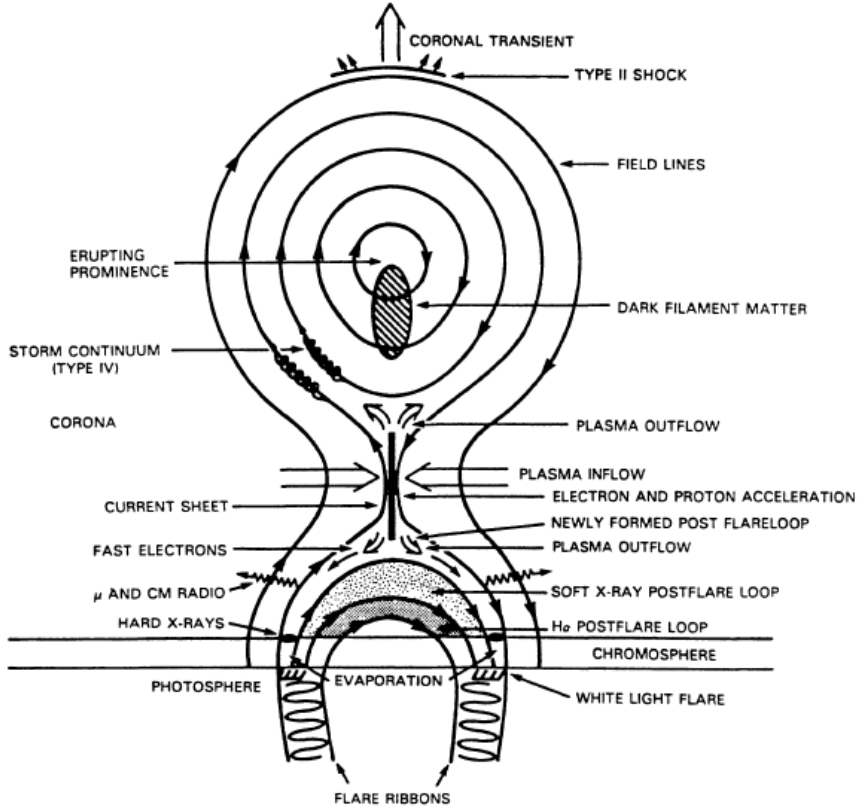


Figure 1.8: Structure of a flare in the Martens and Kuin two-ribbon flare model. Adapted from Martens & Kuin (1989).

lower limit of the energy of flares in CVs given in Figure 10 of Bruch (1992). For dwarf novae the flare typical energy is between  $1.6 \times 10^{32}$  and  $3.2 \times 10^{33}$  ergs and for novalikes it is between  $8.0 \times 10^{33}$  and  $1.6 \times 10^{35}$  ergs. So the flares of CVs are more energetic than stellar flares.

No flare model is capable of satisfactorily explaining both the trigger mechanism, the timing of the different components (radiation, ejected material and accelerated particles), spectral evolution and cooling mechanisms. There are two types of flare morphologies: two-ribbon and compact flares that are thought to be different manifestations of the same phenomenon. Figure 2 of Martens & Kuin (1989) (reproduced in Figure 1.8) shows the Martens and Kuin two-ribbon model of solar flares which is the

following: flares develop in regions of high magnetic field like sun-spot groups. Due to magnetic reconnection of the field lines currents are created in magnetic field loops. The currents heat the plasma to high temperatures ( $10^7 K$ ) producing X-rays and gamma rays. The flares do not have blackbody spectra since the different parts of the flares are responsible for different types of radiation. Hard X-rays are produced by bremsstrahlung. The spiralling of charged particles along magnetic field lines produces non-thermal synchrotron radio emission which is highly polarised. In some flares there is enhanced UV continuum emission, which appears to be produced by free-free emission of material with a temperature in the range  $14\,000 - 50\,000 K$  (Mathioudakis & Doyle 1990). Electrons and protons accelerated away from the reconnection point can recombine and are the source of the  $H\alpha$  emission from the bases of the magnetic field lines which are the two ribbon structures. The optical emission comes from the top of the loops and the ribbon/footpoints of the flare. In some flares we can see line broadening and red and blue asymmetries, which imply random motions of  $100 \text{ km s}^{-1}$  and mass flows of  $1000 \text{ km s}^{-1}$  (Rodono 1986). As well as radiation there is also emission of charged particles (electrons, protons, and heavy nuclei) at high speeds and generation of shock waves. The footpoints of the solar flares are in the chromosphere but the intense heat expands the loop into the corona: this is called chromospheric evaporation.

In this chapter I gave an introduction to CVs and stochastic variability in accreting objects. In the next chapter I describe the astronomical reduction techniques that I used to analyse the data of this thesis. I will also give a brief overview of the high speed CCD camera ULTRACAM. In chapter 3 I describe the time-series methods used. In chapter 4 I discuss the constraints upon the unipolar inductor model for V407 Vul and HM Cnc and in chapter 4 I present observations of these two systems. In chapter 6 I present observations of flickering in cataclysmic variables and I finish by presenting the conclusions in chapter 7.

# **Chapter 2**

## **Observation and Analysis**

In our study of Cataclysmic Variables we are interested in their time variability. Therefore we performed CCD photometric observations to measure their flux (or magnitude) as a function of time. Photometric observations can be used to obtain useful information about the systems e.g. their period, geometry, temperature and in some cases masses (Wood & Crawford 1986). This chapter is divided in three sections. The first describes the data reduction techniques that we use to obtain the light curves from our observations. The second section describes the ultra fast CCD camera ULTRACAM used to acquire the data of this thesis. The third and last section explains the time systems that are usually used in astronomy and how they are related.

### **2.1 Observations and reduction<sup>1</sup>**

#### **2.1.1 CCDs**

In the past, astronomical observations have been performed with photographic plates and photometers. These were often difficult to operate and have several limitations. Photographic plates, for example, have a non-linear response and need to be scanned

---

<sup>1</sup>This section is based on Howell (2000).

to obtain quantitative results. On the other hand photometers could only observe one target at a time and they have to be regularly shifted between the target, the comparison star and the sky. Nowadays we use charged coupled devices (CCDs) for astronomical observations. CCDs revolutionised modern astronomy due to their low noise level, high quantum efficiency (QE) and wide bandpass. CCDs are silicon-based semiconductor detectors whose absorption coefficient is relatively high for wavelengths between 3 500 to 8 000 Å. Therefore they are mainly used in optical photometry, although they are also used as X-ray and UV detectors. To increase the absorption of short wavelength photons the CCDs are either thinned or coated. However, thinner CCDs have lower absorption coefficients at longer wavelengths. Therefore, an anti-reflection coating is commonly used which besides increasing the wavelength range, also increases the absorption coefficient for all wavelengths. The absorption coefficient is closely related to the quantum efficiency of the CCD which is the ratio of the incoming to detected photons.

A CCD is a collection of individual pixels forming a two-dimensional array. Each pixel of a CCD works independently. When a photon hits a pixel, due to the photoelectric effect an electron from the silicon moves into the conduction band. These electrons are then trapped by a potential well created by a positive voltage applied to electrodes until the CCD is readout. Each pixel has three gates which are cycled during the charge transfer procedure. This is called clocking the device.

When the exposure ends, the CCD starts to be readout in the following way: the collected electrons are shifted down one column at a time, while the bottom column is moved to the output shift register. In the output shift register each pixel is shifted horizontally and its charge is measured and converted into a digital number, called an analog-to-digital unit (ADU). This procedure is repeated until all CCD is readout. The gain of the device is the number of photo-electrons needed to produce one ADU. The charge transfer procedure is nearly 99.999 per cent efficient and can be very fast.

However, the conversion between analog (voltage) to digital (ADU) is much slower and limits the readout speed of a CCD. A typical CCD has a readout speed of 200 kHz per pixel, therefore it takes 2 – 100 s (depending of the size) to read the all CCD frame. In some instruments like ULTRACAM the CCDs have an extra unexposed area which can be read while a new exposure is being made. This is called frame transfer and greatly reduces the dead time of the observations. ULTRACAM frame transfer speed is of milliseconds while the time to read the whole CCD is 6 seconds without binning. So for exposures of more than 6 seconds, the deadtime is effectively zero.

The readout speed can seriously limit the time resolution of the data. To make the readout procedure faster several methods were developed: frame transfer, the division of the CCD into four regions that are read simultaneously (e.g. FORS/VLT); increasing the readout speed (this increases the noise of the data); reading only a small region of the CCD (windowing); or adding neighbouring pixels which are read together (on-chip binning). All of these methods are used in ULTRACAM; the CCDs have two readout channels, they have two different readout speeds and are capable of on-chip binning. Furthermore one can define small windows.

### **Readout noise**

Although the charge transfer procedure is virtually noise-free, the same it is not true for the readout process. There are two contributions to the read noise. The first is the production of random electrons by the device which are not due to any incident photon. The second is that the analog-to-digital conversion procedure is not deterministic and the result follows a Gaussian distribution. The resulting  $1\sigma$  error is called the read noise. It is given in electrons per pixel and is characteristic of the CCD. The readout noise depends upon many details of the analogue-digital converter, such as the temperature and the readout speed. The two reading speed modes of ULTRACAM – the slow at  $11 \mu\text{s pixel}^{-1}$  and the fast one at  $5.6 \mu\text{s pixel}^{-1}$  – have respective readout noises of  $\sim 3.5 e^-$  and  $\sim 5 e^-$ .

### 2.1.2 CCD Data reduction

In any measurement we have an associated noise. The determination of the noise is crucial to understand the signal. There are several sources of noise that have to be correctly accounted for before we can measure the counts of a star.

#### Bias Subtraction

Because of statistical fluctuations and to avoid negative numbers, the zero level of the CCD is offset. The bias level is the mean value of the unexposed CCD. In the reduction of an astronomical image the bias level has to be removed so that the errors can be properly determined. There are two methods of estimating the bias level. The first is using a “bias frame” with zero seconds exposure. To reduce statistical noise, several frames should be averaged to produce a master bias. This can be directly subtracted from the object frames or, if the bias is uniform and does not have 2-dimensional structure we can just subtract the mean level of bias frame. The second method consists of having unexposed regions (over scanned) in each image. These are used to compute the mean bias level. They do not provide any information about the spatial variation of the bias but can be very useful in case the bias level varies with time. The bias level should be relatively stable but can drift on timescales of months.

An example of an ULTRACAM master bias is given in Figures 2.1 and 2.2 for the left and right parts of the CCDs. As mentioned above, ULTRACAM has two reading channels, that are read simultaneously to increase the reading speed; one in the left and one in the right. To distinguish the right and left parts of the CCD when positioning the stars, they have different mean bias levels. Therefore if plotted together the small scale structure is lost. The variation of the bias level from pixel to pixel is due to the readout noise. Hence, the bias frame can be used to estimate the readout noise of a CCD. The pixel values of a bias frame follow a Gaussian distribution with  $\sigma$  or RMS

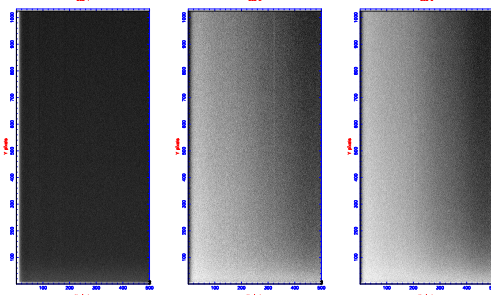


Figure 2.1: Example of an ULTRACAM left bias frame. From left to right we show CCD 1, CCD2 and CCD 3, where the x axis is the pixel number in the x direction and the y axis is the pixel number in the y direction.

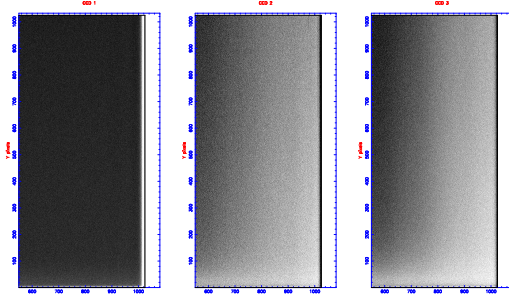


Figure 2.2: Example of an ULTRACAM right bias frame.

equal to the readout noise in ADU or the ratio of the readout noise in electrons and the gain. The mean and the RMS typical values of an ULTRACAM master bias frame are given in Table 2.1.

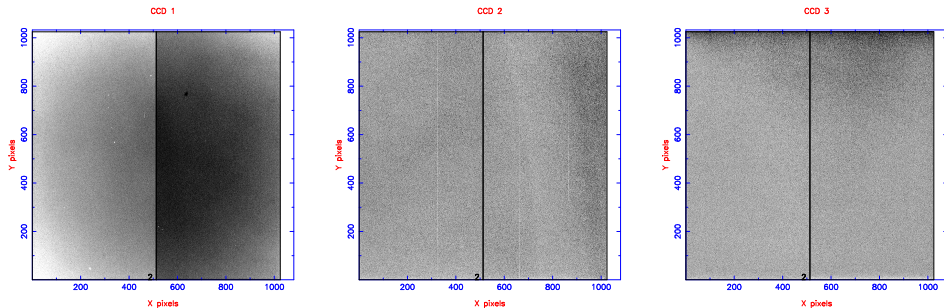


Figure 2.3: Example of an ULTRACAM dark frame

Filter	left		right	
	mean	RMS	mean	RMS
r	2243.0	3.03	2301.6	3.04
g	2148.2	3.09	2214.4	3.36
u	2457.1	3.44	2357.9	3.15

Table 2.1: Mean and RMS of a typical typical bias frame.

### Dark current

Due to thermal effects, electron/hole pairs can be generated spontaneously. This means that at room temperature, electrons (it can be as many as  $2.5 \times 10^4$  electrons pixel $^{-1}$  second $^{-1}$ ) will be freed from the material (dark current) and will be added to the “real” photo-electrons. These can be the dominant source of noise especially for long exposure times. So in astronomical observations the CCDs are normally cooled to reduce the dark current. They can be cooled either by liquid nitrogen or by thermoelectric cooling devices using the Peltier effect. The ULTRACAM CCDs are cooled to 233 K by a Peltier cooler. At this temperature the ULTRACAM CCDs have a dark current of only  $0.05 e^- \text{ pixel}^{-1} s^{-1}$ .

The noise due to dark current follows a Poisson distribution, consequently it is proportional to the square root of the dark current. We can estimate the CCD dark current and subtract it from our observations. To estimate the dark current one takes an exposure with no light (shutter closed). The frame has to be divided by the exposure time and have the bias subtracted. It is recommended to make several of these and then calculate the mean dark frame to reduce statistical fluctuations. If the dark current behaviour is non-linear, a dark frame with the same exposure time as the observations is advisable. An example of an ULTRACAM dark frame is given in Figure 2.3. The mean value of the dark frame is different between the two CCD channels and it is higher for the red CCD.

## **Flat field**

The QE and the gain can be slightly different from pixel to pixel. Consequently, we need to use a flat field image to correct for the different sensitivity of the CCD pixels. The sensitivity of each pixel is wavelength dependent so a flat field is needed for each different filter. To obtain a flat field, the CCD has to be uniformly illuminated. In practise, this is not easy and there are two different types of flat fields that are normally used. One is an image of the inside of a telescope dome illuminated by a light source (dome flats). The other is a sky flat which is an image of a relative empty region of the twilight sky with the telescope spiralling to blur the objects, so that they can be removed by taking the median. As with bias and dark frames is it important to average several bias-subtracted flat frames to compute a master flat. The master flat has to be normalised before it can be used. The ULTRACAM is run in inverted mode to reduce dark current but this has the disadvantage of creating structures in the CCD when the number of counts reaches approximately 50 000, 31 000 and 27 000 for the red, green and blue CCDs, respectively. This happens before normal saturation and we call it peppering because it looks like pepper (Figure 2.4). So care should be taken so that frames that have peppering and saturated pixels are discarded and are not used to produce the final flat image. To perform the flat field correction we divide each object image by the master flat in the respective filter. We show a typical ULTRACAM flat frame in Figure 2.5.

## **Noise analysis**

Knowing accurate readout noise and gain values of the CCDs is important in order to be able to estimate accurate errors of our measurements. To determine the readout noise and gain of the CCDs we can perform a noise analysis. As mentioned above the readout noise can be estimated from the RMS of the bias frame. To obtain the value of the gain we need calibration dome flats with increasing exposure time. These frames

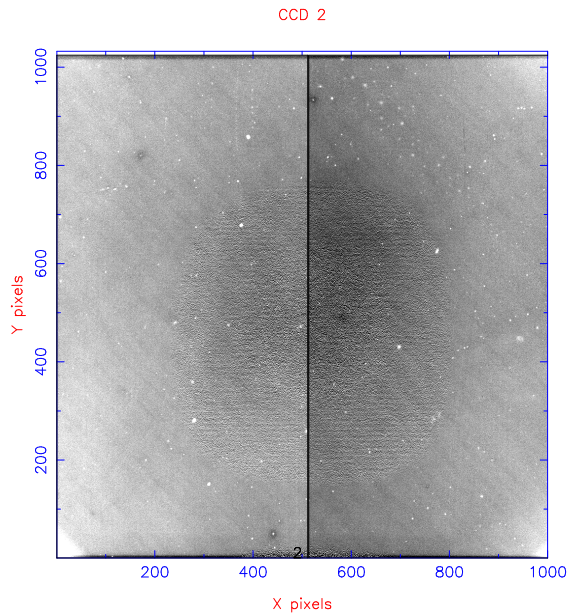


Figure 2.4: Example of peppering in the g' CCD.

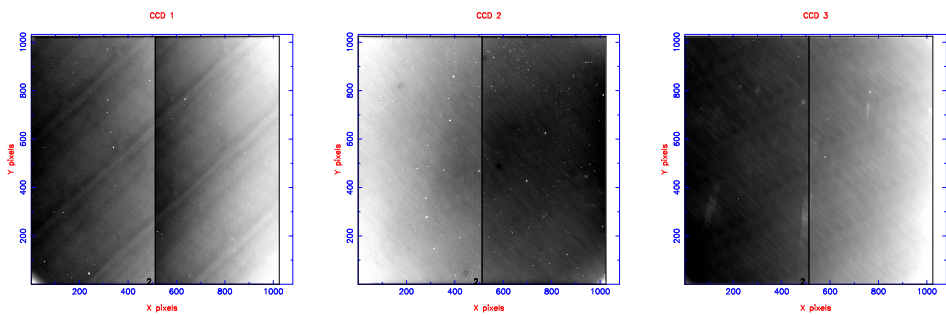


Figure 2.5: Example of an ULTRACAM flat frame

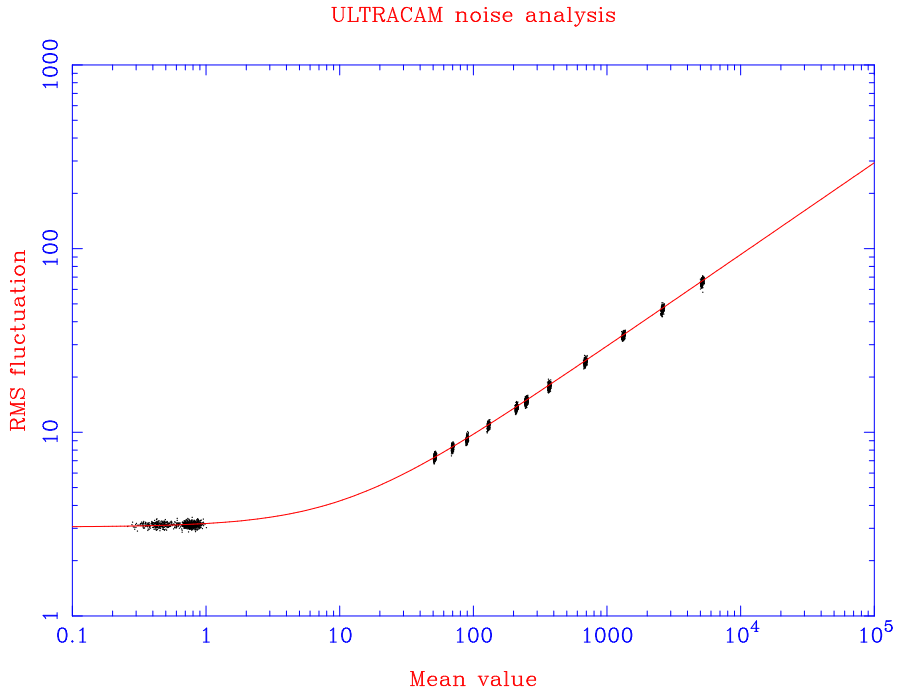


Figure 2.6: Example of the noise analysis of the left frame of the CCD1 in ULTRACAM. The RMS fluctuations of several frames are given as a function of the mean of the counts. These are well described by equation 3.29 with model parameters R=3.16 ADU and G=1.16 electrons/ADU which is shown in red.

have to be bias subtracted and flat field corrected. Then, for each frame we calculate the mean and the RMS value over a set of pixels. The RMS and mean of the counts (C) follow the relationship:

$$\text{RMS} = \sqrt{R^2 + \frac{C}{G}} \quad (2.1)$$

which allows us to determine the readout noise (R) and gain (G). The result of a noise analysis of the left window of the red CCD is given in Figure 2.6.

The readout noise and gain of the three ULTRACAM CCDs is slightly different but for most proposes they can be considered to be the same. However, to obtain correct estimates of the white noise level in the three bands in chapter 6 we had to include the variations of the gain and readout noise.

### 2.1.3 Differential Photometry

Basic calibration and reduction procedures like bias and dark subtraction and flat field correction are the same for astrometry, photometry and spectroscopy. Further calibration might be needed depending upon the specific objectives of the observations. For example, if imaging spatially revolved objects, removal of cosmetic effects might be needed.

I will concentrate on the photometric reduction because it was the technique that I used in this thesis. Photometry is the measure of the flux of an object. We can obtain the absolute flux, the colour or the variation of the flux as a function of time. There are several photometry packages that use different techniques but they all have to follow three basic steps: determine the centre of the object, estimate the background or sky level and finally determine the flux of the object.

#### Centering the object

The image of a point source through the telescope is called the point spread function (PSF) and can be approximated by a two dimensional mathematical function such as a Gaussian, Lorentzian or Moffat profile. A Moffat distribution (Moffat 1969) has more extended wings than the Gaussian so usually describes better the PSF of an image of a star. The Moffat is capable of fitting well both the core and the wings of the PSF due to the extra parameter  $\beta$  which controls the wings. The Moffat distribution as a function of  $r$  from its centre is given by:  $f = h/(1 + (r/r_0)^2)^\beta$ , where  $h$  is the height of the profile and  $r_0$  is the width parameter. We normally use  $\beta \approx 3$ . Although the Gaussian does not give good fits due to its short wings, it has the advantage of being less affected by nearby stars so it can give better results in crowded fields.

To determine the centre of a profile we begin with a rough position and a search box. Then within the search box we collapse the profile in the x and y directions. These

follow approximately a Gaussian distribution from which we can obtain the centre of our object, using Gaussian cross-correlation.

### **Estimating the sky level**

The counts in our object also include counts from the sky background. Therefore, to determine the flux of the object, we first have to remove the contribution of the sky. To estimate the sky background it is usual to place an annulus around the object. The annulus should be big enough to provide a good statistical measurement of the sky but should not include other stars which will contaminate it. The pixels counts that lie inside the annulus are used to estimate the sky level. Different methods can be used to estimate the mean sky count: a straight mean, a median, a mean with rejection of values that are  $3\sigma$  away ("clipped mean"). A mean with a  $3\sigma$  rejection is a very robust method as it will eliminate cosmic rays and possible stars in the annulus. An even better estimation of the sky background can be obtained if after the  $3\sigma$  rejection we construct an histogram of the sky values. After some smoothing, the histogram can be used to compute the mean value of the sky background. A good estimation of the sky background per pixel is very important since it will have a cumulative effect in all the pixels of the object.

### **Determining the flux from the object**

To correct for the different observation conditions i.e. seeing and transparency, we use a comparison star and always compute the number of counts (or magnitude) of our target relative to the comparison star. This is called differential photometry and is based on the assumption that the two stars suffer the same light losses for a given observation. Therefore, apart from the actual technique we use to measure the flux from a star, what is most important is that we use the same technique for the target and the comparison star.

To estimate the flux from the object, we place a circular aperture centred on the object and use the count values of the pixels inside the aperture. There are three techniques we can use to estimate the intensity of the source:

- **Aperture Photometry** Where the flux is simply the sum of the pixels counts within the circular aperture, each subtracted by the sky counts per pixel. There are different ways of dealing with pixels that are partially inside the aperture. They can be either, all rejected, all counted or they can be weighted by the area that lies inside the aperture. The radius of the aperture that should be used depends upon the brightness of the object and the observing conditions and has to be the same for the target and the comparison star. What is normally done is to use several apertures and choose the one that results in the smallest error to the final quantities that we want to measure. In principle, one could think that the larger the aperture size the better, to avoid loss of counts from the object. However, in reality, big apertures have larger errors due to increased contamination from neighbouring objects and the sky. The best aperture is normally around 1.5 times the full width at half maximum (FWHM) (Naylor 1998), but tends to be larger for bright stars.
- **Variable Aperture Photometry** This method is equivalent to aperture photometry for each frame but the size of the aperture varies from frame to frame depending upon the seeing. Hence, the aperture radius is defined as a multiple of the seeing. In each frame, the seeing is estimated by profile fitting of a bright reference star which usually is the comparison star. As for aperture photometry we have to use the same aperture radius for the target and the comparison star in each frame.
- **Optimal Photometry** For faint objects (background limited), Naylor (1998) developed an algorithm to compute an optimal aperture size that maximises the signal-to-noise. The method uses profile fitting of the PSFs to weight the counts.

The PSFs can be fitted with a Gaussian or a moffat profile. This technique is based on the fact the central part of the profile has higher signal-to-noise and therefore should be given higher weight when we determine the flux. It does have advantages for faint objects but it is not advisable for bright ones. It can give poor results if the profiles are different from each other. Most of the software packages include the option to perform optimal photometry.

The best technique to use depends on the data. For crowded fields, profile fitting is likely to give better results, while if the PSF is somehow distorted, aperture photometry is the best one to use. The exact procedure used to reduce our data is given for each specific case. In general, I computed aperture, variable and optimal photometry and compared the results. For aperture and variable photometry I experimented with several aperture radii. Finally, I choose the reduction procedure that gave the highest signal-to-noise. An example of an object frame is given in Figure 2.7 for V407 Vul. The vertical line in the middle of the CCD shows the boundary between the two reading channels of the CCD. We measure the counts of five objects, which in the image have marked apertures. The target star (V407 Vul) is aperture number 1. The main comparison star which is the reference star (used to measure the FWHM) is aperture number 2. We can see that V407 Vul is in a very crowded field and close to a bright star so care was taken to avoid contamination of the target aperture.

#### 2.1.4 Flux calibration

After we obtain the flux of our target relative to a comparison star we might want to calibrate it to absolute flux. For this we need to observe a flux standard star. Flux standards are stars whose absolute flux has been determined and is tabulated so that they can be used as comparison. ULTRACAM uses the Sloan Digital Sky Survey (SDSS) filters. A table of SDSS flux standards can be found in Smith et al. (2002). Due to

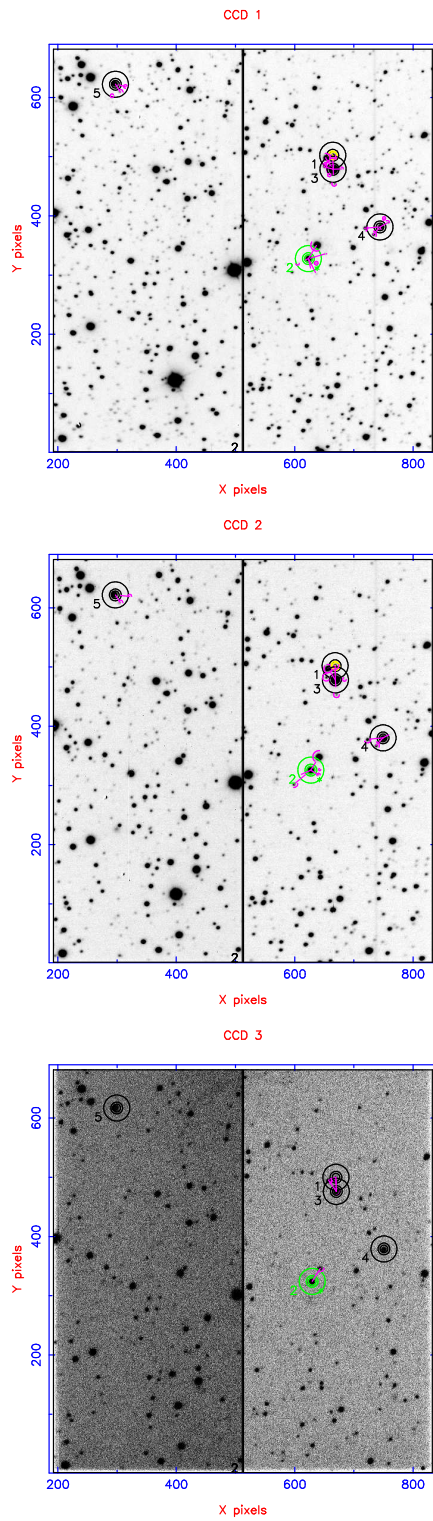


Figure 2.7: Example of an object frame. The object, V407 Vul is marked 1 and the reference star, marked 2, is shown in green. The frame is the combination of 40 bias-subtracted and flat-field-corrected frames. The vertical line shows the border of the two readout channels.

wavelength-dependent extinction of the Earth's atmosphere it is important to choose a standard star with similar colour to the target. To flux calibrate our target, we perform aperture photometry on the target and the standard star and compare their relative flux at the same airmass. No extra comparison star is needed in this case. Often instead of calibrating the target directly we first calibrate the comparison star and afterwards we use it to calibrate the target. Since the observations of the target and flux standard are not simultaneous, the PSF fitting does not give good results. Normally, in this case, the best photometry is obtained with aperture photometry using a fairly large aperture radius. (Note that if the profile is a Gaussian, an aperture radius of  $\approx 3 \times FWHM$  theoretically should contain  $\approx 100$  per cent of the flux of the star).

We can use the following relation to obtain the absolute magnitude of our target:

$$m_t = m_{FS} - 2.5 \log_{10} \left( \frac{F_t}{F_{FS}} \right) \quad (2.2)$$

where  $m$  is the magnitude and  $F$  the flux, the subscripts  $t$  and  $FS$  stand for target and flux standard, respectively.

In case the target and the flux standard have not been observed at the same airmass an additional term has to be added to equation 2.2 which is  $-\kappa_\lambda \times AM$ . Where  $AM$  is the airmass and  $\kappa_\lambda$  is the extinction coefficient for that filter. Each observatory has typical values of the extinction coefficients. We can estimate the extinction coefficient of the night if we have an observation of an object covering a large range of airmass. In this case, we can fit the flux of the star as function of the airmass and obtain the extinction coefficient.

Instead of calibrating the target in magnitudes it is also useful to calibrate the flux in milliJansky (mJy). One Jansky is equivalent to  $10^{-26} \text{ W m}^{-2} \text{ Hz}^{-1}$ . After calibrating the magnitude of the comparison star  $m_C$ , the calibrated flux in mJy of the target can be obtained with:

$$F(mJy) = \frac{F_t}{F_C} 10^{(16.4-m_C)/2.5} \quad (2.3)$$

The conversion from mJy to magnitudes in the “AB” magnitude system (Oke & Gunn 1983; Smith et al. 2002) follows the simple formula:

$$m_{AB} = 16.4 - 2.5 \log F(mJy) \quad (2.4)$$

## 2.2 ULTRACAM

### 2.2.1 Introduction

The only disadvantage of CCDs relative to photometers is poorer time resolution. ULTRACAM (which stand for ULTRA-fast CAMera) was designed to study the astrophysics on the fastest timescales and is capable of reaching a time resolution of  $\sim 500\text{Hz}$  with effectively no deadtime. This fast time resolution was achieved using a conjunction of several methods, as explained above. The duty cycle was increased using frame transfer. The readout speed was doubled using two readout channels per CCD. These two features reduce the dead time to a minimum of 24 milliseconds (which is the frame transferring time) if the exposure time is higher than the readout time of the storage area (which can be up to 6 seconds in the slowest mode). Besides the full frame mode ULTRACAM has two more optional modes which have higher time resolution. This will be explained below.

### 2.2.2 ULTRACAM reading modes

As mentioned above two methods have been applied to achieve a higher time resolution: the window mode and the drift mode. In ULTRACAM it is possible to define smaller windows that can be read faster. The windows are defined in pairs, one window in each channel and it is possible to set up to three pairs of windows. The telescope can be positioned and tweaked so that target and comparison star are inside the chosen windows. ULTRACAM has a field of view of 5 arc-minutes in the WHT and 2.5 arc-minutes when mounted in the VLT. This means there is a high probability of finding a

suitable comparison star in the field of view. The time resolution of the data depends upon the size, position and binning factor of the windows (for exact calculation of the time resolution in each a case see Dhillon & Marsh 2001) . The window-mode can achieve a maximum sampling rate of 10 Hz.

For a higher time resolution ULTRACAM has a drift-mode. Schematics of the different reading modes of ULTRACAM are shown in Figure 2.8. In the drift mode only a pair of windows can be set. The windows should be chosen to lie close to the bottom of the CCD for faster rates. After each exposure instead of transferring the whole frame to the storage area, only the lines containing the window are shifted downwards. This process continues after each exposure, so the storage area is filled with a number of sequenced exposures until the first exposure reaches the output shift register. Hence, the time resolution of the drift mode only depends upon the speed at which a small window is read. Depending upon the size, position and binning factor of the windows, this mode can achieve a maximum of 500 Hz.

Such high time resolution requires that the speed of data transfer and storage of the data acquisition system (hardware and software) must always be higher than the CCD readout speed in order to be efficient. The drift mode also requires a focal-plane mask to prevent the light from the telescope reaching the top regions of the CCD which are later transferred downwards to the windows area. Without this focal-plane mask, charge from sky and stars would accumulate and be transferred to the imaging area before the start of the real exposure. Due to the accumulation of charge outside the imaging area, the drift mode has higher dark current.

Another advantage of ULTRACAM is that it is capable of simultaneous photometry in 3 bands. Besides the obvious advantage of shortening the total observing time without reducing the time resolution of the data that has another advantage. Most astrophysical objects that we are interested in studying at high time resolution are accreting systems which, as already mentioned above show stochastic variability on timescales

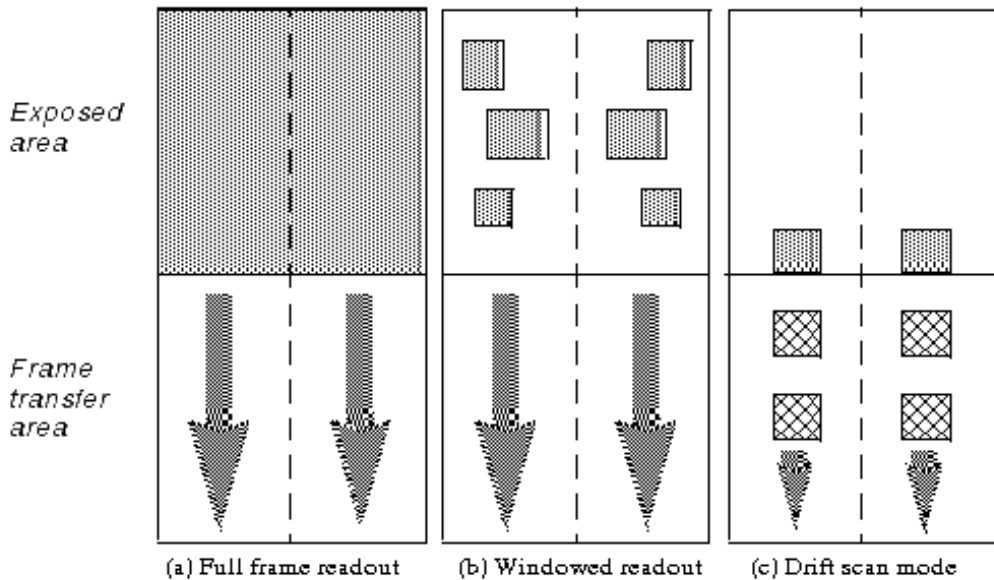


Figure 2.8: The different reading modes of ULTRACAM. Adapted from Beard et al. (2002).

of hours to fractions of a second. Without simultaneous colour information we cannot disentangle time-dependent flickering from the colour variability of the phenomenon we are studying, for example, an eclipse. Three simultaneous colours are necessary to obtain temperatures, since with three colours we can distinguish between a star and a black body.

### 2.2.3 Design

All optical elements of ULTRACAM are coated with broad-band anti-reflection coating. ULTRACAM has an exchangeable collimator which allows it to be used on telescopes of different focal ratio. This also leads to different pixel scales. ULTRACAM has been mounted on the 4.2 m William Hershel Telescope in La Palma and on the 8 m Very Large Telescope in Chile. ULTRACAM is attached to the telescopes by a mounting collar which provides thermal and electric isolation from the telescope. The focal-plane mask used

in the drift mode is mounted in the mounting collar. An schematic of ULTRACAM optical system is shown in Figure 2.9. After passing through the collimator the light is split into three colours, blue, green and red by two dichroic beam-splitters. Then each beam of light passes through a filter before being collected by the respective CCD. The ULTRACAM filters are the SDSS filters  $ugriz$ , which were chosen specially because contrary to the UBVRIZ filters there are minimal overlaps between bands. This is important because of simultaneity. The blue filter is fixed but the red and green arm filter can be changed. The optional filters for the red CCD are  $r$ ,  $i$ ,  $z$  and some other narrow band filters. The optics are mounted on a portable, rigid and open double octopod. An image of ULTRACAM is shown in Figure 2.10 and a photograph of ULTRACAM at the Cassegrain focus of the WHT is shown in Figure 2.11.

The CCDs are nitrogen-cooled, back-illuminated, thinned, EEV 47-20 frame-transfer chips with imaging areas of  $1024 \times 1024$  pixels<sup>2</sup>. The CCDs are controlled by a San Diego State University (SDDU) controller, which time stamps the frames using a GPS receiver. ULTRACAM has its own pipeline data reduction software which can be used to have a quick look at the data whilst observing and is capable of reducing data at the rate it is taken. The ULTRACAM pipeline is a complete reduction package and can be used as well to do a final reduction of the data.

In many astronomical observations accurate timing is indispensable. ULTRACAM times are accurate to  $\sim 1$  millisecond (Lyne et al. 2005; Stevenson 2004). This is achieved through a PCI-CTR05 9513-based counter/timer board whose time is updated every 10 seconds by a GPS antenna. The GPS antenna is accurate to 50 nanoseconds.

## 2.2.4 Science with ULTRACAM

ULTRACAM's ultra fast three colours photometry capabilities were successfully used to study the following astrophysical objects:

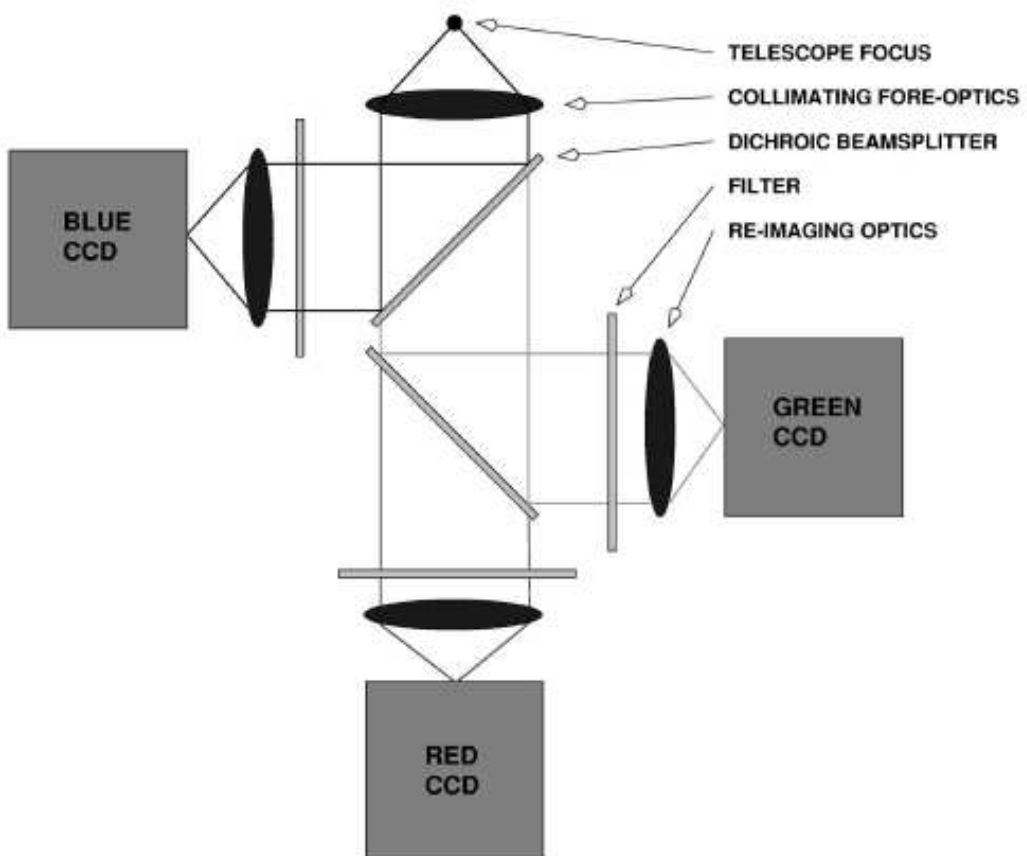


Figure 2.9: Optical components of ULTRACAM. The figure was adapted from Dhillon & Marsh (2001).

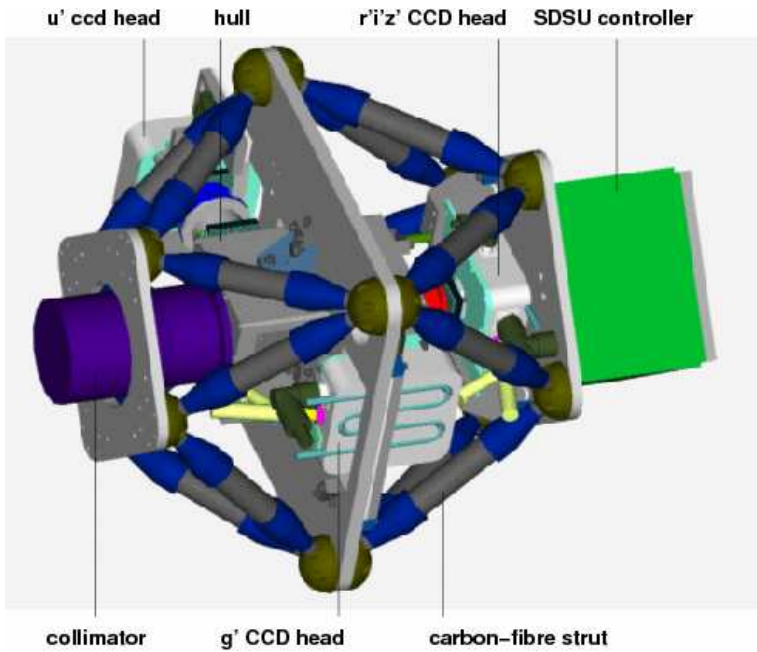


Figure 2.10: CAD image of ULTRACAM showing some of the components. The figure was adapted from Dhillon et al. (2007).

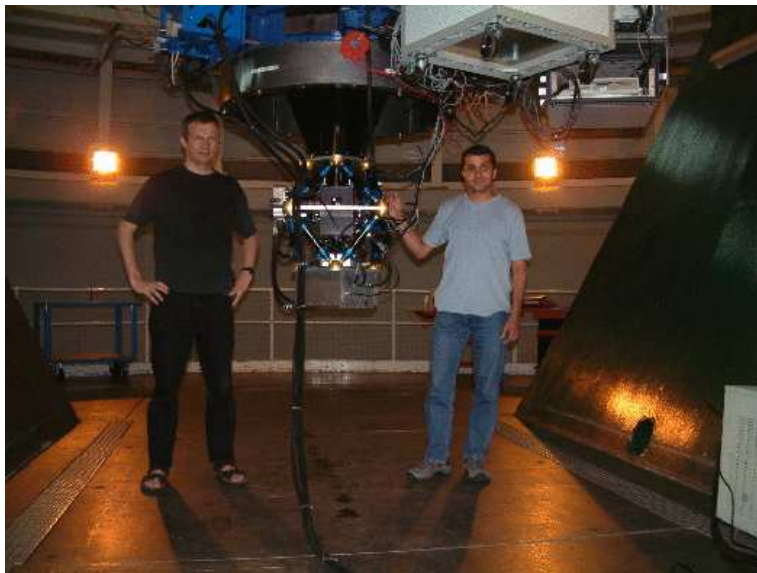


Figure 2.11: Photograph of ULTRACAM mounted on the WHT. The figure was adapted from Dhillon et al. (2007) (courtesy of Sue Worswick).

- Accretion discs around compact objects whose dynamical timescales are from seconds in white dwarfs to milliseconds in neutron stars and black holes (Shahbaz et al. 2003, 2005).
- The geometry of cataclysmic variables and X-ray binaries using eclipse and echo mapping (Feline et al. 2004; Littlefair et al. 2006; Muñoz-Darias et al. 2006).
- Asteroseismology of sdB stars (Aerts et al. 2006; Jeffery et al. 2004).
- Pulsars (Dhillon et al. 2005, 2006).
- Flare stars (Mathioudakis et al. 2006). Where the flares shape and colour can be studied.
- Eclipses (Brinkworth et al. 2006; Maxted et al. 2004), transits and occultations (Roques et al. 2006). In this case higher time resolution allows to better constrain the system parameters and in some cases it can indirectly increase the spatial resolution.

## 2.3 Conversion of systems of time

There are a number of astronomical tools that transform between the different systems of time. However some confusion in the definitions of the time system makes time conversion a frequent source of misunderstanding and errors as I show later in this thesis. In this subsection I define the systems of time most used in astronomy and the relations between them.

The times of astronomical observations cannot be based upon the civil time since this depends upon location, time of the year and political borders. Therefore, in astronomy times are usually given in Universal Time (UT) which is locked to the sun position and whose zeropoint is at the Greenwich meridian. Also due to non-uniformity of

our civil calendar, the date is usually given in Julian Date (JD). The JD is the number of days elapsed since the Greenwich mean noon on the 1 January 4713 B.C.. For simplicity in writing, it is common to subtract 2400000.5 from the Julian Date, hence, obtaining the “modified” Julian date (MJD). MJD and JD are definitions of zero points. Furthermore, due to the finite speed of light, the arrival time of the light from astronomical sources depends upon the position of the observer on the Earth and the position of the Earth in the Solar System, owing to general relativity effects. This difference in light travel time has to be corrected if one wants to compare timing observations of the same object at different times, for example for eclipse timing and pulsar timing. The only point that has a constant position in the solar system is the barycentre. However, depending upon the time resolution and accuracy of the observations several time systems relative to different locations can be used: the time at the centre of the earth is called the terrestrial time (TT), it is also called terrestrial dynamical time (TDT), the time at the centre of the sun, called heliocentric time (HJD) and the time at the barycentre of the solar system (TDB). TT and TDB are consistent with the general theory of relativity.

The difference between these time definitions are more than the light travel time between the different physical locations which is called the geometric correction. Due to Earth’s rotation, the UT time is not uniform and it should be corrected to the atomic time (TAI), which is a statistical time scale based on a large number of atomic clocks. In order for the coordinated universal time (UTC) not to differ from UT1 (which is locked to the Earth) by more 0.9 s at any given time, leap seconds are regularly introduced to UTC. A table with the leap seconds can be found in on <ftp://maia.usno.navy.mil/ser7/tai-utc.dat>, the last leap second was introduced on 31 of December 2005. So at this moment the number of leap seconds is 33. For our observations we approximate TAI by UTC. Furthermore, to obtain the time at the centre of the earth (TT) we have to account for the Earth being in a potential well causing gravitational time dilation. This requires a further correction from TAI of 32.184 s (which includes a zeropoint). Let us

define  $GEO_{corr}$  as the light travel time from the observing site to the centre of mass of the Earth. So we have that

$$TT = MJD + GEO_{corr} + \text{leapseconds} + 32.184 \quad (2.5)$$

TT is a uniform atomic time scale at the geoid which is the equipotential surface defined by the mean ocean surface.

The correction from TT to the TDB is more complicated since the calculation of the exact position of the barycentre of the solar system has to take into account the position of the planets. Besides this geometric correction, two more corrections are needed. These are the Einstein correction and the Shapiro correction. The Einstein correction is the correction of the clocks from the geocentre to the barycentre and includes all the relativistic effects due to the Earth not being an inertial reference frame; gravitational redshift, time dilation due to non-zero velocity, time varying gravitational potential and Doppler shifts. The Shapiro correction accounts for the bending of light near the Sun.

# Chapter 3

## Time series methods<sup>2</sup>

The timing properties of astronomical sources can give valuable physical insight. In this chapter we review time series methods and justify our choosing the Lomb-Scargle periodogram (Lomb 1976; Scargle 1982). A general introduction to Fourier techniques is given, followed by a definition of the Lomb Scargle periodogram with particular emphasis on the normalisation used, which, as will be seen later, is important to separate and quantify the real variability of the data from the different sources of noise. We also discuss how to search for periodicities in the data and ways of computing the significance of peaks in the periodogram which is one of the main objectives in many areas of astronomy and will be used in the next chapters. Furthermore we discuss the importance of red noise leak and how it affects the studies of cataclysmic variables.

To study the periodicities of a data set there are several timing analysis methods that can be used. These can be divided in two basic types: Fourier analysis (Deeming 1975; Lomb 1976; Scargle 1982; van der Klis 1988; Press & Rybicki 1989; Press et al. 1992; Gray 1992; Bracewell 1986) and folding techniques (Stellingwerf 1978; Leahy et al. 1983; Davies 1990, 1991). Fourier analysis methods are based in the decomposition of

---

<sup>2</sup>This section, with exception of the last subsection, is based in Press et al. (1992), Gray (1992), Bracewell (1986) and van der Klis (1988).

the signal into sinusoidal functions of a given frequency, which are Fourier transforms (FT). They are useful when we want to detect a sinusoidal signal even in low signal to noise data. Folding techniques consist of folding the data over trial periods and then analysing the scatter of the resulting profile with an appropriate statistic. Using, for example, the epoch-folding statistic we can obtain the probability of the existence of a periodicity as a function of the trial period. Folding techniques are better than FTs to study non-sinusoidal periodic signals but can fail in the presence of multiple periods.

There are more sophisticated two-dimensional time-frequency methods for studying the time evolution of the power spectrum itself. These are, for example, the dynamic power spectra (DPS) (Strohmayer et al. 1998; Wilms et al. 2001) and the wavelets approach (Grossmann et al. 1986; Press et al. 1992; Szatmary et al. 1994; Foster 1996). To perform DPS we start by computing the Fourier transform of a small set of the original data, then shift the set by one unit in time and compute its FT. This process is repeated until the end of the data is reached. Therefore, we obtain the evolution of the FT with time but since the data sets are not independent, the interpretation of the results is not straight-forward. However, this approach can be very useful in the study of QPOs with time-variable periods. The wavelet map technique does not use sinusoids as basis functions. Instead more complicated functions called wavelets are used. There are several sets of wavelets that can be chosen for each specific case. Contrary to sinusoids these functions have the advantage that they are localised in time. So besides their dependence on frequency (or in this case characteristic scale), wavelets are also a function of time. So wavelet maps are two dimensional.

Fourier techniques (FT) are the most widely used in astronomy. They have well-studied statistical properties making it possible to compute errors and significance values. Using computational methods like the Fast Fourier transform (FFT) (Press et al. 1992), they are relatively fast to compute. A modified version of the Fourier transform, the Lomb Scargle periodogram (Lomb 1976; Scargle 1982), is capable of handling non-

uniformly spaced data, which is often the case in astronomical observations. For all these reasons and also for direct comparison with previous results we applied Fourier techniques to our data.

There are also several methods of time-series analysis in the time domain. In our data analysis we used mainly the auto- and cross-correlation methods (Edelson & Krolik 1988). A definition of these methods will be given towards the end of this chapter. We start by describing the Fourier techniques and its applications to astronomical data.

### 3.1 Fourier transform

Fourier's theorem says that a continuous function of time  $h(t)$  can be written as the integral of sinusoidal functions with amplitude  $H$  as a function of frequency  $f$ .

$$h(t) = \int_{-\infty}^{\infty} H(f)e^{-2\pi ift} df \quad (3.1)$$

The Fourier transform of a function determines the Fourier coefficients i.e.  $H(f)$ . The Fourier transform of  $h(t)$  is:

$$FT[h(t)] = H(f) = \int_{-\infty}^{\infty} h(t)e^{2\pi ift} dt \quad (3.2)$$

So  $h(t)$  and  $H(f)$  form a Fourier pair and are representations of the same physical process in two different domains: the time domain and the frequency domain. Equation 3.1 is called the inverse Fourier transform ( $FT^{-1}$ ) and can be used to recover the original function.

Fourier transforms have many properties (Bracewell 1986) that make the Fourier analysis attractive. They are also used as a computational tool since complex operations in one representation can be equivalent to simpler operations in the other domain. For example, the convolution theorem states that the convolution of two functions in one domain is equivalent to the simple product of the two functions in the other domain.

Another important property of the FT is the Parseval's theorem which states that the total power is the same in both domains:

$$\text{Total Power} = \int_{-\infty}^{\infty} |h(t)|^2 dt = \int_{-\infty}^{\infty} |H(f)|^2 df \quad (3.3)$$

One of the reasons of the success of Fourier techniques as a time-series and mathematical method is the Fast Fourier transform (FFT) algorithm (Press et al. 1992). The FFT reduces the  $N^2$  operations needed to compute a Fourier transform of a N points data set to  $N \log_2(N)$  operations. The FFT algorithm is based on the fact that a Fourier Transform of a set of N data points can be rewritten as a sum of two FTs of N/2 data points each. Used recursively this can significantly reduce the computational time of FTs specially for high N.

## 3.2 Discrete Fourier transform

In most applications instead of a continuous function we have discretely sampled data. Let us consider a function  $h(t)$  sampled at N even intervals of time of length  $\Delta$ . Hence,  $h$  is only defined at  $h(t_k) = h(k\Delta)$ , where  $k = 0, 1, 2, \dots, N - 1$ .

The sampling theorem states that we can not sample frequencies higher than a critical frequency, called the Nyquist frequency, given by:

$$f_c = \frac{1}{2\Delta} \quad (3.4)$$

This also implies that if  $h(t)$  is bandwidth limited to frequencies smaller than  $f_c$  (i.e if  $H(f) = 0 \forall |f| > f_c$ ) then  $h(t)$  is completely determined and given by:

$$h(t) = \Delta \sum_{n=-\infty}^{\infty} h(n\Delta) \frac{\sin(2\pi f_c(t - n\Delta))}{\pi(t - n\Delta)}. \quad (3.5)$$

However, if  $H(f)$  is non zero at frequencies higher than  $f_c$ , these are going to be aliased to the range  $-f_c < f < f_c$  because we can not distinguish frequencies that differ by

multiples of  $1/\Delta$ . A way to avoid this aliasing problem is to pass the signal through a low-pass filter before sampling, but this degrades the signal.

We can estimate the Fourier transform of  $h(t_k)$  in the range  $-f_c < f < f_c$  by approximating the integral with a sum. With  $N$  data points we can only obtain  $N$  independent values for the estimated FT so we can choose the frequencies to be uniformly spaced:

$$f_n = \frac{n}{N\Delta}, \quad n = -\frac{N}{2}, \dots, \frac{N}{2} \quad (3.6)$$

Hence our function in the frequency domain will be given by:

$$H(f_n) = \Delta \sum_{k=0}^{N-1} h(t_k) e^{2\pi i k n / N} = \Delta H_n \quad (3.7)$$

where  $H_n$  is the discrete Fourier transform of  $h(t_k)$ .

Note the values of  $H(f_n)$  at these frequencies are all independent except for the extremes  $H(-f_c) = H(f_c)$ . The discrete Fourier transform has the same properties as the continuous Fourier transform. The discrete inverse of the Fourier transform is given by:

$$h(t_k) = \frac{1}{N} \sum_{n=0}^{N-1} H(f_n) e^{-2\pi i k n / N} \quad (3.8)$$

and the discrete form of Parseval's theorem is:

$$\sum_{k=0}^{N-1} |h(t_k)|^2 = \frac{1}{N} \sum_{n=0}^{N-1} |H(f_n)|^2 \quad (3.9)$$

### 3.3 Power Spectra

Fourier methods have several applications in science and engineering but the most important one for astronomy is the estimation of the power spectrum or power density spectrum (PDS). The PDS is also historically called the Periodogram.

We can use Fourier transforms to estimate the PDS since it is proportional to the squared absolute value of the Fourier coefficients:

$$P(f_i) = C |H(f_i)|^2 \quad (3.10)$$

For real data points, the Fourier transform is symmetric i.e.  $H(f_l) = H^*(f_l)$ , where \* stands for complex conjugate. This implies that the PDS only needs to be defined for zero and positive frequencies i.e.,  $l = 0, 1, \dots, \frac{N}{2}$ . So we estimate the power spectrum in  $N/2 + 1$  frequencies between 0 and the Nyquist frequency. According to Parseval's theorem, the variability power of  $h(t_k)$  is equal to the integral over the PDS.

In the literature there are several normalisations of the power spectrum. The ones most commonly used in binary stars are:

- **Schlittgen normalisation** for which  $C = 1/N$  (Press et al. 1992), is the classical normalisation by the mean-squared amplitude. It is mostly used for mathematical time-series analysis.
- **Leahy normalisation** where  $C = 2\Delta/N\bar{h}$  (Leahy et al. 1983), where  $\bar{h}$  is the mean value of the data. If the time series follows Poisson statistics (as is the case of white noise) then the mean PDS is equal to 2. This implies that the white noise due to the detector counting statistics has power equal to two, which makes it easy to subtract.
- **Miyamoto normalisation** for which  $C = 2\Delta/N\bar{h}^2$  (Miyamoto et al. 1991), it is equivalent to Leahy normalisation divided by the mean value of the data. This normalisation is very useful for comparison of the variability power of different sources because it is independent of the number of the data points, sampling rate and the mean value of the data.

I will use the Miyamoto normalisation for easier comparison with previous and future results. Using Parseval's theorem it is possible to prove that with this normalisation:

$$\int_{f_1}^{f_2} P(f) df = \left[ \frac{\text{RMS}}{\bar{h}} \right]^2 \quad (3.11)$$

where RMS is the root-mean square scatter due to the power between frequencies  $f_1$

and  $f_2$ . This means that the integral of periodogram over a range of frequencies is equal to the normalised variability over the corresponding timescales. Due to these properties the Miyamoto normalisation is the most commonly used in X-ray binary studies.

The periodogram has an interesting property; the precision of each estimated point is independent of  $N$ , i.e. the standard deviation of each point is always 100 per cent. This happens because the information contained in each extra point will be used to estimate the power in an extra frequency. Which means that longer sampling times will produce finer frequency resolution and higher sampling rate (so consequently larger Nyquist frequency) will extend the frequency range.

While the accuracy of each point does not improve for a longer data set, there are techniques to increase the accuracy of the estimation of the periodogram. Suppose we have  $KN$  sampled data points and the  $N$  data points alone are enough to give us the desired frequency resolution. There are two simple ways of reducing the standard deviation of our estimates by a factor of  $\sqrt{K}$ . In the first one, after estimating the periodogram of the  $KN$  data points we bin them in frequency. Each new point would be equal to the sum of the estimates of the  $K$  consecutive points at the mid frequency of the interval. In the second technique, we divide the data points into  $K$  consecutive sets, for which we estimate the corresponding periodogram. Then we average all the periodograms. Although these two techniques are mathematically equivalent the second is computationally faster so it is recommended specially for long data sets.

In general, after we obtain the periodogram we wish to fit a function to it. Therefore, we use a least squares fitting procedure which requires that the data points have Gaussian errors. That is not the case for the periodogram. Papadakis & Lawrence (1993) showed that if we bin the periodogram in logarithm space we will have a consistent estimate of the logarithm of the periodogram. This is particularly important in the presence of coloured noise. They showed that this estimate is less biased than traditional methods and that the data requires less smoothing in order to obtain the desired Gaussian

errors. Equations (18) and (19) of Papadakis & Lawrence (1993) can be used to calculate the binned logarithmic periodogram which we rewrite in our notation. Each point of the new estimation of the periodogram  $P$  can be calculated with:

$$\log [P(f_{ave})] = \frac{1}{M} \sum_j \log [P(f_j)] + 0.253, \quad (3.12)$$

where  $M$  is the number of points in each bin,  $j$  varies over the  $M$  consecutive points and 0.253 is a constant bias of this estimation. The corresponding frequency of each bin is the geometric mean of the frequencies:

$$f_{ave} = \left[ \prod_j (f_j) \right]^{1/M} \quad (3.13)$$

and the expected error is the same for all the bins and approximately equal to  $\sqrt{0.310/M}$ . Papadakis & Lawrence (1993) suggest that  $M = 20$  is enough to obtain a good estimate of the periodogram.

### 3.3.1 Window function

The result of sampling a continuous function onto a discrete set is equivalent to multiplying the original function by a box function and a sampling function. The box sampling function is equal to one at the sampling times and equal to zero everywhere else. The sampling function is an extended periodic series of Dirac delta functions ( $\delta(x)$ ) (van der Klis 1988), which are separated by  $\Delta$ . This implies that the FT of our sample data points is in fact equal to the real FT of the continuous function convolved with the FT of two functions. These are the FT of the box function and the FT of the sampling function. The FT of an infinitely extended periodic series of Dirac delta functions is also an infinite period series of Dirac delta function but separated by  $1/\Delta$ . So the result of the sampling is that the original FT will be repeated every  $2f_C$  so the power above the Nyquist frequency is reflected to frequencies below the Nyquist frequency. This aliasing effect was already explained above as due to loss of information for the highest

frequencies. In case of red noise the power that is above the Nyquist is often very low, so in our case this will not affect our results. Unfortunately the same is not true for the box function and we will see that it can greatly affect our results. In our case the measured power spectrum is approximately equal to the real power spectrum convolved with the power spectrum of a box function which is given by:

$$\left[ \frac{\sin \pi f \Delta N}{\pi f} \right]^2 \quad (3.14)$$

This function falls off as  $\approx (\pi f)^{-2}$  and has oscillatory lobes. It has the effect of broadening the original peaks of the periodogram, where some of the power at each peak is transferred or leaks into the higher neighbouring frequencies. This is often called red noise leakage. It has stronger effects for steep power spectra and will tend to flatten it. Red noise leakage will be discussed later in subsection 3.6 and in Chapter 6 when we analyse our results and we will see that it can greatly affect them.

### 3.4 Lomb Scargle Periodogram

In real life situations, often it is not possible to obtain evenly sampled data due to missing data points and gaps between observations. This is usually what happens in astronomical observations.

It is possible to map unevenly sampled data into even sampled times using, for example, interpolation. In the case of missing data points these can be either set to zero, to the nearest neighbour or interpolated. However, these methods do not give good results and often artificially increase the power at low frequencies. The situation is even more complicated in the presence of large gaps in the data set.

A better method to cope with unevenly sampled data is the Lomb-Scargle periodogram (Lomb 1976; Scargle 1982; Press & Rybicki 1989). This method only uses the measured points and for evenly sampled data is equivalent to the PDS apart from

the normalisation constant. It basically uses least squares fitting of sinusoidal functions with different frequencies.

If we have  $N$  data points  $h_i = h(t_i)$  for  $i = 1, \dots, N$ , the Lomb-Scargle periodogram is defined as:

$$P_N(\omega) = \frac{1}{2\sigma^2} \left[ \frac{[\sum_j (h_i - \bar{h}) \cos \omega(t_j - \tau)]^2}{\sum_j \cos^2 \omega(t_j - \tau)} + \frac{[\sum_j (h_i - \bar{h}) \sin \omega(t_j - \tau)]^2}{\sum_j \sin^2 \omega(t_j - \tau)} \right] \quad (3.15)$$

where,

$$\omega = 2\pi f > 0, \quad (3.16)$$

$$\bar{h} = \frac{1}{N} \sum_{i=1}^N h_i \quad (3.17)$$

$$\sigma^2 = \frac{1}{N-1} \sum_{i=1}^N (h_i - \bar{h})^2 \quad (3.18)$$

$$\tan(2\omega\tau) = \frac{\sum_j \sin(2\omega t_j)}{\sum_j \cos(2\omega t_j)} \quad (3.19)$$

The  $\sigma^2$  normalises the periodogram by the variance of the data. This has the advantage that for Gaussian white noise,  $P_N(\omega)$  has an exponential probability distribution with a mean equal to one. This makes it possible to test if there is a periodicity present in the data by calculating the significance of peaks in the periodogram. The false alarm probability, which is the probability that there is no peak higher than  $z$ , is equal to:

$$1 - (1 - \exp^{-z})^M \quad (3.20)$$

where  $M$  is the number of natural frequencies, whose periodogram powers ( $P_N(\omega_i)$ ) are mutually independent. We are assuming that the data values are independent Gaussian random variables, and that we know the variance of the data *a priori*. Horne & Baliunas (1986a) discuss what is the number of independent variables  $M$ . They conclude that for the significance test to be reliable:

$$M = -6.362 + 1.193N + 0.00098N^2 \quad (3.21)$$

Recently Frescura et al. (2007) repeated Horne & Baliunas (1986a) method and fail to obtain the same result. For the case of evenly spaced data with no oversampling they obtained a number of natural frequencies (also called independent frequencies) equal to the theoretical value of  $N/2$ . In the case of evenly spaced data but with oversampling they obtained a linear dependence of  $M$  with  $N$  (Figure 1 of Frescura et al. (2007)).

If the variance of the data is not known *a priori*, as is the case of any astronomical data set and in practise of any simulation, a modification of the false alarm probability is needed. Schwarzenberg-Czerny (1998a) showed that  $P_N(\omega)$  only follows the exponential probability in the limit of  $N \rightarrow \infty$  and the incomplete beta distribution should be used instead. In this case the false alarm probability is given by:

$$1 - \left[ 1 - \left( 1 - \frac{z}{N/2} \right)^{N/2} \right]^M \quad (3.22)$$

where  $M$  should be interpreted a fitting parameter to the cumulative distribution function and not the number of independent frequencies. In fact the existence of a number of independent frequencies is only guaranteed in the case of evenly spaced data. For unevenly spaced data there are very few or no independent frequencies, so equations 3.20 and 3.22 are not valid (Frescura et al. 2007). Moreover even using the correct statistical distribution for the LSP (Schwarzenberg-Czerny 1998a) in the case of non-evenly spaced data, the parameter  $M$  can only be determined reliably by Monte Carlo methods. Therefore Frescura et al. (2007) concluded that the only way of correctly estimated the significance of a peak is using Monte Carlo simulations and they add that any oversampling can be used as long as the data and the simulations are treated in the same way.

Furthermore only in the case of evenly spaced data it is possible to devise a statistical test to cope with red noise (Vaughan 2005). So for all of the significance tests in the following chapters we used Monte Carlo simulations.

An advantage of the unevenly sampled data is that it is possible to calculate the

periodogram for frequencies higher than the Nyquist frequency because the points that are closer than  $\Delta$  largely remove the ambiguity from any aliasing.

Our data are nearly evenly spaced so I will use the Lomb-Scargle periodogram normalised to the equivalent of the Miyamoto normalisation of PDS. To achieve this one multiplies the equation 3.15 by the normalisation constant A. Where A is:

$$A = \frac{2\sigma^2\Delta}{\bar{h}^2} \quad (3.23)$$

If the data are evenly sampled then our normalised LSP is equal to the PDS (equation 3.10 with  $C = 1$ ) multiplied by:

$$\frac{A}{N\sigma^2} = \frac{2\Delta}{N\bar{h}^2} \quad (3.24)$$

### 3.4.1 White noise level

It is useful to be able to estimate the expected white noise level in our power spectrum in order to confirm our reduction errors and specially to separate the photon noise from other types of noise, for example scintillation. Astronomical instruments measure the number of photons from a source in a given time interval. So each data point has a measurement error that follows Poisson statistics. This appears as a white noise component in the power spectrum. We divide the counts of the target by the counts of the comparison and in the limit of large numbers we assume that the count ratio follows a Gaussian distribution. So to calculate the level of the white noise let us assume that each of the data points  $h(t_k)$  follows a Gaussian distribution with mean equal to the measurement error of each point ( $\sigma_k$ ). Using equation 3.10 and equation 3.7 we can

compute the expectation value of the PDS:

$$\langle P_j \rangle = \langle H_j H_j^* \rangle = \sum_l \sum_k \langle h(t_l) h(t_k) e^{2\pi i k j / N} e^{-2\pi i l j / N} \rangle \quad (3.25)$$

$$= \sum_l \sum_k \langle h(t_l) h(t_k) \rangle e^{2\pi i j(k-l)} \quad (3.26)$$

$$= \sum_l \sum_k \sigma_l^2 \delta_{lk} \quad (3.27)$$

$$= \sum_k \sigma_k^2 \quad (3.28)$$

Using equation 3.24 we obtain the expected white noise level for our normalisation of the LSP in case of evenly spaced data which is:

$$P_{noise} = \frac{2\Delta \sum_k \sigma_k^2}{N h^2} \quad (3.29)$$

### 3.5 Correlation Function

The correlation function is used to compare two functions shifting one by a lag  $\tau$ . The correlation function measures how much the two functions are equal as a function of  $\tau$ . When the two functions are different it is called cross-correlation and when we are comparing one function with itself it is called auto-correlation. The discrete correlation of two functions  $g(t_k)$  and  $h(t_k)$  is:

$$CCF_j = \sum_k g_{j+k} h_k \quad (3.30)$$

The discrete correlation theorem says that in the frequency domain the correlation of  $g(t_k)$  and  $h(t_k)$  is equivalent to the product of the FT of  $g(t_k)$  by the complex conjugated of the FT of  $h(t_k)$ . Therefore the auto-correlation function is proportional to the inverse Fourier transform of the power spectrum. The errors of two measurements of the same source at a given time are not independent. Therefore the two data sets have correlated errors which will often cause a spurious peak at zero lag.

If the data are not evenly spaced, Edelson & Krolik's (1988) method of computing the discrete correlation function can be used, for which is also possible to calculate

meaningful errors. If we use interpolation to transform the data to an evenly spaced grid the correlated errors will spread over several bins. The advantage of the Edelson & Krolik's (1988) method is that the correlated errors will only affect the correlation at zero lag and do not affect other lags.

In astronomy, the cross-correlation is often used to compare the flux of the source in two bands or to compare continuum data with emission lines. If emission is simultaneous in different bands this implies a common origin. However, there are cases where the flux in one band lags the flux in other band. Kanbach et al. (2001) report an intriguing result where the optical precedes the X-rays. But in general and in agreement with the theory the optical lags the X-rays (e.g. Maccarone et al. (2000) and Malzac et al. (2003)). This implies that the X-rays and optical have different sources and that the optical light is due to reprocessing or reflection of the original X-ray flux. The size of the emitting region can be inferred from the auto-correlation function and the lags between the two bands are related to the light travel time i.e. relative position of the two emitting sources.

However, interpretation of the cross-correlation is not straight forward and the results depend on assuming the correct emission physical model. In summary, auto- and cross-correlation can be very useful when testing specific physical models, but are difficult to interpret on their own. Moreover Fourier spectra techniques often give better results than the auto- and cross-correlation (van der Klis et al. 1987; Malzac et al. 2004).

### 3.6 Simulation of power law light curves

This subsection explores the correspondence between a feature in a light curve and the shape of the power spectrum. The presence of a significant peak in the power spectrum is understood as repetition of a light curve feature at the respective frequency of the peak. The white noise component in the power spectrum, which has a constant value at

all frequencies, is due to random Gaussian variability of the flux around a mean level. But what features in the light curves correspond to the red noise part of the spectrum? Red noise arises from random flares in the light curve but in this case the flare amplitude and frequency are correlated. Cataclysmic variable stars have a red noise power spectrum, which can often be described by a broken power law (for example Section 6.3.5). The equation for a broken power law is:

$$P = w + \frac{a_1}{1 + (f/f_b)^\alpha}, \quad (3.31)$$

where  $w$  is the white noise,  $f_b$  is the break frequency of the power law and  $\alpha$  is the power law index. The break frequency is somehow related to the size of the emitting region and it marks a break in the correlation between frequency and amplitude of the variations;  $a_1$  is related to the total variability power. The power law index  $\alpha$  measures the steepness of the spectrum and is the parameter that we are more interested in. Specifically what is the difference in the morphology of the light curves for different  $\alpha$ .

### 3.6.1 Power spectral index

Using a power law model for the power spectrum given by equation 3.31 and the method of Timmer & Koenig (1995), we simulated light curves with different power law indices. This method uses the inverse of the Fourier transform to obtain the amplitudes and phases that compose the simulated light curve. In Timmer & Koenig (1995), the amplitudes are randomly drawn from a  $\chi^2$  distribution with two degrees of freedom which is the correct way of simulating light curves. So this method is superior to other methods that only randomise the phases and not the amplitudes.

To simulate the light curves we assume no white noise, a break frequency at 1 mHz and we normalised the light curve by its standard deviation. This implies that the original power normalisation is lost so we had to artificially adjust the power law to match the simulations in the plots. To compare with our observations of CVs in Chapter

Original $\alpha$	$\alpha$	$f_b$ (mHz)
0.5	0.521±0.006	3.000±1.360
1.0	1.014±0.003	1.143±0.374
1.5	1.520±0.003	1.244±0.264
2.0	2.016±0.003	1.049±0.179
2.5	2.162±0.003	0.140±0.206
3.0	2.056±0.004	0.048±0.600
4.0	1.814±0.002	0.035±0.308
10.0	1.794±0.003	0.029±0.001

Table 3.1: Fitted parameters  $\alpha$  and  $f_b$  of the LSP of the simulated light curves for increasing values of  $\alpha$ . The original  $f_b$  is 1 mHz.

we simulate light curves with a total length of 3 hours sampled at 20 Hz. Examples of light curves for increasing values of  $\alpha$  are shown in Figure 3.1. For a very flat power spectrum  $\alpha = 0.5$ , the light curve appears to be just white noise. For  $1.5 \lesssim \alpha \lesssim 3.0$  the simulated light curves closely resemble the light curves of CVs and accreting objects like LMXBs. For very steep power spectra the light curves are very smooth. The lack of high frequency variability results in a noise-free looking light curve but also means that the light curve lacks spikes; there are no steep rises/falls.

We also investigated what are the power spectra of the light curves seen in Figure 3.1. Or in other words if we can recover the input power spectra. We computed the Lomb-Scargle periodograms of the the simulated light curves and binned them in logarithm space using the method of Papadakis & Lawrence (1993). This method transforms the logarithm of LSP into a consistent estimator of the logarithm of the power spectral density so it can be fitted using least-squares fitting. The binned LSP is given in Figure 3.2 where we also show the shape of original power spectrum and a least squares fit to the LSP using a broken power law. The fitted parameters  $\alpha$  and  $f_b$  are given in Table 3.1. We can see that for power law indices less than 2 we can recover very well the original power spectrum but, in case of steeper power laws, red noise leak greatly affects the power spectrum and changes its shape. For some specific parameters

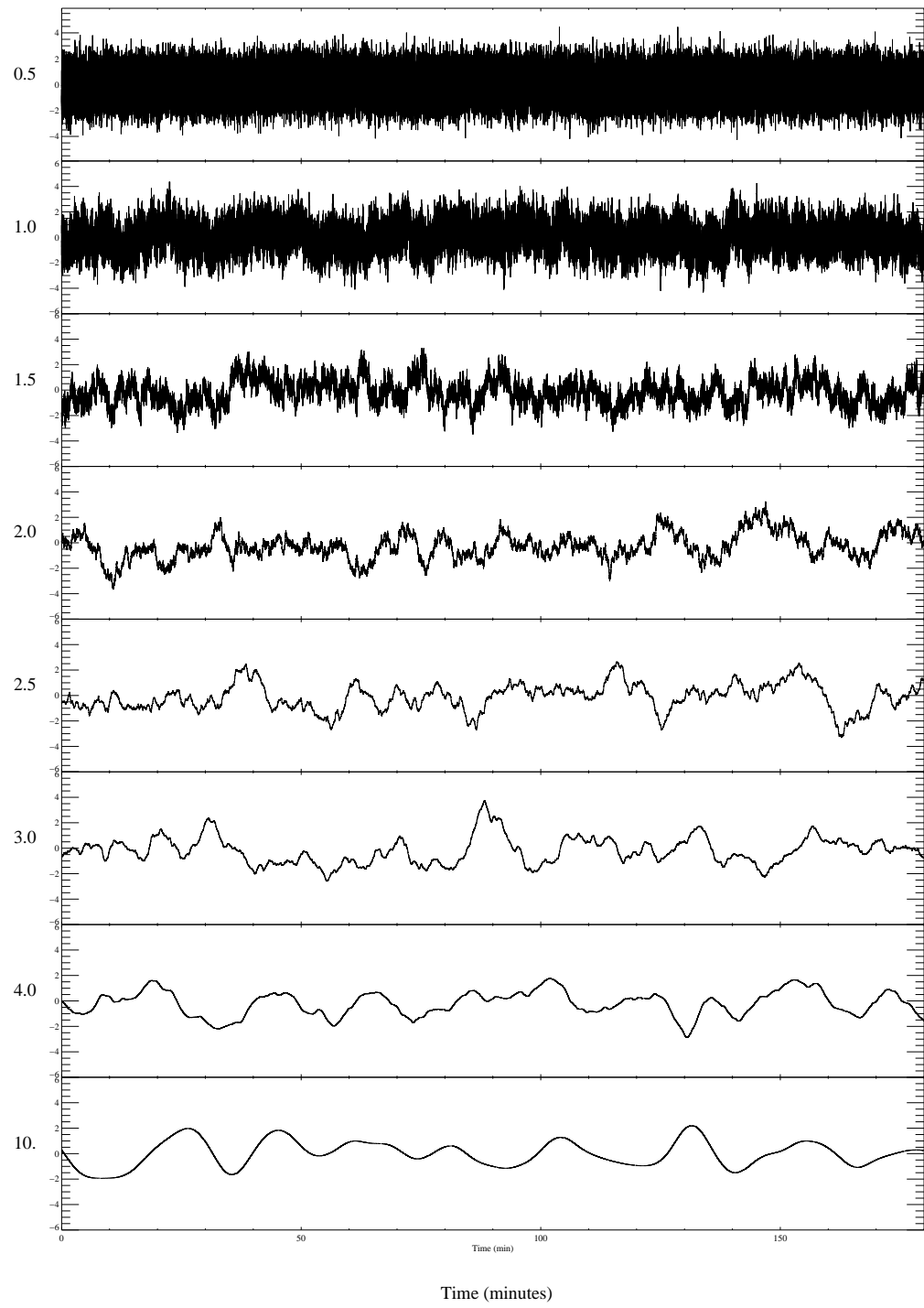


Figure 3.1: Simulated light curves with different power indices. From top to bottom  $\alpha = 0.5, 1.0, 1.5, 2.0, 2.5, 3.0, 4.0$  and 10.0, which are also given in the left of the plots. The frequency break is always at 1 mHz.

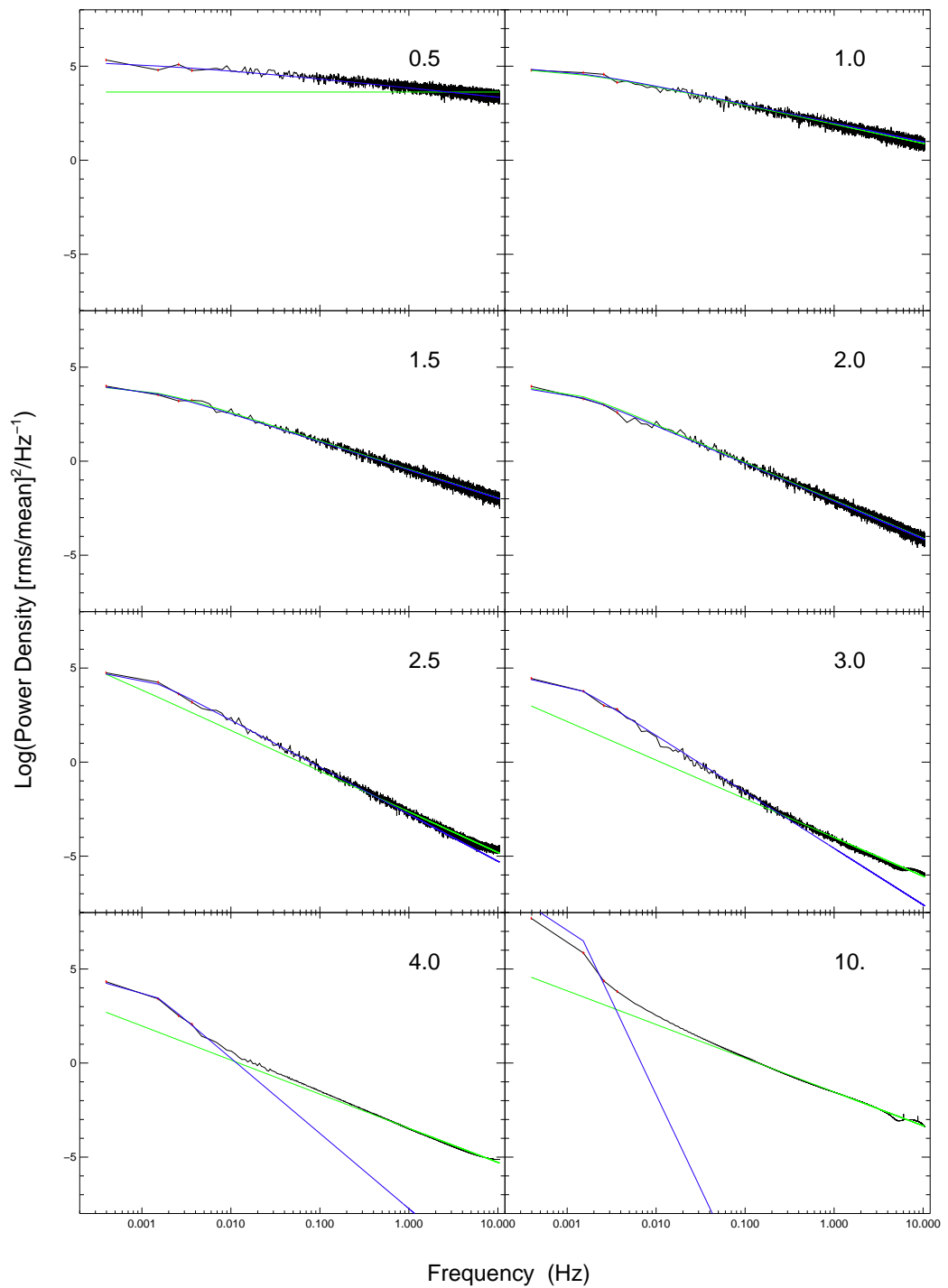


Figure 3.2: LSP of the simulated light curves shown in Figure 3.1, in the same order. The original broken power law model that was used to simulate the light curves is shown in blue and a fit to the LSP using all the points is shown in green. The slope is of the original power law is shown in top right of each plot.

we can also see the appearance of lobes due to red noise leak at the high frequencies that can in some cases be misinterpreted in terms of QPOs. For power spectrum whose original power law indices are greater than 2, we obtained a fitted  $\alpha$  of approximately 2 and also an inaccurate frequency break.

Red noise leak affects the power at the high frequencies, but since there are more points at high frequencies they dominate the fit. This implies that ultimately the fit is dominated by the red noise leak. Depending upon the original power spectral shape there may be only a few low frequency points in the LSP which conserve the original power law shape (although they have lower power). Therefore, the fit might be statistically good with a low  $\chi^2$  hiding the existence of the red noise leak. It is important to realise that it is the shape of the LSP that is distorted and not the fit that is bad; the fit just reflects that distortion. In fact the higher the red noise leak, the better the fit will be. However if we analyse the fits by eye, we realise the divergence between the fit and the power spectrum at low frequencies. This result implies that, in particular for CVs, all the fits should be confirmed by eye and that we cannot trust automatic least-squares fitting.

### 3.6.2 Frequency break

To investigate the effect of the frequency break in the light curves we also simulated light curves with different frequency breaks. Three examples with  $\alpha = 2$  and  $f_b = 0.25, 1.0$  and  $4.0 \text{ mHz}$  are shown in Figure 3.3. As we can see in the light curves, the break frequency determines the size of the largest flares. However there is also some degeneracy between the frequency break and the power law index, where a light curve with a frequency break at higher frequency appears to have a flatter power law, due to the relative strength of the longer to shorter flares.

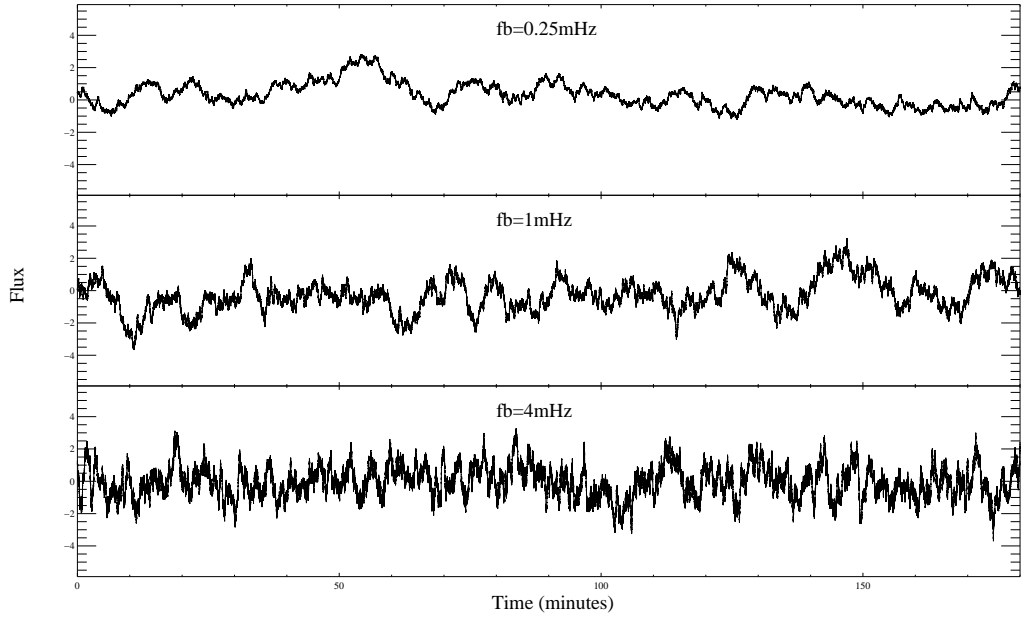


Figure 3.3: Simulated light curves with the same power index equal to 2 and different frequency breaks. From top to bottom  $f_b = 0.25, 1.0$  and  $4.0\text{ mHz}$ . We repeat the  $\alpha = 2$  and  $f_b = 1\text{ mHz}$  of Figure 3.1 for easier comparison.

### 3.6.3 Length of the light curve

We expect that recovering the steepness of the LSP depends upon the relation between the frequency break and length of the observation. In principle if one increases the length of the observation one should obtain a better estimate of the power spectral index. Since the red noise leak is due to the finite size of our window (3.3.1) one would expect that on increasing the window size, the leakage would decrease. We investigate the effect of changing the total length of the light curves upon our ability to recover the real power spectrum indices for steep power spectra (steeper than 2). For  $\alpha = 3$  and  $f_b = 1.0\text{ mHz}$  we simulated light curves with different lengths: 1 hour, 3 hours, 5 hours and 10 hours. We compute their binned LSP which are shown in black in Figure 3.4, a fit to the LSP is shown in green and we also show the original power spectrum in blue. The fitted parameters  $\alpha$  and  $f_b$  which correspond to broken power law shown in green are given in Table 3.2. We can see that the length of the observation does not

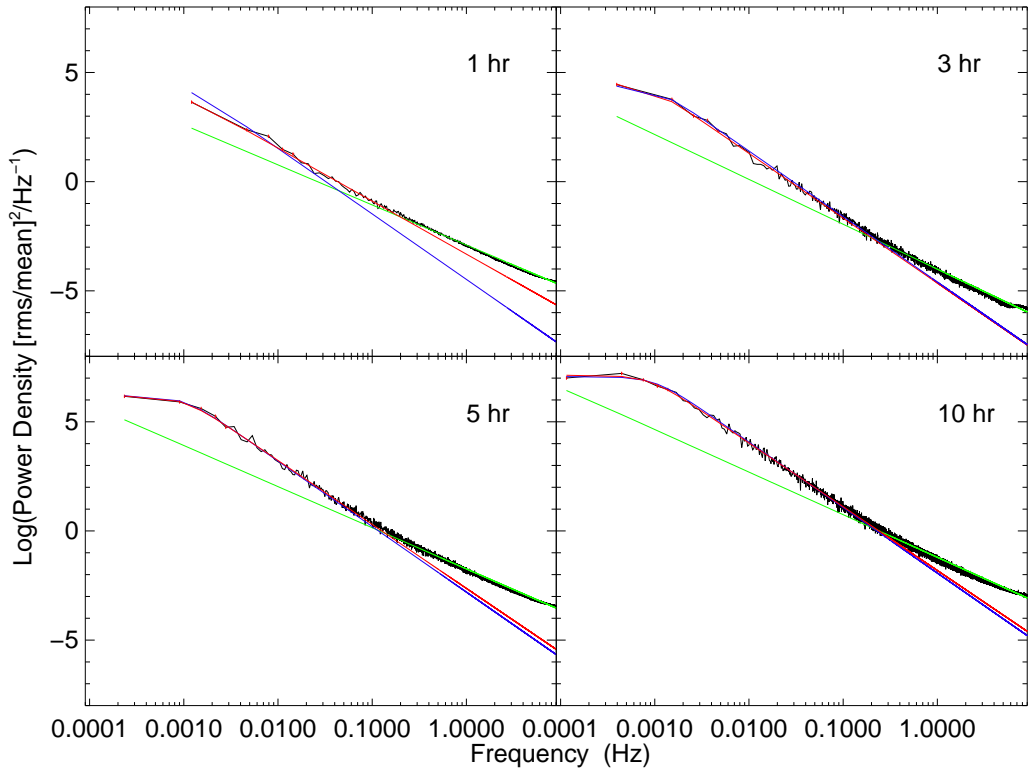


Figure 3.4: LSP of the simulated light curves for different light curve length. From left to right and top to bottom the respective light curves have 1, 3, 5 and 10 hours. The original broken power law model that was used to simulate the light curves is shown in blue ( $\alpha = 3.$ ,  $f_b = 1 \text{ mHz}$ ) and a fit to the LSP using all the points is shown in green. The fit to the LSP using only the first 50 points is shown in red.

have any effect upon the fitted parameters since the fit is completely dominated by the high frequencies which in turn are dominated by red noise leak. The low frequencies are not well fitted and we can not determine the low frequency break. Although the leakage is always  $\propto f^{-2}$  we can see from the plots that the red noise leak takes over at higher frequencies for longer light curves.

However, there are also good news, as we can see from Figure 3.4 that at low frequencies the LSP shape closely resembles the original power spectral shape. The extent of the power spectrum that was not affect by red noise leak depends strongly upon the original  $\alpha$ ,  $f_b$  and the length of the observation. But for this specific case we can

<b>LC length</b> (hours)	$\alpha$	$f_b$ mHz
1	$1.836 \pm 0.004$	$0.056 \pm 1.913$
3	$2.056 \pm 0.004$	$0.041 \pm 0.700$
5	$1.885 \pm 0.002$	$0.040 \pm 0.001$
10	$1.951 \pm 0.002$	$0.042 \pm 0.001$

Table 3.2: Fitted parameters  $\alpha$  and  $f_b$  of the LSP of the simulated light curves for different length of the light curve. The original parameters are  $\alpha = 3$  and  $f_b = 1$  mHz.

<b>LC length</b> (hours)	$\alpha$	$f_b$ mHz
1	$2.430 \pm 0.040$	$0.76 \pm 0.371$
3	$2.971 \pm 0.060$	$0.83 \pm 0.128$
5	$2.929 \pm 0.062$	$0.98 \pm 0.120$
10	$2.920 \pm 0.087$	$0.87 \pm 0.110$

Table 3.3: Fitted parameters  $\alpha$  and  $f_b$  of the LSP of the simulated light curves for different length of the light curve. In this case we only fitted the first 50 points. The original parameters are  $\alpha = 3$  and  $f_b = 1$  mHz.

try to recover the original power spectrum shape by fitting only the low frequency points. The fitted power law model using just the first 50 points is also shown in Figure 3.4 in red. We can see that the power spectra are well fitted at the low frequencies. In Table 3.3 we give the corresponding fitted parameters  $\alpha$  and  $f_b$  which, for a light curve length greater than or equal to equal 3 hours, are in agreement with the original model. If we use a number of points ranging form 20 to 100 we obtain the same results so this method is reasonably robust. (Note that each binned point of the LSP has 50 original points.)

We conclude that for light curves longer than 3 hours this method allows us to recover the original power index. However our ability to do so depends on the number of points used in the fit and the combination of  $\alpha$ ,  $f_b$  and length of the observation. We repeated the procedure for higher  $\alpha$  and concluded that we can only recover the original  $\alpha$  when we fine tune the number of points used. Therefore we expect that in general this technique will fail, specially in the presence of noise. However it is a

powerful test of the presence of red noise leak, which is present whenever the fitted  $\alpha$  is higher than 2 for low frequencies and approximately 2 for high frequencies. The main problem of this method is that it depends upon the low frequencies of the power spectrum which have large errors. Depending on the number of points we can obtain different estimates of  $\alpha$  and, as it can be seen in the tables above, the errors of the fitted parameters do not reflect the true uncertainty of the power spectral shape. If we use this method the only way to estimate the errors of the parameters is by Monte Carlo simulations trying out different values of parameters until the LSP of the simulation can describe the real LSP both at high and low frequencies. A more consistent method to determine the power spectral index in the presence of red noise leak is described in the next subsection. Other methods have been developed to recover steep power spectra using data tapering, polynomial detrending or non-Fourier methods (Deeter & Boynton 1982; Deeter 1984). These methods are rarely used because their effect on the RMS power and on any real periodicities is not known. Moreover, for example the method of Deeter (1984), has a poor frequency resolution.

### 3.6.4 High frequency pass filter

In our quest for a method that allows us to recover the original power spectrum shape when we are affected by red noise leak we tested the use of a high frequency pass filter. We follow the same procedure as above to simulate light curves using a broken power law model but this time we include noise to be closer to real data. We use the exact times and errors of a real observation that will be presented in chapter 6. Our tested power spectral model has a frequency break at 2 mHz and increasing values of  $\alpha$ . For each trial  $\alpha$ ,  $a_1$  was adjusted in order to fit the real power spectrum of the CV. After simulating the light curves for each  $\alpha$  we computed the LSP of the light curves and the LSP of the filtered light curves. We filtered the light curves by subtracting a mean light curve calculated with a running mean over a 3 minutes interval. This means that

<b>Original <math>\alpha</math></b>	<b><math>\alpha</math> no filter</b>	<b><math>\alpha</math> filter</b>
<b>0.50</b>	0.403±0.030	0.405±0.030
0.75	0.684±0.014	0.687±0.014
<b>1.00</b>	0.962±0.010	0.963±0.010
1.25	1.236±0.010	1.239±0.010
<b>1.50</b>	1.516±0.012	1.497±0.012
1.75	1.749±0.015	1.748±0.015
<b>2.00</b>	1.892±0.016	1.991±0.018
2.25	1.729±0.015	2.203±0.022
<b>2.50</b>	1.940±0.012	2.471±0.026
<b>3.00</b>	1.442±0.019	2.751±0.031
<b>4.00</b>	1.611±0.016	1.927±0.013
5.00	1.427±0.018	1.922±0.008
<b>10.00</b>	1.759±0.014	1.974±0.002

Table 3.4: Values of  $\alpha$  of the original power law and of the simulated unfiltered and filtered light curves. The original frequency break is equal to 1 mHz and  $a_1$  was adjusted to the LSP of the real data. The lines in bold correspond to the LSPs of Figure 3.5.

we are removing periods in the light curve longer than 3 minutes i.e. frequencies lower than  $\sim 5.0$  mHz will be cutoff. In Figure 3.5 we show the LSP of the filtered light curves for increasing values of  $\alpha$  in black and the respective broken power law fit is shown in green. We also show for comparison a heavily-binned LSP of the unfiltered light curve in blue and the original power spectrum shape in red. In Table 3.4 we give the  $\alpha$  of the original power spectrum, the fitted  $\alpha$  of the LSP of the unfiltered and filtered simulated light curves. Note that for the filtered light curves we did not include frequencies lower than the cutoff frequency in the fit.

We conclude that this method is able to remove the red noise leak for light curves with  $\alpha < 3$ . Although it has the disadvantage of losing the low frequency information making us unable to measure the low frequency break, we can recover the high frequency shape of the power spectrum and probe the high frequencies.

It is interesting to look closely at the shape of an LSP affected by red noise leak, for example the LSP of the model power spectrum with  $\alpha = 2.5$  shown in Figure 3.5. In this case the difference in the slope of the LSP is easily missed by an automatic least

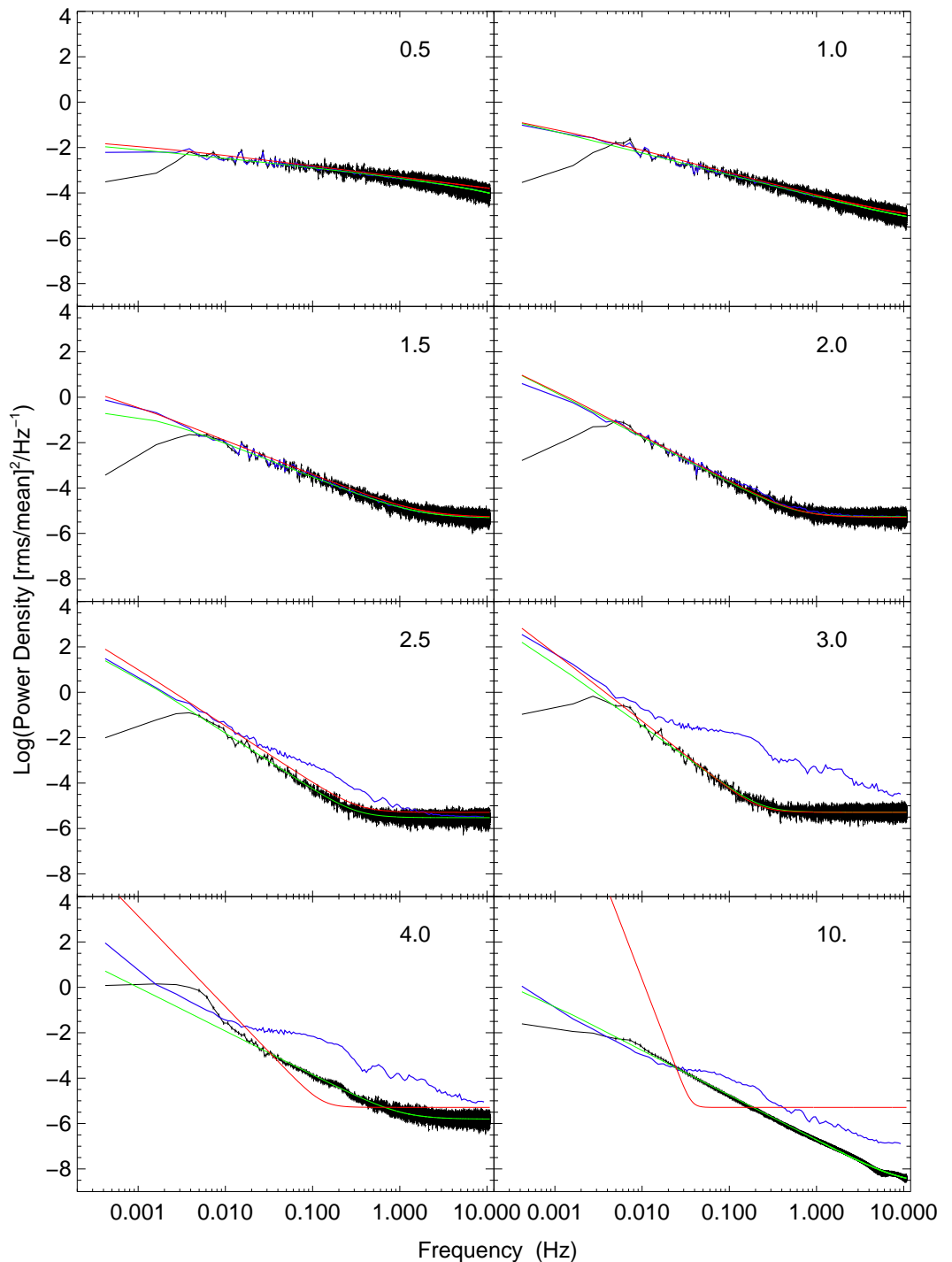


Figure 3.5: LSP of the simulated filtered light curves for increasing values of  $\alpha$ . From top to bottom, left to right  $\alpha = 0.5, 1.0, 1.5, 2.0, .2.5, 3.0, 4.0$  and  $10.0$  and  $f_b = 1\text{ mHz}$ . The original broken power law model that was used to simulate the light curves is shown in red and a fit to the LSP of the filtered light curve is shown in green. We also show a heavier binned LSP of the unfiltered light curve in blue.

squares fitting procedure and even by eye. However, there is a feature at 0.7 Hz that resembles a QPO and it might be taken as real but it is in fact the oscillation lobe of the power spectrum of the window function. Once again care should be taken when analysing this type of features since even when they are statistically significant they might be caused by red noise leak.

We investigate what would be the best value of the frequency cutoff for high pass filter. We expect than the majority of CVs has a value of  $\alpha$  lower than 3 so we used the example with  $\alpha = 3$  shown above and tried the following cut off frequencies: 20.0 mHz, 8.0 mHz, 5.0 mHz, 2.5 mHz and 1.0 mHz. We concluded that a cut frequency of 5.0 mHz is a good compromise between removing most of the red noise leak and maintaining the maximum of low frequency information.

In summary we strongly advise that all the fits to the LSP of red noise process are tested for the presence of red noise leak. If red noise leak is confirmed an attempt to recover the original power spectral index can be done using two methods depending in which part of the power spectrum we are interested in. If we are interested in the low frequencies one can fit the low frequency part of the LSP and obtain a more reasonable estimate of  $\alpha$  and  $f_b$ . If we are more interested in determining the power spectral index and recovering the shape of the LSP at high frequencies we can use a high pass filter which is a more robust method, since it does not depend upon choosing the right number of points to fit. We tested this method in the presence of noise and it works well if  $\alpha$  is lower than 3 for an appropriate choice of the filter cut-off frequency. An advantage of this method is that when it does not work ( $\alpha > 3$ ) the resultant LSP will have the same signs of red noise leak as before it was filtered (i.e. an  $\alpha \sim 2$ ). These two methods will give reasonable results if appropriate parameters are used and are complementary, but they always should be tested by Monte Carlo simulations. Only when the simulations are able to describe both the low frequencies and the high frequencies of the LSP we can be reasonably confident in the value of  $\alpha$  and  $f_b$ .

We will use both these techniques when studying the power spectra of cataclysmic variables in chapter 6.

## Chapter 4

# Constraints upon the unipolar model of V407 Vul and HM Cnc<sup>3</sup>

### 4.1 Introduction

In recent years, much attention has been paid to what are possibly the shortest period binary stars known, V407 Vul ( $P = 570$  s, (Cropper et al. 1998; Motch et al. 1996)) and HM Cnc ( $P = 321$  s, (Israel et al. 1999)). Both of these stars show highly modulated X-ray light curves, which are on for about 60 per cent of the time and off for the remaining 40 per cent (Cropper et al. 1998; Israel et al. 1999). Both stars also show only one period (and its harmonics) at all wavelengths observed (Ramsay et al. 2000, 2002a; Israel et al. 2002). These and other properties have lead to the suggestion that the periods may be orbital, only possible for a pair of compact objects, most likely white dwarfs. This would make these systems strong emitters of gravitational waves and possible progenitors of the semidetached AM CVn stars.

There are several rival models for these systems. V407 Vul was first suggested to be an intermediate polar (IP), in which case its 9.5 min period would be the spin period

---

<sup>3</sup>This section was published in Barros et al. (2005)

of an accreting magnetic white dwarf (Motch et al. 1996). However, the lack of any other period representative of a longer period binary orbit lead Cropper et al. (1998) to suggest instead that V407 Vul was a polar containing a white dwarf with a strong enough magnetic field to lock its spin to the orbit, making it the first known double degenerate polar. This model received a blow when no polarisation was detected (Ramsay et al. 2000), which lead Wu et al. (2002) to develop a unipolar inductor model. In the unipolar inductor model, a slight asynchronism between the spin period of a magnetic white dwarf and the orbital period within a detached double white dwarf binary creates an electric current between the two components of the binary. The dissipation of this current powers the observed X-ray flux. Following Wu et al. (2002), an alternative double white dwarf model was developed by Marsh & Steeghs (2002) and Ramsay et al. (2002b). They proposed that accretion could be taking place without a disc (Nelemans et al. 2001a), because for periods below  $\sim 10$  min and for plausible system parameters it becomes possible for the mass transfer stream to crash directly on to the accreting white dwarf. HM Cnc, although of a shorter period, is so similar to V407 Vul that all the above models apply equally well to it as they do to V407 Vul. Finally, the IP model was resuscitated by Norton et al. (2004) with a model in which we see the systems almost face-on with the X-ray variations caused by the accretion stream flipping completely from one magnetic pole to the other each cycle.

There is as yet no clear winner out of the various models, all of which face difficulties. In the direct impact model, we expect the (orbital) period to be increasing, whereas measurements show it to be decreasing in both V407 Vul (Strohmayer 2002, 2004) and HM Cnc (Hakala et al. 2003; Strohmayer 2003; Hakala et al. 2004). The weakness of optical emission lines in HM Cnc and V407 Vul also seems hard to reconcile with an accreting binary, even though direct impact may produce weaker line emission than disc accretion (Marsh & Steeghs 2002). The weakness of the optical emission lines is probably also the most difficult fact to accommodate within polar or IP models,

because all such systems discovered to date exhibit strong lines in their spectra. The IP model (Norton et al. 2004) is also unattractive for the fine-tuning it requires for two independent systems. The unipolar inductor model faces only a theoretical problem: it is short lived ( $\sim 1000$  years) because it lives off the spin energy of one of its two white dwarfs. As yet, no way of creating/maintaining asynchronism in the face of strong dissipation has been proposed (see Dall'Osso et al. (2006b)). It does however nicely match the decreasing period of both systems, and so can justly be claimed to be the leading model at present (Hakala et al. 2004).

Until a better alternative is found, we are faced with trying to select the least worst amongst the models and every model must be tested as far as possible against the available observations. In this chapter, we examine whether the X-ray light curves are compatible with the unipolar inductor model, an area not considered in detail by Wu et al. (2002). In section 4.3 we define the geometry that we use to describe the Wu et al. (2002) model, then we present our results in section 4.4. We begin however by reviewing the observational constraints deduced from the X-ray light curves.

## 4.2 Observational Constraints

Our aim is to see if the observed light curves have a natural explanation under the electric star model. In doing so, it is important to avoid fine detail as probably all models fail at this level. For instance, in its simplest form of a small spot at the equator, the direct impact model gives 50:50 on/off, not the observed 60:40 ratio. However, it is not impossible to imagine that vertical structure near the impact site along with heating spreading downstream from it could lead to an increase of the “on” phase. Thus, we try to distill key features which should be explained on any model, without being over specific in our selection. We identify the following key constraints:

- I. The bright phase during which X-rays are seen from the heated spots has to *last*

*for less than 0.6 of the cycle.* While, as described above, it is possible to extend the visibility period of a given simple model, it is much harder to decrease it, so we believe that this is a fundamental restriction upon any model.

- II. The bright phase has to be *more than 0.4 of the cycle* because the maximum size of a spot (see later) extends the visibility period by 0.2 of a cycle at most.
- III. The phase of the X-ray maxima must deviate from a smooth long-term trend by at most 0.2 of a cycle, in order to match the observations (Strohmayer 2004, 2003).
- IV. The light curves show no hint of eclipses and so we take the orbital inclination angle  $i$  to satisfy:

$$\cos i \geq \frac{r_1 + r_2}{a} \quad (4.1)$$

where  $r_1$  and  $r_2$  are the radii of the two stars and  $a$  is the binary separation.

### 4.3 The Geometric Model

Following the model presented by Wu et al. (2002) we consider a system in which one star (which we call the secondary star) orbits within the magnetic field of its companion, the primary star. An asynchronism between the spin of the primary star and the orbit induces an electric current to flow along the field lines connecting the two stars, with energy dissipated mainly where these field lines enter the surface of the primary star. In the Jupiter–Io system the observed emission lies within  $6^\circ$  of the theoretically predicted foot point (Clarke et al. 1996). In our case, we expect the emission to be even nearer to the foot point because of the smaller degree of asynchronism.

Our task is to identify the positions of these foot points and then work out for how long they are visible for a given orbital inclination. We treat them as points in order to allow the model to match the 40 per cent dark phase during which X-rays disappear (constraint I, section 4.2) as easily as possible. To allow the model flexibility in matching

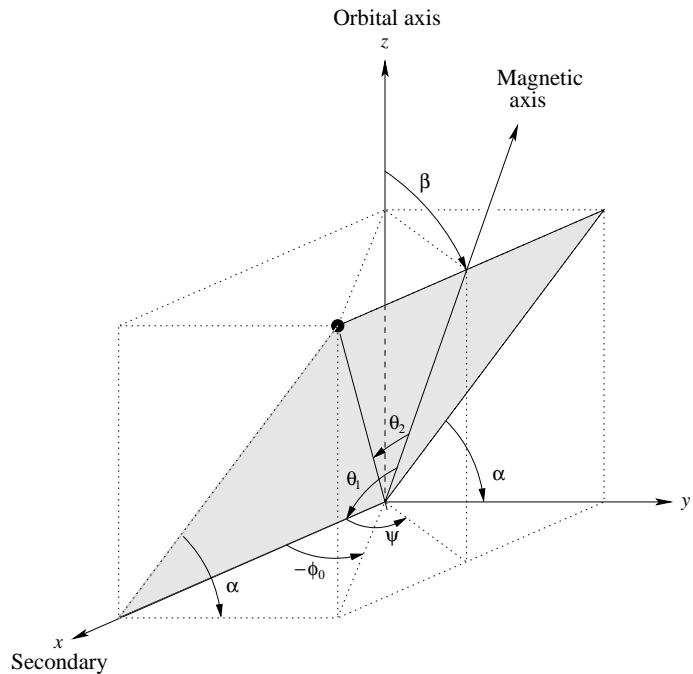


Figure 4.1: Orientation of the primary relative to the orbital axis and direction of the secondary's centre. We also define the orientation of the magnetic field of the primary, tilted by  $\beta$  from the  $z$  axis and whose projection in the  $x$ - $y$  plane makes an angle  $\psi$  with the  $x$ -axis. The dot represents where the field line that goes through the secondary crosses the surface of the primary, the position of the spot makes an angle  $\theta_1 - \theta_2$  with the  $x$ -axis.

the bright phase, we allow for the maximum size of the spots, as described at the end of this section.

We will now describe the geometry of the model with reference to Figure 4.1. We work with a right-handed Cartesian coordinate system ( $x,y,z$ ) centred upon the primary star, with the  $x$ -axis pointing towards the secondary star, the  $y$ -axis parallel to the direction of motion of the secondary star, and the  $z$ -axis along the orbital axis (Figure 4.1). The axis of the magnetic dipole is tilted by an angle  $\beta$  (often called the magnetic colatitude) with respect to the spin and orbital axes, which we take to be aligned. The azimuthal angle or magnetic longitude of the dipole  $\psi$  is defined by the angle between its projection on to the orbital plane (the  $x$ - $y$ -plane) and the  $x$ -axis. In the model of Wu et al. (2002), there is an asynchronism between the period of the binary and the spin period of the magnetic white dwarf. Therefore  $\psi$  is the angle that completes a cycle every few days owing to the asynchronism between the orbital frequency  $\omega_o$  and the spin frequency of the primary star  $\omega_s$ :

$$\psi = (\omega_s - \omega_o)t + \psi_0. \quad (4.2)$$

Wu et al. (2002) estimate the asynchronism  $(\omega_s - \omega_o)/\omega_o$  to be 1 part in 1000. This means that all possible azimuths of the magnetic axis compared to the line of centres of the two stars are explored within  $\sim 1000$  orbits, which is only a few days. If the magnetic axis is tilted with respect to the orbital axis, such azimuth variation causes the phase of the light curve maxima to vary back and forth relative to any long term trend. By applying the condition III upon the phase, we effectively assume that the X-ray observations have sampled all possible relative orientations of the magnetic axis (all values of  $\psi$  have been explored) and therefore we insist that the constraints of the previous section are satisfied for all  $\psi$ . Ideally this would be the case and indeed with sufficient observations one can get very close to it. We will consider how close we are to this in reality in section 4.4.1.

We define the positions of the foot points by where the magnetic field line that passes through the centre of the secondary star crosses the surface of the primary star. This field line lies in a plane defined by the  $x$ -axis and the magnetic dipole vector, which makes an angle  $\alpha$  with the orbital plane, Figure 4.1. We define the orientation of the foot points in this plane with two angles  $\theta_1$  and  $\theta_2$ , which measure the angle between the dipole axis and  $x$ -axis, and the angle between the dipole axis and the foot point, respectively.

Using the equation for dipole field lines  $r = C \sin^2 \theta$ , we can deduce the following relation between  $\theta_1$  and  $\theta_2$

$$\sin \theta_2 = \sqrt{\frac{r_1}{a}} \sin \theta_1. \quad (4.3)$$

while from simple geometry one can show that

$$\cos \theta_1 = \cos \psi \sin \beta, \quad (4.4)$$

and that

$$\cos \alpha = \frac{\sin \psi \sin \beta}{\sqrt{(\sin \psi \sin \beta)^2 + \cos^2 \beta}}. \quad (4.5)$$

To be able to calculate the visibility of the spot from the Earth, we need the orbital phase  $\phi$  and the orbital inclination angle  $i$ , which we define in the standard manner, i.e.  $i = 90^\circ$  for an edge-on eclipsing system,  $\phi = 0^\circ$ , when the magnetic primary star is at its furthest from Earth. With all angles defined, a given spot is visible while

$$\cos(\phi - \phi_0) > -\frac{h}{A} \quad (4.6)$$

where

$$A = \sin i \sqrt{\cos^2(\theta_1 - \theta_2) + \cos^2 \alpha \sin^2(\theta_1 - \theta_2)}, \quad (4.7)$$

$$h = \cos i \sin \alpha \sin(\theta_1 - \theta_2), \quad (4.8)$$

and

$$\tan \phi_0 = \frac{-\cos \alpha \sin(\theta_1 - \theta_2)}{\cos(\theta_1 - \theta_2)}. \quad (4.9)$$

For given values of  $\beta$ ,  $i$ ,  $\psi$  and  $r_1/a$ , it is a straightforward matter to calculate the remaining variables, and in particular to calculate the fraction of the cycle over which the spot can be seen. Before describing these calculations, we pause to consider the issue of the size of the foot points, which is important for the second of our constraints, which defines the minimum period over which the spots are visible.

The sizes of the foot points are related to the size of the secondary star. If the latter is tiny, then so too are the foot points. Wu et al. (2002) give an equation for the size of the foot points (A1 of their appendix A) from which we deduce that the maximum extent in longitude of the foot points, is of order  $2r_2/a$  radians. This will lengthen the bright phase by a corresponding amount. The maximum extent is thus set by the maximum relative size of the secondary, which is itself set by Roche geometry. For equal mass ratios, we deduce a maximum longitude extent of about  $40^\circ$ , which could extend the bright phase by  $\sim 10$  per cent of the cycle. To be conservative, we assume a maximum lengthening of 0.2 for all models, as outlined in constraint II of section 4.2.

In our model we assume that the X-rays are only emitted at one of the two foot points. Allowing both spots to contribute makes matters worse. Although the restriction that the bright phase lasts for more than 40 per cent of the cycle becomes easier to satisfy, it is more difficult to fit the 40 per cent dark interval. The phase restriction is also affected negatively: for most configurations only one spot would be visible at a given time, but when the two spots are visible there would be a change in  $\psi$  leading to a phase shift.

### 4.3.1 Computations

We computed the fraction of the cycle for which one of the foot points is visible as a function of magnetic colatitude  $\beta$  (from 0 to  $180^\circ$ ) and orbital inclination (0 to  $90^\circ$ ). In order to implement our assumption that we have observed all possible values of  $\psi$ , we search for the maximum and minimum values of the spot visibility over a finely spaced

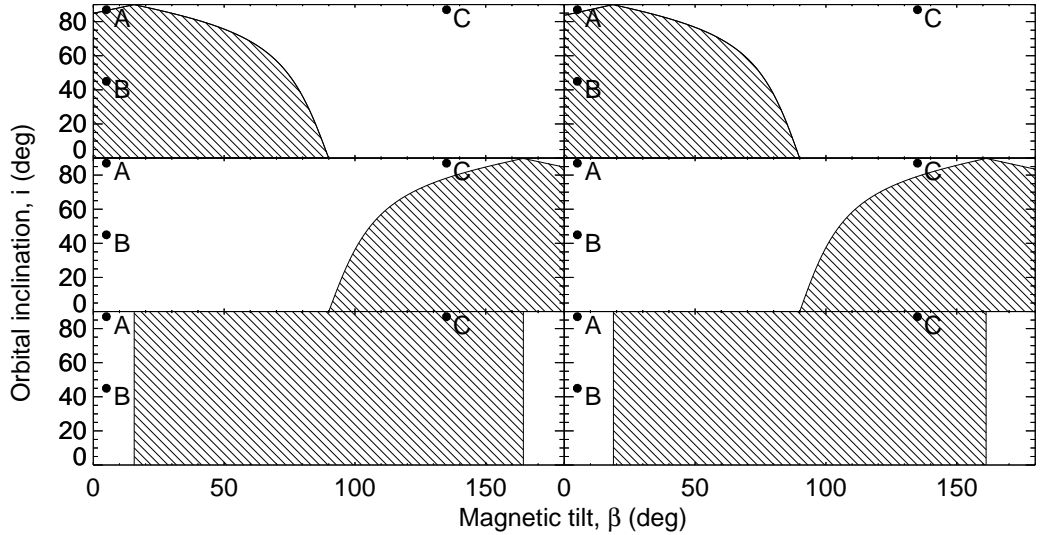


Figure 4.2: Geometrical constraints for the unipolar modal, for V407 Vul in the left-hand panel and for HM Cnc in the right-hand panel. The shaded areas represent the parameter space ruled out by the restrictions I, II and III respectively in the top, middle and bottom panels. The typical light curves of systems with combination parameters marked as A, B and C will be shown in Figure 4.4.

array of  $\psi$  values from 0 to  $180^\circ$  (symmetry allows us to avoid searching over  $360^\circ$ ). In order to obey the constraints of section 4.2, we must have that:

1. the *maximum* time that the spot is visible must be *less* than 0.6 of a cycle;
2. the *minimum* time that the spot is visible must be *more* than 0.4 of a cycle.

The masses of the white dwarfs have to be less than  $1.4 M_\odot$  (Chandrasekhar's limit) and larger than the Roche lobe filling mass: for HM Cnc  $M_1, M_2 > 0.12 M_\odot$  and for V407 Vul  $M_1, M_2 > 0.065 M_\odot$ . We calculated the binary separation using Kepler's third law and the radius of the white dwarf using Eggleton's mass-radius relation quoted by Verbunt & Rappaport (1988).

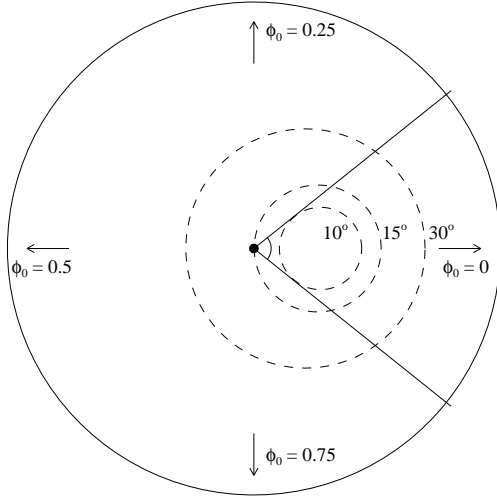


Figure 4.3: Track of the heated spot (dashed lines) viewed from above the primary star (outermost circle) for different choices of inclination of the magnetic field  $\beta$ . For  $\beta$  smaller than the critical angle  $\beta_c$ , the track is always on the side facing the secondary (towards the right). In this case, the X-ray pulse phase varies over a restricted range indicated here by the two tangential lines for  $\beta = 10^\circ$ . For  $\beta$  greater than  $\beta_c$ , the heated spot makes a complete circle around the polar axis of the primary star causing a complete phase shift of the X-ray pulses over one beat period.

## 4.4 Results

We start by discussing how the constraints of section 4.2 restrict the possible values of the magnetic tilt  $\beta$  and the inclination angle  $i$  for typical white dwarf masses of  $0.6 M_\odot$  (Figure 4.2). The first constraint (top panels) rules out combinations of low inclination and small angle between the magnetic field and the spin axis. This is because we would be looking at the north pole and the spot would also be in the northern hemisphere, i.e. it would be visible for most of the time, which would violate the maximum 60 per cent bright phase. Note that there is a critical magnetic colatitude when  $\beta_c = \theta_2$  given by

$$\tan \beta_c = \sqrt{r_1/a} \quad (4.10)$$

such that, when the magnetic axis is tilted away from the secondary star ( $\psi = 180^\circ$ ), the foot point lands upon the spin pole of the primary star and will therefore always be visible, no matter the orbital inclination. For  $M_1 = M_2 = 0.6 M_\odot$ ,  $\beta_c = 15^\circ$  for V407 Vul

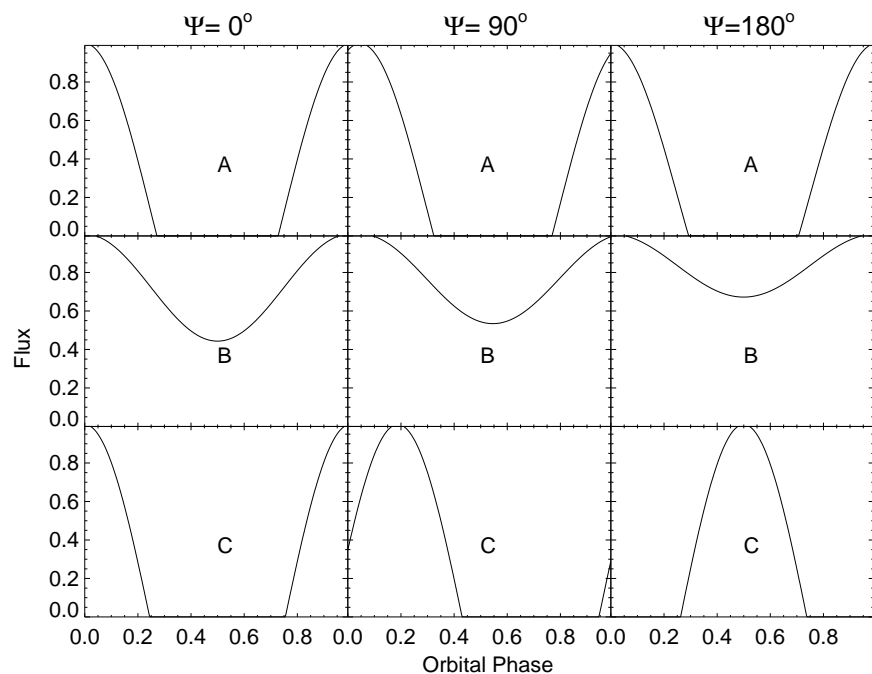


Figure 4.4: The figure shows examples of X-ray phase light curves for V407 Vul. A, B and C represent different choice of parameters shown in Figure 4.2 with three possible  $\psi = 0^\circ, 90^\circ$  and  $180^\circ$  to illustrate the phase shift. For A,  $\beta = 5^\circ$  and  $i = 87^\circ$ , for B,  $\beta = 5^\circ$  and  $i = 45^\circ$  and for C,  $\beta = 135^\circ$  and  $i = 87^\circ$ . In all the figures, the flux is normalised to unity.

and  $19^\circ$  for HM Cnc. This critical value is clear in Figure 4.2.

The second constraint is symmetric to the first, so that the foot point cannot lie too close to the south pole without leading to too short a visibility fraction (central panels of Figure 4.2).

The third constraint, that of phase, is highly restrictive as it removes all colatitude values in the range  $\beta_c < \beta < 180 - \beta_c$ . In other words, the magnetic and orbital axes must be nearly aligned in order for the phases not to wander. The reason for this is that, for  $\beta$  in the excluded range, the phase switches by  $180^\circ$  depending upon whether the magnetic dipole is oriented towards or away from the secondary star. This would show up as a large deviation in the X-ray pulses from a smooth trend. Note that our exact phase constraint ( $< 0.2$  of a cycle variation) is actually a little more restrictive still because significant phase wander occurs as  $\beta$  nears  $\beta_c$ .

To better illustrate this, Figure 4.3 shows the track of the heated spot on the primary star during one beat period as seen in the rotating frame of the binary. We can see that, for  $\beta < \beta_c$  (or the symmetric case  $\beta > 180 - \beta_c$ ), the phase offset is restricted to lie within the region defined by the two tangential lines to the small dashed circle but for  $\beta > \beta_c$  the phase offset goes through a complete cycle. For the dipole field we assume one can show that the tracks are perfect circles.

To visualise the three constraints, Figure 4.4 shows examples of the light curves using some combinations of parameters that illustrate the problems of this geometry. When  $\beta = 5^\circ$  and  $i = 87^\circ$  (marked A on Figure 4.2) the light curve obeys the first three constraints and it is similar to the observed data. In the second case considered,  $\beta = 5^\circ$  and  $i = 45^\circ$  (B in Figure 4.2) the spot is always visible and therefore fails to obey constraint I. In the third example,  $\beta = 135^\circ$  and  $i = 87^\circ$  (C) the phase constraint is not complied with and there is a large phase shift between  $\psi = 0^\circ$ , and  $\psi = 180^\circ$ .

The fourth and last constraint is the restriction that the system does not eclipse. This is independent of magnetic tilt and depends only upon the masses of the two stars

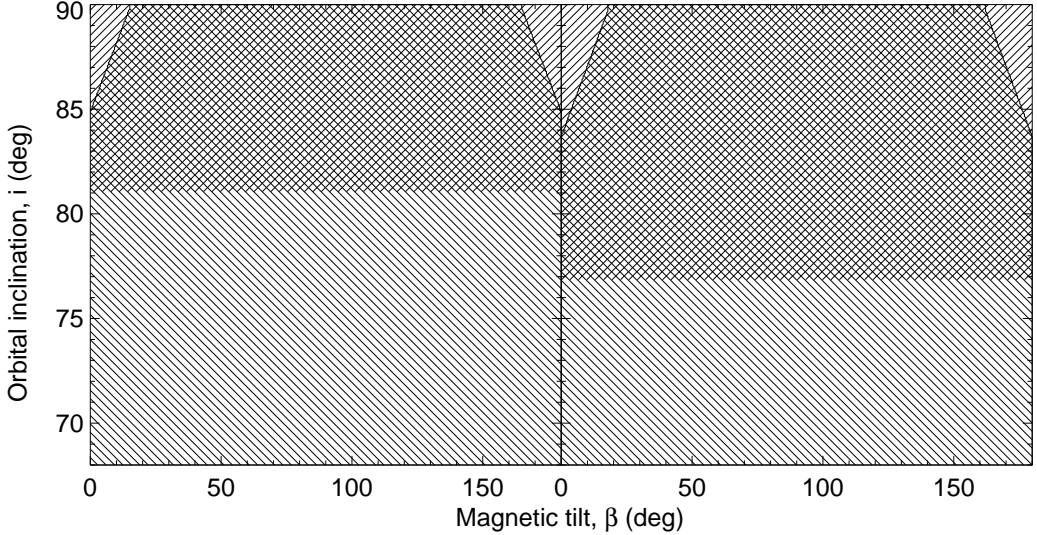


Figure 4.5: The lines going from top left to bottom right represent the parameter space ruled out by the combination of the constraints I, II and III for V407 Vul in the left-hand panel and for HM Cnc in the right-hand panel. The only regions left out are two triangles in the top corners of the parameter space. However, these are also ruled out when we include the absence of eclipses, which rules out the regions shown by the oppositely sloped lines. Therefore, we are left with no possible solution in the case of  $M_1 = 0.6 M_\odot$  and  $M_2 = 0.6 M_\odot$ . Note that the vertical scale here has been adjusted to show only the top parts of Fig. 2

for a given orbital period.

In Figure 4.5, we show the possible values allowed by the combination of all the constraints mentioned above, for  $M_1 = M_2 = 0.6 M_\odot$ ; other white dwarf masses will be considered later. The figures also show the maximum inclination for which the system will not have eclipses (horizontal lines). Together, the constraints rule out all parameter combinations.

#### 4.4.1 Detailed analysis of the phase constraint

We assumed for simplicity that we have seen all possible values of the angle  $\psi$  which measures the azimuth of the magnetic dipole within the binary. However, in this section, we investigate further if this is really the case or if the observations of the two systems carried out so far are insufficient to eliminate the possibility that the systems were only

observed over a small range of  $\psi$ , thereby increasing the available region of parameter space.

We only used the X-ray data because, according to the unipolar inductor model, the optical flux is from the secondary star and is therefore locked to the orbit.

Wu et al. (2002) deduced that, for V407 Vul, an asynchronism of 1 part in 1000 would be enough to explain the luminosity observed.

The degree of asynchronism is a little arbitrary so we explored several values in the range 1 part in 100 000 to 1 part in 700 for V407 Vul. We used the dates and durations of the X-ray observations of V407 Vul to compute the phase shifts that would have been seen for a set of degrees of asynchronism in this range. The largest asynchronism of 1 part in 700 is set by the length of the longest observation and is such that this observation covered an entire beat cycle. A degree of asynchronism larger than this returns us to our original assumption of complete coverage of  $\psi$ . The phase shifts were then fitted with a quadratic ephemeris and the scatter around the ephemeris was minimised by subtraction or addition of whole cycles where necessary. This process simulates the treatment of the observed pulse times by, for example, Strohmayer (2004) and acts to reduce the phase shifts somewhat. Finally, the values were minimised over the (unknown) phase offset  $\psi_0$  by repetition of the computation for 40 values equally spaced around a cycle and retention of the minimum shift calculated. This is in the spirit of trying to give the unipolar inductor model the benefit of the doubt where possible.

We applied the same method to HM Cnc. In this case, the observations were much shorter and so our range of the degree of asynchronism is 1 part in 100 000 to 1 part in 80, which corresponds to the period of the longest observation which was made with *XMM-Newton*. We reduced archival *XMM-Newton* data from November 2002 to complement the phase timing by Strohmayer (2003). Using the latest published value for the period  $P$  and its derivative  $\dot{P}$  (Hakala et al. 2004) and the phase 0 of the phase folded X-ray light curve of Israel et al. (2003) MJD = 52225.36153  $\pm$  0.00004 for

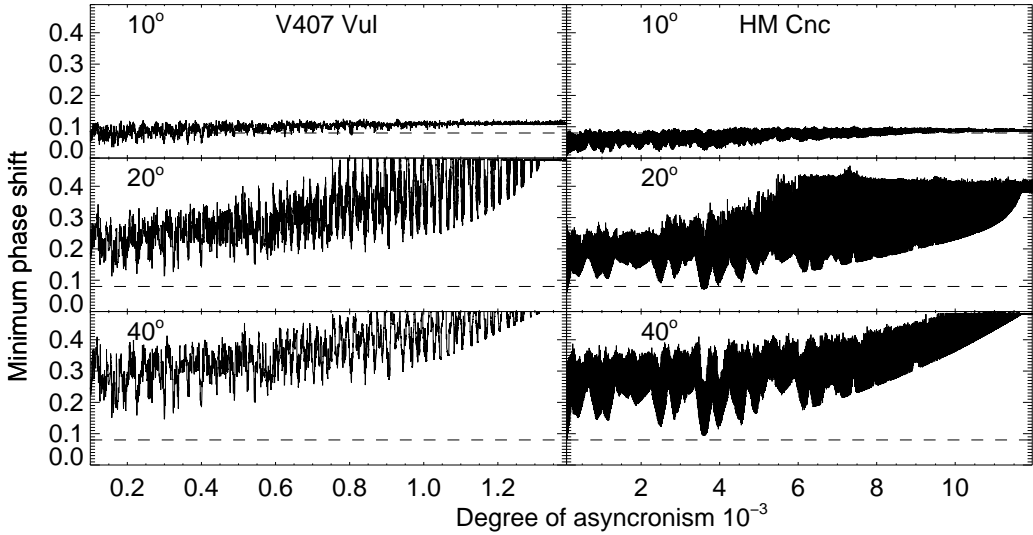


Figure 4.6: The minimum phase shift relative to a quadratic ephemeris as a function of the degree of spin/orbit asynchronism for  $\beta = 10^\circ$ ,  $20^\circ$  and  $40^\circ$ . The dashed line represents the maximum phase shift measured in the observations of the two stars, which is 0.08.

comparison, we obtained a phase shift for November 2002 close to zero, so we include the times for these observations in our study. However, given present uncertainties in both  $P$  and  $\dot{P}$ , we cannot rule out a larger phase shift between any of the observations.

Our results are shown in Figure 4.6 in which we plot the phase shift, minimised over  $\psi_0$ , as a function of the degree of asynchronism that would have been seen in the past observations of V407 Vul and HM Cnc, for different inclinations of the magnetic field  $\beta$  if the Wu et al. (2002) model is correct. (Note that the phase shift is independent of the orbital inclination  $i$ .)

As expected from our simple phase constraint, small angles of  $\beta$  such that  $\beta < \beta_c$  do have low enough phase shifts to match the observations, which show at most a deviation of 0.08 cycles for both systems. For V407 Vul, when  $\beta > \beta_c$ , even the minimised values that we plot are consistently larger than is observed, although the phase shifts do not match the value of 0.5 that we would predict for perfect observational coverage. In other words, the observations of V407 Vul are extensive enough that our conclusion

that the region  $\beta_c < \beta < 180 - \beta_c$  is ruled out by the absence of phase shifts remains unchanged.

The much sparser observations of HM Cnc on the other hand, do not allow us to rule out large  $\beta$  angles with confidence as some frequencies show relatively small phase shifts. Clearly more observations of HM Cnc are required. Having said this, if the unipolar inductor model were to be let off the hook by this means, it would be at a significant price because then the X-ray phases measured so far would not necessarily be a true reflection of the orbital phase and the present indications of spin-up (Hakala et al. 2004), which depend in large part upon ROSAT data, could well be spurious.

## 4.5 Discussion

In this section, we will discuss the limitations of our analysis, the effect of varying the white dwarf masses and the effect of the spot size upon the allowed parameter space.

### 4.5.1 Effects of different masses

All of the constraints depend upon the masses of the white dwarfs, so in this section, we explore whether changing the mass can allow some models to work. Increasing the size of the primary star helps by shifting the foot points towards its equator. Therefore, we expect an easing of the problem for small primary star masses, except that this will make the eclipse restriction harder to satisfy. Increasing the mass of the secondary star, on the other hand, is entirely beneficial because it increases the maximum inclination angle for which there is still no eclipse. However, it has to be said that there is some inconsistency here with respect to the foot point size, which will be nowhere near our assumed maximum. If this could be taken into account reliably, it would count against large masses for the secondary star, but we do not attempt to allow for this subtlety here.

For V407 Vul, we find that a very small area of the  $\beta-i$  parameter space is allowed for  $M_1 = 1.4 M_\odot$  and  $M_2 > 1.3 M_\odot$ , or for  $M_1 = M_2 = 1.3 M_\odot$ . The parameter space allowed requires the magnetic and spin axes to be nearly aligned ( $\beta < 2^\circ$  or  $\beta > 178^\circ$ ), the system to have a very specific orbital inclination ( $88.2 < i < 88.8^\circ$ ) and masses right at the top of the range for white dwarfs. Together, the combination is very unlikely and we will see below that it causes other problems. The case of HM Cnc is still tougher, and there are only possible solutions for  $M_1 = 1.4 M_\odot$  and  $M_2 = 1.4 M_\odot$ , which are even more restrictive for both  $\beta$  and  $i$  ( $\beta < 1.5^\circ$  or  $\beta > 178.5^\circ$  and  $87.8 < i < 88.3^\circ$ ).

There are no known white dwarfs with masses as high as required here. Moreover, even if the masses really were this high, they would be in severe conflict with one of the main pieces of evidence in favour of the unipolar model, which are the measurements of decreasing period, presumed to be caused by gravitational radiation. We computed the values of the spin up of the systems for the lowest masses that have any available parameter space assuming a detached binary driven only by gravitational radiation loss. For the case of V407 Vul with  $M_1 = M_2 = 1.3 M_\odot$  the spin up rate would be  $\sim 3.6 \times 10^{-16} \text{ Hz s}^{-1}$ , some fifty times the measured value reported by Strohmayer (2004) of  $7.0 \pm 0.8 \times 10^{-18} \text{ Hz s}^{-1}$ , while in the case of HM Cnc for  $M_1 = M_2 = 1.4 M_\odot$  the spin up rate would be  $\sim 2.3 \times 10^{-15} \text{ Hz s}^{-1}$ , five times the measured value reported by Strohmayer (2003) and Hakala et al. (2004) of  $6.00 \pm 0.1 \times 10^{-16} \text{ Hz s}^{-1}$ . In consequence, even the tiny region of parameter space that is opened up at high mass fails to match up against what we know of these systems.

#### 4.5.2 Spot Size

We assumed a maximum spot size that would extend the visibility of a point spot for 0.2 of a cycle, which corresponds to the secondary star filling its Roche lobe, i.e. a very low mass secondary. However, as seen in our analysis, the problems facing the unipolar model are eased at high masses. As the spot size depends greatly on the secondary

mass, the actual size of the footprints for the masses considered before would be only 0.02 of a cycle for  $M_1 = 0.6 M_\odot$  and 0.003 for  $M_1 = 1.4 M_\odot$  in the case of V407 Vul. With such a small spot size, it would be impossible to accommodate the model because, for example, if we force the bright phase to be more than 0.5 of a cycle, we eliminate all the values that were allowed by constraint I, i.e. the first two constraints alone would rule out the model.

There are some effects that might help make the spot larger, for example the X-rays could perhaps come from a vertical extended region (along the field lines), that would allow us to see them for a little bit longer, although this might be difficult to reconcile with the thermal nature of the X-ray spectrum. Perhaps the foot points can leave a trail along the azimuthal direction ( $\phi_0$ ), that would enlarge the size of the emitting region. The theoretical estimates of the cooling time-scale indicate that trailing is unlikely to be significant (Stockman et al. 1994), but we can in any case show that increasing the visibility duration has only a limited effect in helping the unipolar model. In Figure 4.7, we show the effect of increasing the spot size upon the available parameter space. Only for very large spot sizes, covering  $> 0.3$  of a cycle in azimuth, is possible parameter space opened up. (Note that 0.6 is the largest possible azimuth extent given the need for a 40 per cent off period.)

In summary, even a fairly radical alteration to allow much larger spots than are predicted by the unipolar model at best opens up a small region of parameter space with  $\beta > 173^\circ$ ,  $74^\circ < i < 81^\circ$ . It is clearly unlikely that these apply to two independent systems.

## 4.6 Conclusion

Assuming a dipolar field geometry, and that the spin and orbital axis are aligned, we find that the unipolar inductor model presented by Wu et al. (2002) cannot match the X-ray

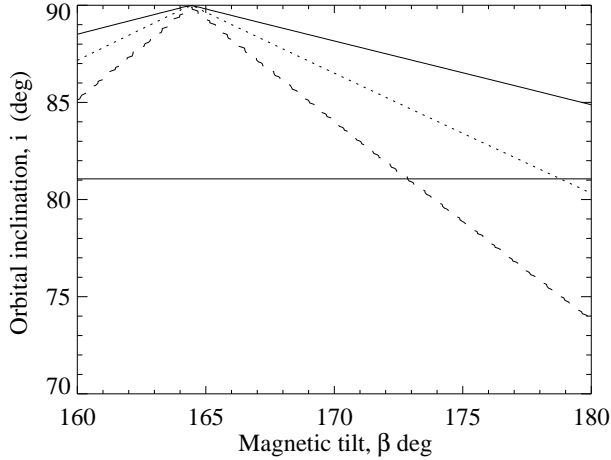


Figure 4.7: The top-left region of the parameter space where we show the constraint II for several maximum spot sizes: 0.2 of a cycle (solid line), 0.3 of a cycle (dotted line) and 0.6 of a cycle (dashed line), for white dwarf masses of  $0.6 M_{\odot}$  for V407 Vul. The allowed regions are always above the lines. So for the spot sizes larger than 0.3 of a cycle, there is a small allowed region in parameter space which is also below the horizontal eclipse constraint.

light-curves of the two systems V407 Vul and HM Cnc. It fails because the foot points that produce the X-rays are situated quite close to the magnetic poles, while at the same time the magnetic axes are forced to lie almost parallel to the spin axes of the primary stars to avoid excessive phase shifts in the X-ray pulses. This then means that, to obtain the near 50:50 on/off light curves observed, both systems have to be seen at such high orbital inclination ( $> 88^\circ$ ) that they would eclipse, and yet no eclipses are seen. High masses for the component stars permit tiny regions of viable orbital inclination/magnetic inclination parameter space, but lead to very large gravitational wave losses inconsistent with observed period changes. If for some reason the heated spots are much larger than the unipolar model predicts, a small region of parameter space is allowed, but even this requires fine tuning for two systems. The only remaining chinks of light for the unipolar inductor model are that HM Cnc, owing to relatively sparse X-ray coverage, could have a relatively highly inclined dipole without our having spotted the large phase shifts so

far, or possibly the field configurations are very different from a dipole in the two stars. Further observations are encouraged to close this loophole. We have been careful where possible to err in favour of the unipolar inductor model; we still have to conclude that it is not viable in its current form.

# Chapter 5

## ULTRACAM Photometry of the ultracompact binaries V407 Vul and HM Cnc<sup>4</sup>

### 5.1 Introduction

V407 Vul (RXJ1914.4+2456) (Motch et al. 1996) and HM Cnc (RXJ0806.3+1527) (Israel et al. 1999; Burwitz & Reinsch 2001) were both discovered in the *ROSAT* all sky survey and have very similar X-ray properties. An overview of the properties and models for these two systems is given in section 4.1. The unipolar inductor model, along with the IP model, is favoured by the observed decrease in pulsation periods (Strohmayer 2002; Hakala et al. 2003; Strohmayer 2003, 2004; Hakala et al. 2004) although recently accreting models with long-lasting spin-up phases have been developed (D'Antona et al. 2006; Deloye & Taam 2006). The shapes and phases of the X-ray light curves on the other hand count against the unipolar inductor model (Barros et al. 2005), as seen in chapter 4, which can only accommodate the high X-ray luminosity of V407 Vul

---

<sup>4</sup>This section was published in Barros et al. (2007)

with a white dwarf that spins faster than its orbit (Marsh & Nelemans 2005; Dall'Osso et al. 2006a,b). The accreting double-degenerate models on the other hand lead to high accretion rates and strong heating of the white dwarf, particularly in the case of HM Cnc, which is required to be at a distance of 4–20 kpc, and well out of the Galactic plane (Bildsten et al. 2006; D'Antona et al. 2006). At the moment therefore, there is no clear winner, or even leading contender amongst the models and better observational constraints are a priority. Previous studies of the systems have focused mainly upon the properties of the X-ray light curves with optical data used mainly to track the decreasing periods with less attention being paid to the shapes of the light curves. With the work of D'Antona et al. (2006) and Deloye & Taam (2006) adding uncertainty to the interpretation of the period change measurements, the light curves themselves take on more significance. In this chapter we present high-speed photometry of these systems in three simultaneous bands taken in the hope of using the optical characteristics to learn more about the systems. In section 5.2 we report our observations and data reduction. In section 5.3 we present our results. In section 5.4 we use our results to try to determine the origin of the optical pulses and explore the consequences for the accretion geometry in these systems.

## 5.2 Observations and reduction

We observed with the high-speed CCD camera ULTRACAM (Dhillon & Marsh 2001) mounted on the 4.2 m William Hershel Telescope (WHT) in La Palma on May 2003 and August 2005, and mounted on the UT3 unit (Melipal) of the Very Large Telescope (VLT) in Chile in November 2005. For V407 Vul we have observations on five consecutive nights from the 21<sup>st</sup> to 25<sup>th</sup> of May, 2003 with a total of approximately 3600 frames of 9.7 s exposure in the  $i'$ ,  $g'$  and  $u'$  filters and another 2000 frames of 15 s exposure in five extra nights from the 27<sup>th</sup> of August to the 1<sup>st</sup> of September 2005 in  $r'$ ,  $g'$  and  $u'$ .

<b>Target</b>	<b>Telescope</b>	<b>Date</b>	<b>UT</b>	<b>Seeing, clouds</b>
V407 Vul	WHT	21 May 2003	05:33 - 06:25	1.0, clear
V407 Vul	WHT	22 May 2003	03:28 - 04:24	1.0, clear
V407 Vul	WHT	22 May 2003	04:54 - 06:25	1.0, clear
V407 Vul	WHT	23 May 2003	02:25 - 04:24	1.0, clear
V407 Vul	WHT	24 May 2003	02:48 - 03:41	1.0, some
V407 Vul	WHT	24 May 2003	04:50 - 06:18	1.0, clear
V407 Vul	WHT	25 May 2003	01:45 - 02:29	1.2, clear
V407 Vul	WHT	25 May 2003	03:19 - 04:41	1.2, clear
V407 Vul	WHT	27 Aug 2005	21:10 - 01:02	1.1, clear
V407 Vul	WHT	28 Aug 2005	21:05 - 22:38	0.9, clear
V407 Vul	WHT	30 Aug 2005	20:50 - 23:55	0.8, dusty
V407 Vul	WHT	31 Aug 2005	20:49 - 22:56	0.7, dusty
V407 Vul	WHT	01 Sep 2005	20:45 - 22:58	0.9, dusty
HM Cnc	WHT	21 May 2003	22:11 - 23:30	1.2, clear
HM Cnc	WHT	22 May 2003	21:54 - 22:57	1.0, clear
HM Cnc	WHT	23 May 2003	21:57 - 22:54	1.0, clear
HM Cnc	WHT	25 May 2003	21:55 - 22:39	1.3, clear
HM Cnc	VLT	27 Nov 2005	05:03 - 06:51	1.3, clear
HM Cnc	VLT	28 Nov 2005	05:10 - 08:47	1.0, clear
HM Cnc	VLT	29 Nov 2005	05:35 - 08:51	0.8, clear

Table 5.1: Observation log.

For HM Cnc we have around 2000 frames taken in four nights from the 21<sup>st</sup> to 25<sup>th</sup> of May with 10.1 s exposures in  $i'$ ,  $g'$  and  $u'$  and another 18 000 frames taken in November 2005 in  $r'$ ,  $g'$  and  $u'$  with exposures of 1–6 s. The observing conditions are summarised in Table 5.1. All the times were transformed to TDB, and then shifted to time as observed at the solar system barycentre using the IDL routine *barycen* and recorded as a modified Julian day MJD (TDB). The data were reduced using the ULTRACAM pipeline. We tried “optimal” photometry (Naylor 1998), variable aperture photometry and fixed aperture photometry to extract the light curves. Optimal photometry gave the highest signal-to-noise with the exception of the  $r'$  band in the August 2005 data, for which we used a fixed aperture radius. Optimal photometry requires the profiles to be identical in shape and can cause difficulties if this is not the case and we believe that in this one case this outweighed the improvement in stochastic noise. The subsequent

data analysis was carried out with IDL. V407 Vul is in a crowded field so care was taken to prevent the sky annulus from being contaminated by other stars. It is trickier to allow for the faint stars that can contaminate the target aperture in poor seeing. These are a particular problem in the  $i'$  filter (May 2003 data) where we found the flux could increase by as much as 5 per cent in the poorest seeing. Although relatively few of the data were affected by this, we corrected for it by fitting and removing the trend of flux versus seeing from the  $i'$  data. Finally, the  $g'$  data from the second half of the second run of the 22<sup>nd</sup> of May 2003 and the second half of the second run of the 24<sup>th</sup> of May 2003 could not be used because V407 Vul was unfortunately positioned close to a column of poor charge transfer on the  $g'$  CCD.

In the May 2003 observations of V407 Vul we used two comparison stars, one (c1) for the  $i'$  and  $g'$  bands and the other (c2) for the  $u'$  images (because c1 was too faint in  $u'$ ). The position relative to the target and the magnitudes of these comparison stars and the one used for HM Cnc are given in Table 5.2. In the August 2005 observations of V407 Vul we only used comparison star c2 because c1 was saturated in  $r'$  due to the longer exposure time. This run also suffered from Saharan dust that led to an extra and variable extinction of  $\sim 0.5$  mag at the zenith making it impossible to derive an absolute calibration to better than 0.2 mag. Therefore we used the  $g'$  and  $u'$  magnitudes of c2 calculated in May 2003 to calibrate the August 2005 data. To obtain the  $r'$  magnitude of c2, we applied the same correction as for  $g'$ .

The measured mean magnitudes of the systems are given in Table 5.3. As far as possible, the magnitude calibration was carried out by comparing the target and the comparison at the same airmass as we did not have sufficiently long runs to estimate accurate extinction coefficients. The uncertainties of the comparison star for HM Cnc are dominated by the uncertainties in the extinction coefficients for the night both in May 2003 ( $i'$ ) and in August 2005 ( $r'$ ,  $g'$  and  $u'$ ) because in this case we did not observe the target and the comparison at exactly the same airmass and some correction

<b>Comparison</b>	$\Delta\alpha$ (arcsec)	$\Delta\delta$ (arcsec)	$i'$	$r'$	$g'$	$u'$
V407 Vul c1	+3.1	-8.4	14.21±0.01	Saturated	16.26±0.01	19.78±0.03
V407 Vul c2	+39.5	-37.0	15.73±0.01	16.08±0.1	16.96±0.01	18.84±0.03
HM Cnc	-16.9	-16.4	15.25±0.11	15.31±0.10	16.00±0.11	17.73±0.12

Table 5.2: Position and magnitude of the comparison stars used to flux calibrate the data.

<b>Target</b>	$i'$	$r'$	$g'$	$u'$
V407 Vul May 2003	18.95±0.05	-	20.30±0.06	21.56±0.10
V407 Vul Aug 2005	-	19.3±0.1	20.29±0.06	21.53±0.08
HM Cnc May 2003	21.5±0.1	-	20.9±0.1	20.5±0.1
HM Cnc Nov 2005	-	21.21±0.10	20.77±0.11	20.51±0.12

Table 5.3: Magnitudes measured for the two targets.

was needed.

## 5.3 Results

### 5.3.1 Ephemerides

To compare our optical data with the published X-ray data we had to fold our data, on the X-ray ephemeris. Unfortunately none of the ephemerides published so far (Israel et al. 2003, 2004; Strohmayer 2004, 2005; Ramsay et al. 2006a) give the covariance terms of the fitted coefficients which are needed for a correct evaluation of the uncertainties. Therefore we had to digitise and fit the data of Strohmayer (2004, 2005) and Ramsay et al. (2006a) so that we could obtain a timing solution whose uncertainties we could compare with our data. When we did this we realised that there was an inconsistency between the ephemerides of V407 Vul published by Strohmayer (2004) and Ramsay et al. (2006a). After investigation we concluded that Strohmayer's (2004) ephemeris is probably in error because the ROSAT times were not corrected from UTC to TT. We therefore use our fit to Ramsay et al.'s (2006a) ephemeris (Table A.1) for V407 Vul which is similar to the ephemeris given in Ramsay et al. (2006a) but has a slightly

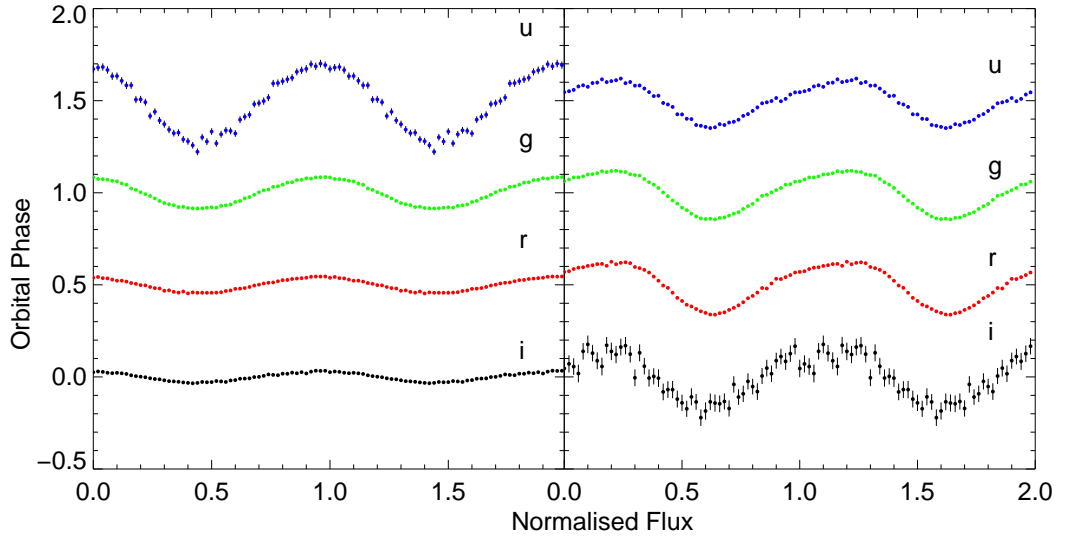


Figure 5.1: Phase-folded light curves of V407 Vul (left-hand panel) and HM Cnc (right-hand panel) using the ephemeris from Table A.1 and Strohmayer (2005). The flux is normalised to unity in each case. The different filters are displaced vertically for clarity.

different  $\dot{\nu}$ . For HM Cnc we used Strohmayer's (2005) ephemeris. Both ephemerides and respective covariance terms are given in Appendix A where we provide full details of our investigations.

### 5.3.2 V407 Vul

We show our phase-folded light curves of V407 Vul folded on the ephemeris of Table A.1 on the left-hand panel of Figure 5.1. The two data sets (May 2003 and August 2005) were rebinned to 100 phase bins using inverse-variance weighting to maximise the signal-to-noise ratio.

We computed the Lomb-Scargle periodogram (Lomb 1976; Scargle 1982) and confirmed the previously measured period of 569 s. We then tested how close the signal is to a perfect sinusoid by fitting a sine wave at the fundamental frequency and at the second and third harmonics. The third harmonic is consistent with zero. The results for the relative amplitude and the phase at maximum of the fundamental (i.e. the “first harmonic”) and the second harmonic are shown in Table 5.4 which also shows

	<b>V407 Vul</b>			<b>HM Cnc</b>		
	$a_2/a_1$	$\phi_1$	$\phi_2$	$a_2/a_1$	$\phi_1$	$\phi_2$
i'	0.079±0.030	0.961±0.012	0.458±0.16	0.207±0.064	0.122±0.010	0.335±0.025
g'	0.053±0.014	0.970±0.005	0.388±0.08	0.157±0.025	0.117±0.004	0.338±0.012
u'	0.095±0.036	0.977±0.012	0.544±0.05	0.131±0.050	0.118±0.008	0.285±0.031
r'	0.024±0.015	0.960±0.020	0.361±0.099	0.202±0.009	0.1616±0.0014	0.362±0.0034
g'	0.039±0.012	0.961±0.013	0.444±0.14	0.188±0.005	0.1659±0.0008	0.356±0.0022
u'	0.012±0.022	0.961±0.033	0.340±0.27	0.205±0.014	0.1700±0.0022	0.342±0.0055

Table 5.4: First and second harmonic decomposition of the optical light curves for V407 Vul and HM Cnc.  $a_1$  and  $a_2$  are the semi-amplitudes of the first and second harmonics, respectively, and  $\phi_1$  and  $\phi_2$  their phases of maximum light on Table A.1's and Strohmayer's (2005) ephemeris. In the case of HM Cnc, the measurements at the top and bottom come from the WHT and VLT, respectively, hence the marked difference in the uncertainties.

Filter	Semi-amplitude (%)	$t - t_0$ (s)	$\phi$ (cycles)
i'	3.03±0.06	-4.9±1.8	0.9612±0.0032
g'	8.47±0.09	0.0±0.9	0.9698±0.0016
u'	20.50±0.61	3.9±2.7	0.9767±0.0047
r'	4.39±0.06	-0.7±1.2	0.9596±0.0021
g'	8.70±0.07	0.0±0.7	0.9607±0.0013
u'	21.64±0.44	0.0±1.8	0.9607±0.0033

Table 5.5: Results of single harmonic sinusoid fitting for V407 Vul. The first three lines show the results for the May 2003 data and the last three lines show the results obtained in August 2005. The times mark the position of the maximum phases and are  $T_0 = 52782.191666$  for May 2003  $T_0 = 53612.9483393$  for November 2005. The phases are relative to the ephemeris of Table A.1.

the corresponding results for HM Cnc. We also fitted a sinusoid with frequency fixed to the value derived from the ephemeris of Table A.1 at our observing date to obtain a normalised amplitude of variation and the time (or equivalently the phase) of the maximum. The normalised amplitudes, the phase and the time-shifts relative to the g' band are presented in Table 5.5. The amplitude increases strongly towards short wavelengths but there is no observable phase shift with wavelength. From Table 5.5 we calculate a difference of phase between our two runs of  $0.0089 \pm 0.002$ . This could be taken to be as a significant shift in phase, however the uncertainty only represents the

measurement error. When we include the uncertainty of the ephemeris calculated with equation (A.2) we obtain  $0.0089 \pm 0.019$ , and therefore we conclude that there is no significant variation of the phase shift between the optical and the X-rays between the two epochs of our observations and that the new ephemeris can be used to extrapolate to later times. To compare the optical phases with the X-ray light curves it is important to notice that the absolute error of the phase due to the ephemeris of Table A.1 is 0.0090 for May 2003 and 0.019 for August 2005.

### 5.3.3 Pulsation astrometry of V407 Vul

A totally unexpected feature of V407 Vul is that its optical spectrum is dominated by that of a late G/early K star which cannot fit within a 10 min period binary orbit (Steeghs et al. 2006). Although this immediately suggests the IP model in which one expects a main-sequence secondary star (Norton et al. 2004), the star shows no radial velocity variations at a level that rules out orbital periods typical of cataclysmic variable stars ( $\leq 1$  day, Steeghs et al. 2006). Alternatives are that this star is a line-of-sight coincidence (the field is a crowded one), or it could be part of a triple system with the variable. To discriminate between the latter possibilities we searched for variations in the position of V407 Vul on its 569 s period. The idea behind this “pulsation astrometry” is that although we cannot spatially resolve the variable and G star components of V407 Vul directly, we can use the pulsations of the variable to try to detect their separation because their mean position will move back and forth between the variable and the G star as the variable brightens and fades. This method is sensitive to separations well below the seeing.

We measured the position of V407 Vul relative to nearby stars in the field. We then computed the amplitude of the best-fitting sinusoid over a range of frequencies for both the  $x$  and  $y$  positions in each of the three filters as shown in Figure 5.2. We computed false alarm probabilities using Monte Carlo simulations (finding values that

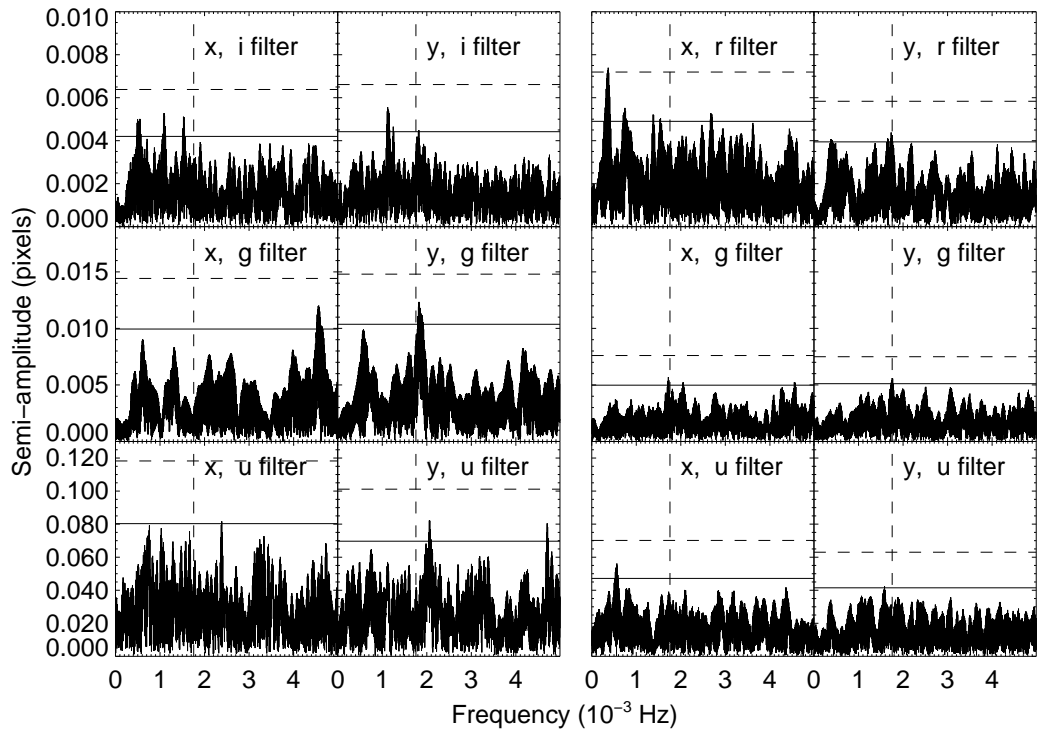


Figure 5.2: Each panel shows the amplitude spectra of the  $x$  (left-hand panel) and  $y$  (right-hand panel) variation of the position of V407 Vul for the three filters  $i'$  or  $r'$ ,  $g'$ , and  $u'$  from top to bottom. The left-hand panel shows the May 2003 data while the right-hand panel shows the August 2005 data. The vertical dashed lines show the position of the 569-s period. The solid horizontal lines show the 99.9 per cent significance level for a known period and the dashed horizontal lines show the same level for an arbitrary period.

agree with the theoretical values of Schwarzenberg-Czerny 1998b). In Figure 5.2 we show the 99.9 per cent detection threshold for a known period (horizontal solid lines) and also the 99.9 per cent detection threshold for an arbitrary unknown period (dashed lines). We choose the 99.9 per cent level because it corresponds to a detection limit of about “ $3\sigma$ ”. Note that the detection criterion is more stringent when we do not know the period because a penalty must be paid for searching multiple independent periods (Horne & Baliunas 1986a). We include this level to show that there are no such detections of any other periodicities. In the case of V407 Vul we know the period that we are looking for so it is the lower threshold represented by the solid lines that applies. As mentioned above, the  $g'$  data of the May 2003 run were partially affected by poor charge transfer in a column close to V407 Vul. This has more of an effect upon position (especially at the levels we measure here) than on flux, so for the position measurements we discarded the 50 per cent of the  $g'$  data where V407 Vul was closest to the column, but as a result reduced the sensitivity of the  $g'$  band data in the left-hand side of the figure.

There are detections of a signal at the 99.9 per cent level in the  $y$  position data in both  $r'$  and  $g'$  of the August 2005 run. Figure 5.3 shows a phase-folded, binned plot of the  $y$  position for these two cases. The time of maximum excursion roughly corresponds with the time of maximum light as expected, and both data sets are consistent with each other in this respect. However, the signal is tiny, with an amplitude of just 0.005 pixels or 0.0015 arcsec, and so we endeavoured to test the reliability of this detection as far as we were able. The most obvious problem is that V407 Vul is in a crowded field and so the position measurements could be affected by other stars. There are two stars within 1.5 arcsec of V407 Vul that can be seen in Figure 2 of Ramsay et al. (2002b). To check how these stars affected our measurements we first tested whether the detection depended upon the full width at half-maximum (FWHM) of the seeing. We divided the data in two parts, higher and lower FWHM. The reduction of data size lead to no

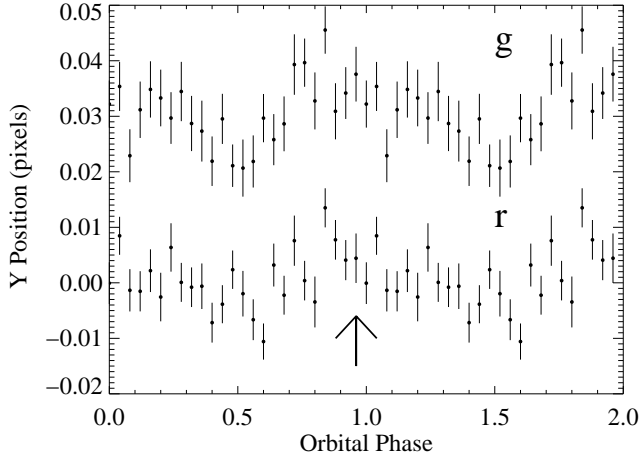


Figure 5.3: Position variation for  $g'$  and  $r'$  phase-folded on the X-ray ephemeris period for the data sets that show a significant signal. The arrow shows the position of the maximum of the flux.

detection in either case but the significance of the peaks was higher in the small FWHM data set. The reverse would have been expected had blending with the two nearby stars been the cause.

We measured the centroids by cross-correlation with 2D Gaussians of fixed width. This allows us to assess the effect of the Gaussian width upon the measured amplitude. As the FWHM of the Gaussian increases, we expect to see a more pronounced impact of the nearby stars. Therefore if it is the nearby stars rather than the G star that are responsible for the variation, we expect an increase of measured amplitude with Gaussian width. In fact we see the reverse as Figure 5.4 shows, at least in the  $y$  positions for which we have detections. The  $x$  positions do show a distinct upturn at large FWHM owing to the much brighter star 5 arcsec east of V407 Vul of star B (Ramsay et al. 2002b) which was positioned to the left-hand side of V407 Vul in our data.

As a final check we carried out simulations of our position measurements using parameters matching the stars that we could see nearby V407 Vul, including the two very close ones mentioned above. This leads to the dotted line in Figure 5.4. In viewing

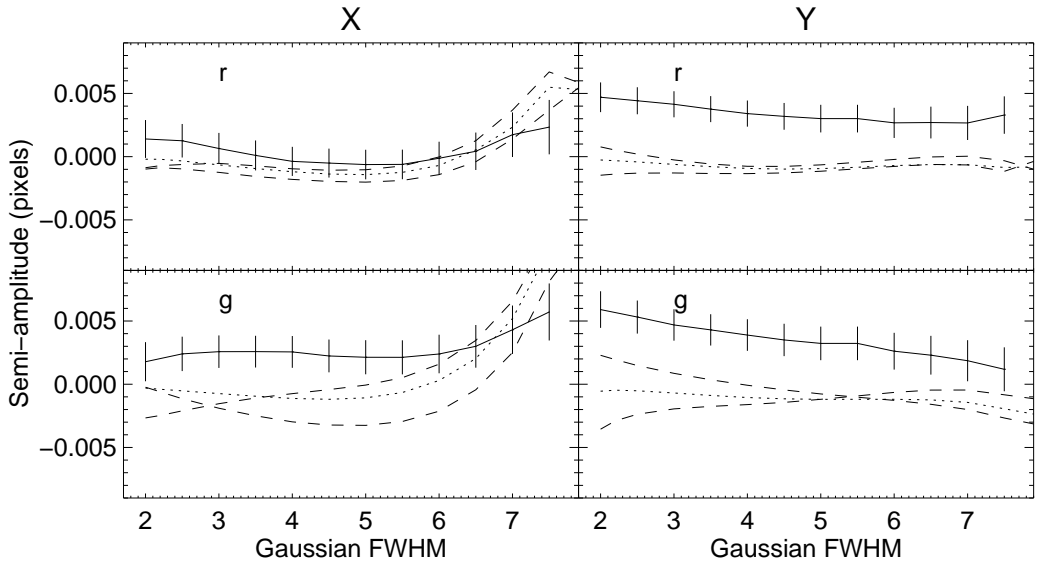


Figure 5.4: The dependence of the amplitude of the variation of the position upon the width of the Gaussian used to calculate the position. The data are plotted as a solid line, the simulations accounting for the known stars are plotted as dotted lines (no noise) and dashed lines (with noise). The simulations with noise have similar errors to the data but these errors were not plotted for clarity. The plate scale is  $0.3 \text{ arcsec pixel}^{-1}$ .

in this figure it must be recognised that the data are not independent and so to some extent the trends with FWHM can just reflect noise; the dashed lines in the figure show two simulations of the effect that noise can have upon the simulated amplitudes. These show that for the  $y$  positions the measured amplitudes are indeed significantly larger than the simulated values, and provide further confidence in the reality of the detection.

We conclude, albeit tentatively, that we have detected a change in the spatial position of V407 Vul that is correlated with its pulsations and that the change in position is because the G star we see in its spectrum is not exactly coincident with the variable. We predict that the G star should be below V407 Vul in our field which roughly corresponds to south of V407 Vul. We obtain amplitudes of the position variation which we denote by  $p$  of  $0.00512 \pm 0.0012$  and  $0.00514 \pm 0.0010$  pixels for  $g'$  and  $r'$ , respectively.

The value of  $p$  is related to the separation on the sky  $d$ , the fractional amplitude of the flux variation  $a$  as listed in Table 5.5 and the fractional contribution of the G star

to the flux at minimum light  $f$ , through the following relation:

$$p = \left( \frac{a}{a+1} \right) f d. \quad (5.1)$$

Using the measured values for  $a$  and  $p$  we calculate  $f_{r'}d = 0.0366 \pm 0.0073$  arcsec and  $f_{g'}d = 0.0192 \pm 0.0046$  arcsec. This gives a value of  $f_{g'}/f_{r'} = 0.52 \pm 0.16$ . This is consistent with the spectra of the G star from which Steeghs et al. (2006) estimate that  $f_{r'} > 0.85$  and  $f_{g'} > 0.6$ . These numbers also match the amplitude of the flux variation whose significant drop from  $u'$  to  $g'$  to  $r'$  (Table 5.5) can be explained by dilution of an underlying variable with a constant amplitude with wavelength, as for HM Cnc. If we assume  $f_{g'} = 0.7$  we obtain  $d \sim 0.027$  arcsec; this compares with the upper limit of 0.1 arcsec set by Steeghs et al. (2006). The distance to the G star of 1 kpc estimated by Steeghs et al. (2006), leads to a minimum separation of  $\sim 30$  au, equivalent to a period of 120 yr, and means that the G star cannot be the direct cause of the optical and X-ray pulsations. Nevertheless it may well be associated with the system in the form of a hierarchical triple, a point we return to after we have presented the light curves of HM Cnc. We finish by noting that our failure to detect anything in the  $u'$  band is to be expected. Assuming typical colours for the G star and a hot spectrum for the variable, we expect that if  $f'_g = 0.7$ , then  $f'_u = 0.3$ . The effect of this reduction in  $f$ , which is to make any movement more difficult to detect is in large part offset by a factor 2.1 increase in  $a/(1+a)$ , but then we are faced with a factor 8 worse sensitivity in the  $u'$  band, and the result is that there is no detection in the  $u'$  band data.

### 5.3.4 HM Cnc

We present the phase-folded light curves of HM Cnc using Strohmayer's (2005) ephemeris in the right-hand panel of Figure 5.1.

We computed the Lomb-Scargle periodogram to confirm HM Cnc's 321 s period and we noticed that the relative strength of the second harmonic is higher than that

<b>Filter</b>	<b>amplitude</b> (%)	$t - t_0$ (s)	$\phi$ (cycles)
i'	14.77±0.95	1.7±3.2	0.121±0.010
g'	13.48±0.34	0.0±1.3	0.116±0.004
u'	13.08±0.66	0.5±2.6	0.118±0.008
r'	13.54±0.12	-1.30±0.45	0.1615±0.0014
g'	12.74±0.07	0.00±0.27	0.1656±0.0009
u'	11.90±0.17	1.32±0.72	0.1697±0.0023

Table 5.6: Results of single harmonic sinusoid fits to the HM Cnc data. The times mark the phases of maximum light and are referenced to two times:  $T_0 = 52782.895768$  for the May 2003 data and  $T_0 = 53702.3368167$  for the November 2005 data.

of V407 Vul, as has already been pointed out by Israel et al. (2002). This is indeed clear from the non-sinusoidal shape of the light curves in Figure 5.1. The results of the relative strength of the first and second harmonic and their phases are shown in Table 5.4. The second harmonic is approximately 15 per cent of the fundamental and its maximum occurs 0.2 of a cycle after the maximum of the fundamental. This results in an asymmetry in the light curve whose rise time is longer than its decline; we discuss its origin in Section 5.4.

We applied the same method as for V407 Vul to obtain the normalised amplitude of variation and the time and phase of the maximum. These results are presented in Table 5.6. In this case the amplitude of the variation decreases slightly for shorter wavelengths which reinforces the picture that in V407 Vul the change with wavelength is due to dilution at long wavelengths by light from the G star. For HM Cnc the normalised amplitudes of variation are smaller than the  $u'$  band for V407 Vul (which is the least contaminated by the constant star). This could be easily explained by the inclination of the plane of the orbit and/or differences in temperatures of the stars.

The higher signal-to-noise ratio of the VLT data from November 2005 reveals a trend with waveband in the phase of the fundamental which is progressively delayed towards short wavelengths. To test whether the trend is significant, we carried out an

*F*-ratio test comparing two models, one of a constant phase in the three bands versus one of a linear trend of phase with wavelength, using the central wavelengths of each band: 3543, 4770 and 6222 Å. The *F*-ratio is the ratio between the  $\chi^2$ /(number of degrees of freedom) of one fit divided by the same quantity for the other fit. We only had three points so the constant model has two degrees of freedom while the straight line fit has just one. The values of the  $\chi^2$  are 10.82 and 0.068 for the constant and straight line, respectively, giving an *F*-ratio of 79.5. This is significant at the 90 per cent level but not at 95 per cent, so, although suggestive, there is no significant shift.

After publication we realised we made a mistake in the definition of the *F*-ratio. The correct *F*-ratio of two models used to fit *n* points, where model 1 has *k* parameters, model 2 has *k+g* parameters is:

$$F_{ratio}(g, n - (k + g)) = \frac{\frac{\chi_1^2 - \chi_2^2}{g}}{\frac{\chi_2^2}{n - (k + g)}} \quad (5.2)$$

In our case *k* = 1, *g* = 1 and *n*=3, so the correct *F*-ratio is 158 but the conclusions still hold.

Table 5.6 shows that there is a phase difference of  $0.050 \pm 0.004$  between our two runs (May 2003 to November 2005) where this is the measurement error only. As with V407 Vul, we also have to add the uncertainty of the ephemeris (see Appendix A). The error of the difference of phases due to the uncertainty of the ephemeris calculated using equation (A.2) and the correlation coefficients given in Table A.3 is 0.013. So there is a phase difference between the two runs of  $0.050 \pm 0.014$ . Therefore there is marginally significant variation in phase which might mean that there is a variation of the phase shift between the optical and the X-rays or, more likely, that the spin up rate is varying. The uncertainty in the absolute phase calculated using equation (A.1) is 0.005 for the May 2003 data and 0.01 for the November 2005 data. These are useful to compare the optical phases with the X-ray phases, and as we shall see next there is a significant phase shift between the two.

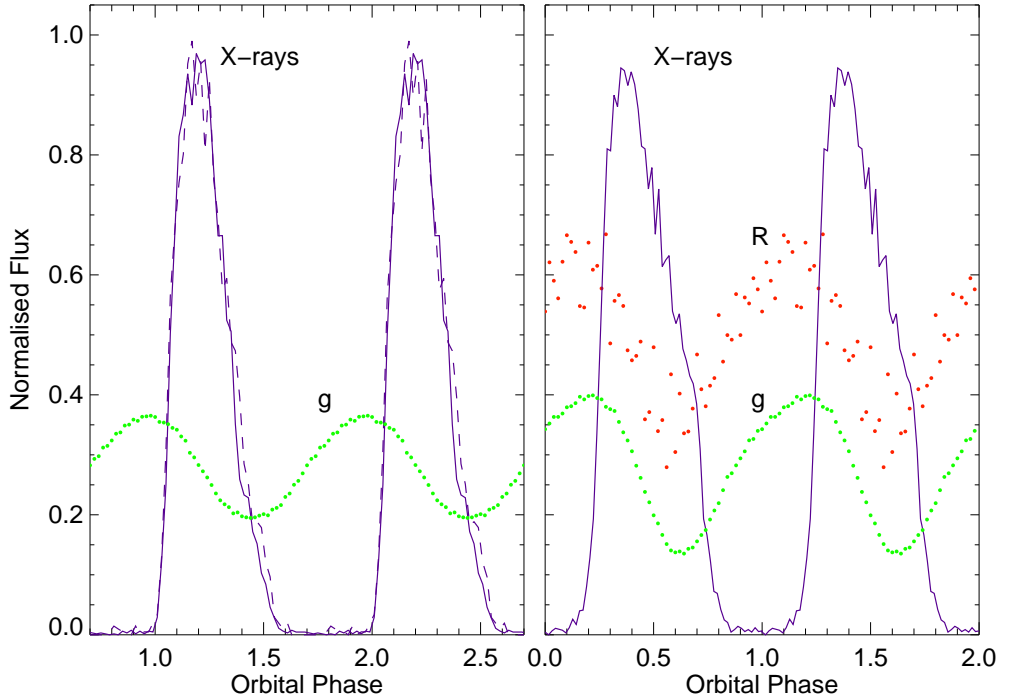


Figure 5.5: X-Ray/optical phase-folded light curve of V407 Vul (left-hand panel) and HM Cnc (right-hand panel) using the ephemeris of Table A.1 and (Strohmayer 2005), respectively. For the X-ray light curves of V407 Vul we reanalysed Chandra observations, with the solid line showing data from 19<sup>th</sup> February 2003 and the dashed line from 24<sup>th</sup> November 2003. For HM Cnc, the X-rays were adapted from Strohmayer (2005). We overplot the optical  $g'$  band showing our results. For HM Cnc we also show the VLT/FORS data (Israel et al. 2002) taken in the R filter (top).

### 5.3.5 The Optical/X-Ray phase shift of HM Cnc

The relative phases of the optical and X-ray light curves are an important constraint upon models. Israel et al. (2003, 2004) found that optical and X-ray light curves of HM Cnc were in antiphase as might be expected for an X-ray emission region facing the secondary star, contrary, for example, to expectations based upon the direct impact model.

In the right-hand panel of Figure 5.5 we present the X-ray and optical light curves folded on Strohmayer's (2005) ephemeris. Our phase shift differs from the studies of Israel et al. (2003) by around 0.2 cycles. To test if this was a genuine change in the

system, we reduced some of the archival *R*-band VLT data from the 12<sup>th</sup> of December 2002 used by Israel et al. (2004). We reduced these data with the ULTRACAM pipeline and applied the same methods and time conversions as for the WHT/ULTRACAM data. The results are also shown in the right-hand panel of Figure 5.5 and agree nicely with our ULTRACAM data. Clearly the system phase is stable and there are no problems with the times of either data set. The difference must be due to the data reduction. We confirmed our timing results with three different data reduction packages so we believe that our relative phase is correct and suspect that there is a problem with the values of Israel et al. (2003, 2004). We were able to confirm the X-ray phase of Israel et al. (2003, 2004) so assume that there is a problem only with the optical timings. The shift of 0.2 cycles is about 1 min, which is suggestively close to the  $\sim 64\text{s}$  offset between UTC and TDB. Dr Israel was kind enough to confirm that such an error was possible.

### 5.3.6 Flickering

The random stochastic variations known as “flickering” are one of the hallmarks of accreting systems. We therefore looked for any signs of flickering in our data. A plot of the light curves after removing the sinusoidal variation is shown in Figure 5.6.

The light curves are very constant except for long time-scale variability of HM Cnc during the November VLT run. The observations of HM Cnc started at high airmass, so some of variations seen could be a consequence of extinction, except that  $u'$  does not look much more variable than  $g'$  or  $r'$ . Therefore we believe that this may be true variability of the source and not an artefact.

In both systems the magnitudes measured in the two observing runs agree well within the errors. In the case of V407 Vul we also searched for any flux variation on longer time-scales. We had data from the “auxiliary port” of the WHT taken on the 10<sup>th</sup> of April 2003 and also Liverpool Telescope data taken on the 5<sup>th</sup> of September 2004. The different data sets were all within 10 per cent of each other.

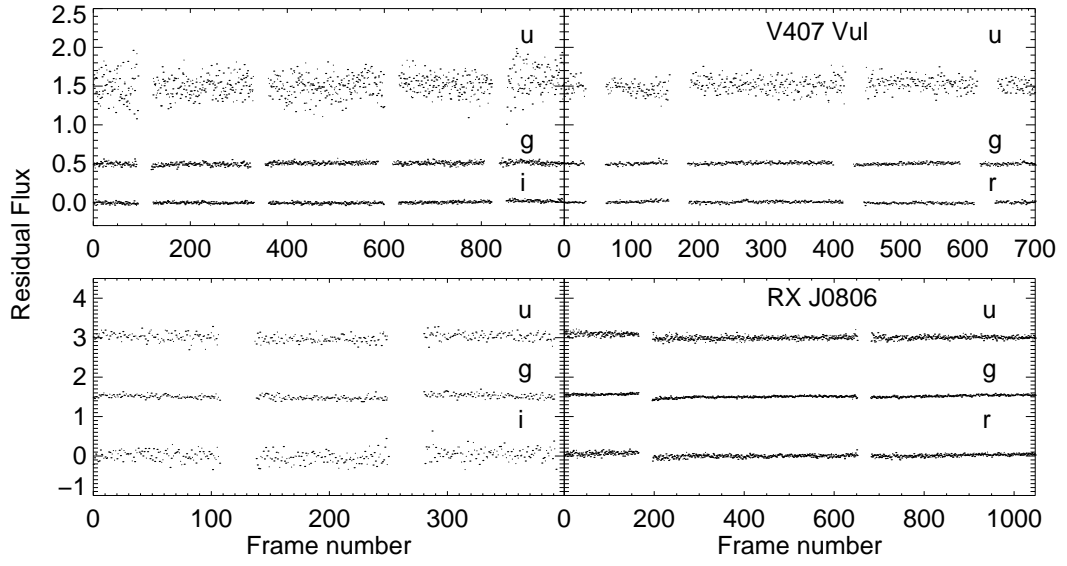


Figure 5.6: V407 Vul (top panel) and HM Cnc (bottom panel) light curves after removal of the sinusoidal pulsations. For each object the data from the first observing period is in the left-hand panel and the second in the right-hand panel. There are no significant variations of either source. We inserted gaps between different nights.

We estimated the variability of these systems by calculating the RMS of the light curves after removing the sinusoidal variations. We filtered the short-term variations to minimise the photon noise. We also filtered longer term variations so we could compare our short runs with a longer run on the cataclysmic variable SS Cyg (Chapter 6). For the August 2005 V407 Vul run we obtain an RMS variability of 0.7 per cent in  $r'$  and 0.8 per cent in  $g'$ . For the November run on HM Cnc we obtain an RMS variability of 1.6 per cent in  $r'$  and 1.0 per cent in  $g'$ . We use these runs as they have the highest signal-to-noise, nevertheless the variability still contains a significant component of photon noise. We do not quote the variability in  $u'$  because it is completely dominated by photon noise. For comparison, applying the same filtering of the data to data on the well-known CV SS Cyg, we obtain an RMS variability of 3.0 per cent in  $r'$  and 5.0 per cent in  $g'$ . As mentioned above, the fraction of the G star in the  $g'$  band of V407 Vul is of order 70 per cent. Therefore its intrinsic variability is of order 2.5 per cent, assuming the variations are not dominated by photon noise. This is a factor of 2 less than SS Cyg and a factor of

4 if one accounts for SS Cyg's dilution by its secondary star (North et al. 2002). Other cataclysmic variable stars we looked at are similar to SS Cyg, so we conclude that the measured variability in V407 Vul and HM Cnc is much less than in normal cataclysmic variable stars.

The lack of obvious flickering is a point against accreting models, although not a conclusive one as there are wide variations in the amount of flickering shown by definitively accreting binaries (see Chapter 6), and one cannot be certain that it should have been detected. It does however suggest that most of the optical light does not come directly from the accreting region.

## 5.4 Discussion

### 5.4.1 The X-ray versus optical phases

The correction to the relative X-ray versus optical phase of HM Cnc that we have identified makes it very similar in this respect to V407 Vul: in each system the X-ray flux peaks  $\sim 0.2$  cycles after the optical flux. This can be added to the shapes of the light curves as evidence that these two stars are indeed related systems, as is evident from Figure 5.5. We will now investigate what this result implies for the different models.

In the majority of models, the X-rays come from a spot on the primary star which moves in and out of view as it rotates. The exception is the IP model where the modulation is the result of the accretion stream flipping from one pole to the other although it seems unlikely that such a process can really switch off the X-rays as completely as observed. Less attention has been paid to the optical pulsations. Within double degenerate models, these seem likely to originate from the heated face of the secondary star which would naturally explain their near-sinusoidal shape and, perhaps, the absence of flickering. Such heating may be a result of the X-ray emission from the primary star, or the primary star could simply be hot as a result of compressional heating

(Bildsten et al. 2006).

Assuming that we are correct about the main site of optical emission, Figure 5.7 shows the geometrical arrangement that explains the relative phases of the optical and the X-ray light curves. In this model the 0.2 cycles delay of the X-ray peak relative to the optical peak implies that the X-ray emission spot is rotated  $\sim 0.3$  cycles from directly facing the secondary star, in the direction of the orbit.

This is not the whole story however, because in HM Cnc at least the optical light-curve is somewhat saw-toothed in shape. As our Fourier decomposition shows, this is caused by a significant second harmonic that happens to peak at the same phase as the X-rays, as seen in the difference  $\phi_2 - \phi_1 \approx 0.2$  in Table 5.4. The natural explanation for this is that the X-ray emission spot is also the site of some optical light. If this is a localised region so that the shape of its light curve can be approximated by a truncated sinusoid [ $f(\theta) = \cos \theta$  for  $-\pi/2 < \theta < \pi/2$ ,  $f(\theta) = 0$  otherwise], then it can produce a second harmonic. It will also contribute some first harmonic as well, which means that the first harmonic emission that we see is the combination of contributions from the heated face of the secondary star and the spot on the primary star. This retards the optical phase so that the observed 0.2 cycle shift is an underestimate of the true shift between the emission from the heated face and the X-ray emission.

If the optical emission truly can be approximated by the truncated sinusoid, then for HM Cnc we find that we can fit the phases and harmonic amplitudes if the X-ray spot leads the heated face of the secondary star by  $\sim 0.26$  cycles (i.e. a little more than  $90^\circ$ ) and the optical emission from the spot on the primary star peaks at  $\sim 75$  per cent of the amplitude of the emission from the heated face. While this is probably rather simplistic, it demonstrates that the simple model illustrated in Figure 5.7 is capable of explaining some secondary details of the data. With this decomposition of the optical light, the X-ray emission site is  $\sim 90^\circ$  ahead of the secondary star and it is then not clear if the X-rays can directly heat the secondary star or not. V407 Vul has a much

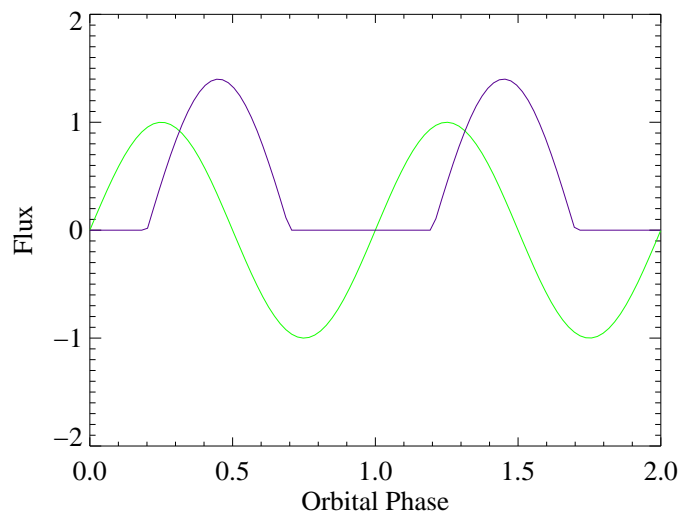
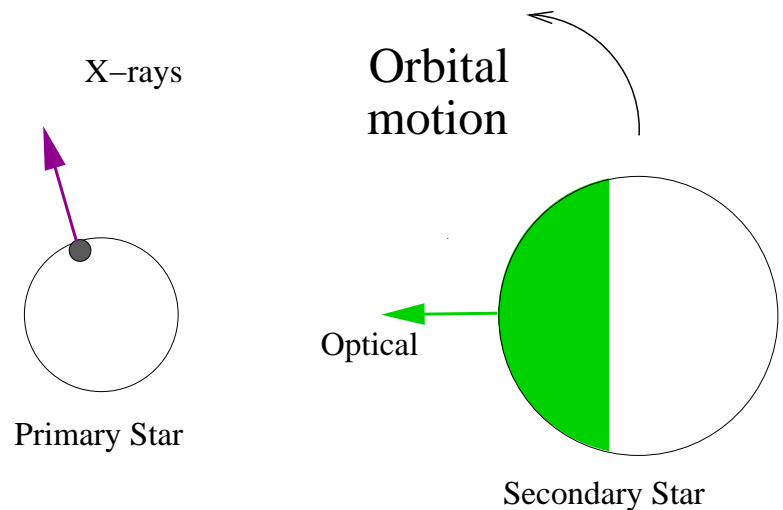


Figure 5.7: In the top panel we show a schematic picture of the primary star (left-hand side) with an X-ray emitting spot which has a peak of X-ray emission in the direction indicated by the dashed arrow. The relative sizes of the two stars are drawn to match masses of  $M_1 = 0.53 M_\odot$  and  $M_2 = 0.12 M_\odot$  (see text). The secondary star, which orbits counterclockwise, has a heated face (shaded) whose peak emission is in the direction of the solid arrow. The figure is arranged to give the optical (solid) and X-ray (dashed) light curves shown on the bottom panel, which have the same relative phasing as both V407 Vul and HM Cnc.

weaker second harmonic, and so in this case the spot is presumably the full 0.3 cycles or  $\sim 110^\circ$  ahead of the secondary star and cannot see it directly.

The X-ray/optical phase shifts in V407 Vul and HM Cnc are very naturally explained by both the direct impact and double-degenerate polar models. The accretion spot in normal polars is observed to lead the secondary star by of order 0.1 – 0.3 cycles (Cropper 1988) and a similar shift is expected in the direct impact model, depending upon the system parameters (Marsh et al. 2004). As Figure 5.7 shows, this is exactly what is required to match the observations. On the other hand, as far as we can see, there is no natural explanation for the phase shift in the unipolar inductor model for which one would expect anti-phasing, unless there is some as yet undiscovered mechanism for displacing the magnetic footprint of the secondary star in advance of its orbit. This is difficult given that the orientation of the primary star relative to the secondary star changes relatively rapidly in the unipolar inductor model and so a fixed orientation is hard to contrive. The X-ray/optical phase-shift is also a difficulty for the IP model of Norton et al. (2004) for which they also predict anti-phasing with the optical pulses appearing as the accretion stream switches to the hidden pole, the X-rays going to zero at this point. IPs are sufficiently complex that an offset as observed would not perhaps be that surprising, but in any case there are other more serious difficulties with the IP model (Cropper et al. 2004).

The direct impact model can be used to predict the phase and thus, if it is true, constrain the masses of the binary components. We define the impact angle as the angle between the X-ray emission site and the secondary star. We calculate the impact angle for over a grid of  $M_1$  and  $M_2$ . In Figure 5.8 we show contours of same impact angle where the shaded areas represent the probable regions where the systems lie. The uncertainties in the angle are higher for HM Cnc than for V407 Vul because of the existence of the second harmonic component. In the same figure we also plot the dynamic stability limit (dashed line). We conclude that for V407 Vul  $0.4 < M_1 < 0.55 M_\odot$

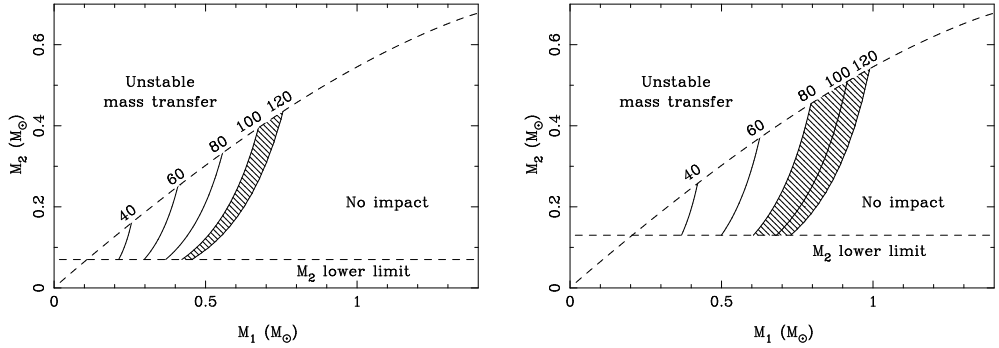


Figure 5.8: We show the system mass constraints for V407 Vul (left-hand panel) and HM Cnc (right-hand panel) if we assume the direct impact model. The upper dashed line shows the dynamic stability limit. We show contours of equal impact angle. Note that the maximum impact angle is approximately  $130^\circ$  which corresponds to the transition between the disc and direct impact accretion.

and  $0.08 < M_2 < 0.4 M_\odot$  and for HM Cnc  $0.6 < M_1 < 0.9 M_\odot$  and  $0.12 < M_2 < 0.45 M_\odot$ .

#### 5.4.2 A limit on the bolometric luminosity of HM Cnc

The temperatures calculated in this section were recalculated after the publication of the original work because of the new HM Cnc ultraviolet (UV) flux measurements by Galex<sup>1</sup>. The UV fluxes are specially important to be able to constrain the maximum temperature of the system.

Pursuing the idea of the heated face further leads to a lower and upper limit upon the bolometric luminosity of HM Cnc assuming that the double degenerate models are correct (unfortunately the G star in V407 Vul's spectrum precludes the same calculation). The idea is to constrain the temperature of the heated face from the spectrum of the pulsations, which since it is a measure of the flux from the primary star at a distance equal to the orbital separation, which is approximately known, gives us a luminosity. A slight complication is that we do not know for sure whether the X-rays or the primary star's photosphere is responsible for the irradiation. This ultimately leads us to two different possible limits. We begin by obtaining the weaker of the two which applies in

---

<sup>1</sup><http://galex.stsci.edu/GR2/>

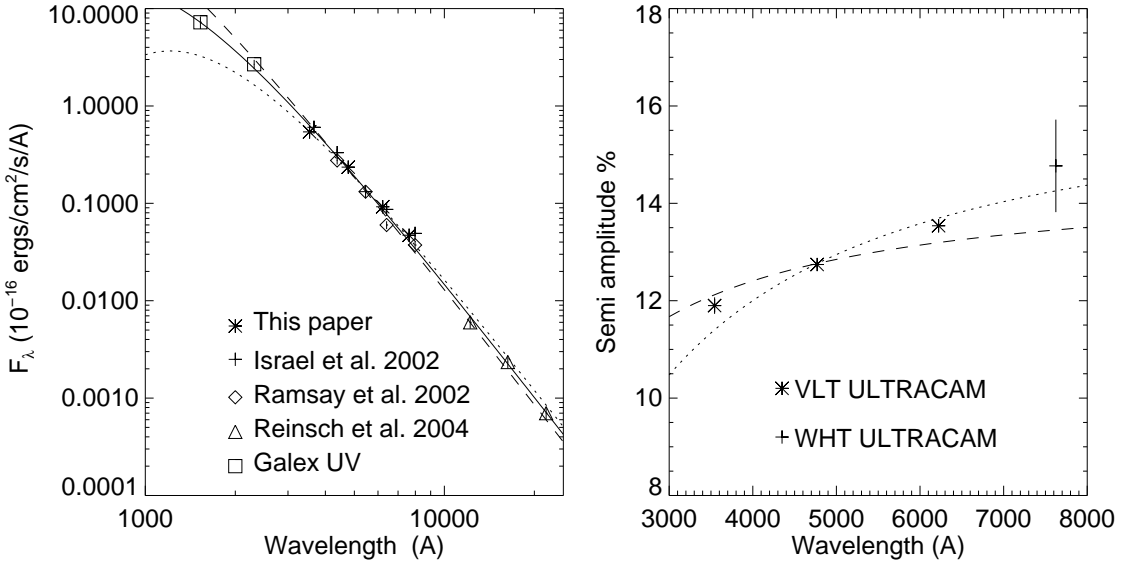


Figure 5.9: In the left-hand panel we show the mean fluxes of HM Cnc compared to two blackbody spectra. The best fit is the solid line (37 300 K), the lowest temperature consistent with the data is the dotted line ( $T_1 = 24\,000$  K). And the highest temperature is the dashed line ( $T_1 = 65\,600$  K). The right-hand panel shows the pulsation amplitudes that we measure compared to the ratio of two blackbodies ( $B_\lambda(T_{\text{irr}})/B_\lambda(T_1)$ ) to place a lower limit upon the temperature of the pulsed light  $T_{\text{irr}}$  of 17 900 K (dotted line) and an upper limit of 43 000 K (dashed line).

the case of X-ray heating, and then consider the revised limit necessary if the photosphere is responsible for the heating.

### Temperature of the heated face

We first derive a lower and an upper limit on the temperature of the spectrum using our magnitudes and those reported by Ramsay et al. (2002a), Israel et al. (2002), Reinsch et al. (2004) and the new UV flux obtained with Galex as shown in the top panel of Figure 5.9. Two black-body spectra are shown, each scaled to give the minimum  $\chi^2$ . One, with temperature 37 300 K (solid line) is the global best fit, while the two other (dotted and dashed), with temperature 24 000 K and 65 600 K which correspond respectively to the minimum and maximum temperature that gives a  $\chi^2$  within the 99 per cent confidence threshold. We take this to be the possible temperature of HM Cnc

given its UV, optical and infra-red fluxes. We assume further that this reflects the temperature of the primary star,  $T_1$ , since if it is the secondary star, the primary star would have to be extremely hot to produce a significant reflection effect. Armed with the lower limit of  $T_1 > 24\,000\,\text{K}$ , we can then use the pulsation amplitudes to place a similar lower limit upon the temperature of the irradiated face of the secondary star  $T_{\text{irr}}$  using the ratio of blackbody spectra, as shown on the right of Figure 5.9. Again taking the 99 per cent confidence limit, we find that the temperature of the irradiated face must be at least  $T_{\text{irr}} > 17\,900\,\text{K}$ ; this limit rises to  $23\,500\,\text{K}$  if we use the best-fit value for  $T_1$  of  $37\,300\,\text{K}$ . Similarly we can use the upper limit of the temperature of the primary star to obtain an upper limited of the irradiated face of the secondary star which is  $43\,000\,\text{K}$ . The lower limit on the temperature of the irradiated face leads directly to a lower limit on the bolometric luminosity of the primary star since assuming that the irradiation dominates the intrinsic luminosity of the secondary star we have

$$L_{\text{bol}} = 4\pi a^2 \sigma T_{\text{irr}}^4, \quad (5.3)$$

where  $a$  is the separation and  $\sigma$  is the Stefan-Boltzmann constant. The strictest lower limit comes from taking the smallest separation, which corresponds to the smallest masses for the two-component stars. We used  $M_1 = 0.53\,\text{M}_\odot$  and  $M_2 = 0.12\,\text{M}_\odot$  which ensures that the secondary star can fit within its Roche lobe and that mass transfer is stable (Marsh et al. 2004); a smaller value for  $M_1$  could be used if the system is detached, but would be largely compensated for by the need for a higher value of  $M_2$  to avoid mass transfer. Our masses and the period of  $321\,\text{s}$  imply a separation of  $a = 0.089\,\text{R}_\odot$  (these values were used to scale Figure 5.7). Scaling from the Sun we therefore find that  $L_{\text{bol}} > 0.73\,\text{L}_\odot = 2.8 \times 10^{33}\,\text{ergs s}^{-1}$ .

This is already a significant lower limit as it is somewhat higher than, but consistent with, the X-ray luminosity of  $L_X \sim 5 \times 10^{32}\,\text{ergs s}^{-1}$  at  $500\,\text{pc}$  distance estimated by Israel et al. (2003). However, we have pushed the temperature down to marginally

<b>E(B-V)</b>	$\chi^2_{best}$	$T_{best}$ (K)	$T_{min}$ (K)	$T_{max}$ (K)
0.0	32.9	37280	24000	65600
0.005	33.8	38360	24800	66860
0.01	34.7	39480	25770	68140
0.02	36.8	41880	27910	70700
0.03	39.4	44510	30350	73160
0.04	42.6	47430	33200	75350
0.05	46.6	50690	36650	76940
0.06	51.5	54380	41060	77360
0.07	57.7	58550	47400	75350
0.08	65.4	63380		

Table 5.7: The best fit, minimum and maximum allowed temperatures of the primary star for different values of reddening. The 99 per cent confidence level of  $\chi^2$  is 64.7.

acceptable values. For instance, the best-fitting temperature  $T_1 = 37\,300\,\text{K}$  which leads to  $T_{\text{irr}} > 23\,500\,\text{K}$  raises the luminosity limit by a factor of 3, which hints at a larger distance than Israel et al. (2003) assumed.

Comparing with white dwarfs of similar temperature and mass (Bragaglia et al. 1995), the absolute magnitude of the primary star is bounded by  $M_V < 10.3$ . Given  $V = 21.1$  (Israel et al. 2002), and assuming that reddening is negligible, this suggests that  $d > 1.5\,\text{kpc}$ , although this limit can be lowered if we adopt a higher mass for the primary star.

We have assumed that interstellar extinction is negligible. A non-zero extinction will allow a higher primary star temperature. We can study the effects of reddening calculating the minimum and maximum temperatures as a function of the extinction. This is shown in Table 5.4.2. We can see that with 99 per cent confidence level the E(B-V) has to be lower than 0.08. This is in agreement with the maximum value of extinction calculated by Schlegel et al. (1998) of  $E(B - V) = 0.028$  for the position of HM Cnc. In Figure 5.10 we show the allowed parameter space of temperature of the primary star and extinction for different confidence levels.

These limits apply if it is the X-rays that drive the heating, but it may well be

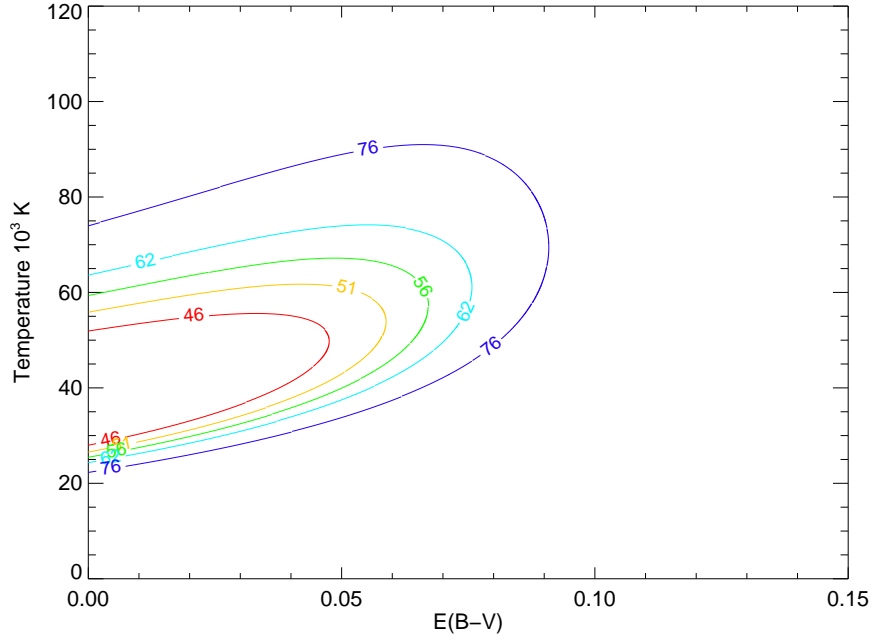


Figure 5.10:  $\chi^2$  map for the primary star temperature and extinction parameter space showing 90, 95, 97.5, 99 and 99.9 per cent confidence levels (from inside out).

that it is the photosphere of the primary star itself that is important. The spot position  $\sim 90^\circ$  ahead of the secondary means that the spot may not be able to see the secondary star at all. This leads to a simple but important modification as we now show.

### **Heating driven by the primary star's photosphere**

If the primary star's photosphere drives the heating then this sets a relation between  $T_1$  and  $T_{\text{irr}}$ :

$$T_{\text{irr}}^4 = T_2^4 + \left(\frac{R_1}{a}\right)^2 T_1^4, \quad (5.4)$$

where  $T_2$  is the temperature of the unheated photosphere of the secondary star,  $R_1$  is the radius of the primary star,  $a$  is the orbital separation and we have assumed that all incident flux is absorbed and for simplicity we do not try to account for the range of incident angles over the heated face, but just consider the substellar point. As we said earlier, if  $T_2$  is significant, it is hard to get much of a reflection effect, so we take it to

be negligible and therefore

$$T_1 = \left( \frac{a}{R_1} \right)^{1/2} T_{\text{irr}}. \quad (5.5)$$

The masses adopted above give the smallest ratio of  $a/R_1$  leading to  $T_1 = 2.58T_{\text{irr}}$ . This equation was used to bootstrap from the lower limit on  $T_{\text{irr}}$  to a new lower limit of  $T_1$ , which was then used to place a new lower limit on  $T_{\text{irr}}$  using the procedure of the previous section. We obtained updated limits as follows:  $T_{\text{irr}} > 34\,900$  K and  $T_1 > 90\,000$  K. The heated face temperature rises by a factor of 1.9, and so the lower limit on the bolometric luminosity rises by a factor of 15 to  $L > 10.6 L_\odot = 4.0 \times 10^{34}$  ergs s<sup>-1</sup>. Again comparing with white dwarfs of similar temperature and mass (Bragaglia et al. 1995), the absolute magnitude of the primary star is bounded by  $M_V < 8.0$ . Given  $V = 21.1$  Israel et al. (2002), and assuming that reddening is negligible, we must have  $d > 4.2$  kpc. This would place HM Cnc more than 2.5 kpc out of the plane, and it would possibly be a halo object. We note that a halo-like transverse velocity of 200 km s<sup>-1</sup> and our distance limit imply a proper motion  $< 0.01$  arcsec yr<sup>-1</sup>, below the limit of 0.02 arcsec yr<sup>-1</sup> placed by Israel et al. (2002).

Assuming that secondary heating is not driven by X-rays we obtain  $T_1 > 90\,000$  K. This is higher than the upper limit on the temperature of the primary deduced from the spectral colours  $T_1 < 65\,600$  K. So probably the X-rays do contribute to the heating of the secondary star.

Our distance limits do not discriminate between accretion models which work best for large distances, in excess of 4 kpc (Bildsten et al. 2006; D'Antona et al. 2006) and the unipolar inductor model which works well for  $d < 1$  kpc (Dall'Osso et al. 2006a,b). However, they do suggest that ultraviolet observations may have a value in tightening the lower limits upon temperatures and hence the distance.

### 5.4.3 Direct impact or polar?

We have lumped the accreting double-degenerate models, direct impact and polar together as “accretion models”, as we think they provide equally good explanations for our data. For V407 Vul the double-degenerate polar model suggested by Cropper et al. (1998) was discarded when no polarisation was found (Ramsay et al. 2002b). In the case of HM Cnc, Reinsch et al. (2004) have claimed a detection of circular polarisation but at a low level given the faintness of the target (0.5 per cent) that needs confirmation. However, we think that the polar model may have been written off prematurely as there are some very high-field polars which show very little polarisation (AR UMa, Schmidt et al. 1996; V884 Her, Szkody et al. 1995, Schmidt et al. 2001) and strong soft X-ray components, very much like V407 Vul and HM Cnc. It has been suggested that this is because the shocks are buried in these systems, due to the high accretion rates, rather as Marsh & Steeghs (2002) suggested for the direct impact model. Polars show stronger optical line emission than either V407 Vul or HM Cnc, but this is not a strong argument against the polar model since the systems, if they are double degenerates, would be helium-rich and very compact, and so different from normal CVs.

### 5.4.4 Period changes in V407 Vul and the G star

We have shown that the G star does not play a direct role in the variability of V407 Vul but it could be gravitationally bound to the variable, in which case it may cause an apparent period change through variable light travel time effects. How significant could this be? Assuming that the G star has mass  $M$ , then the maximum acceleration of the binary along the line of sight is  $\sim G_c M/a^2$  where  $a$  is the separation of the binary and the G star. The subscript  $c$  in the gravitational constant is to avoid confusion with the G star. This leads to a quadratic term in the usual  $T_0 + PE + CE^2$  ephemeris equal to

$$C = \frac{G_c M P^2}{2ca^2}, \quad (5.6)$$

where  $c$  is the speed of light and  $P$  the orbital period. This leads to an apparent rate of period change given by

$$\dot{P} = \frac{G_c M P}{c a^2}. \quad (5.7)$$

Taking  $a$  to be comparable to the projected separation at 1 kpc of 27 au, and  $M = 1 M_\odot$  gives  $|\dot{P}|_{\max} \sim 1.6 \times 10^{-11} \text{ ss}^{-1}$ . This is about five times larger than the observed value (Strohmayer 2005) and thus we conclude that the G star has the potential to have a significant effect upon the rate of period change measured in this system. This adds an extra uncertainty that may allow both the unipolar inductor (Marsh & Nelemans 2005; Dall'Osso et al. 2006a,b) and accreting models (D'Antona et al. 2006) to match this system more easily than has been the case to date. Continued observations in order to place limits upon or detect a relative proper motion between the variable and the G star would be of interest for testing the triple star model. We estimate the orbital velocity of the G star to be  $\sim 3 \text{ km s}^{-1}$ , which is perhaps detectable given a long enough period of time.

## 5.5 Conclusion

We have presented optical photometry of V407 Vul and HM Cnc in  $i'$ ,  $r'$ ,  $g'$  and  $u'$  bands taken with the high-speed CCD camera ULTRACAM. For V407 Vul we have a hint of detection of a third component in the system at 0.027 arcsec from the variable. We believe this to be the G star that is seen in the spectrum of V407 Vul, which therefore cannot be the secondary star of the variable. We cannot distinguish whether it is a line-of-sight coincidence or a triple system.

For HM Cnc we find a new phasing of the X-ray and optical data which renders it indistinguishable from V407 Vul with the optical pulses 0.2 cycles ahead of the X-ray pulses. The offsets are naturally produced by double-degenerate accreting models of the systems, both polar and direct impact, but seem hard to reconcile with the unipolar

inductor and IP models. The optical light curves of HM Cnc are non-sinusoidal and a Fourier decomposition shows that there is likely a contribution to the optical light from the same site as produces the X-rays.

On the assumption that the optical pulses of HM Cnc are the result of irradiation of the secondary star within a double degenerate binary, and using the relative constancy of the fractional pulsation amplitude with wavelength, we place a lower limit on the distance to the system of  $> 1.5$  kpc. If it is the photosphere of the accretor rather than the X-ray site that is responsible for the heating, then this limit rises to  $d > 4.2$  kpc. Space UV observations are the best hope for strengthening these constraints.

Finally we remark that both the polar and direct impact models provide equally good explanations of our observations and that there are high magnetic field polars that show similar properties to V407 Vul and HM Cnc i.e. very soft X-ray spectra and low polarisation.

# Chapter 6

## Flickering of Cataclysmic Variables

### 6.1 Introduction

Flickering, one of the most ubiquitous features of accretion discs, consists of random variability of the flux without any visible periodicity. It is present in the light curves of cataclysmic variables stars, X-ray binaries, active galactic nuclei and T Tauri stars. Studying accretion discs in cataclysmic variables has advantages: they are optically bright, so that they can be studied from the ground, their accretors have large radii, allowing us to probe the fastest frequencies, and the light from accretion dominates their brightness.

Flickering looks like a continuous superposition of individual flares. A property of flickering is the relationship between amplitude and duration of a flare. Thus, the power spectrum of a light curve is proportional to a power of the frequency “ $f$ ” of the flare  $\propto f^{-\alpha}$  where typically the power index  $\alpha$  is  $\approx 2$ , but flattens at frequencies smaller than  $10^{-3}$  Hz (Elsworth & James 1982, 1986). This linear relation in logarithm space means that flickering is self-similar and makes the power spectrum an excellent way of characterising the flickering, which is why it is commonly used, especially in X-ray binaries and AGN. This kind of red noise is expected in a turbulent flow because the

larger eddies that emit more light, have longer characteristic timescales.

The first clue for the origin of flickering came after the study of U Gem by Warner & Nather (1971). They concluded that in this system flickering comes from the hot spot where the mass transfer stream hits the disc. Therefore flickering would be caused by inhomogeneities in the mass transfer stream that cause variations of brightness where the stream hits the disc, i.e. in the hot spot. However, later observations of other systems contradicted this explanation because no increase of flickering was seen in the phases where the hot spot was visible (see for example Warner 1974). In fact, there are systems that show strong flickering when the hot spot is eclipsed (for example HT Cas (Patterson 1981)). Early eclipse mapping of the flickering led to the conclusion that it appears to originate mainly in the inner regions of the accretion disc (Warner & Cropper 1983; Horne & Stiening 1985) and the hot spot has only a small contribution. In his study of four eclipsing systems, Bruch (2000) concluded that in general flickering comes from the inner accretion disc but in specific systems (e.g. IP Peg) the hot spot flickering can dominate.

Eclipse mapping techniques are helpful in determining the spatial origin of the flickering. Applying these techniques to V2051 Oph, Baptista & Bortoletto (2004) were able to separate the low frequency from the high frequency flickering. For the low frequency analysis they use filtered data which is dominated by the low frequencies. For the high frequency analysis they cut off frequencies lower than 0.006 Hz. They concluded that the low frequency flickering comes from the overflowing gas stream with enhanced flickering along the stream trajectory. That can be explained in terms of the stream penetration model of Bath et al. (1983a,b). Baptista & Bortoletto (2004) also confirm that the high frequency flickering comes from the inner accretion disc. These results led them to propose that the hot spot and mass stream would be responsible for the low frequency flat part of the power spectrum while the accretion disc flickering produces the high frequency red noise. Further confirmation of these results would

be very important to disentangle the different sources of flickering and to understand the physical mechanisms of flickering. Comparing their high frequency flickering results with Bruch (2000), Baptista & Bortoletto (2004) found marginal evidence of a relation between frequency and radius of the accretion disc. This is a major prediction from the flickering models and should be tested further.

The first quantitative and systematic analysis of flickering was done by Bruch (1992). He proposed a mathematical definition of the flickering that would identify single flares by looking for extremes in the light curve. A maximum/minimum is identified if the three pixels surrounding its either side are lower/higher by a specific amount  $\delta$ . A suitable choice of  $\delta$  allows the comparison between different light curves independently of observing conditions and therefore it could be applied to any data set. This allows a formal and uniform way of calculating parameters like the flare rate, the amplitude of flares as a function of duration and gradient of the rising and decaying time of a flare. His estimation of the timescales and flickering energy favoured models where flickering rises predominantly in the inner disc. Later Fritz & Bruch (1998) used a larger sample of CVs to study the dependence of the power law index “ $\alpha$ ” and the flickering power upon the type of CV and the photometric state. He found that for dwarf novae there is some segregation of CV type in the  $\alpha$ -power plane. He also found that the flickering power varies with the square root of the total brightness along the outburst cycle while  $\alpha$  seems to increase slightly in superoutburst. All attempts to correlate flickering with system parameters fail, possibly because the driving mechanisms of flickering are complex and non-linear.

The origin of flickering and its physical mechanisms remain poorly understood. The hot-spot flickering is thought to be due to unstable mass transfer from the secondary star and variable dissipation as the stream hits the disc (Warner & Nather 1971). According to the model of Bath et al. (1983a,b) and Shu (1976) the stream can penetrate the disc or partially overflow it which gives rise to more areas of flickering enhancement.

In the case of the flickering coming from the accretion disc; a superposition of shots from a self-organised critical state (Yonehara et al. 1997) is capable of reproducing power law spectra of the correct form. This however lacks a physical model. One popular model is that of turbulence in the accretion disc. This was first treated mathematically by Bruch (1992). If there is turbulence in the accretion disc, the turbulent energy can be released as a flare. The kinetic energy trapped in the eddy is the major source of energy available. It is higher in the inner accretion disc where it is enough to explain the observed flickering energy.

Another model for flickering are magnetic flares in the accretion disk. Dynamo effects can amplify the magnetic field of a disc (Galeev et al. 1979; Balbus & Hawley 1991). This may give rise to magnetic flares in the disc corona (Burn & Kuperus 1988; Poutanen & Fabian 1999; Kawaguchi et al. 2000). The superposition of many individual flares would constitute the flickering. If the magnetic energy is released gradually this would happen on the shearing timescale, which is the time to store/release magnetic energy in a loop (Burn & Kuperus 1988) and that agrees well with the flickering timescale. Furthermore, the size of a flare would correlate with the radius where it was produced.

Balbus & Hawley (1991) showed that the importance of magnetic fields in driving the evolution of accretion discs as a source of viscosity is higher than was previously thought (as mentioned in Chapter 1). Due to the magneto-rotational instability (MRI), even an initial small magnetic field will lead to turbulence and consequential transport of angular momentum outwards. The MRI is the only instability known which is capable of explaining the high viscosity observed in accretion discs (for a review see Balbus (2003)). Magneto-hydrodynamic simulations of AGN starting with a thick torus and including the MRI naturally evolve to a thick Keplerian disc, a strongly magnetised corona and a jet (Hawley & Balbus 2002). Some simulations show variability on a wide range of timescales (for example Hawley & Balbus (2002)). These results are promising, but further work is still needed to understand the low ionisation regimes of

DN and proto-planetary discs (Balbus 2003).

The major problem of this model is that the larger flares should rise predominantly in the outer disc. Recently King et al. (2004) proposed an improvement to the model which is capable of producing larger flares in the inner disc, where the energy is higher. On their model the magnetic field in each annulus varies randomly. When, by chance, the magnetic field of neighbouring annuli are aligned, this enhanced local field can launch an outflow (wind or jet) and drive angular momentum loss, i.e. accretion. Simulations show that the resulting power spectra depend upon the relative magnitude of the viscous and local magnetic alignment timescales. King et al. (2004) were able to reproduce a power spectral index,  $\alpha = 1$ , if the two timescales are similar,  $\alpha = 2$  when the viscous timescale is longer and a mix of the two if it is the local magnetic alignment timescale that is longer. In all these cases the power spectrum shows a break at a timescale equal to the local magnetic alignment timescale at the inner edge (which is longer than the dynamical timescale) and becomes steeper at higher frequencies. Note than in this model the break frequency might not linearly correlate with the mass of the accretor. However such correlation has been reported in LMXBs (Nowak et al. 1999; Uttley et al. 2002). Although the model of King et al. (2004) was proposed for black hole accretion discs, the authors argue that it applies to all kinds of accretion discs.

Another possible source of flickering is unsteady mass accretion onto the white dwarf. It was proposed by Elsworth & James (1982) that instabilities in the inner accretion disc or in the boundary layer would break steady accretion into blobs. As each blob is accreted it releases energy so the accretion luminosity varies continuously. A similar model is used to explain the flickering in Polars (Chapter 1). If we assume a thin boundary layer this model implies that most flickering would be released as X-rays that would have to be thermalised in an optically thick environment to be observed as optical flickering. Rutten et al. (1992) suggested that the boundary layer may be thicker than was previously thought which would mean that it had a lower temperature (Duschl

& Tscharnuter 1991; Bruch & Duschl 1993). This lower temperature is in agreement with some observations (Ferland et al. 1982; Belloni et al. 1991). In the case of thicker boundary layers no thermalisation of the hard X-rays would be needed.

Since the boundary layer emits a considerable amount (up to 50 per cent) of the total luminosity of the cataclysmic variable and flickering can amount to 25 per cent of the total luminosity, Bruch (2000) considered that only the boundary layer would have enough energy to produce the amount of flickering observed although this also depends upon the assumed spectrum of the flickering energy.

Each model predicts a characteristic timescale for the flares. However, regardless of the physical mechanism that produces the flares, we know that the shortest timescale in the accretion disc is the dynamical timescale. Since it is minimal in the inner disc, in principle, the highest frequency variation in the luminosity can only come from the inner parts. This suggests a correspondence between frequency and the radius where the flickering is emitted. Moreover, it also implies that there is a maximum frequency that an accretion disc can produce and which corresponds to the dynamical timescale of the inner disc radius, i.e. between 1 and 50 seconds. So we may expect to see a break in the power spectrum at the corresponding frequency. This high frequency break has never been seen in CVs because the time resolution and/or the signal-to-noise of the observations has not been high enough. ULTRACAM is a high speed CCD camera in three filters capable of obtaining a time resolution of more than 300 Hz. We used ULTRACAM mounted on the 4.2m William Hershel telescope (WHT) and on the 8m Very Large Telescope (VLT) in Chile to study the high frequency flickering in CVs and look for the high frequency break. We observed 14 cataclysmic variables at a resolution of 20 Hz. We chose the brightest CVs observable at the time to achieve a reasonable signal-to-noise even with such short exposures. In Table 6.1 we present the classification, orbital periods and other known periods of the CVs that were observed. Because ULTRACAM allows simultaneous photometry in three filters:  $u'$ ,  $g'$  and  $r'$  it

also allows us to test the correlation of the flickering between different wavelengths and to analyse the spectrum of the flaring.

## 6.2 Observations and reduction

Our data were taken with the high speed CCD camera ULTRACAM on November 2003 at the WHT in La Palma and on May 2005 at the VLT in Chile. ULTRACAM is a multicolour photometer which allows us to obtain simultaneous photometry in the three bands  $r'$ ,  $g'$  and  $u'$ . We used the ULTRACAM drift mode to obtain a high sampling rate and probe the highest frequencies in the systems. Our data have exposure times between 0.04 sec and 0.1 seconds with a dead time  $\leq 3\text{msec}$ . In our first observational run at the WHT we had two nights of telescope time in the 11<sup>th</sup> and 12<sup>th</sup> of November 2003 during which we observed seven cataclysmic variables for around three hours each. In our second observational run we had two more nights of telescope time at the VLT. Our observations were spread over several days from the 11<sup>th</sup> to the 21<sup>st</sup> of May 2005 during which we observed eight CVs. Originally we intended to observe each CV for about three hours. However, we shortened the observation of those CVs which showed very little flickering. In Table 6.2 we present the observation log which shows the observation times, sampling rate and the observation conditions for each CV.

The data were reduced using the ULTRACAM pipeline. Due to the high time resolution of the data it was not obvious what would be the best reduction technique. Therefore we experimented with different aperture radii using normal aperture photometry, variable aperture photometry and “optimal” photometry (Naylor 1998) to extract the light curves and compare the three methods. We found that the “optimal” photometry was not adequate for our analysis because it artificially increased the inherent variability of our systems. Probably this is because short exposure images of point stars taken by large telescopes have speckle patterns. Therefore, the stellar profiles are not

<b>Star</b>	<b>Type</b>	<b>Subtype</b>	$P_{Orb}$ hours	$P_{Other}$ min	$M_{WD}$ $M_{\odot}$	<b>Ref</b>
SS Cyg	DN	UG	6.603		1.19±0.02	1a-d
V592 Cas	NL/IP?	UX/SU	2.762	175.8, 21.		2a-c
KR Aur	NL	VY	3.907		0.59±0.17	3a-d
LS Peg	NL/IP	VY/SW	4.195	30.9, 33.5		4a-c
RW Tri	NL	UX/SW?	5.565		0.45±0.15	5a-e
HQ Mon	NL?	UX?	7.584			6a
BZ Cam	NL	VY/SU?	3.689	225.1		7a
CM Del	NL	UX/VY?	3.888		0.48±0.15	3b, 8a
WX Cen	NL?	SS?	10.007			9a
BV Cen	DN	UG	14.643		0.83±0.10	10a-c
V345 Pav	NL	UX	4.754			11a, 11b
UU Aqr	NL	UX/SW/SU	3.926	252.1	0.67±0.2	12a-c
MU Cen	DN	UG	8.208		1.2±0.2	1a
FO Aqr	NL/IP		4.849	20.9, 22.5		14a-g

References in the table. 1a=Friend et al. (1990), 1b=Mauche (2004), 1c=McGowan et al. (2004), 1d=Bitner et al. (2007), 2a=Taylor et al. (1998), 2b=Kato & Starkey (2002), 2c=Prinja et al. (2004), 3a=Shafter (1983b), 3b=Shafter (1983a), 3c=Honeycutt & Kafka (2004), 3d=Kozhevnikov (2007), 4a=Taylor et al. (1999), 4b=Rodríguez-Gil et al. (2001), 4c=Baskill et al. (2005), 5a=Robinson et al. (1991), 5b=Smak (1995), 5c=Poole et al. (2003), 5d=Vande Putte et al. (2003), 5e=Groot et al. (2004), 6a=Patterson, J. 2003, <http://cba.phys.columbia.edu/communications/news/2003/march9.html>, 7a=Patterson et al. (1996), 7b=Greiner et al. (2001), 7c=Kato & Uemura (2001), 8a=Shafter (1985), 9a=Oliveira & Steiner (2004), 10a=Gilliland (1982), 10b=Hollander et al. (1993), 10c=Sion et al. (2007), 11a=Buckley et al. (1992), 11b=Buckley et al. (1992), 12a=Baptista et al. (1994), 12b=Vande Putte et al. (2003), 12c=Patterson et al. (2005), 14a=Hellier et al. (1989), 14b=Marsh & Duck (1996), 14c=Beardmore et al. (1998), 14d=Patterson et al. (1998), 14e=Williams (2003), 14f=Evans et al. (2004), 14g=Andronov et al. (2005)

Table 6.1: Types and periods of cataclysmic variables taken from Ritter and Kolb Catalogue. The types of CVs are DN=dwarf novae, IP=intermediate polar and NL=novalike. The subtypes of CVs are SH=non-SU UMa, SS=supersoft X-ray source, SW=SW Sex, UG=U Gem or SS Cyg subtype, UX = UX UMa, VY = VY Scl. The apparent magnitudes are given in Table 6.3

Star	Telescope	Date	UT	Sampling Hz	Seeing, clouds arcsec
SS Cyg	WHT	2003-11-11	19:12 - 22:36	16	1.3, clear
V592 Cas	WHT	2003-11-11	22:36 - 1:54	18	1.9 [1-5], clear
KR Aur	WHT	2003-11-12	01:54 - 05:25	16	1.3, clear
LS Peg	WHT	2003-11-12	19:06 - 22:28	16	1.4, clear
LS Peg	VLT	2005-05-18	07:28 - 10:33	19	0.9, clear
RW Tri	WHT	2003-11-12	22:28 - 02:12	16	1.3 [0.8-4.5], clear
HQ Mon	WHT	2003-11-13	02:12 - 03:32	16	1.4, clear
BZ Cam	WHT	2003-11-13	03:32 - 06:51	16	1.7, clear
CM Del 1	VLT	2005-05-11	06:46 - 10:15	18	0.6, clear
CM Del 2	VLT	2005-05-21	05:50 - 07:00	18	0.7, clear
WX Cen	VLT	2005-05-14	02:06 - 03:02	23	1.0, clouds
BV Cen	VLT	2005-05-17	03:26 - 05:31	22	0.9 [0.5-3],clear
V345 Pav	VLT	2005-05-17	05:41 - 10:35	25	0.9 [0.4-2.7], clear windy
UU Aqr	VLT	2005-05-19	08:06 - 10:24	20	0.6, clear
MU Cen	VLT	2005-05-21	04:38 - 05:45	10	0.8, clear
FO Aqr	VLT	2005-05-21	07:10 - 10:18	20	1.0 [0.4-2.7], clear

Table 6.2: Observation log. When the seeing was highly variable we show the seeing range inside brackets.

identical as speckle patterns depend upon the exact isoplanatic angle. Optimal photometry requires identical profiles for target and comparison star (Naylor 1998) and therefore does not work well at high-speeds.

To further aid us choosing the best reduction we also compared the power spectra of the light curves obtained with the different photometry techniques and aperture radii. The power spectrum is useful in separating the real long term variability (timescales of minutes) of the stars from the reduction noise (timescales of seconds). The reduction procedure can only increase the noise so our aim was to minimise the power spectrum. As mentioned above, optimal photometry increases the variability power, specially in the range of 0.03 to 3 Hz by two orders of magnitude raising it to  $10^{-2}$  (RMS/mean) $^2$ Hz $^{-1}$ . We found that fixed and variable aperture photometry were similar; we chose the variable aperture photometry to cope best with variable seeing. We found that the “optimum” aperture radius varied for each observation run. Therefore, for each case, we chose the

aperture radius that would maximise the signal-to-noise ratio. Too large or too small an aperture radius will increase the noise for frequencies higher than 0.1 Hz.

All the comparison stars were well behaved except for WX Cen, which was affected by clouds. We show WX Cen's light curve but no analysis of these data was carried out.

Due to the brightness and colour of our targets, it was not always possible to find good comparison stars. This problem is particularly important for the  $u'$  band of V592 Cas, LS Peg, BZ Cam, BV Cen and V345 Pav where the target was brighter than the comparison star. Therefore, for these CVs the  $u'$  filter light curve shown is the ratio of the counts of the target in  $u'$  to the counts of the comparison in  $g'$ . However, for cross-colour comparison, flux calibration and colour-colour plots, we use the ratio of the target and comparison in  $u'$  to compute the differential photometry light curve. The  $u'$  band of BV Cen had too low counts to recover and this object was also left out of our analysis.

For the final light curve we also cleaned cosmic rays. Our reduction procedure does not have an automatic way of removing cosmic rays. They usually appear as sharp peaks or dips in the light curve and are easy to spot. We investigated each frame with a candidate cosmic ray and discarded the points were it was confirmed. For each filter, and each star no more than 10 out of 100 000 points were discarded due to cosmic rays. All the following data analysis was done using IDL and the IDL Astronomy Library. The times are given in MJD.

We flux-calibrated the data following the usual procedure. The CVs' apparent magnitudes are given in Table 6.3. For the WHT November 2003 observing run we did not have a sufficient airmass range for any object in order to calculate the extinction coefficients. Therefore we used extinction coefficients obtained in previous ULTRACAM observations;  $K'_r = 0.083$  mag/airmass,  $K'_g = 0.17$  mag/airmass and  $K'_u = 0.49$  mag/airmass to calibrate the 2003 data. For the VLT May 2005 observing run we used CM Del

<b>Star</b>	<i>r'</i>	<i>g'</i>	<i>u'</i>
SS Cyg	11.51±0.03	12.18±0.03	12.22±0.11
V592 Cas	12.70±0.04	12.66±0.04	12.63±0.16
KR Aur	13.28±0.03	13.25±0.03	13.21±0.09
LS Peg	12.26±0.03	12.20±0.03	12.02±0.17
RW Tri	12.80±0.03	12.91±0.03	13.22±0.07
HQ Mon	13.20±0.03	13.10±0.03	13.23±0.12
BZ Cam	13.02±0.06	12.94±0.06	12.70±0.39
CM Del 1	14.09±0.02	14.10±0.02	14.37±0.06
CM Del 2	13.69±0.02	13.68±0.02	13.91±0.03
BV Cen	12.85±0.04	13.61±0.03	14.70±0.21
V345 Pav	13.29±0.06	13.63±0.03	14.28±0.14
LS Peg	12.18±0.04	12.09±0.02	11.98±0.12
UU Aqr	13.76±0.04	13.91±0.03	13.94±0.07
MU Cen	14.41±0.04	15.13±0.03	15.74±0.03
FO Aqr	13.79±0.05	13.76±0.03	13.78±0.04

Table 6.3: Mean apparent magnitudes of the cataclysmic variables observed.

observation in the 11<sup>th</sup> to calculate the extinction coefficients in each filter which are  $K'_r = 0.069$  mag/airmass,  $K'_g = 0.15$  mag/airmass and  $K'_u = 0.47$  mag/airmass. These we use to flux calibrate the 2005 data.

## 6.3 Results

### 6.3.1 Light Curves

We show the light curves of our objects in Figure 6.1. For display purposes the observations were normalised and binned to 1 second. As explained above for V592 Cas, LS Peg, BZ Cam and V345 Pav, the *u'* light curve was obtained dividing the target in *u'* by the comparison star in *g'*. The eclipses at the end of the light curves of RW Tri and V345 Pav were cut from the data of Figure 6.1 and are shown in higher detail in Figure 6.2. At first glance, we see that some systems show strong flickering in their light curves and others like HQ Mon, WX Cen and BV Cen hardly vary. Flickering is a characteristic of accreting systems, although some systems show low levels of variability.

To the best of our knowledge all CVs are reported to flicker although there are some systems which show changes of flaring state (like AE Aqr which shows extreme flaring events (Bruch & Grutter 1997). RS Oph was reported not to flicker after the outburst of 2006 (Zamanov et al. 2006) which led the authors to assume that the accretion disc was destroyed by the outburst. The systems of our sample that show lower variability power are the ones that have longer periods. It is not clear whether this is significant. Due to the bad observing conditions and low signal-to-noise we will not analyse the light curves of WX Cen and BV Cen. There are no published light curves of HQ Mon although long term variability has been reported (Wahlgren et al. 1985). As a CV of low variability, HQ Mon will be used as a reference extreme system.

The light curves show that the variability in the three bands is highly correlated and that the amplitude of the variation is higher for the  $u'$  band confirming the results of Bruch (1992). It is interesting to notice that the flickering looks different for the different stars. For example the shapes of the flares differ. However, for the same star (LS Peg and CM Del) observed on different nights the light curve appears similar. Note that even the small structures seen in Figure 6.1 are real variability intrinsic to the source, since our binning removed variations that were only due to noise. To illustrate this point we show an expanded full resolution  $g'$  band light curve of KR Aur in Figure 6.3

Most light curves show variations around a mean magnitude but in KR Aur, FO Aqr, BZ Cam and V345 Pav the mean flux of the CV seems to increase in the second half of the observation which may be due to orbital variability or a change of state. For example, for KR Aur, it is probably due to the hot spot. But long term variability could only be studied with much longer observations and are beyond the scope of our study.

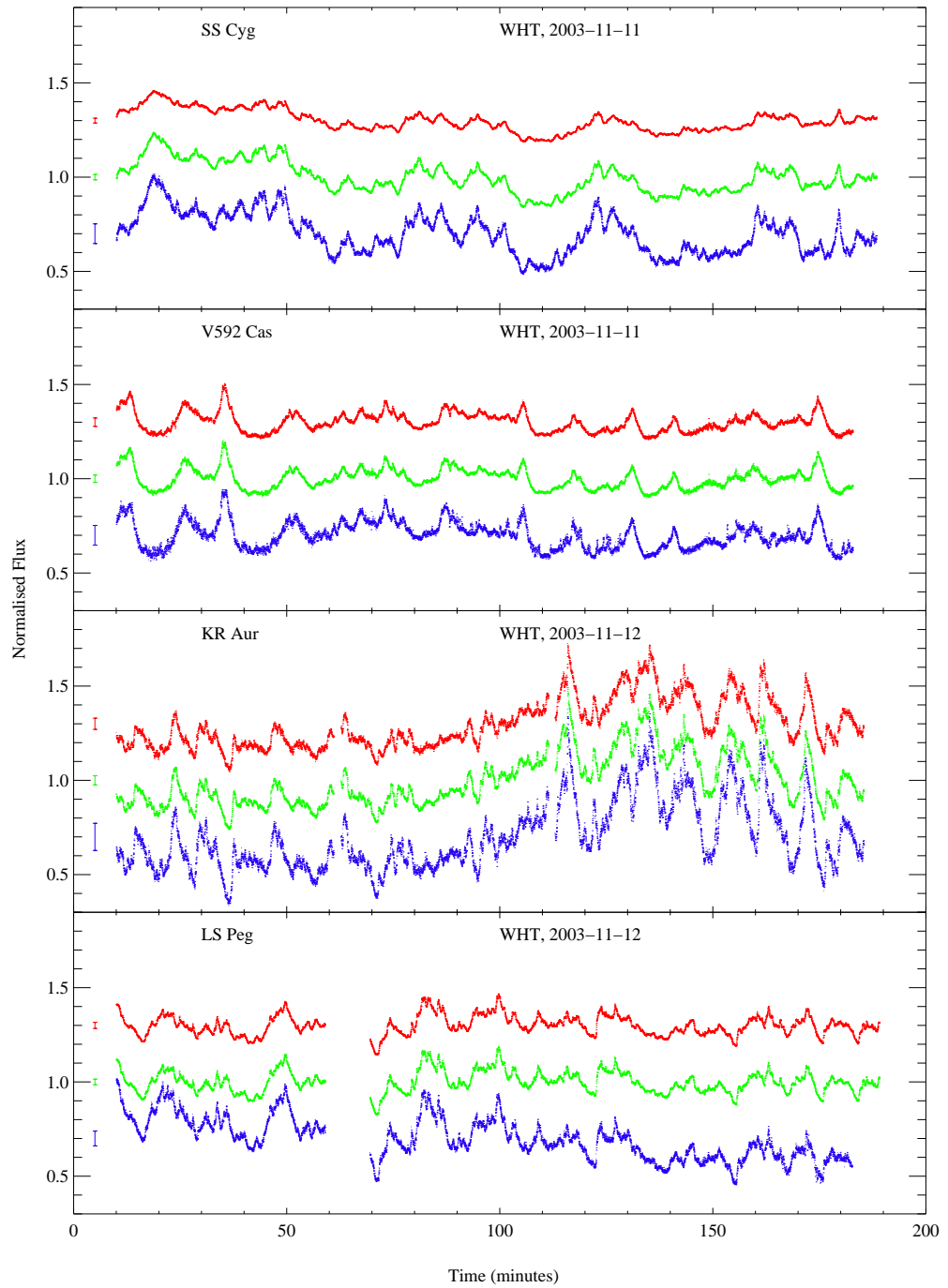


Figure 6.1: Light curves of the CVs with 1 second binning. In each panel the top red is the  $r'$  filter light curve, the middle green is the  $g'$  filter light curve and the bottom blue is the  $u'$  filter light curve. The flux is normalised to unity and the different filters were displaced vertically by 0.3 for clarity. The  $r'$  was displaced upwards and the  $u'$  downwards. The mean errors due to photon statistics in each filter are shown in the left of the light curves. The errors were multiplied by 10 for clarity.

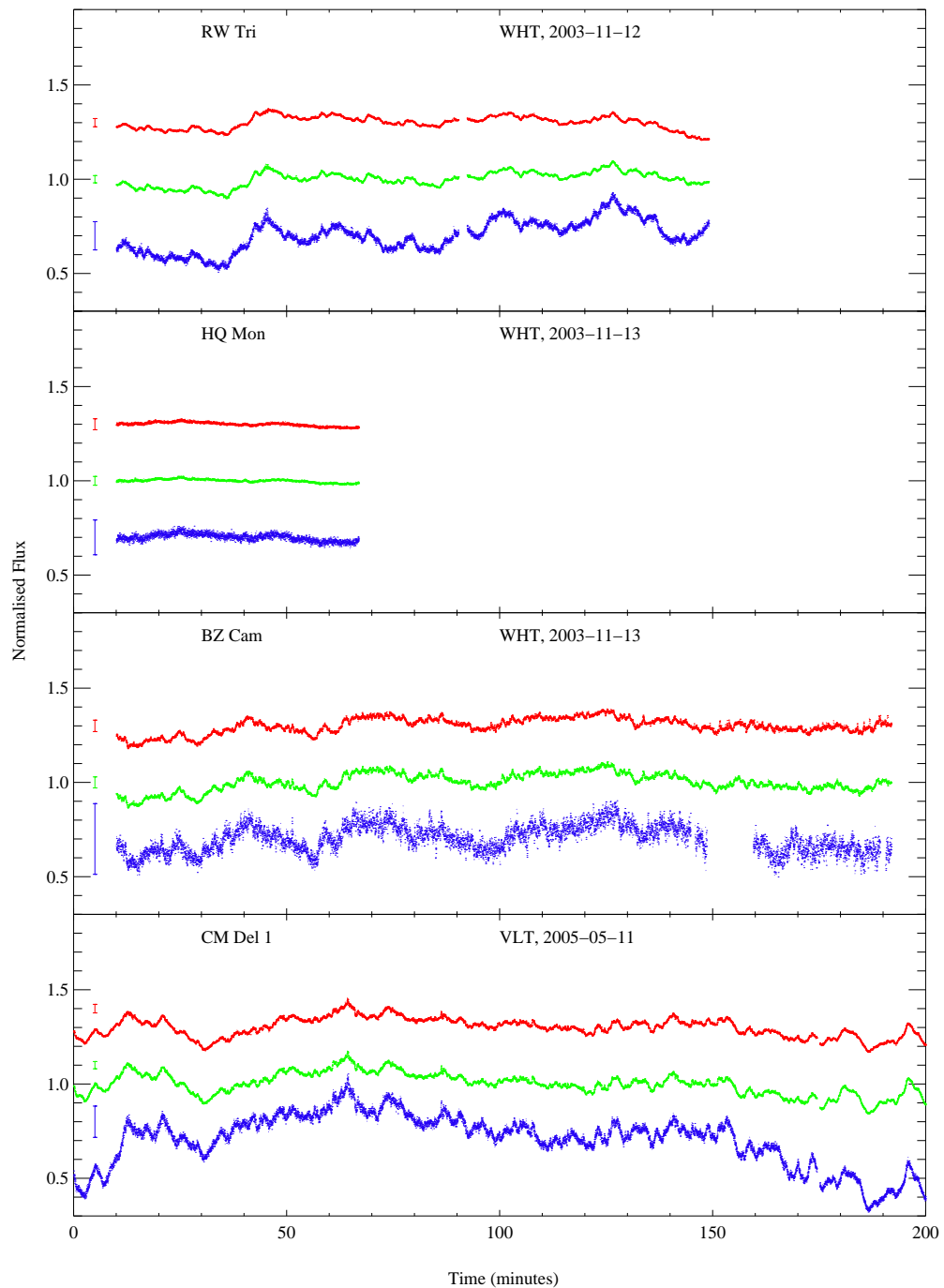


Figure 6.1: continued

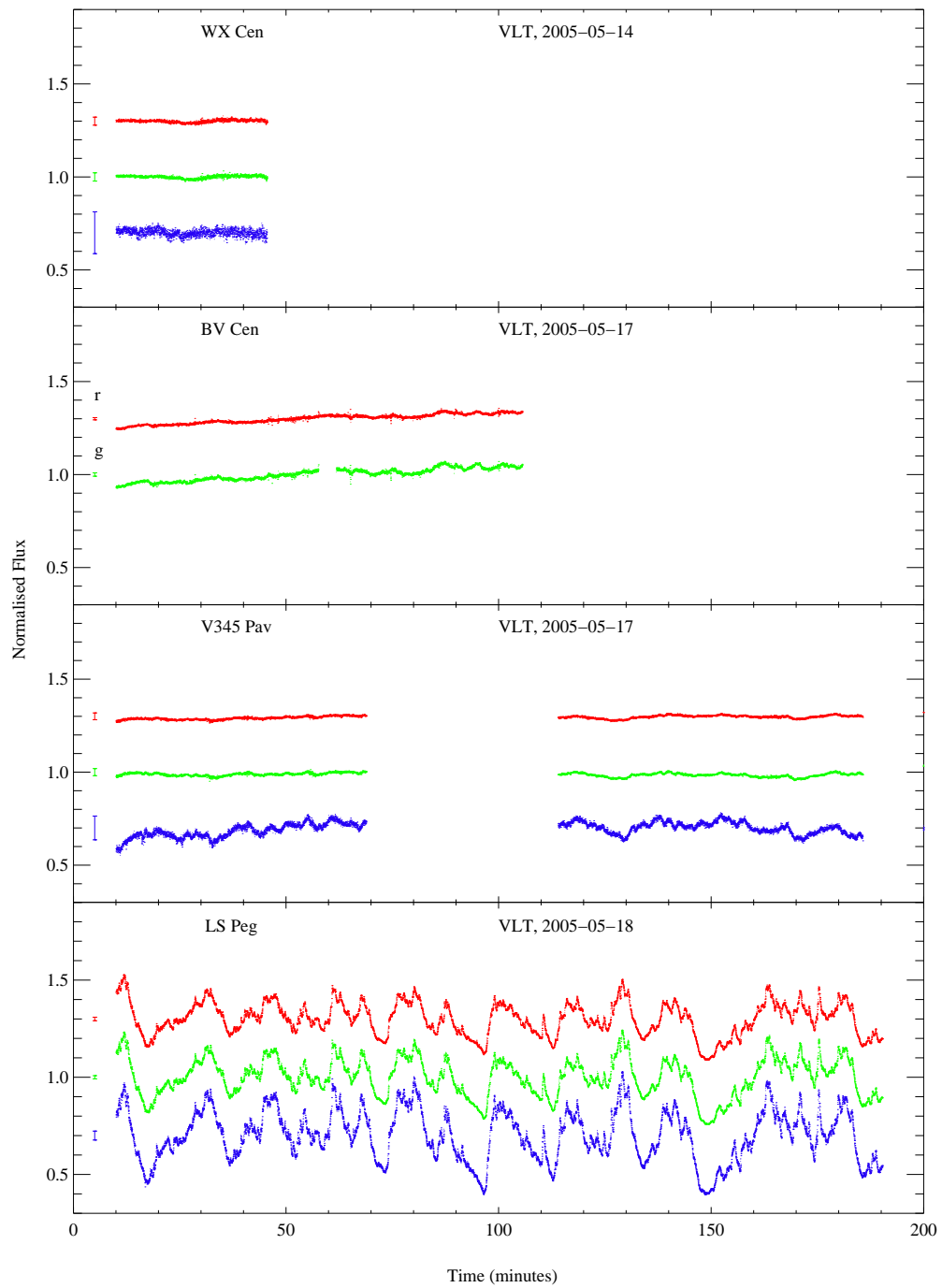


Figure 6.1: continued

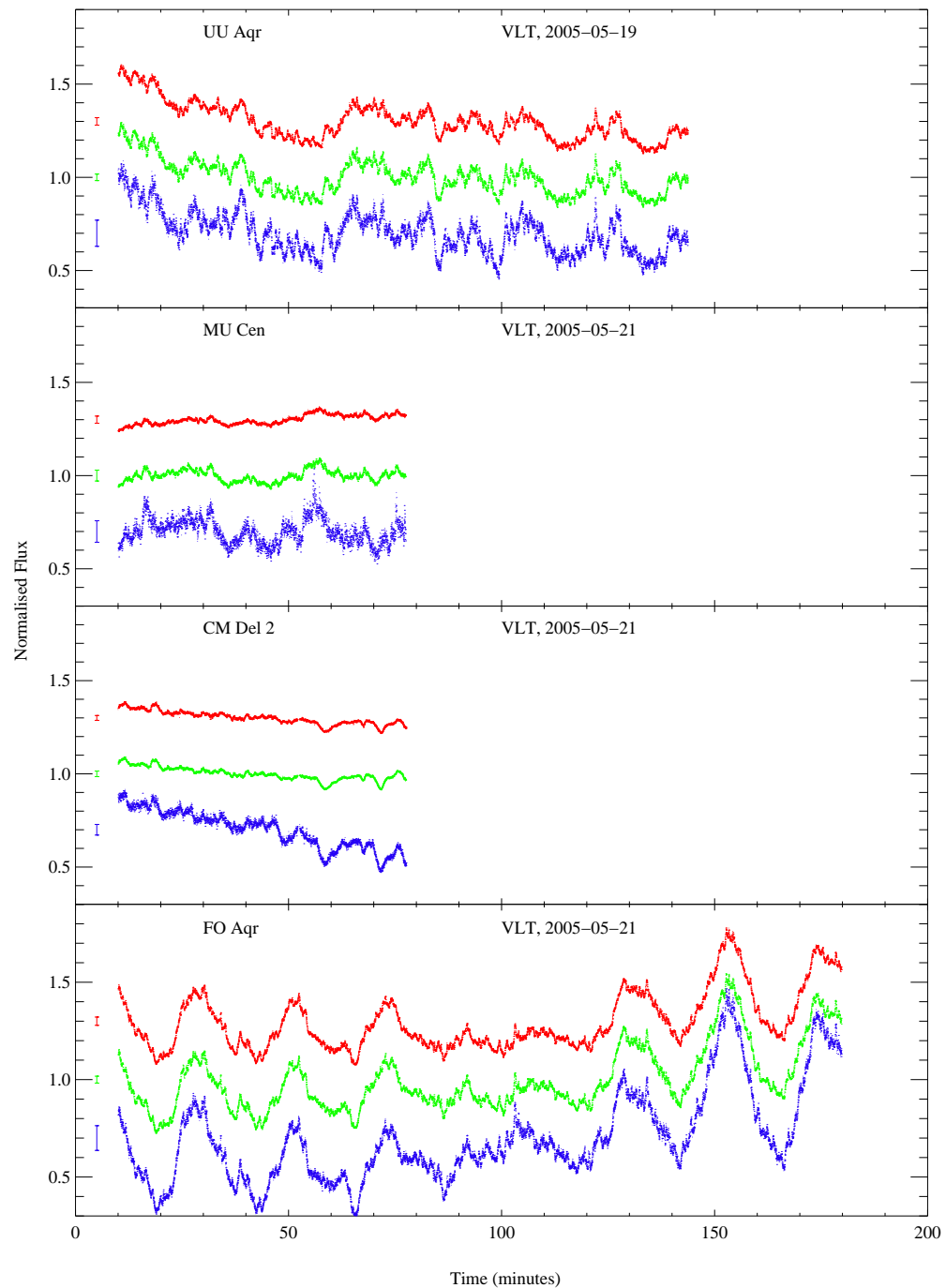


Figure 6.1: continued. Note that FO Aqr is an intermediate polar.

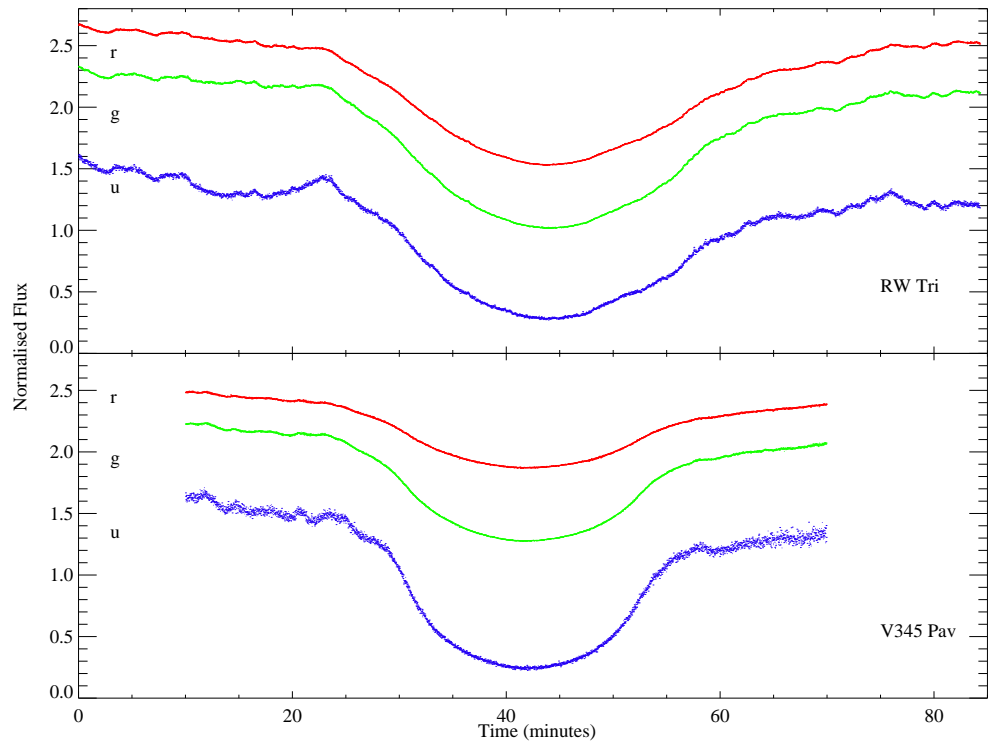


Figure 6.2: Eclipse light curves of RW Tri and V345 Pav with 1 second binning. In each panel the top in red we show the  $r'$  filter light curve, in green the  $g'$  filter light curve and in blue we show the  $u'$  filter light curve. The flux is normalised to unity and the different filters were displaced vertically for clarity. The  $r'$  and  $g'$  data were displaced upwards by 1.2 and 0.8 respectively. The eclipses were in the last part of the observation interval so we only show the light curve of RW Tri 117 minutes after the start of the observations and V345 Pav light curve 233 minutes.

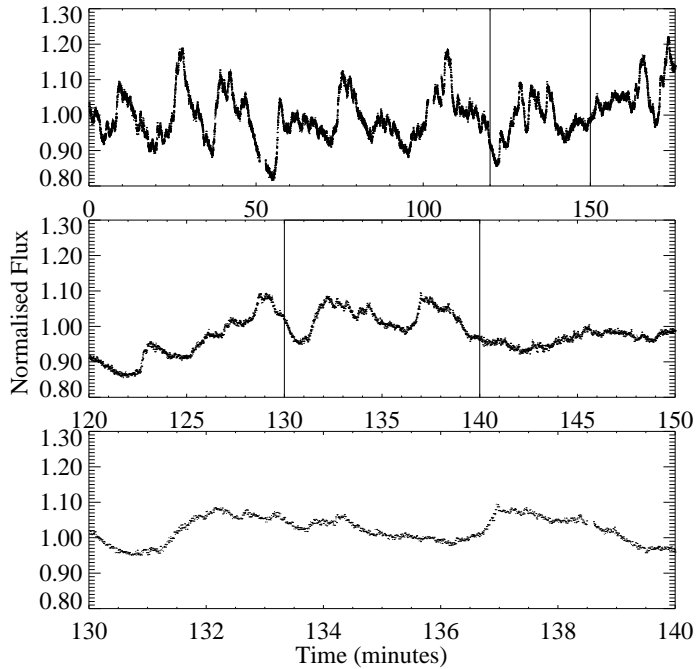


Figure 6.3: Full resolution  $g'$  filter light curves of KR Aur expanded. The vertical lines show the region that was expanded in the panel directly below it.

### 6.3.2 Cross Correlation

We computed the cross correlation function between the  $g'$  band versus the  $r'$  band and the  $u'$  band versus the  $g'$  band. We use the Edelson & Krolik (1988) method for unevenly sampled data. There were no lags between the filters; we would have seen lags longer than 0.1 seconds. So we confirm previous results that the optical emission of CVs is simultaneous in all colours.

### 6.3.3 Flickering Colour

We computed the flux ratio diagram for our data binned to 10 seconds which is shown in Figure 6.4. In the plot we also show as dots the flux ratio of main sequence stars (Pickles 1998) transformed to the Sloan filters by Gaensicke (priv comm). To estimate the emission of known astrophysical sources and mark their position in our flux ratio figure we use the ULTRACAM system response which includes the filter band-passes

and the quantum efficiencies of the CCDs. We computed the flux ratios of a blackbody with temperature between 3000 K and 100 000 K, which are shown as a dashed line. Note that the star (\*) shows the position of a blackbody of infinite temperature. For high temperatures ( $T > 100\,000$  K) the blackbody emission is the Rayleigh-Jeans tail and the optical colours lose sensitivity to temperature. We also computed the flux ratio of optically thick accretion discs with accretion rates of  $10^{-10} M_{\odot} \text{ yr}^{-1}$  to  $10^{-8} M_{\odot} \text{ yr}^{-1}$ , shown as a solid line and of optically-thin gas (pure hydrogen) with temperatures between 5000 K and 100 000 K, which is shown as a green solid line. The mean flux ratio of two sources stage lies on a line connecting them in the flux ratio diagram.

Besides the mean position of the CVs in the flux diagram we are more interested in how the colours evolve in time. This will allow us to have an idea of the colour of flickering light. The position in the flux ratio diagram at maximum light is on the line that connects the “colour” at minimum light and the “colour” of the source that produced the flare. The data was colour coded according to the  $g'$  magnitude. The brightest points are shown in blue, next green and yellow and the faintest points are shown in red. The mean colour of the points in each bin is showed as overplotted dots. To better analyse the variation of the flickering colour we show the zoom of Figure 6.4 centred in each CV in Figure 6.5, whose axis are relative to the values given on the figure. We can see that there is a strong correlation between colour and  $g'$  flux. In all observed CVs except for UU Aqr and HQ Mon, as the flux rises the overall colour becomes bluer moving, towards the top left of the flux-ratio diagram. We will explore further the variation in each case.

The dwarf novae (DN) SS Cyg, BV Cen and MU Cen have very different colours to the IPs and Novalikes. The accretion rates in dwarf novae are lower and therefore the accretion discs are colder and fainter. This implies that in most DNe it is possible to see the secondary stars in the spectra, contrary to the case of the high accretion rate systems. The secondary stars of DNe are of spectral type K-M which are the redder main

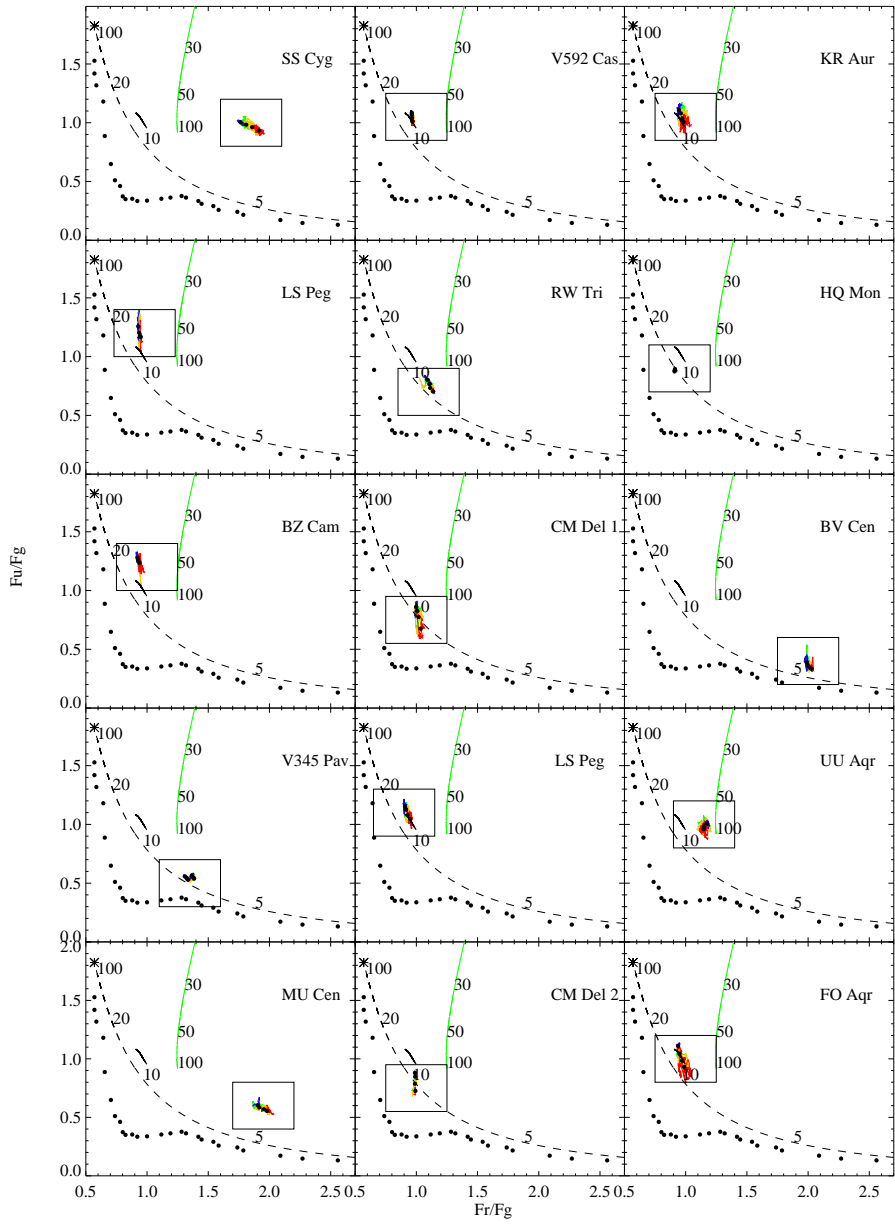


Figure 6.4: Flux ratio diagram for the observed CVs. Main sequence colours are shown as dots with the O stars at the top left and the K stars at the lower right. The black dashed line shows the position of black bodies, where \* shows the colour of an infinite temperature blackbody. The green solid line shows colours of optically thin emission. The temperatures are marked in units of 1000K. The black solid line shows colours of accretion discs with accretion rates of  $10^{-10} M_{\odot} \text{ yr}^{-1}$  to  $10^{-8} M_{\odot} \text{ yr}^{-1}$ . Our data is colour coded according to the  $g'$  magnitude. From bright to faint the colours are blue, green, yellow and red. The points were binned to 10 seconds. The box shows the region that will be zoomed in Fig 6.5.

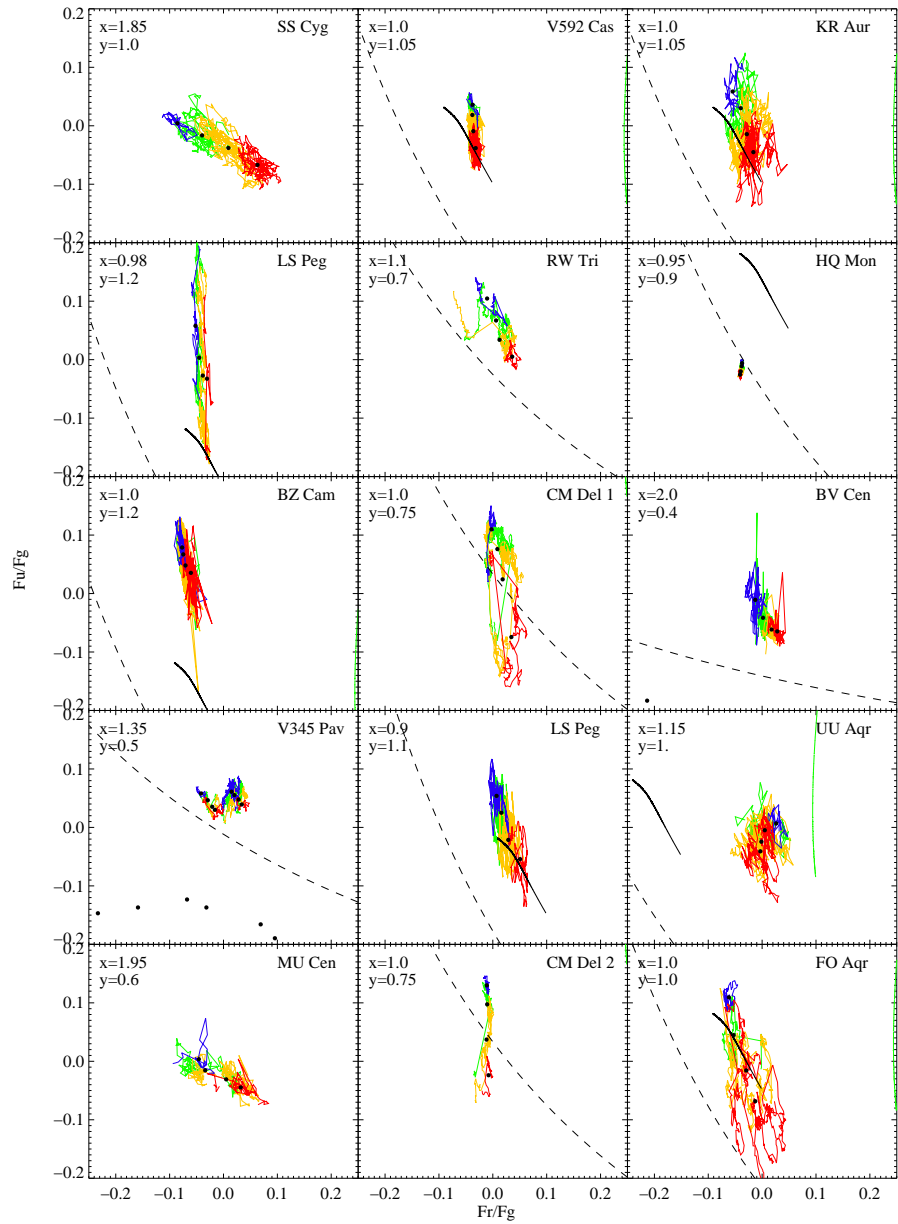


Figure 6.5: Flux ratio diagram for the observed CVs. Zoom of the box shown in Fig 6.4. The x and y values are relative to the values given on the top left corner of the figure.

sequence stars in the bottom right of our figures. At minimum light the DN BV Cen and MU Cen have colours that result from the sum of the colour of the secondary star plus a bluer component. This blue component is the accretion disc whose colours can be explained by optically thick emission. In the rise to maximum of a flare the colour changes towards the upper left. This means that the optically thin or thick accretion disc becomes hotter, or at least it becomes brighter adding more blue light. The secondary star of the dwarf nova SS Cyg has a spectrum of a K4 star. The colour of SS Cyg is a combination of the secondary star colour with an optically thin emission source with temperature of approximately 30 000 K. This is in agreement with the current model for SS Cyg in quiescence whose inner accretion disc is reported to be either optically thin or evaporated onto a corona that would in turn be also optically thin. At maximum flare, the optically thin emission source reaches a temperature of 60 000 K.

At minimum light all the observed IPs (V592 Cas, LS Peg and FO Aqr) lie close to the accretion disc line in the flux ratio diagram indicating that their optical emission is dominated by the accretion disc. At maximum light they become bluer rising almost vertically in the flux ratio diagram. The colour of the extra component can be explained by a mixture of optically thick and optically thin emission.

The novalike variables show a higher dispersion of colours. At minimum light most of them lie close to the accretion disc or the black body line. In case of KR Aur, RW Tri, BZ Cam and V345 Pav the evolution of the flares is towards the upper left which in this case implies that the extra flux comes from a very hot ( $T \geq 80 000$  K) optically thick source or that an optically thick source became hotter. In UU Aqr the source of flares is optically thin. The flare colour of CM Del resembles the IPs and its source is probably a mixture of optically thick and optically thin material. The flares of HQ Mon can be explained by optically thin emission or by extra light from the accretion disc. V345 Pav shows two levels of non-flickering light depending upon the visibility of the hot spot. The hot spot is visible in the last part of our observation so the constant

Star	Optically Thin	Optically Thick	Accretion Disc
SS Cyg	✓		
V592 Cas	✓	✓	
KR Aur		✓	✓
LS Peg		✓	
RW Tri		✓	✓
HQ Mon	✓	✓	
BZ Cam		✓	
CM Del 1	✓	✓	✓
BV Cen	✓	✓	
V345 Pav		✓	
LS Peg		✓	
UU Aqr	✓		
MU Cen	✓	✓	
CM Del 2	✓	✓	✓
FO Aqr		✓	✓

Table 6.4: Dominant source of flickering for each CV.

flux is slightly higher. To separate the colour of the flares from the colour of the hot spot we divided the light curve in two parts which are shown in the figure. Note that the flares have the same slope in both flux levels of the non-flickering light. A summary of the dominant flickering sources of emission for each CV is given in Table 6.3.3.

We conclude that in all cases the colours of the flares can be explained by thermal emission, optically thick, optically thin or a mixture of both. There is no need to invoke other emission mechanisms to produce the flares. Besides a difference in colour of the non-flickering light for the different CV type there seems to be a difference in the colours of the flickering light. However there are some outliers like CM Del and UU Aqr.

### 6.3.4 Intrinsic Variability and sources of noise

There are three sources of variability in CVs, orbital modulation, magnetic modulation and flickering. The observation of CVs shows extra variability due to photon noise statistics and scintillation. The photon noise is uncorrelated so adds power to all frequencies. The error of the number of counts in a pixel due to photon noise is equal to the square

root of the number of counts. This error can be propagated through and is shown in the left of Figure 6.1. The mean errors in the WHT run for the  $g'$  filter are of order of 0.6 per cent for a bright system like LS Peg and of 1.0 per cent for a fainter system like KR Aur. For the VLT run and also for the  $g'$  filter we have errors between 0.4 per cent for LS Peg and 1.0 per cent for V345 Pav.

Scintillation is the other source of noise and is due to the turbulence of the atmosphere. Atmospheric turbulence causes “flying shadows” on the ground whose pattern changes intrinsically and is also shifted by winds. Contrary to the angular seeing which conserves the flux of the light, scintillation involves focusing/defocusing of the light by turbulent elements, which results in flux variability.

At low frequencies the power of scintillation scales with the cube of the airmass, with the  $-4/3$  power of the telescope aperture, is nearly independent of wavelength and is approximately white noise (Young 1967). The aperture of the telescope acts as a low pass filter decreasing the scintillation power for frequencies  $f_b > V_p/(2\pi a)$ , where  $V_p$ , is the wind speed and  $a$  is the telescope aperture radius. For  $f \gg f_b$  the scintillation power has a slope of  $-5/3$  until approximately 100 Hz. For our observations the break point was at 1.5 Hz for the WHT and 0.4 Hz for the VLT. Using the estimate for the low frequency power given in Figure 1 of Dravins et al. (1998) the error of the counts is approximately 0.8 per cent for WHT and 0.3 per cent for the VLT, so of the same order of magnitude as the photon noise. At longer exposure times ( $> 1$  sec)  $f_b$  is higher than the Nyquist frequency and the scintillation noise is approximately white over all the spectrum. In most previous studies of flickering the variability due to scintillation was always either lower than the photon noise or it could be described and treated as a photon noise due to the low timing resolution. However in our case scintillation will affect our results and has to be accounted for.

### 6.3.5 Power spectrum analysis

To study the different timescales of the variability we computed the Lomb Scargle periodogram (LSP) (Lomb 1976; Scargle 1982). We opt for LSP instead of the discrete Fourier transform because we have small gaps between runs and some missing points so our data is not entirely evenly sampled. For a couple of stars we also have bigger gaps that can be correctly accounted for with the LSP method without loss of uniformity.

We define our LSP according to equation 3.15 and we use the normalisation constant A, given in equation 3.23 to obtain the equivalent to the Miyamoto normalisation of the PDS. We choose this normalisation because the integrated periodogram is equal to the square of the total RMS variability of the time series normalised by the square of the mean count rate (van der Klis 1995). This allows us to directly compare the variability of different targets.

In Figure 6.6 we show the LSP of our targets for the  $g'$  filter. The LSP was binned and fitted in the logarithmic space using the method of Papadakis & Lawrence (1993). We used a 20 $\times$  binning factor which considerably decreases the frequency resolution of the LSP and increases the lowest frequency measured. However, this transforms the original periodogram into a consistent estimator of the logarithm of the power spectral density and allows us to apply the least squares method to fit the LSP. The errors of the binned logarithm periodogram were set to the theoretical value given by equation 20 of Papadakis & Lawrence (1993), which is 0.12 for all binned points. We further binned the LSP at high frequencies using equally spaced frequencies in the logarithm space for clarity of plotting.

Figure 6.6 also shows a least squares fit to the LSP (green solid line) using a broken power model given in Equation 3.31. We can see that the power law dominates the LSP at lower frequencies and the high frequencies are dominated by the white noise and as we will see in the next subsections by scintillation and red noise leak. The

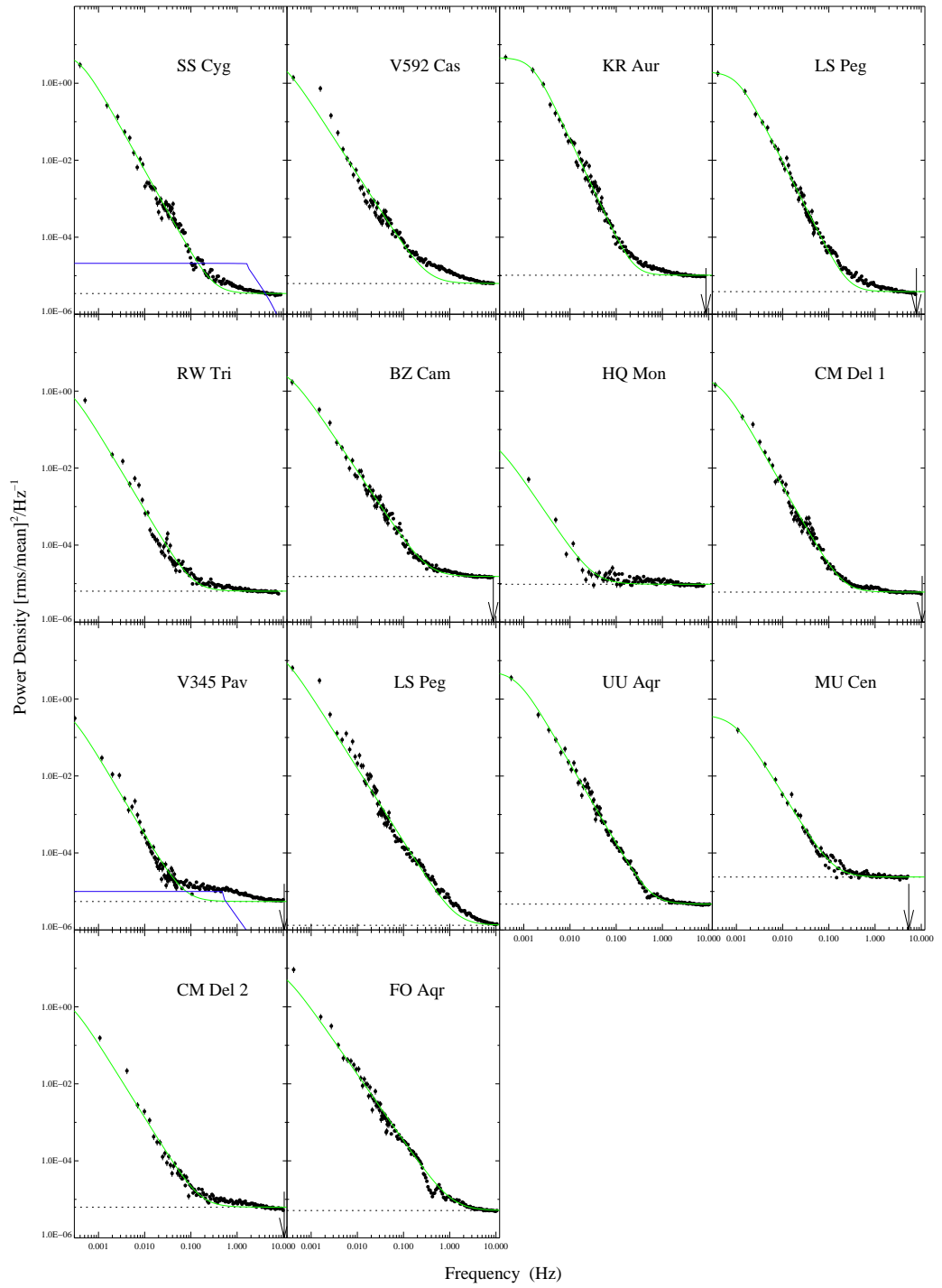


Figure 6.6: Lomb Scargle Periodogram of the  $g'$  filter light curves of the CVs. The fitted broken power law model is shown in green. The white noise level is shown as a dashed line. The blue line shows our estimation of the scintillation noise for two systems.

presence of scintillation will affect the least squares fitting of the power spectrum. To minimise the effect of scintillation we discarded the high frequency points. Hence, after using all points of the power spectrum to estimate the white noise level we keep this fixed and refit only the frequencies between  $2 \times 10^{-4}$  Hz and 0.1 Hz.

In the case of evenly spaced data we expect a white noise power given by equation 3.29. Our data are almost evenly spaced so we do not expect a large deviation from this value. In most cases our theoretical prediction of white noise agrees very well with white noise level seen in the LSP distribution. The fitted white noise level is shown as a dashed line in the periodogram plots. For MU Cen, CM Del2 and the  $u'$  filter of some the VLT targets the theoretical prediction of the white noise level underestimates the measured level. We could not find any obvious reason why this should be the case, but at least in the  $u'$  case, it can be the result of pickup noise to which  $u'$  is specially sensitive.

As it can be seen in Figure 6.6 the broken power law model is not an especially good fit of the periodogram. Other models could fit the periodogram better, for example a multi-lorentzian model. We choose the broken power law because of its relative simplicity, small number of parameters and also for comparison with previous studies. Moreover we chose it because we believe that the extra features in LSP of these CVs are not real but are due to two different types of noise. We will show that there is extra power at high frequencies due to scintillation and leakage from the low frequencies to the high frequencies which distorts the original periodogram. The first sign of red noise leak is that the power law indices obtained in the least squares fitting to the periodogram mentioned are all approximately 2. We will explore the other signs of red noise leak below. But we will start by estimating the power due to scintillation.

### **Extra power due to scintillation**

As seen in Figure 6.6 the power law model is a bad fit around frequencies of 0.6 Hz, where there is extra power. The amount of extra power is different for each CV but in some cases is relatively strong. The power is consistent with what we expect for scintillation. Moreover it appears to drop at about the frequency expected for a given telescope aperture. Estimations of scintillation noise are shown in Figure 6.6 in blue. To estimate the scintillation spectra we used the values of Figure 1 of Dravins et al. (1998) for a 4 m and 8 m telescope and we assumed a mean airmass of 1.3. We also approximate the high frequency power to a  $-5/3$  power law and included the diffraction for 0.05 sec exposures. The diffraction has no effect upon the theoretical power spectral shape of the scintillation until the Nyquist frequency.

It is difficult to make an estimation of the scintillation power better than to a order of magnitude since it varies through the night. Moreover, when we divide the counts of the target through the comparison star we are already correcting for some of the scintillation, but some remains because the paths of the light of the two stars are slightly different. At large enough angles we are basically doubling the scintillation noise. We analysed the LSP of the target and comparison star separately and concluded that the ratio of the target to comparison star generally shows lower scintillation power than the comparison star alone, but that could reflect transparency variations.

We investigated further the amount of noise expected due to scintillation using high-time resolution observations of two constant stars. Our observations were taken with ULTRACAM on the WHT on the 11<sup>th</sup> of the August 2005. We have a total of 55 min of observation with an exposure time of 0.025 s. One of the stars observed is TYC 6377 – 171 – 1 which is brighter than any of the CVs observed; its comparison star has similar brightness. In Figure 6.7 we show the LSP of the ratio of the constant stars and the LSP of KR Aur as an example.

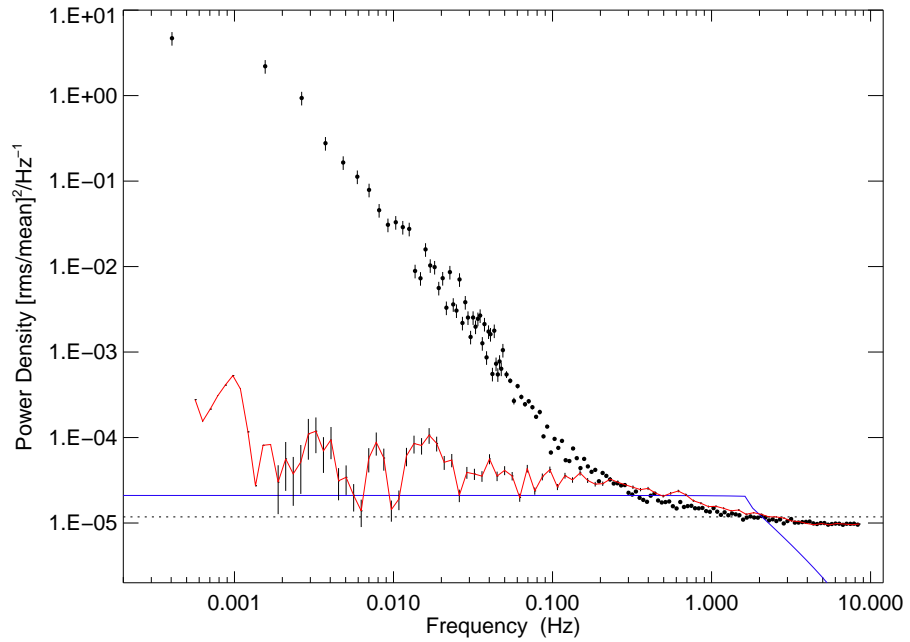


Figure 6.7: Comparison of the  $g'$  filter LSP of the non-variable stars (solid red line) with the LSP of KR Aur (black dots) we also show the expected level of the scintillation noise in this observation.

So we conclude that the extra noise around 1 Hz is due to scintillation and does not come from the CVs. Unfortunately, the presence of scintillation will not allow us to probe the highest frequencies and look for the high frequency break as was originally intended in this study. After we discovered this problem with the WHT data we applied for the VLT time. In the VLT the collecting area of the telescope is four times the WHT one and with the increase in signal-to-noise we expected a decrease of the scintillation and a decrease of the turn off point. Despite the fact that the scintillation noise decreased as expected, this was not still enough to be able to see any high frequency break: the power spectra of CVs are so steep that it is not possible in our data to be sure of the presence of high frequency flickering let alone a break.

## Effects of red noise leak

As mentioned above the fitted power law indices of the CVs are approximately 2. This is a sign of red noise leak (section 3.6). Moreover other signs of red noise leak can be seen in the LSPs of SS Cyg, LS Peg, UU Aqr and FO Aqr. They show a very broad hump followed by a broad peak that could be described as a QPO at high frequencies. Moreover the periodogram of V582 Cas shows two different power law slopes. As seen in section 3.6 these are all signs of red noise leak. As mentioned above (section 3.3.1 and 3.6) red noise leak is particularly important for steep LSPs (i.e.  $\alpha > 2$ ). Although the fitted power law indices of some these systems are among the lowest from our sample (e.g. V592 Cas  $\alpha = 1.87$  and FO Aqr  $\alpha = 1.73$ ), this is not a contradiction. Red noise leak transfers power from the low frequencies to the high frequencies, decreasing the steepness of the periodogram. Therefore there is a systematic bias in the shape of the LSP that is affected by red noise leak that will make the fit underestimate the power law index “ $\alpha$ ” which in turn will hide the original problem.

To recover a power LSP affected by red noise leak we follow the procedure developed in section 3.6. Therefore we applied the filtering method using a high pass filter with a cut of frequency of 5.6 mHz so that even for the systems where the white noise dominates at lower frequencies, there is still a range of frequencies left after the filtering to fit the power law. When we filtered the data all of the low frequency information is lost, this includes both the power at low frequencies and the estimated low frequency break. This information is important if any attempt to describe the power spectrum is to be made. Moreover, as shown in section 3.6, the lower frequencies are the least affected by red noise leak and can be used to recover the original power spectrum slope. To recover the low frequencies we combined the low frequencies of the unfiltered LSP ( $< 0.1$  Hz) with the high frequencies of the filtered LSP ( $> 0.1$  Hz) and obtained a combined LSP. The combined LSP has the advantage of having lower leakage than the

original LSP while maintaining the low frequency information.

Again we used the broken power law model of Equation 3.31 to fit the LSP. After obtaining the value of the white noise using all the points in the LSP we re-fitted the LSP using only frequencies lower than the frequency where the LSP starts to be dominated by white/scintillation noise. We conclude that for the  $g'$  filter all the fits seem good except for V592 Cas and FO Aqr (that maintained  $\alpha = 2$ ) where we suspect that this high frequency filter was not enough to remove the leakage. We tried other cutoff frequencies but the results did not change. So we opt for using the same cut off frequency for all the CVs.

Given that the filtering method did not work for V592 Cas and FO Aqr we applied the other method outlined in section 3.6 so we fitted only the lowest frequencies. As discussed above the number of points to be used is rather subjective. We tried different numbers of points and tested the results by Monte Carlo simulations. We chose the model whose simulation best described the original LSP. We will explain how we performed the Monte Carlo simulations in detail in the next subsection.

In Figure 6.8 we repeat the plots of the observed LSPs of the CVs in the  $g'$  filter in black. We also show the combined LSP cleaned of red noise leak in the blue and the fit to the combined LSP in green. The values of the model coefficients are given in Table 6.5, 6.6 and 6.7 for the  $r'$ ,  $g'$  and  $u'$  filters respectively. The break frequency was forced to be higher than  $2 \times 10^{-4}$  Hz which corresponds approximately to the lowest frequency that we can obtain for the typical three hour length of our observations. The square root of the integral of the periodogram is the normalised RMS variability. Therefore, the RMS depends upon the limits of the integration which in turn depend on the length of the observation. So we chose to calculate the RMS for two specific intervals so it can be compared with other studies. The percentage RMS given in the tables is the square root of the integral of the LSP, R1 is the percentage RMS due to variability between  $f = 1 \times 10^{-3}$  Hz and  $f = 1 \times 10^{-2}$  Hz and R2 between  $f = 1 \times 10^{-2}$  Hz

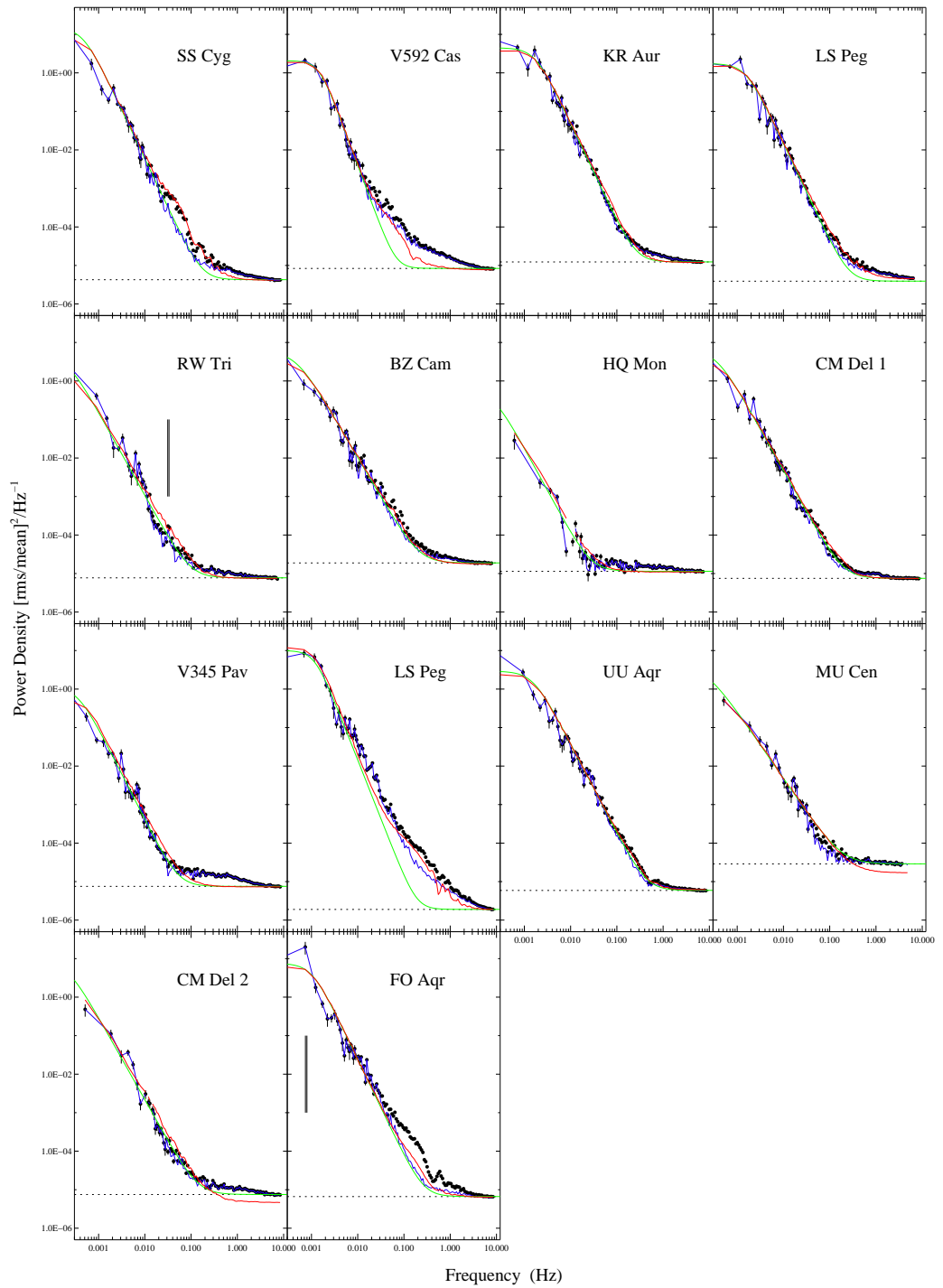


Figure 6.8: Lomb Scargle Periodogram of the  $g'$  filter light curves of the CVs. The observed LSP is shown in black and the combined filtered LSP is shown in blue. The broken power law model is shown in green and the results of the simulation based on this model are shown in red. The vertical lines show the position of the significant peaks.

Star	$10^6 w$	$a_1$	$\alpha$	$f_b$ (mHz)	R1 % $\frac{\text{RMS}}{\text{mean}}$	R2 % $\frac{\text{RMS}}{\text{mean}}$
SS Cyg	3.389	$6.93 \pm 3.33$	$2.56 \pm 0.05$	$0.42 \pm 0.09$	2.22	0.38
V592 Cas	11.066	$2.00 \pm 0.67$	$3.21 \pm 0.53$	$1.43 \pm 0.34$	4.01	0.45
KR Aur	18.008	$4.53 \pm 2.31$	$2.34 \pm 0.06$	$1.27 \pm 0.33$	6.37	1.71
LS Peg	4.419	$1.31 \pm 0.34$	$2.54 \pm 0.06$	$1.61 \pm 0.22$	3.98	0.94
RW Tri	9.436	$2.45 \pm 2.06$	$2.25 \pm 0.07$	$0.38 \pm 0.15$	1.16	0.24
BZ Cam	19.150	$9.60 \pm 14.75$	$1.85 \pm 0.05$	$0.22 \pm 0.19$	2.52	0.96
HQ Mon	16.878	$0.16 \pm 0.10$	$1.78 \pm 0.14$	$0.20 \pm 0.00$	0.32	0.08
CM Del 1	10.252	$5.93 \pm 4.32$	$2.13 \pm 0.04$	$0.30 \pm 0.11$	2.12	0.59
CM Del 2	9.397	$18.85 \pm 6.93$	$2.28 \pm 0.08$	$0.20 \pm 0.00$	1.60	0.46
V345 Pav	6.988	$0.57 \pm 0.46$	$2.10 \pm 0.06$	$0.25 \pm 0.11$	0.55	0.16
LS Peg	2.250	$7.43 \pm 3.51$	$2.99 \pm 0.41$	$1.19 \pm 0.34$	6.99	0.93
UU Aqr	7.648	$1.47 \pm 0.60$	$2.43 \pm 0.05$	$1.97 \pm 0.40$	5.10	1.57
MU Cen	19.051	$6.80 \pm 2.91$	$2.10 \pm 0.09$	$0.20 \pm 0.00$	1.54	0.44
FO Aqr	9.661	$5.55 \pm 3.82$	$2.50 \pm 0.20$	$1.04 \pm 0.30$	5.88	1.27

Table 6.5: Parameters of the broken power law model for the LSP for the  $r'$  filter data. The percentage RMS variability is the square root of the integral of the LSP, R1 is the percentage RMS variability between  $f = 1 \times 10^{-3}$  Hz and  $f = 1 \times 10^{-2}$  Hz and R2 is the percentage RMS variability between  $f = 1 \times 10^{-2}$  Hz and  $f = 0.1$  Hz.

and  $f = 0.1$  Hz. These are measures of the relative variability over these frequencies. The percentage RMS variability was calculated using the broken power law model of the LSP instead of the real data because of contamination of periodicity's in the light curve (for example in the case of FO Aqr) and the extra noise.

### 6.3.6 Simulations

As seen in Section 3.6 we can only test the goodness of our fits by Monte Carlo simulations. So we simulated light curves using Timmer & Koenig's (1995) method. We used equation 3.31 as our model and the model coefficients in Table 6.5, 6.6 and 6.7. The white noise term was added later to reduce aliasing effects. We used the errors of the points to generate the white noise. This will give a noise level exactly equal to the theoretical level predicted by Equation 3.29 which as already mentioned can be somewhat different from the white noise fitted value. This accounts for the difference

<b>Star</b>	$10^6 w$	$a_1$	$\alpha$	$f_b$ (mHz)	<b>R1</b> % $\frac{\text{RMS}}{\text{mean}}$	<b>R2</b> % $\frac{\text{RMS}}{\text{mean}}$
SS Cyg	4.262	$14.81 \pm 6.56$	$2.53 \pm 0.04$	$0.45 \pm 0.09$	3.65	0.65
V592 Cas	8.359	$2.07 \pm 0.61$	$3.25 \pm 0.49$	$1.46 \pm 0.30$	4.15	0.45
KR Aur	12.343	$4.47 \pm 1.91$	$2.54 \pm 0.06$	$1.70 \pm 0.35$	7.66	1.86
LS Peg	3.898	$1.74 \pm 0.46$	$2.53 \pm 0.06$	$1.53 \pm 0.21$	4.40	1.02
RW Tri	7.713	$5.00 \pm 1.46$	$2.16 \pm 0.06$	$0.20 \pm 0.00$	1.16	0.31
BZ Cam	18.801	$5.83 \pm 4.75$	$2.05 \pm 0.05$	$0.46 \pm 0.20$	3.21	1.00
HQ Mon	11.424	$0.64 \pm 0.73$	$2.21 \pm 0.32$	$0.20 \pm 0.00$	0.39	0.10
CM Del 1	7.489	$6.42 \pm 4.40$	$2.15 \pm 0.04$	$0.35 \pm 0.12$	2.53	0.70
CM Del 2	7.491	$9.27 \pm 3.37$	$2.16 \pm 0.07$	$0.20 \pm 0.00$	1.72	0.47
V345 Pav	7.513	$1.15 \pm 0.80$	$2.37 \pm 0.05$	$0.35 \pm 0.11$	0.91	0.19
LS Peg	1.896	$9.98 \pm 4.45$	$3.04 \pm 0.40$	$1.17 \pm 0.31$	7.92	0.99
UU Aqr	5.907	$2.91 \pm 1.34$	$2.32 \pm 0.05$	$1.54 \pm 0.36$	6.12	1.87
MU Cen	28.767	$4.43 \pm 1.98$	$1.75 \pm 0.13$	$0.20 \pm 0.00$	1.84	0.79
FO Aqr	6.619	$7.55 \pm 5.28$	$2.50 \pm 0.10$	$1.01 \pm 0.29$	6.68	1.43

Table 6.6: Parameters of the broken power law model for the LSP for the  $g'$  filter data. The percentage RMS variability given in these tables is the square root of the integral of the LSP R1 is the percentage RMS variability between  $f = 1 \times 10^{-3}$  Hz and  $f = 1 \times 10^{-2}$  Hz and R2 is the percentage RMS variability between  $f = 1 \times 10^{-2}$  Hz and  $f = 0.1$  Hz.

<b>Star</b>	$10^6 w$	$a_1$	$\alpha$	$f_b$ (mHz)	<b>R1</b> % $\frac{\text{RMS}}{\text{mean}}$	<b>R2</b> % $\frac{\text{RMS}}{\text{mean}}$
SS Cyg	60.139	$26.51 \pm 10.41$	$2.37 \pm 0.05$	$0.44 \pm 0.09$	5.17	1.10
V592 Cas	73.189	$3.31 \pm 1.15$	$3.16 \pm 0.65$	$1.42 \pm 0.39$	5.17	0.60
KR Aur	112.760	$9.59 \pm 3.65$	$2.34 \pm 0.05$	$1.47 \pm 0.30$	10.42	2.93
LS Peg	36.828	$4.84 \pm 1.71$	$2.36 \pm 0.05$	$1.21 \pm 0.22$	6.25	1.60
RW Tri	120.517	$27.78 \pm 44.06$	$2.11 \pm 0.07$	$0.21 \pm 0.16$	2.49	0.56
BZ Cam	149.970	$12.35 \pm 11.06$	$1.64 \pm 0.04$	$0.24 \pm 0.15$	3.91	1.90
HQ Mon	185.633	$0.90 \pm 0.75$	$1.83 \pm 0.24$	$0.20 \pm 0.00$	0.72	0.28
CM Del 1	140.299	$33.45 \pm 29.99$	$2.12 \pm 0.04$	$0.29 \pm 0.13$	4.91	1.38
CM Del 2	160.080	$138.90 \pm 50.06$	$2.14 \pm 0.08$	$0.20 \pm 0.00$	4.37	1.16
V345 Pav	96.975	$1.07 \pm 0.36$	$2.64 \pm 0.07$	$1.16 \pm 0.19$	2.78	0.54
LS Peg	76.077	$81.98 \pm 32.76$	$2.95 \pm 0.43$	$1.22 \pm 0.34$	24.0	3.41
UU Aqr	108.598	$11.31 \pm 5.78$	$2.01 \pm 0.05$	$0.82 \pm 0.24$	8.07	2.85
MU Cen	676.302	$20.50 \pm 7.66$	$1.65 \pm 0.08$	$0.20 \pm 0.00$	4.40	2.10
FO Aqr	130.204	$25.38 \pm 22.30$	$2.50 \pm 0.30$	$0.78 \pm 0.28$	9.61	1.92

Table 6.7: Parameters of the broken power law model for the LSP for the  $u'$  filter data. The percentage RMS variability given in these tables is the square root of the integral of the LSP R1 is the percentage RMS variability between  $f = 1 \times 10^{-3}$  Hz and  $f = 1 \times 10^{-2}$  Hz and R2 is the percentage RMS variability between  $f = 1 \times 10^{-2}$  Hz and  $f = 0.1$  Hz.

in the white noise level of the fitted model and the simulations.

We created a light curve with half of sampling time ( $\Delta t' = \Delta t/2$ ) and with three times the length of our data. To conserve the length of the light curve when doubling the sampling time we have to double the number of points (so,  $N' = 6N$ ). When generating a light curve with a higher sampling rate than the original data it is also important to set to zero power in frequencies above the original Nyquist frequency otherwise when interpolating there will be aliasing at high frequencies. We interpolated the middle section of the simulated light curve to our observing times. We carried out 100 simulations and averaged their LSPs. Timmer & Koenig's (1995) method uses the inverse Fast Fourier Transform (FFT) to reconstruct the light curves from a given power spectrum. We define the inverse FFT as:

$$FFT^{-1} = B \sum_{n=1}^N H_n e^{-2\pi i nk/N} \quad (6.1)$$

where  $B$  is the normalisation factor needed for consistency between the original and the simulated light curves. The inverse Fourier transform of a Fourier transform of a function is equal to the original function if we use the right normalisation. In our case we have to take into account that we changed the sampling rate and the number of points and we have the extra normalisation factor  $A$ . Here we are assuming that the data are evenly spaced and that the LSP will be equivalent to the FFT power spectrum apart from  $A$ . If we correctly calculate the Fourier sums one can prove (appendix B) that the normalisation of the simulated light curve should be:

$$B = \frac{\bar{h}}{2 \sqrt{N' \Delta t'}} \quad (6.2)$$

In Figure 6.8 we also show the LSPs of the simulations in red. We further binned the LSP and the simulations at high frequencies using equally spaced frequencies in the logarithm space for clarity of plotting. We also performed simulations of the direct least squares fitting of the LSP whose model is shown in Figure 6.6 and concluded that the

simulation of the new models are much closer to the observed LSP specially at high frequencies. Our combined filtered LSP technique can recover power spectra steeper than 2. However  $a_1$  is still underestimated because of the leakage i.e. the original power spectra had higher power than what we measure in the LSP which has leaked to the higher frequencies of the unfiltered LSP. This accounts for the fact that at low frequencies the simulation has lower power than its model. Moreover our technique does not give optimal results which in this case could only be obtained by a method similar to what was used by Done et al. (1992) and Uttley et al. (2002). They performed Monte Carlo simulations for the different coefficients covering a wide range of parameter space. Then they determined the statistical significance of each model by comparing its simulation and the real data. Unfortunately we were not able to apply their method due to time limitations. However we do not expect that the results would be very different since our method gives good initial estimates for the coefficients which were confirmed by Monte Carlo simulations and saves brute force simulations.

In Figure 6.9 we show examples of simulated light curves. These figures show that it is possible to simulate light curves very similar to the real data. This indicates that the power spectrum correctly describes the CVs and no extra information seems to be needed (such as phase). If the power spectrum of a cataclysmic variable star is a pure power law its information is limited. We can learn more from the periodogram if there are other features like periodicity's, QPOs, DNOs and breaks.

### 6.3.7 Comparison of power spectra

We will start to qualitatively compare the characteristics of the LSP of the different cataclysmic variables in the  $g'$  filter since it has the higher signal-to-noise. Later we will address the difference of the LSP for different filters. The LSPs of the CVs are reasonably well described as a broken power law. Apart from the flickering, there are some low peaks in some of the LSPs. But the only statistically significant periods are a

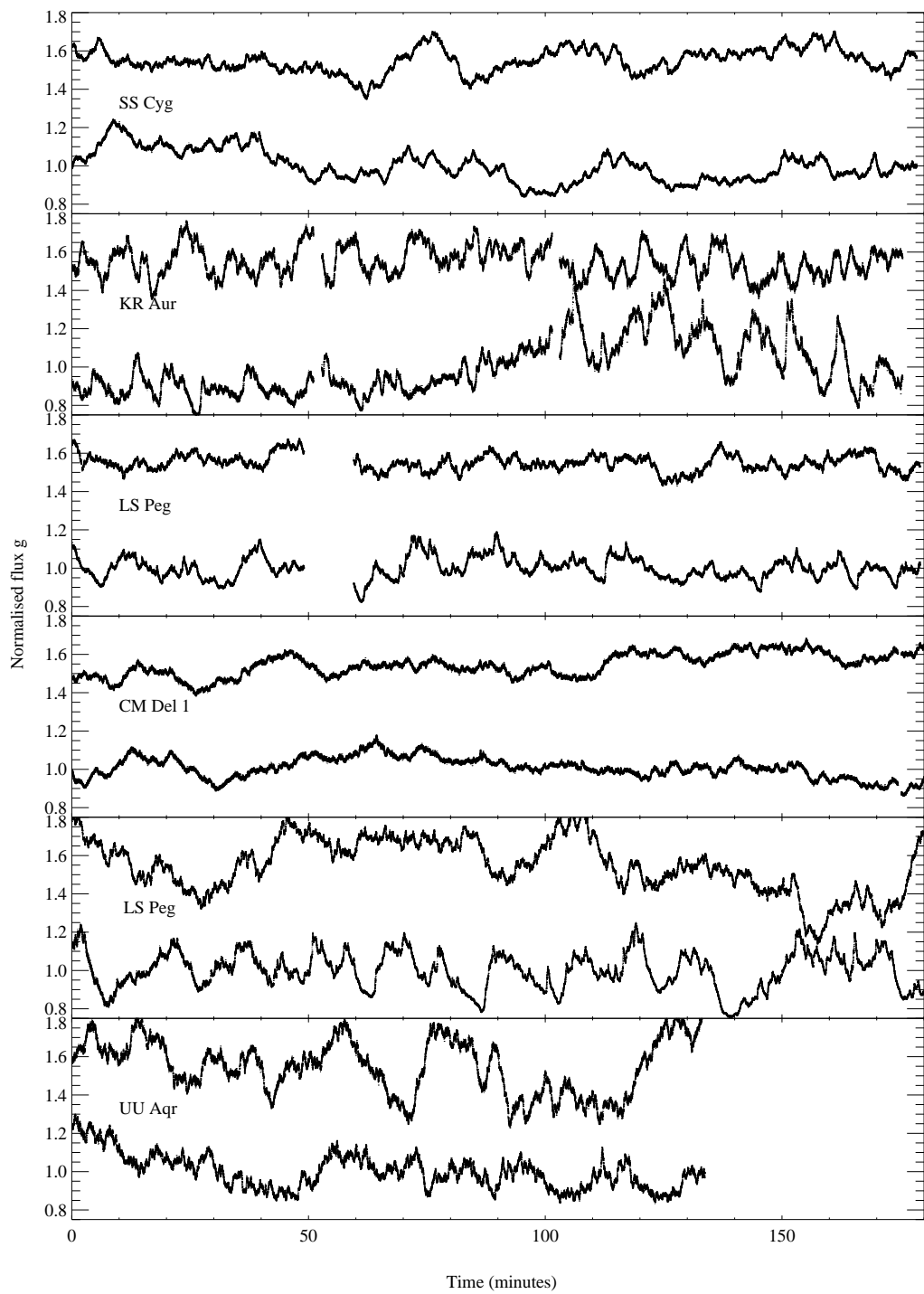


Figure 6.9: Along with the observed light curves in the  $g'$  filter in the bottom of each panel we show the simulated light curves in the top of each panel for some of the observed CVs.

30 s periodicity in RW Tri (section 6.4.1) and the known oscillations of the intermediate polar FO Aqr at 21 and 22 min, which are the respectively the spin period of the white dwarf and the beat period. The peaks are obvious in the unbinned LSP but are flattened in the binned LSP. This strong periodicity is also easily seen directly in the light curve. Other systems have reported periods in the range that we studied but the signal is lower than FO Aqr's and the corresponding peaks in the power spectrum are not easily seen.

From our CV sample, KR Aur and LS Peg (VLT observation) show the highest RMS variability (Tables 6.5, 6.6 and 6.7). The one with lowest variability is HQ Mon, as easily seen in the light curve, followed by V345 Pav. Note that the eclipsing systems have low variability power in comparison with the other CVs. This may be coincidence or might be due to self absorption by the disc in these high inclination systems. In the  $g'$  filter the power spectral index ranges from 1.75 to 3.25 with V592 Cas having the steepest LSP and MU Cen the shallowest. Note that only MU Cen has a power law index  $\alpha$  lower than two. This means that MU Cen has relatively large variability at high frequencies. Our values of the power law index are generally higher than the previous estimation of the power spectral index of CVs (for example Bruch (1992)).

Comparing the two observations of LS Peg we measure double the power in the second observation than in the first. Unfortunately, due to the steepness of the spectrum, both observations of LS Peg are affected by substantial red noise leak. This red noise leak dominates the periodogram between 0.1 and 2 Hz, as can be seen in Figure 6.8 and the filtering was not enough to completely remove the leakage. So although we confirm that with the VLT we were able to probe higher frequencies before we were dominated by photon and scintillation noise, we were not able to see any break in the power spectrum due the red noise leak. In both observing runs LS Peg has lower white noise than the other stars because it is brighter.

The second observation of CM Del was shorter (only 1 hour) due to lack of time. Therefore the break frequency is not well defined. In the second observation we

registered a slightly lower variability power in the three filters.

We measure the low frequency break for all systems except the ones where the total observation time was less than 3 hours: RW Tri (whose last part of the observation was cut due to the eclipse), HQ Mon, MU Cen and the second observation of CM Del. In these systems it is important to artificially cut off the fitted LSPs so that we don't have extra red noise leakage when we use the power law fits to obtain the simulated light curves. The power law index must flatten to  $< 1$  at low frequencies to prevent divergence of the integral giving the RMS, and we know that this happens in reality because observations on different days have similar mean levels.

In some cases our ability to determine the low frequency break can be questioned due to red noise leak. The periodicities of FO Aqr add further difficulties in measuring the frequency break in this system so the error is seriously underestimated. Other systems which have periodicities that are not significant in our study can also suffer from the same problem. Therefore we only trust values of frequency break which are higher than 0.5 mHz. This is the case for V592 Cas, KR Aur, LS Peg and UU Aqr. A low frequency break in KR Aur was previously reported by Kato et al. (2002) at  $\approx 0.4$  mHz who also measured a power law index of 1.63. The frequency breaks of LS Peg in the two observations agree within the errors which indicates that there were no changes of frequency break for the two observations contrary to what happens with the variability power

The low frequency break is perhaps a sign of the limits of the outer accretion disc. So we expect that longer period systems will have lower frequency breaks than short period systems. This correlation was reported by Zurita et al. (2003) for the case of LMXBs. Our data shows a hint of this expected correlation since we do not measure a break for systems with periods longer than 4.2 hours. However for systems in which we do measure a break we found no correlation between orbital period of the system and the break frequency. This can mean that our errors are underestimated or that the correlation if it exists, might be more complex and depend upon other parameters.

Figure 6.10 shows the LSP dependence on wavelength. We can see that the shape of the LSP of the three filters is very similar. The  $u'$  band is less sensitive so it has a higher white noise. However, the  $u'$  has approximately one and half times the overall true power of the other bands even accounting for the higher white noise level. The  $g'$  has slightly more ( $\approx 20$  per cent) power than the  $r'$  but overall the two filters are very similar. The slope of the power spectra ( $\alpha$ ) is the same for the  $r'$  and about 20 per cent shallower for the  $u'$  filter, except for V345 Pav. This indicates that the  $u'$  has more high frequency power which confirms the results of Bruch (1992). The only “notable” difference between bands is the bump in KR Aur that is only seen in the  $r'$ . We don’t know what causes it but if we divide the light curve in three sets, each set shows the extra bump in  $r'$  but not in  $g'$ .

To conclude we did not find the high frequency break as we expect but this might be due to the scintillation noise and the fact that the power spectra are steeper than was previously though. This will be discussed further in Section 6.4.3. We confirm the results of Bruch (1992) that the  $u'$  filter has more overall variability power and also that it has relatively more high frequency power than the other filters  $r'$  and  $g'$ .

### 6.3.8 Variability throughout the eclipses of RW Tri and V345 Pav

As mentioned above, eclipse mapping of the flickering has been used to locate the source of the flickering. It lead to the conclusion that the flickering originates both in the inner accretion disc and in the hot spot (Bruch 2000) with possible contributions from stream penetration and stream overflow (Baptista & Bortoletto 2004). The relative contribution of the sites depends on the system. We use our observations to test this model for higher frequencies. We analyse how the high frequency flickering varies with orbital phase for two eclipsing systems, RW Tri and V345 Pav. In both cases, we have approximately one orbit with the eclipse at the end of the light curve. Both eclipsing systems are novalikes with low amplitude orbital humps, so we expect that

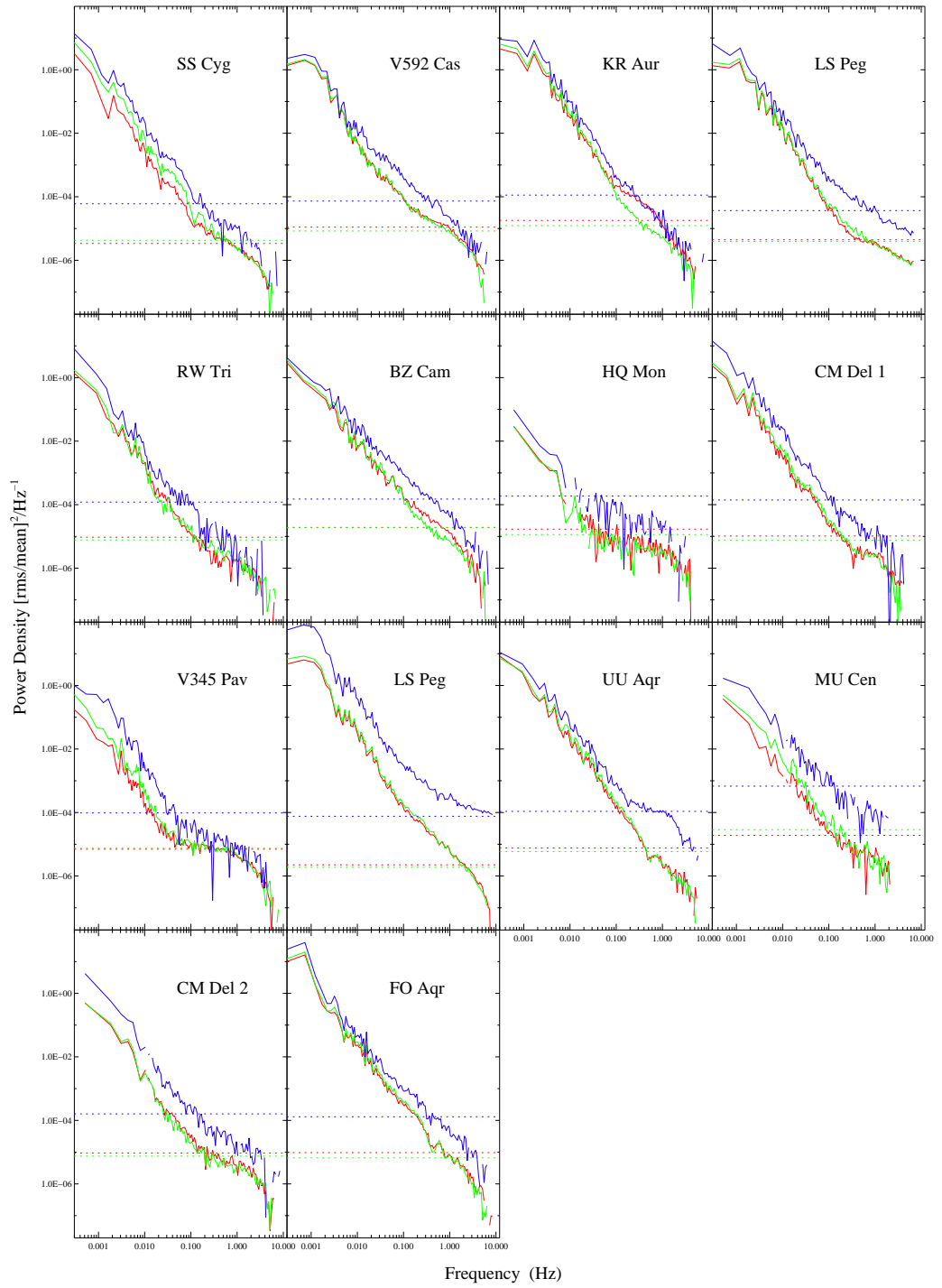


Figure 6.10: Comparison of the LSP in different filters the  $r'$  filter is shown in red, the  $g'$  filter in green and the  $u'$  filter in blue. The white noise was subtracted and its value is shown as a horizontal dashed line with the colour of the respective filter.

the inner accretion disc will dominate the flickering light. Two methods have been used to disentangle the constant light from the flickering light present in a light curve. They are called 'single' and 'ensemble' methods. For a discussion about the advantages of each method see Bruch (2000). Unfortunately since we have only single eclipses, we cannot apply either method for measuring the flickering amplitude throughout the eclipse. Instead we estimate the flickering based upon the deviation of each point from a smoothed light curve, concentrating upon high frequencies. We decided to study the flickering variability between 5 minutes and 10 seconds. As can be seen in the LSP of RW Tri and V345 Pav at frequencies higher than 0.1 Hz, we are dominated by white noise. We pass the data through a low pass filter to remove the variability on timescales shorter than 10 seconds. This was accomplished using a running mean. To remove the variability on timescales longer than 5 minutes we subtract a smooth version of the original light curve. The result is shown in Figure 6.11 and 6.12 for RW Tri and V345 Pav respectively. We show the light curve with the two smoothed versions and the residual difference for the three filters. In these figures we also show as vertical lines the minimum light and half-depth points. These points are thought to be close to the ingress and egress of the white dwarf because the eclipse is deep. This is because most of the light comes from the inner parts of the disc and the white dwarf and is roughly symmetric around it.

From the plots we can see that, for both stars, the residuals decrease considerably only between the half-depth points. The residuals in the outer halves of the eclipse are identical to the residuals out of eclipse. No asymmetry is seen in the residuals phase between the two half-depth points. The minimum of eclipse corresponds approximately to the middle of the reduction of the residuals. So we can conclude that the source of flickering is smaller than the disc but centred in the disc. In RW Tri there is a hump in the residuals that could correspond to the egress of the white dwarf. A larger number of eclipses would be needed to confirm this result. Note that the shape of the residuals near

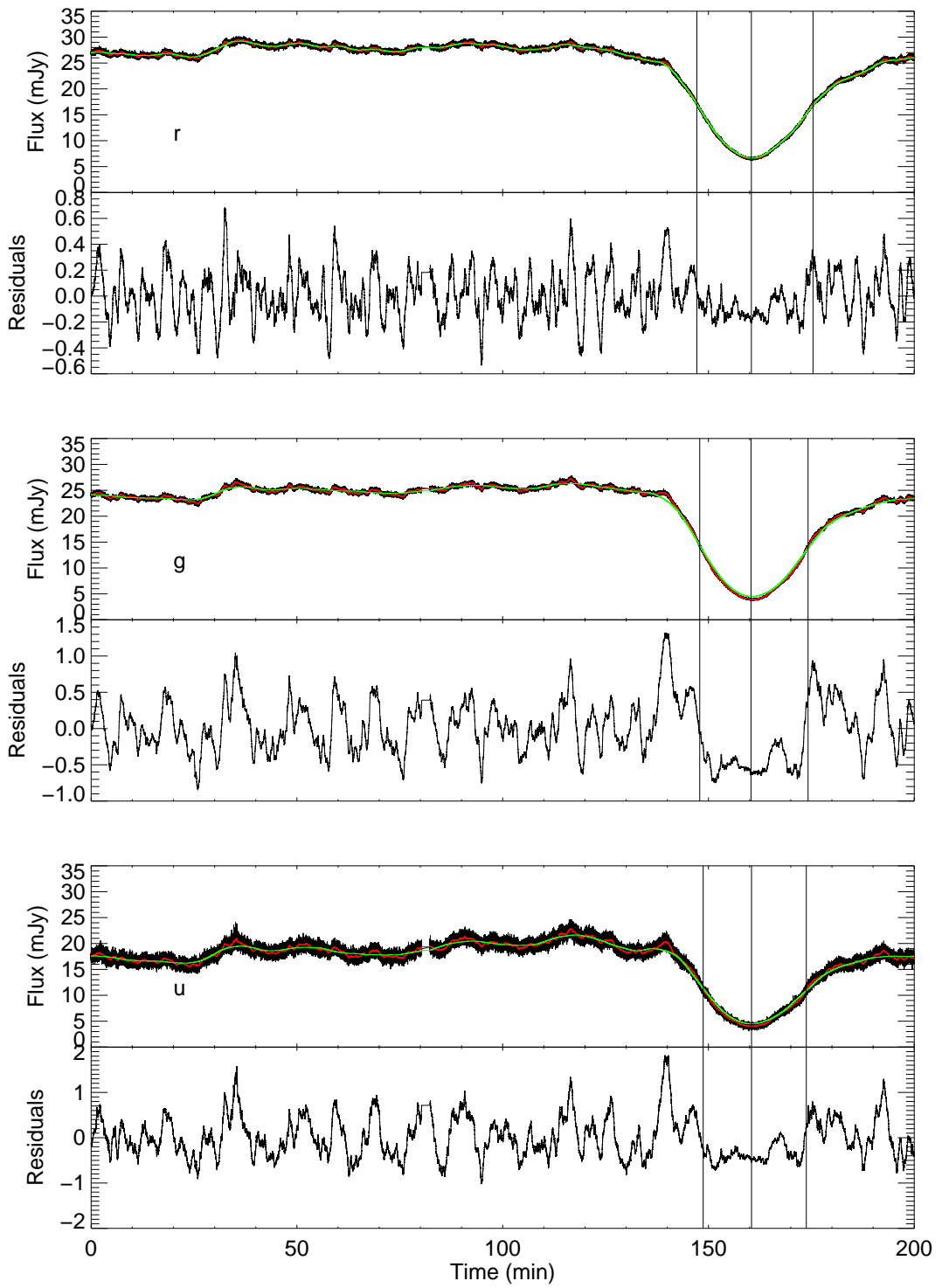


Figure 6.11: In the top panels we show the light curve of RW Tri for  $r'$ ,  $g'$  and  $u'$  filters, in the bottom panels we show the residual variability between 10 seconds and 5 minutes timescales. We also show as vertical lines the time of minimum light and the time of half-depth points.

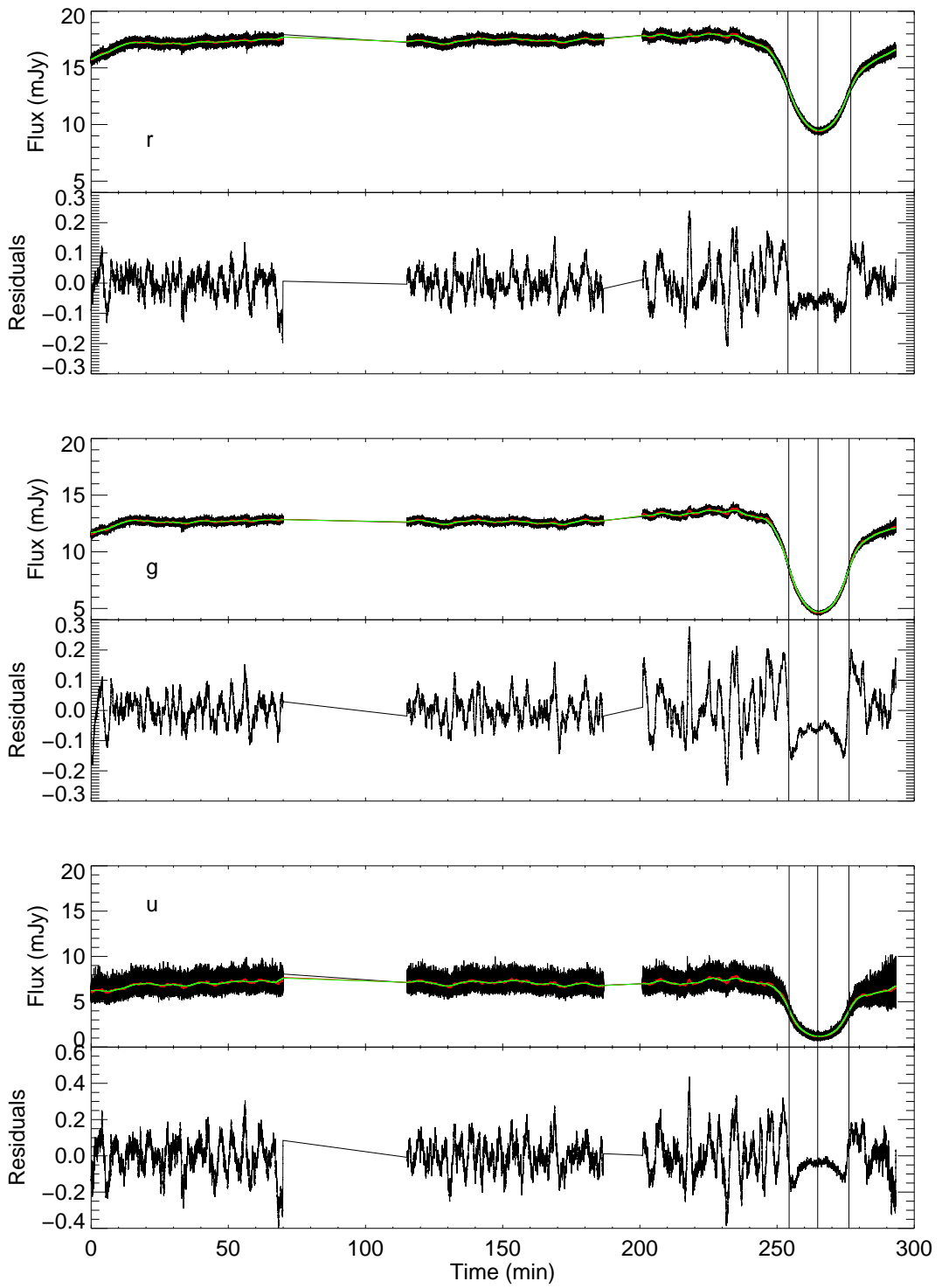


Figure 6.12: In the top panels we show the light curve of V345 Pav for  $r'$ ,  $g'$  and  $u'$  filters, in the bottom panels we show the residual variability between 10 seconds and 5 minutes timescales. We also show as vertical lines the time of minimum light and the time of half flux.

the minimum of eclipse is affected by the error in correctly accounting for the eclipse shape which again requires more examples.

We cannot see any sign of the hot spot in the light curve of V345 Pav. In RW Tri there is a increase in flux 30 minutes after the start of our observation that could be due to the hot spot becoming visible. However, there is no apparent enhancement of flickering while the hot spot is visible.

We conclude that flickering in RW Tri and V345 Pav on timescales from 10 seconds to 5 minutes comes from a region close to the white dwarf. This result does not imply that the outer accretion disc does not flicker, it could be the responsible for the variability on longer timescales or it could be outshone by the hot inner disc. These results are in agreement with previous studies (Warner & Cropper 1983; Horne & Stiening 1985; Bruch 1996, 2000; Baptista & Bortoletto 2004).

## 6.4 Discussion

### 6.4.1 Periodicities in the presence of red noise

In this section we address the issue of detection of periodicities in the presence of red noise. Several authors pointed out that in the presence of red noise there is a tendency of the eye to identify low frequency random peaks as real (for example Press (1978)). This problem can be aggravated by the use of the wrong probability distribution to estimate the significance of the peaks.

As mentioned above each independent frequency of the periodogram follows a chi-square distribution with 2 degrees of freedom,  $\chi_2^2$ . Note that to be strictly correct we should use the beta distribution instead of the  $\chi_2^2$  distribution since we do not know the true variance of the data (Schwarzenberg-Czerny 1998a). But we not include this smaller effect compared to the red noise here. In studies of periodicities it is generally assumed that our signal is a combination of white noise and a periodic signal. To

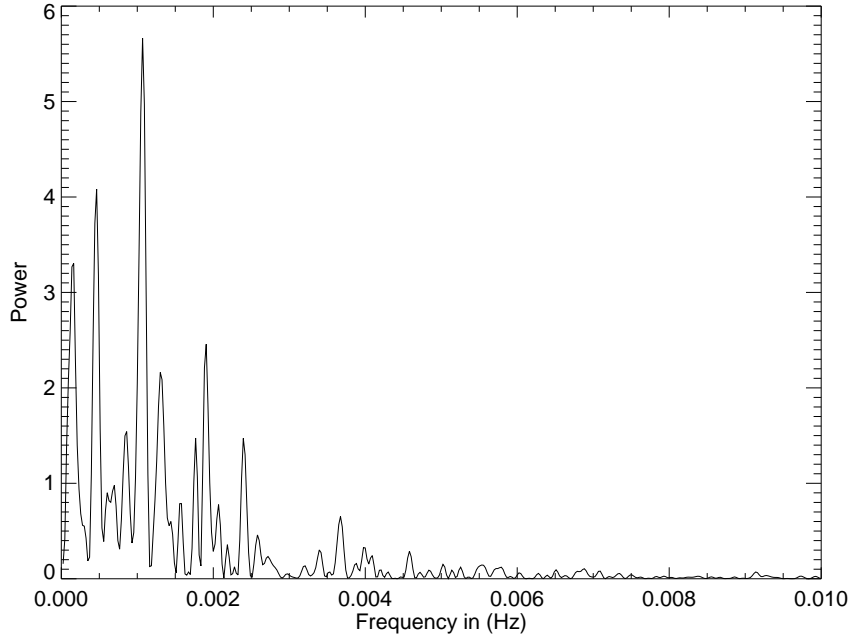


Figure 6.13: Low frequency Lomb Scargle periodogram for the  $g'$  filter of the WHT observation of LS Peg.

calculate the significance of a peak in the data we assume the null hypothesis, where the data points are independent random variables, normally distributed. If we assume white noise the probability of a peak height greater than  $z$  is:

$$P(>z) = 1 - (1 - e^{-z})^M \quad (6.3)$$

where  $M$  is the number of independent frequencies (Horne & Baliunas 1986b).

But in case that the signal has red noise, this probability has no meaning. A linear plot of the power spectrum might show, several high peaks at low frequencies that would be significant if we assume white noise but could nevertheless be noise.

We will demonstrate this with the case of our LS Peg observations. In figure 6.13 we show a linear plot of the LS Peg LSP which shows several peaks. If we assume white noise the threshold value of the false alarm probability at 99 per cent confidence level is 0.0044 and at 99.9 per cent confidence level is 0.0046 in our normalisation. So all low frequency peaks would be significant. We can go further in our analysis and note

that the second highest peak at approximately 0.0005 Hz is in fact a double peak and corresponds to the 30.9 and 33.4 minutes known periodicities of LS Peg (Table 6.2). If this peak is real then we might assume the highest peak in the periodogram which is at slightly higher frequency is also real. Although this peak might be real we will show that it is not significant.

Vaughan (2005) developed a method to calculate the significance of peaks for a power law PDS. This basically consists of de-reddening the PDS, dividing it by the best fit power law and then calculating the significance levels of any candidate peak using equation 16 of Vaughan (2005). Vaughan (2005) also presents a method for the case when the power spectrum is not a simple power law. However, these methods do not work for our case because we have a non-uniformly sampled time series and the frequencies are not independent. Hence, we use instead Monte Carlo simulations to determine the significance of a peak in the presence of red noise. Note that Monte Carlo simulations depend upon the correct assumed power law shape for the power spectra density which we can only estimate. Using a broken power law given by equation 3.31 and the fitted coefficient values of the LS Peg WHT observation given in Table 6.6 we simulated 10 000 light curves using the method explained above in section 6.3.5. We then calculated the LSP of the fake light curves and use this to calculate the false alarm probabilities at the 99 per cent and 99.9 per cent confidence levels which we show in Figure 6.14. Note that 99.9 per cent level corresponds to a detection limit of about “ $3\sigma$ ”. We conclude that none of the peaks in the LS Peg LSP is significant.

Since ULTRACAM obtains photometry in three different filters we could think that if a peak is common to more than one filter it would have a higher probability of being real. Although this is true for instrumental errors it is not true from the statistical point of view because the three filters are not independent. They are three views of the same realisation and not three different realisations. A detection in all three filters is a necessary (within the error threshold) but not sufficient condition for the detection of a

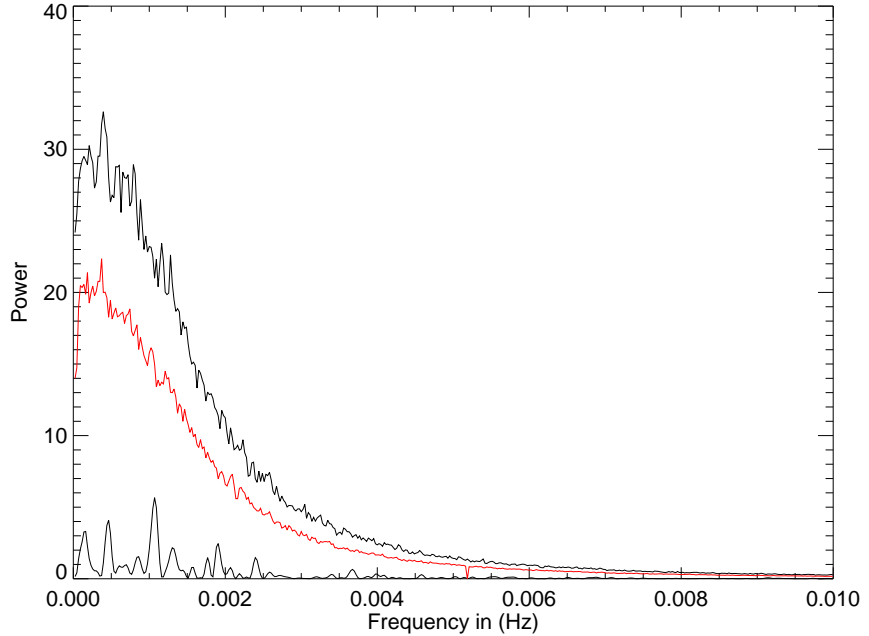


Figure 6.14: Low frequency Lomb Scargle periodogram for the  $g'$  filter of the WHT observation of LS Peg. We include the false alarm probability significance levels; the 99 per cent is shown in red and the 99.9 per cent is shown in black.

periodicity.

Ideally we should calculate the correct false alarm probabilities for all our observations to look for any real periodicities in the systems but due to the need for extensive computational time and memory requirements this is not viable for our data set. We only investigate the periodicities of LS Peg and RW Tri which are the ones that appeared more significant. Therefore we can not rule out the presence of any other periodicities in the other CVs.

We tested the peak seen in the LSP of RW Tri at  $\sim 0.03$  Hz by Monte Carlo simulations following the same procedure as above for LS Peg and using the power law parameters for RW Tri given in Table 6.6. Although the peak is seen in the three filters we choose to test the  $g'$  filter because it is the one that has higher signal-to-noise. The results of the Monte Carlo simulations are shown in Figure 6.15. We detected

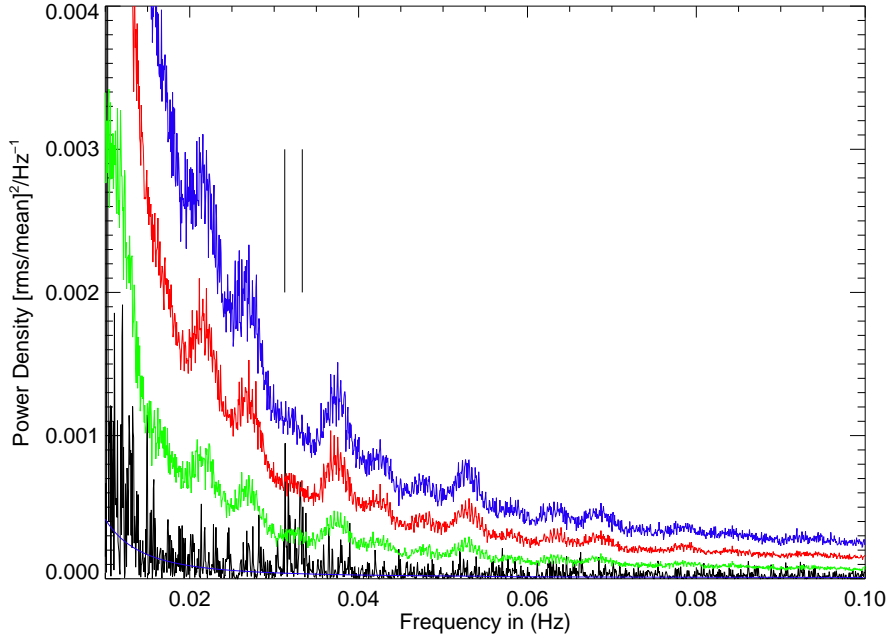


Figure 6.15: Lomb Scargle periodogram for the  $g'$  filter of RW Tri. We also show the significance levels of the false alarm probability at 90% in green, 99% in red 99.9% in blue. The vertical lines show the position of the significant peaks. The power spectrum model used in the simulations is shown as blue solid line below.

two periodicities which we call  $f_1$  and  $f_2$  which are both significant at 99 per cent confidence level. This corresponds to periods of  $31.8 \pm 0.4$  s and  $30.1 \pm 0.3$  s respectively. These periods are on the borders of quasi-periodic oscillations (QPOs) and dwarf novae oscillations (DNOs).

We applied least squares fitting to the logarithm of the LSP as before but we add a Lorentzian model to the power law model to describe the peak. The power law parameters were kept fixed to the values of Table 6.6. We define the Lorentzian as:

$$\frac{a_2}{(f - f_0)^2 + (\lambda/2)^2} \quad (6.4)$$

where  $f_0$  is the frequency of the peak,  $\lambda$  is FWHM of the peak and  $a_2$  is the height of the peak. The fitted parameters of the Lorentzian for each peak are given in Table 6.8 where we also give the quality factor and coherence time of the peaks. Since the peaks

Peak	$f_0$ Hz	$\lambda$ mHz	$a_2$ $\left[ \frac{\text{RMS}}{\text{mean}} \right]^2 / \text{Hz}$	$Q$	$\tau$ s
1	$0.0315 \pm 0.0004$	$0.8 \pm 0.6$	$3 \pm 2 \times 10^{-11}$	$42 \pm 30$	$425 \pm 95$
2	$0.0332 \pm 0.0003$	$0.6 \pm 0.1$	$4 \pm 1 \times 10^{-11}$	$55 \pm 2$	$530 \pm 28$

Table 6.8: Fitted parameters of the Lorentzian model for the peaks of RW Tri in the  $g'$  filter.

have very low coherence time we conclude that they are high-frequency QPOs and not DNOs. As far as we know these periodicities have never been seen in RW Tri.

We further investigated the QPOs using a sliding periodogram and concluded that in the beginning of our observation there is a periodicity in the light curve at  $\sim 0.033$  Hz which disappears and gives place to a periodicity at a higher frequency  $\sim 0.036$  Hz. The latter has relatively high amplitude but due to its low coherence time it is not significant. When this peak disappears a new periodicity appears at a lower frequency  $\sim 0.031$  Hz. All periodicities disappear during eclipse.

QPOs and DNOs have been observed in many CVs (Warner 1995, 2004). The DNOs have periods of 6–380 s and the QPOs have periods of 30–5000 s with much lower coherence than DNOs. Sometimes both DNOs and QPOs are present in a light curve. Warner (2004) presents a model where DNOs and QPOs are related phenomena and connected with the magnetic nature of the primary star. In these systems the primary star would have a lower magnetic field than IPs but depending upon the accretion rate could be able to magnetically channel accretion producing DNOs and could give rise to travelling waves that would produce the QPOs.

#### 6.4.2 The steepness of the power spectrum

As we have seen in Section 6.3.5 the power spectrum of the CVs we observed are steeper than we expected and what has been previously reported, resulting in leakage. We suspect that other studies of flickering in CVs might have been equally affected by red noise leak, particularly studies with a large number of systems like Bruch (1992) and

Fritz & Bruch (1998) where it would be difficult to control the fits for every system. For example Bruch (1992) measures power law indices between 1.42 (EX Hya) and 2.8 (AE Aqr). The lower values might have been underestimated. To obtain  $\alpha$ , Bruch (1992) fitted the PDS with a pure power law using least squares fitting for frequencies between 0 and 0.025 Hz. Bruch (1992) admits that a poorly defined low frequency break which he calls a hump can influence the measure  $\alpha$  and will explain his values of  $\alpha$  lower than 2. We do not know how he obtained power law values higher than 2. As seen in section 3.6 a power law model steeper than 2 will always show an power law index lower than 2 due to red noise leak, even for long baselines. Note that his data have different total observation times. For example, for SS Cyg his observations range from one hour to five hours. His measured  $\alpha$  for SS Cyg is between 1.96 and 2.64, this can be due to real variations in power spectra shape or reflect a different power spectral slope at different frequencies that can be real or not, as the example of V592 Cas shows. But probably  $\alpha$  is closer to 2.64 which agrees with our results and the lower estimates only reflect the red noise leak.

Apart from the extra noise due to photon noise, scintillation and red noise leak, there is nothing else in the power spectrum of the CVs studied except a red noise power law from  $f = 2 \times 10^{-4}$  Hz up to a frequency of approximately 0.5 Hz where the noise starts to dominate the power law. This was surprising, since as already mentioned above we expected a high frequency break, if there was not so much extra noise. In the next section we will investigate the timescales present in accretion discs and compare it with our results for the observed CVs.

### 6.4.3 Timescales of the flickering

As mentioned above the flickering in CVs can originate either in the mass transfer stream (hot spot, stream penetration and stream overflow) or the accretion disc. The hot spot flickering is reported to be on timescales of the order of minutes (Baptista &

Bortoletto 2004) which is in agreement with the theoretical models (Bruch 1992; Bath et al. 1983a,b). This is longer than the timescales of flickering in the disc which can range between tenths of seconds to minutes.

We will focus on the high frequency flickering which originates in the disc. The critical timescales of accretion discs are the dynamical, thermal and viscous timescales (Pringle 1981). We follow the estimation of timescales from Bruch (1992) and we will start by defining the dynamical frequency that is given by:

$$\tau_{dyn} = 2\pi \sqrt{\frac{r^3}{GM_1}} = \frac{2\pi}{\Omega} \quad (6.5)$$

where  $\Omega$  is the angular velocity at the radius  $r$ .

If the source of flickering is magnetic discharges in the accretion disc, the flickering timescale would be the shearing timescale, which corresponds to a gradual release of energy in the flare and is given by Eq 4 of Burn & Kuperus (1988):

$$\tau_{sh} = \frac{4\pi}{\Omega} = 2\tau_{dyn} \quad (6.6)$$

If we assume the model of King et al. (2004) for the flickering, the relevant timescale is local magnetic alignment timescale  $\tau_{mag}$ . This depends upon the probability that the magnetic field of the neighbouring annulus at the radius  $r$  is aligned ( $\tau_d(r)$ ) which is parameterised as  $\tau_d(r) = k_d\Omega^{-1}$ .  $k_d$  is determined by the physics of the disc and is always much higher than 1. The local magnetic alignment timescale is given by (Livio et al. 2003):

$$\tau_{mag} \sim \tau_d 2^{r/H} = \frac{k_d 2^{r/H}}{\Omega} = k_d 2^{r/H} \tau_{dyn} \quad (6.7)$$

where  $H$  is the vertical height of the disc. Therefore, it is always longer than the dynamical timescale.

If the source of flickering is turbulence in the accretion disc, the timescale for the turbulence is given by the viscous time scale (Pringle 1981):

$$\tau_{vis} = r^2/\nu \quad (6.8)$$

where  $\nu$  is the viscosity. For an  $\alpha$  disc, the viscosity is parametrised as  $\nu = \alpha c_S H$ . Where  $c_S$  is the speed of sound. In this case, the viscous timescale can be written as:

$$\tau_{vis} = \left[ \frac{r}{H} \right]^2 \frac{\tau_{dyn}}{\alpha} \quad (6.9)$$

Hence also the viscous timescale is much longer than the dynamical timescale.

Therefore we conclude that the shortest timescale is the dynamical timescale so we expect a decrease in power for frequencies higher than the inner accretion disc frequency. Hence the power spectrum should show a break at this frequency. For non-magnetic systems and for a thin boundary layer, the inner accretion disc radius is approximately the radius of the white dwarf. Hence, the highest frequency in an accretion disc is:

$$f_{max} = \frac{1}{2\pi} \sqrt{\frac{GM_1}{r_{WD}^3}} \approx 1.839 \sqrt{\frac{m}{r_6^3}} \text{Hz} \quad (6.10)$$

where  $m$  is the white dwarf mass given in solar masses and  $r_6 = r_{WD}/10^6 m$ .

If we assume Eggleton's mass-radius relation quoted by Verbunt & Rappaport (1988), the maximum frequency is only dependent on the mass of the white dwarf. The dependence of the maximum frequency upon the white dwarf mass is shown in Figure 6.16. For all systems we expect a break frequency between 0.01 and 1 Hz. So we would expect to see this break in our power spectrum.

We see no break in the power spectrum for any of the CVs studied. This is probably due to the steepness of the spectrum. Since we expected a much shallower power spectrum we overestimated the real power at high frequencies. Given the new values of the power spectra slopes we can conclude that we are dominated by the white noise at 0.01–0.5 Hz depending upon the system. This restricts the possibility of finding a break to very under-massive white dwarfs in bright systems. Moreover we can not rule out that a break is hidden by the extra power at high frequencies due to red noise leak and scintillation.

To conclude, due to noise we can not rule out the existence of frequency breaks

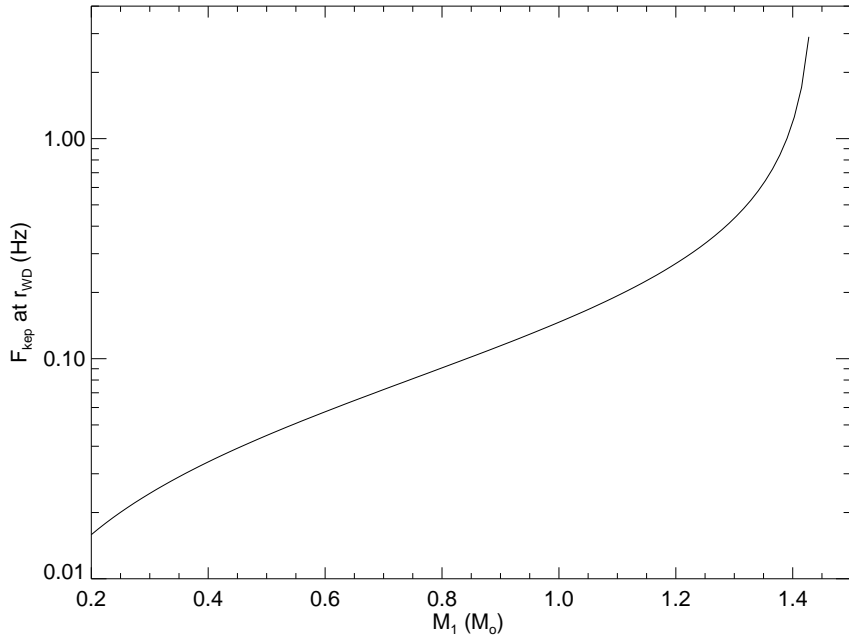


Figure 6.16: Dynamical frequency at the radius of the white dwarf as a function of the white dwarf mass.

as predicted by equation 6.10. There is no strong evidence for any feature in the power spectra of CVs corresponding to the timescale of the inner disc expect for the QPOs of RW Tri. From figure 6.16 we can conclude that these have periods close to the dynamical timescale at the surface of a  $0.36 M_{\odot}$  white dwarf. RW Tri's white dwarf mass was reported by Smak (1995) to be  $0.45 \pm 0.15 M_{\odot}$ . So the periodicities come from a region very close to the white dwarf surface. If we assume that the dynamical timescale is really the shortest timescale in the accretion disc this further restricts the white dwarf mass to be higher than  $0.36 M_{\odot}$ .

#### 6.4.4 Comparison with Soft X-ray Transients

Soft X-ray transients (SXTs) are a type of low-mass X-ray binary that are normally in quiescence but occasionally show optical and X-ray outbursts. These outbursts have recurrence times of decades and typically last for months. They are thought to have

similar origin to dwarf nova outbursts. Low mass X-ray binaries (LMXBs) have different properties than CVs because the much higher accretion rates together with the deeper potential well means that the inner accretion disc emission is strong in X-rays. The optical emission in LMXBs is powered mainly by the reprocessing of X-rays (van Paradijs & McClintock 1995) which irradiate the accretion disc and drive its evolution. However in quiescent SXTs the optical flux is too high to be explained by reprocessing of X-rays alone (Hynes et al. 1998; Kanbach et al. 2001; Zurita et al. 2003; McClintock et al. 2003). They have very low accretion rates and are similar to cataclysmic variables although their primary stars are black holes or neutron stars instead of white dwarfs. The higher mass of the primary star basically has two consequences: The first is that the companion star can be more massive than the companion star of CVs (they can also have evolved companions), so in general their orbital periods are longer. The second is that the potential well is deeper and the inner accretion disc is hotter, emitting X-rays. In quiescence their optical luminosity is dominated by variability from the accretion disc, the hot spot and light from the companion star (van Paradijs & McClintock 1995) which shows ellipsoidal modulation (e.g. Haswell (1996) and Shahbaz et al. (2003)). The inner accretion disc is thought possibly to be truncated with either a quasi-spherical inflow at small radii which emits inefficiently called an advective dominated accretion flow (ADAF) (Narayan et al. 1996), a magnetised corona (Galeev et al. 1979; di Matteo et al. 1999) or the base of a jet (Markoff et al. 2001; Gallo et al. 2006).

To conclude SXTs are in some ways scaled versions of the CVs. Although the inner accretion discs of SXTs and CVs are different, their cooler outer accretion discs are presumably very similar. So if the flickering comes from the outer regions of the accretion disc, it should have similar properties in both objects. We will test this hypothesis by comparing the flickering in CVs and the flickering of quiescent X-ray binaries.

Two black hole X-ray transients were also observed with ULTRACAM mounted on the WHT so they are ideal as comparisons. V404 Cyg was observed in September

2002 (Shahbaz et al. 2003). It has a orbital period of 6.473 days (Casares et al. 1992). XTE J1118+480 was observed in June 2003 (Shahbaz et al. 2005) and it has the shortest orbital period for SXTs of 4.08 hours (Zurita et al. 2002). However, due to the faintness of both targets, the time resolution of these observations is much lower than our observations of the CVs. V404 Cyg was observed with sampling rate of 0.2 Hz in the  $g'$  and  $i'$  bands ('slow' data) and at 4.2 Hz in the  $i'$  band ('fast' data). XTE J1118+480 was observed at a sampling rate of 0.086 Hz in the  $g'$  and  $i'$  bands ('slow' data) and at 0.61 Hz in the  $i'$  band ('fast' data). Due to the light from the companion stars these objects are much redder than CVs. So the signal to noise ratio is higher for the  $i'$  band. The low signal-to-noise of the 'fast'  $g'$  band and  $u'$  band data makes them not usable. In Shahbaz et al. (2003) and Shahbaz et al. (2005) the authors computed the power density spectrum using the same method (LSP) and the same normalisation as ours. So we can directly compare our results. Just to confirm that our methods were exactly the same we re-reduced the V404 Cyg data of the 10<sup>th</sup> of September 2002. We follow the authors approach and remove the contaminating star contribution. Since our particular observation corresponded to orbital phase 1, we approximate the ellipsoidal modulation by a constant. Shahbaz et al. (2003) removed a physical model of the ellipsoidal modulation so their results are more accurate than ours, but for comparison purposes our approximation is good enough. The  $g'$  and  $i'$  light curves of V404 Cyg are shown in Figure 6.17. We can see that the light curve of V404 Cyg is more spiky than the light curves of CVs shown in Figure 6.1. This can also be seen if we directly compare our CV light curves with the light curves of these objects given in Shahbaz et al. (2003) and Shahbaz et al. (2005).

We applied the same method to compute and fit the LSP of V404 Cyg as original carried out for the CVs (section 6.3.5), since here we were not affected by red noise leak. However, in this case, we fitted a simple power law instead of a broken one because the power spectrum shows no sign of a low frequency break. If we assume that the

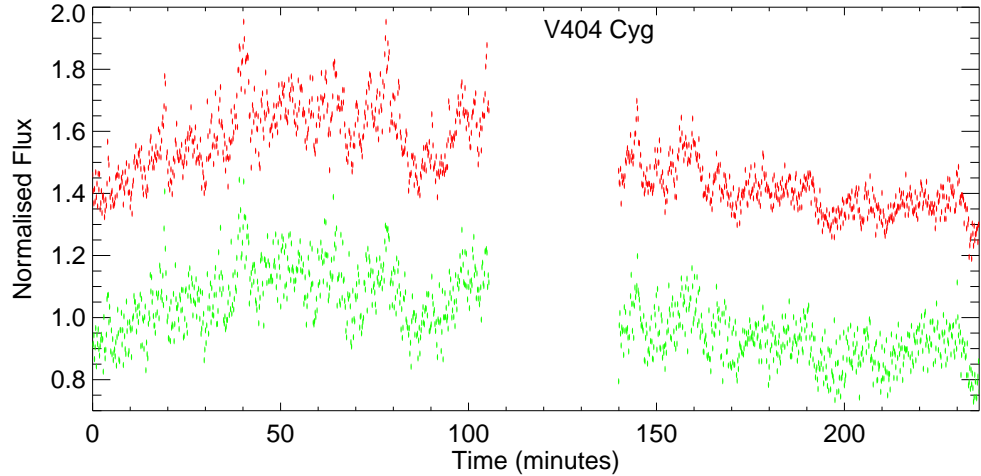


Figure 6.17: Light curves of the V404 Cyg with 10 seconds binning. The top red is the  $i'$  filter light curve, the bottom green is the  $g'$  filter light curve. The flux is normalised to unity and the  $i'$  filter was displaced vertically by 0.15 for clarity.

low frequency break is related to the radius of the outer disc we expect that the low frequency break in SXTs is at lower frequencies than in CVs. Moreover since at this lower sampling rate we are not affected by scintillation noise we used all the points of the LSP for the fit. The fitted parameters are given in Table 6.4.4. The power law indices can be compared with the values obtain in Shahbaz et al. (2003) which are 1.23 for the  $g'$  filter and 1.56 for the  $i'$  filter. Our value of the  $\alpha$  the in  $i'$  filter is lower than was previously obtained and could be due to our incorrect removal of the ellipsoidal variation or difference in the reduction procedure. Our normalisation indeed matches the one used by Shahbaz et al. (2003) so we conclude that our results can be directly compared. The lower time resolution of the V404 Cyg data does not allow calculation of the percentage RMS variability  $R2$  for the higher frequency interval  $f = 1 \times 10^{-2}$  Hz and  $f = 0.1$  Hz so we only calculated  $R1$  which corresponds to frequencies between  $f = 1 \times 10^{-3}$  Hz and  $f = 1 \times 10^{-2}$  Hz and its given in Table 6.4.4. The value of  $R1$  for V404 Cyg is similar to  $R1$  of the higher variability CVs. However flickering power for the CVs is a lower limit since the contribution of the secondary star was not removed, contrary to V404 Cyg.

Filter	$10^6 w$	$a_1$	$\alpha$	R1 % RMS mean
$i'$	217.282	$0.09 \pm 0.04$	$1.36 \pm 0.08$	4.43
$g'$	3517.407	$0.11 \pm 0.07$	$1.28 \pm 0.10$	3.69

Table 6.9: Fitted parameters for power law model for the LSP for the  $i'$  and  $g'$  filter data of V404 Cyg. The power is the square root of the integral of the LSP, R1 is the percentage RMS variability between  $f = 1 \times 10^{-3}$  Hz and  $f = 1 \times 10^{-2}$  Hz.

We can conclude that V404 Cyg's LSP is much shallower than any of the CVs observed, although the steepness of the spectra varies by as much as 20 per cent for observations on different days. This also happens for the two observations of LS Peg. Shahbaz et al. (2003) compared their results and other LSPs of quiescent SXTs ( $\alpha = -1$  to  $-1.52$  from Zurita et al. (2003) and Hynes et al. (2003)) with the slopes of the power spectrum of CVs reported by Bruch (1992). They concluded that the slopes of the LSPs in quiescent dwarf novae are generally steeper than those of SXTs. Since we obtained a higher value for the slopes of CVs than Bruch (1992) this conclusion is now stronger. A direct comparison of the LSP of V404 Cyg and of SS Cyg is given in Figure 6.18. At frequencies below the QPO feature at 21.5 min which was reported by Shahbaz et al. (2003) the LSPs of both objects are very similar over the low frequency range. A wider frequency range would be needed for a more definitive conclusion. For higher frequencies the slopes clearly diverge until the LSP of V404 Cyg is dominated by the white noise. This implies that the flickering in these two systems has different origins. Shahbaz et al. (2003) argues that the large flares in V404 Cyg are produced in the outer accretion disc. They also propose that the 21.5 min QPO comes from the transition zone between the optical thin outer disc and the inner region. The flares colour is consistent with optically thin gas at temperature of 8000 K. In this interpretation there would be a correspondence between the frequency of a flare and the radius at which it was produced. A similar result was obtained by Uemura et al. (2004) for V4641 Sgr which reports that the origin of the longer flares is thermal while the origin of the shorter flares is non-thermal.

If we assume the QPO features at 21.5 min ( $f=7.75 \times 10^{-4}$  Hz) corresponds to the boundary between the accretion disc and the inflow region and if we also assume a relationship between the frequency and radius where the flare is produced, we conclude that the outer accretion discs of SXTs and CVs are indeed similar but the inner accretion disc is different. The optical coming from the inner region cannot have thermal origin since the optical thermal emission expected from the inner parts of the accretion disc is too feeble (Merloni et al. 2000; McClintock et al. 2003; Uemura et al. 2004). Instead the optical is thought to be produced by synchrotron radiation in a ADAF region, a corona or a jet. Although we cannot distinguish between the models that produce the optical we can conclude that the inner accretion region of SXTs has more relative high frequency variability than the inner accretion discs of CVs.

Shahbaz et al. (2005) concluded that the LSP of XTE J1118+480 is only slightly shallower than the CVs if we assume the power law plus QPO model while if we assume a broken power law model the LSP is steeper than 2 and indistinguishable from the CVs. But this high value of the power law index is not typical of SXTs and is also not typical of XTE J1118+480. We searched in the literature for published power law slopes of SXTs which we show in Table 6.10, where we also include the results reported above from Shahbaz et al. (2003) and Shahbaz et al. (2005). We will only consider measurements of the power law slopes in quiescence because we do not know if the power spectra slope changes in outburst. As mentioned above some SXTs continue in the low/hard state even in outburst. Tomsick et al. (2004) reports that in the low/hard state of XTE J1650-500, the power spectrum maintains its shape over a large range of luminosities while the luminosity drops to quiescence although the characteristic frequencies significantly decrease. Even if this is confirmed, the systems that reach the high/soft state in outburst might change their power spectral shape as happens in persistent LMXBs. Due to the low luminosity of the SXTs in quiescence, the timing properties of only a small number could be studied.

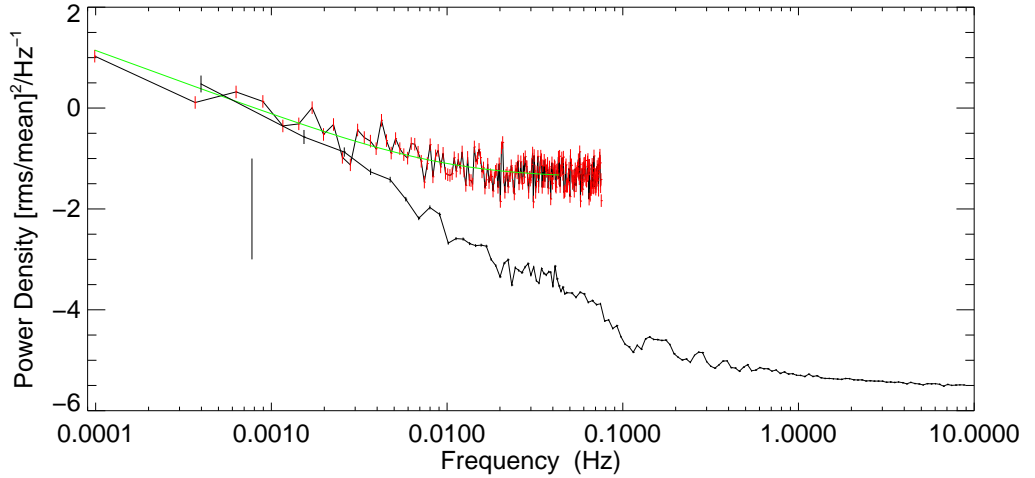


Figure 6.18: Comparison of the LSP of the  $g'$  filter of V404 Cyg (green) and SS Cyg after removing the ellipsoidal modulation for V404 Cyg. The vertical line shows the position of the 21.5 min QPO feature reported by Shahbaz et al. (2003).

As shown in Table 6.10, all the SXTs have power law indices less than 1.6 except for the XTE J1118+480 observation by Shahbaz et al. (2005). The mean value of the power law slope is 1.43 (where we exclude GS2000+25 whose value is an indication of white noise dominance (Zurita et al. 2003)). This compares with our mean value of the power law slopes of CVs in the  $g'$  filter of  $\sim 2.4$  (Table 6.6). So we conclude that SXTs LSP are generally shallower than the LSP of the CVs, or in other words the SXTs show more high frequency flickering.

This suggests that the inner region of SXTs is also a source of optical variability (Motch et al. 1982; Fabian et al. 1982; Hynes et al. 1998; di Matteo et al. 1999) which can not have thermal origin. In this case the optical is thought to come from non-thermal synchrotron radiation (Uemura et al. 2004) either in the ADAF region (Narayan et al. 1996), in the magnetic corona (Galeev et al. 1979; di Matteo et al. 1999) or in the jet (Markoff et al. 2001; Gallo et al. 2006). Gallo et al. (2006) argues that only composite models with ADAF+jet and corona+jet or models where the inner disc is the base of a jet can explain the observed outflow in quiescence. Furthermore emission from

SXTs	filter	$\alpha$	$f_b$	RMS	Reference
			(mHz)		
GX 339-4	WL	$1\pm0.1$			Motch et al. (1982)
J0422+22	WL	$1.14\pm0.01$			Zurita et al. (2003)
J0422+32	IR	0.9			Reynolds et al. (2007)
A0620-00	V	1.52	0.95	0.06	Hynes et al. (2003)
A0620-00	WL	$0.99\pm0.01$			Zurita et al. (2003)
GS2000+25	WL	$0.28\pm0.01$			Zurita et al. (2003)
V404 Cyg	R	$0.99\pm0.09$			Zurita et al. (2003)
V404 Cyg	$g'$	$1.12\pm0.2$		3.7 %	Shahbaz et al. (2003)
V404 Cyg	$i'$	$1.46\pm0.2$		4.4 %	Shahbaz et al. (2003)
Nova Mus 1991	V	1.56	$>0.3$	0.06	Hynes et al. (2003)
XTE J1118+48	optical	1.36??	0.3	13 %	Malzac et al. (2003)
XTE J1118+48	$g'$	$2.9\pm0.3$	$1.0\pm0.7$		Shahbaz et al. (2005)
XTE J1118+48	$i'$	$2.3\pm0.2$	$1.9\pm0.3$		Shahbaz et al. (2005)

Table 6.10: Published optical and infrared variability characteristics of SXTs in quiescence

the jets has been reported to extend from radio to the infrared (Fender 2001; Fender et al. 2003) and even to the optical (McClintock et al. 2001; Chaty et al. 2003).

As mentioned above, in quiescence SS Cyg is thought either to have an optically thin accretion disc or an inner region similar to SXTs (ADAF or corona) (Mahasena et al. 2001; Meyer & Meyer-Hofmeister 1994). Our comparison of power spectra favours the optically thin accretion disc model for SS Cyg since it does not show a change in the power spectrum slope as it happens in the SXTs.

#### 6.4.5 Flares in M stars

We use ULTRACAM observations of EQ Peg B (Mathioudakis et al. 2006) which is a known flare star to compare its flares with the flickering of CVs. The observations were taken in the 4<sup>th</sup> of November 2003 with ULTRACAM mounted on the WHT. We have approximately four hours of observation with a time resolution of 0.073 s in which we observed 3 flares. Unfortunately, the second flare is quite small and was affected by clouds so its colour might be distorted. We applied the same reduction techniques

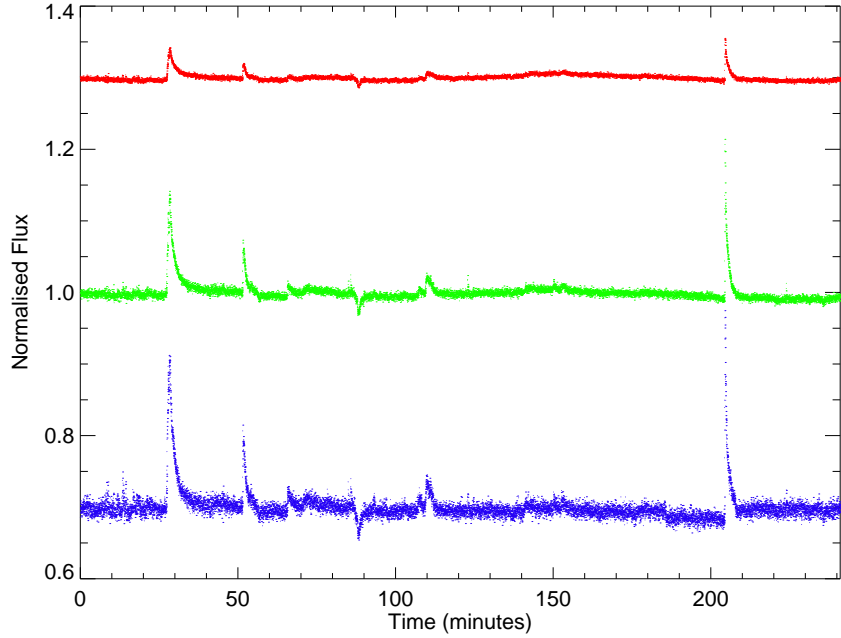


Figure 6.19: Light curve of EQ Peg B binning to 1 second. The flux was normalised and was divided by 10 for the  $u'$  band. The  $r'$  filter is shown in red and was displaced upwards by 0.3. The  $g'$  is shown in green and the  $u'$  is shown in blue and was displaced downwards by 0.3 for clarity.

as for the CVs observations and obtained a calibrated light curve which is shown in Figure 6.19. We obtained mean magnitudes of  $11.7 \pm 0.11$  in  $r'$ ,  $13.20 \pm 0.12$  in  $g'$  and  $15.79 \pm 0.43$  in  $u'$ .

We are mainly interested in studying the colours of the flares. We show the flux ratio diagram of EQ Peg B flares in Figure 6.20 for comparison with Figure 6.4. Since in this case we have separate flares and a constant continuum it is more instructive to plot directly each flare than the colour-coded 4 flux levels. The flux ratio of EQ Peg B in quiescence is consistent with that of a M4 star ( $F_r/F_g = 4.0$  and  $F_u/F_g = 0.1$ ) as expected. A zoom of Figure 6.20 is shown in Figure 6.21.

We confirm the well known correlation between  $\Delta U$  and the U-V colour for stellar flares. In these figures we can see that EQ Peg B flares follow the same type of track in the flux ratio diagram as the flickering in CVs. If we considered only the last and

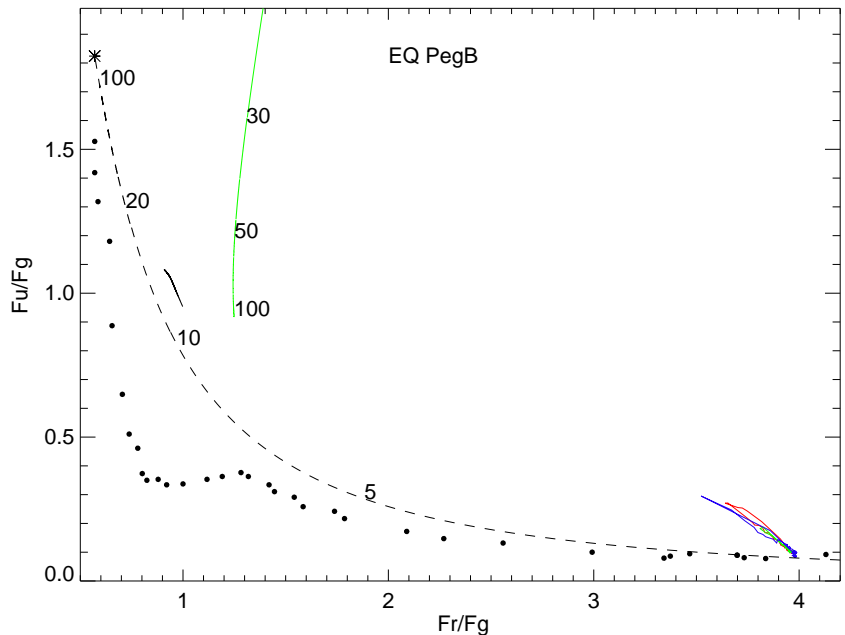


Figure 6.20: Flux ratio diagram for EQ Peg B. The first flare is shown in red, the second in green and the third and last is shown in blue. The main sequence is shown as dots with the O stars at the top left and the M stars at the lower right. The back dash line shows the position of black bodies. The green solid line shows colours of optically thin emission. The temperatures are marked in units 1000 K. The back solid line shows colours of accretions discs with accretion rates of  $10^{-10} M_\odot \text{ yr}^{-1}$  to  $10^{-8} M_\odot \text{ yr}^{-1}$ . The points were binned to 10 seconds. The flare region will be zoom in Fig. 6.21.

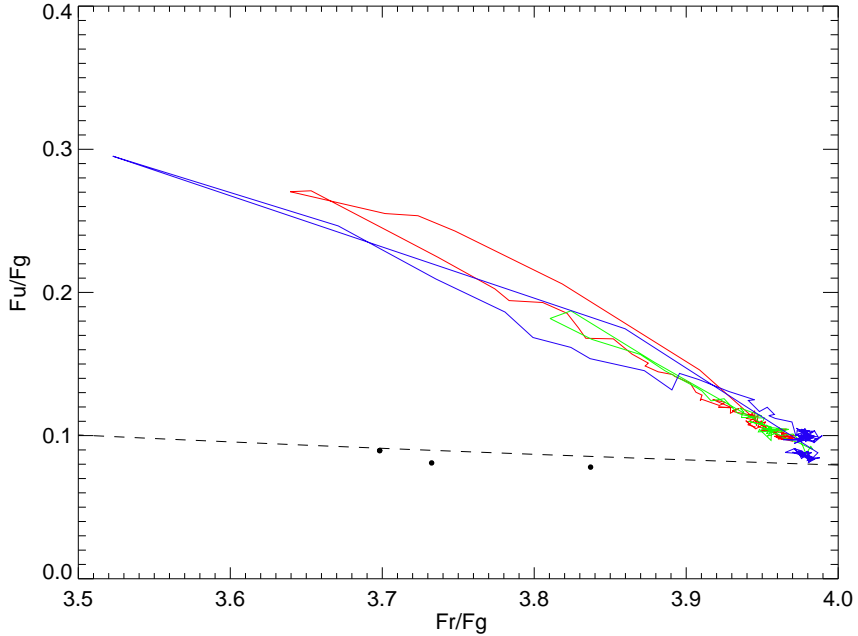


Figure 6.21: Flux ratio diagram for EQ Peg B. Zoom of the flares shown in Fig. 6.20.

strongest flare we would not be able to distinguish if the flare material was optically thick or optically thin. However, the first flare is smaller which implies a lower temperature and its colours are only consistent with optically thin emission. So we conclude that the two flares were produced by optically thin emission. The first flare reaches a temperature of  $\approx 30\,000$  K and the third and last flare reaches a temperature of  $\approx 50\,000$  K.

### Shape of Flares

The classical definition of a flare, which is a rapid rise to maximum followed by a quasi exponential decline has long been defined (Bopp & Moffett 1973). Higher time resolution of flares show that they are more complex than previously thought. Some flares appear to have two components one of which has a quasi-exponential decline that comes from the flare itself and extra emission from material that was heated by the flare, which has a slower decay time. Depending upon the angle of observation, the combination of the two components can give rise to different flare morphologies (Kunkel 1967; Tovmassian

et al. 2003).

In accreting systems the situation is even more complex since we do not see single flares. Instead the light curve is the result of the superposition of flares which can be composed of flares with different shapes and sizes. Statistical methods have been used to derive the size and shape of the flares (Priedhorsky et al. 1979; Miyamoto & Kitamoto 1989; Maccarone et al. 2000; Maccarone & Coppi 2002; Malzac et al. 2004) but often they just test existing models and assume the shape of shots and do not focus the on physical mechanism that produces the flares (Priedhorsky et al. 1979; Miyamoto & Kitamoto 1989; Maccarone et al. 2000).

The flares we observed in EQ Peg show a rapid rise followed by an quasi-exponential decline like the classical definition of flare. However, for example just the day before our observation a different morphology flare was seen (Mathioudakis et al. 2006) which resembles some of the CVs larger flares (Figure 6.1).

### **Comparison with CVs**

The behaviour of flares in the flux ratio diagram is quite similar to flickering in dwarf novae suggesting that both types are produced in optically thin regions. In case of the stellar flares this is the star corona so we can infer that for DN the flares are also produced in the corona above the accretion disc. For IPs and novalikes the source of flares is either optically thick or a mixture of optically thick and thin emission. By analogy we can imagine that the flares are produced in the corona above the disc and they heat the disc below, which is a source of optically thick emission. This analogy favours a magnetic origin of the flares that in both cases would be produced by magnetic reconnection events.

## 6.5 Conclusion

We studied stochastic variability (flickering) of fourteen cataclysmic variable stars on timescales of 3 hours to 0.05 s. We applied Fourier techniques to the data to study the variability at different timescales. The timescales present in the accretion disc of CVs are thought to be: the shearing timescale, the magnetic alignment timescale, the viscous timescale and the dynamical timescale. The shortest timescale is the dynamical timescale that reaches a minimum in the inner accretion disc. So we expect a frequency break at the corresponding frequency which is between 0.02 and 2 Hz. Our main aim was to detect this high frequency break. However this was not possible due to the steepness of the power spectra. We found that the power spectra of CVs are much steeper than what was previously thought (Bruch 1992); the power  $\propto f^{-(1.81-3.0)}$  in the  $g'$  and  $r'$  filters although the periodogram is generally less steep in the  $u'$  filter. We suppose that due the steepness of the spectrum previous studies of CVs have been affected by leakage from lower frequencies to higher frequencies which lead to an underestimate of the true steepness of the power spectra. We measure the percentage RMS variability on frequencies ranging from  $10^{-3}$  to  $10^{-2}$  Hz, which is around 2.4 per cent in the  $g'$  and  $r'$  filters and about 4.5 per cent in the  $u'$  filter.

We were able to confirm that the variability is simultaneous in the three bands down to 0.1 s implying that they are causally connected on short timescales. Moreover using a crude eclipse analysis method we concluded that flickering on timescales of 10 s to 5 min in RW Tri and V345 Pav comes from a region close to the white dwarf in agreement with previous results.

We detected two statistically significant quasi-periodic oscillations with periods of 30 and 32 s, which last for about  $\sim 10$  cycles. If these periods are dynamically related they come either from the inner disc or the white dwarf surface.

We also studied the colour of the flares taking advantage of the simultaneous

three colour information. We concluded that the colour of the flares is correlated with their flux and they have similar behaviour to stellar flares in the flux ratio diagram. We take this as a indication that they have the same origin; they are produced by magnetic reconnection events which in case of accretion disc is due to the Balbus-Hawley instability. The flares in CVs are brighter than the stellar flares, which might mean that there are superpositions of several flares at a given time.

Finally we compared CVs and Soft X-ray Transients in quiescence, and concluded that in SXTs the flickering comes from the inner accretion disc which seems to have a different origin than the flickering in CVs. In this case high frequency flickering appears to have a non-thermal origin, being produced by synchrotron radiation. SXTs have more high frequency flickering than CVs.

# **Chapter 7**

## **Conclusion and Future Work**

### **7.1 The nature of V407 Vul and HM Cnc**

V407 Vul and HM Cnc have been the subject of much attention of several groups seeking to uncover their nature and which of the current four models for these two systems best describes them. This interest is due to their status as the shortest period binaries known, which has consequences for the binary evolution theories. Furthermore they are strong emitters of gravitational waves and may be used as test systems for the gravitational wave detector LISA. LISA will be able to determine the true nature of these systems if the other methods fail.

At the start of this thesis it proved hard to decide which, if any, of the models; unipolar inductor, intermediate polar, polar and direct impact accretor, is correct. Compared to typical accreting systems, HM Cnc has weak optical line emission, while V407 Vul has none at all. This favours the unipolar inductor model which is the only one without accretion. The decrease in the observed period (Strohmayer 2002; Hakala et al. 2003; Strohmayer 2003, 2004; Hakala et al. 2004) also favours the unipolar model as well as the IP model. Therefore the unipolar model was considered to be the favourite for these two systems (Hakala et al. 2004).

However in chapter 4 we show that the unipolar model in its current form can not explain the shapes and phases of the X-ray light curves. The asynchronism between the orbital period of the systems and the spin period of the magnetic white dwarf required to power the unipolar inductor means that the phase of the pulsations is not locked to the orbit. This is because if the angle between the magnetic axis and the spin axis is higher than a critical angle  $\approx 17^\circ$ , the accretion spot will circle around the magnetic pole at the beat period of the system, and large phase shifts would be seen. So we conclude that the spin and magnetic axis are almost aligned. However in this configuration the geometry that would produce the 40/60 per cent off/on phase observed in the X-rays implies that we should see eclipses, that are not seen. Our calculations showed that it is only possible to obtain the observed X-ray shape if the white dwarfs are both very massive but in this case the gravitational wave radiation would be inconsistent with the observed spin-up rate of the systems. So we conclude that the unipolar inductor model for V407 Vul and HM Cnc can only work if the field geometry is different from a dipole. White dwarfs with magnetic field different from a dipole have been observed (Schwope 1995; Wickramasinghe & Ferrario 2000; Euchner et al. 2005). Another unlikely possibility, in case of HM Cnc, is that we have not seen the phase shifts due to poor X-ray coverage.

After we published our results, D'Antona et al. (2006) and Deloye & Taam (2006) developed models that state that double degenerate AM CVns pass through an initial long lasting phase where the period decreases before starting to increase. In the case of D'Antona et al. (2006) this would happen because the secondary white dwarf would have a hydrogen envelope, so the star would not be fully degenerate yet. In the case of Deloye & Taam (2006) the period would initially start by decreasing because the mass-transfer would be very high and the Roche lobe would be below the donor's photosphere. Deloye & Taam (2006) estimated that V407 Vul can remain in this state for  $\sim 5 \times 10^5$  years; for comparison Dall'Osso et al. (2006b) estimate a lifetime of  $10^4 - 10^6$  years for V407 Vul. For HM Cnc the estimated timescale of the spin up phase for the direct impact model

is of  $10^2 - 10^3$  years (Deloye & Taam 2006) while the study of Dall'Osso et al. (2006b) find that for HM Cnc the unipolar inductor can be maintained forever. The difficulties of the unipolar inductor model in explaining the X-ray phase and the fact that it is possible to obtain a long-lasting spin up in the direct impact model, has rebalanced the double degenerate accreting versus non-accreting models in favour of the former.

In Chapter 5 we present light curves of V407 Vul and HM Cnc in  $i'$ ,  $r'$ ,  $g'$  and  $u'$  bands taken with the high-speed CCD camera ULTRACAM. We found that HM Cnc optical and X-ray emission are not in anti-phase as predicted by the unipolar model and as previously reported (Israel et al. 2003, 2004) but the optical maximum is 0.2 cycles ahead of the X-ray maximum. This makes HM Cnc and V407 Vul X-ray/optical phasing very similar. This new phasing is naturally explained by the double-degenerate accreting models: the direct impact and polar models. Furthermore we decompose the optical light curves of HM Cnc into two components which are consistent with one component due to the irradiation of the secondary and the other component coming from the same site that produces the X-rays. If the optical is produced by irradiation of the secondary by X-rays we place a lower limit in the distance to HM Cnc of  $> 1.5$  kpc. This limit is higher if the secondary can not see the X-rays but is instead irradiated by the hot primary photosphere  $d > 4.2$  kpc.

For V407 Vul we suspect that the G star seen in its spectra is a third component of the system. We have a hint of a detection of this third component that is at 0.027 arcsec from the variable. Only longer baseline observations would be able to distinguish whether it is a line-of-sight coincidence or a triple system.

Also in chapter 5 we suggest that the polar model might have been discarded too soon when no polarisation was found in the systems. In fact, there are very high magnetic field polars that show very soft spectra and low polarisation because in this case this shock is buried as is predicted to happen in the direct impact model. A buried shock would also explain the lack of flickering in the light curves of V407 Vul and

HM Cnc. In this case the only difference between the two double degenerate accreting models would be the accreting spot's location. In the direct impact model the accreting spot is near the equator while in the polar model it is at higher latitude.

These results brought further difficulties to the unipolar inductor model. This leads us to conclude that it is no longer the best model for the systems unless the recent detection of radio emission from HM Cnc (Ramsay et al. 2007), which is a sign of the unipolar induction, is confirmed. In this case the unipolar inductor model would have to be adjusted by for example a quadrupole field or by changing the magnetic component of the binary to a neutron star.

Recently Ramsay (2007) has refitted the X-ray spectrum of the V407 Vul and concluded that this can be well explained by a simple blackbody plus an absorption component that has non-solar neon abundances. This makes both the X-ray spectrum and intrinsic temperatures of V407 Vul and HM Cnc very similar, so they should be explained by the same model. He also concluded that the X-ray spectrum is similar to a non-accreting neutron star, or an accreting white dwarf. If instead of a magnetic white dwarf we consider a magnetic neutron star, the unipolar inductor model still has difficulties to explain the luminosity of V407 Vul.

## 7.2 Stochastic variability in CVs

In chapter 6 we changed our focus to stochastic variability in CVs. We obtained high time resolution optical photometry of fourteen cataclysmic variable stars. Our data were taken with the ULTRACAM mounted on the WHT and the VLT. The small number of systems did not allow us to see a difference in the characteristic variability of the different classes of CVs. The power spectra of CVs were thought to be proportional  $f^{-2}$  (Elsworth & James 1982, 1986; Bruch 1992; Fritz & Bruch 1998), however we found that most of our observed CVs have power spectra steeper than 2. This could be due to some bias

in our selection sample but is more likely due to a bias in the previous measurements of power law slopes which did not account for low frequency leakage. Due to red noise leak, power spectra steeper than 2 will appear to have a slope  $\approx 2$ .

Due to leakage and scintillation noise we were unable to detect the expected high frequency break in the power spectra of cataclysmic variables due to the inner accretion disc.

We confirm Bruch's (1992) results that the  $u'$  filter has more variability power and has a shallower power spectrum than the  $r'$  and  $g'$  bands. We also confirm that the three filters are simultaneous to within 0.1 s.

We report two QPOs in RW Tri with periods of 30 and 32 s which are statistically significant at 99 per cent confidence level. A sliding periodogram technique led us to conclude that during our observation three different QPOs were present but only one was dominant at a given time.

We observed one eclipse for two of the systems, RW Tri and V345 Pav. Analysing the RMS variability on timescales of 10 s to 5 min as a function of phase, we concluded that in both these systems the flickering comes from a region close to the white dwarf, i. e. the inner accretion disc or the boundary layer.

We compared the flickering in CVs with stellar flares and concluded that they have similar behaviour in the flux ratio diagram so they probably have a similar nature and they can be explained by both optically thin and optically thick emission. This suggests that both types of flares are produced by magnetic reconnection (King et al. 2004) which in case of CVs is due to the magneto rotational instability (Balbus & Hawley 1991).

We compared the slope of the optical power spectrum of our CVs with the slopes of Soft X-ray Transients in quiescence. We concluded that the latter have much shallower power spectra than the former. Therefore SXTs have more high frequency flickering than CVs. This supports models where part of the optical emission in SXTs

is produced by synchrotron radiation in the inner regions near the black hole or in a jet.

### 7.3 Future work

In chapter 5 we compare the flickering in V407 Vul and HM Cnc with the flickering in SS Cyg and concluded that the ultra-compact candidates have very little or no flickering. This would imply that if the objects are accreting then most of the optical light would not come from the accreting region but would probably originate in the heated face of the secondary star. However if we compare the flickering in V407 Vul and HM Cnc with low variability CVs like HQ Mon and V345 Pav and considering the faintness of both V407 Vul and HM Cnc, we conclude that we cannot rule out the existence of flickering in these systems. Therefore longer observations are needed to study the long time variability of these objects.

Besides the methods we described in chapter 3 and applied in chapter 6 to study steep power spectra, other methods have been used. One of these was applied by Scott et al. (2003) and uses non-squared windows, whose power spectrum falls-off faster than  $f^{-2}$ . Scott et al. (2003) chose the Hann window;  $w_k = \sin^\alpha(\pi k/N)$  with  $\alpha = 2$  whose power spectrum falls-off as  $f^{-6}$  (Harris 1978), so it can recover power slopes smaller than 5. However this method requires uniformly sampled data. The authors argue that in their case interpolation of the data to a uniform grid does not affect their results. We would need to check if this also holds for our data. It would be interesting to compare the results of both methods in a future work .

Although several periodicities have been detected in CVs (QPOs and DNOs) their cause is still unknown. However the fastest periodicities are thought to come from the inner accretion disc or the surface of the white dwarf. So the study of these high frequencies periodicities such as the one detected in RW Tri is an alternative to detect the existence of a high frequency break to probe the inner accretion disc. As a future

work I would like to study the colours of the QPOs has their frequency changes to determine where they come from.

## Appendix A

# Ephemeris of V407 Vul and HM Cnc

### A.1 Ephemerides

#### V407 Vul's ephemeris

As we mentioned in Section 5.3.1, in order to calculate the uncertainty in the published ephemerides we need the covariance terms of the fitted coefficients that are not given in any published work. Therefore we had to digitise and fit the X-ray data in order to obtain a timing solution whose uncertainties we could compare with our data. To digitise the data we applied the Linux utilities *pstoedit* and *xfig* to the postscript figures from the published papers to obtain the coordinates of the points and their error bars. Such a process can at best match the original data, and can potentially degrade it, but in this case the precision of the postscript data is good enough that it has no measurable effect; we were able to confirm our numbers directly in one case after Dr Ramsay kindly sent us his data. For V407 Vul's ephemeris we digitised the bottom panel of Figure 6 from Strohmayer (2004) and Figure 1 from the recently published ephemeris

$t_0$ (TDB)	49257.533373137
$\phi_0$	0.003(30)
$\nu$ (Hz)	0.00175624626(39)
$\dot{\nu}$ (Hz s $^{-1}$ )	9.9(1.9) $\times 10^{-18}$
$r(\phi_0, \nu)$	-0.92074289
$r(\phi_0, \dot{\nu})$	0.86174740
$r(\nu, \dot{\nu})$	-0.98817908

Table A.1: Ephemeris of V407 Vul derived from Ramsay et al. (2006a). The uncertainties of the parameters are given within parentheses. We also give the correlation coefficients for the fitted parameters.

of Ramsay et al. (2006a) that extends the ephemeris to April 2004. These figures show the residuals in phase relative to a given timing solution. In each case we applied the given timing solution to the observation times and added the phase residuals to obtain the phases as a function of time. We then fitted a timing solution similar to the one used by Strohmayer (2004), i.e.  $\phi(t) = \phi_0 + \nu(t - t_0) + \dot{\nu}(t - t_0)^2/2$ . We included an extra term ( $\phi_0$ ) because we fixed  $t_0$  to be the same as Strohmayer (2004), so this value is no longer arbitrary. We obtain the same fitted parameters as Strohmayer (2004) but slightly different parameters to those of Ramsay et al. (2006a). For reasons we shall explain, it is our fit to the data of Ramsay et al. (2006a) that is given in Table A.1. This corresponds to  $\dot{P} = -3.21(61) \times 10^{-12}$  ss $^{-1}$  which can be compared with the value  $\dot{P} = -3.31(09) \times 10^{-12}$  ss $^{-1}$  from Ramsay et al. (2006a). Our uncertainty is six times larger than that of Ramsay et al. (2006a) and the values are slightly different because we allowed more freedom in the fit. We think our fit is the correct one because there is no reason that the fit has to have zero value and gradient at  $t = 0$ , as was effectively assumed by Ramsay et al. (2006a), who fitted only a parabolic term.

Comparing the two ephemerides we found that the value of the frequency derivative was not consistent. Moreover if we calculate the phase of the maximum of our observation with the ephemeris from Strohmayer we obtain  $0.8170 \pm 0.0016$  for the May 2003 and  $0.7328 \pm 0.0013$  for August 2005 (different from 0.97 of Table 5.6 from Ram-

say et al. 2006a). This suggests that the two ephemerides have different zero points contrary to what was stated in the respective papers. Next we compared the phases predicted by the two ephemerides expecting to see a constant offset between the two. Instead we found a drift between one ephemeris and the other. The phase difference started at approximately zero for the first observation with ROSAT (so indeed the two ephemerides had exactly the same zero point) but were 0.15 cycles apart for the last Chandra observation. Therefore we re-analysed the ROSAT data from the 30<sup>th</sup> April 1996 and phase-folded it on Strohmayer's (2004) ephemeris, but obtained the same phasing as Ramsay et al. (2006a). We can only obtain the same phasing as Strohmayer (2004) if we do not apply the UTC to TT correction. In the ROSAT documentation it says that the times are in UTC<sup>1</sup>. The error in the ROSAT times causes Strohmayer (2004) to underestimate the rate of spin-up in V407 Vul, and this is why his frequency derivative is lower than that of Ramsay et al. (2006a).

To be sure of the correct phasing between the X-ray and optical light curves of V407 Vul we used the ephemeris of Table A.1 and applied it to Chandra data taken on 19<sup>th</sup> of February 2003 and 24<sup>th</sup> November 2003, which were taken before and after our May 2003 observation. We obtained the same relative phasing of the optical and X-rays at each epoch. When we use the ephemeris of Ramsay et al. (2006a), the two Chandra X-ray light curves are almost perfectly aligned (Figure 5.5), but if we use Strohmayer's ephemeris, there is a distinct shift between them. We take this as further evidence of a problem with Strohmayer's ephemeris.

To conclude, we used the ephemeris that resulted from refitting the data Ramsay et al. (2006a) to give the ephemeris listed in Table A.1. In the top panel of Figure A.1 we show the residuals of our fitted phases for V407 Vul after removal of a constant frequency model with  $\nu_0 = 0.001\,756\,248\,272\,1063$  Hz. We also show the fitted parabola minus the linear fit. For future reference we give the times of the rise to maximum in

---

<sup>1</sup><http://wave.xray.mpe.mpg.de/rosat/doc/>

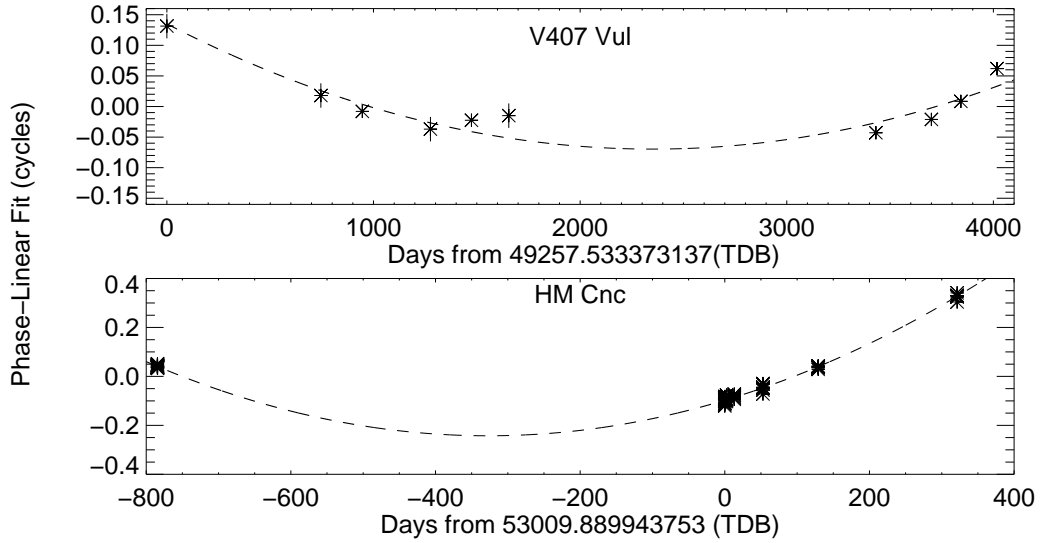


Figure A.1: Phase residuals of V407 Vul (top panel) and HM Cnc (bottom panel) after subtraction of constant frequency models. The dashed line shows our parabola ephemeris subtracted the linear fit. The data before subtracting the constant ephemeris is given is Table A.2.

Table A.2.

For V407 Vul we performed an  $F$ -ratio test for the parabola versus the linear fit. The  $\chi^2$  value of the parabola is 23.4 and of the linear fit is 115, we have 10 points so we obtain an  $F$ -ratio = 4.33 which is significant at the 95 per cent confidence level but not at 99 per cent. As mentioned above, after publication we found that our  $F$ -ratio formula was incorrect. Using equation (5.2) the  $F$ -ratio = 27 which is significant at the 99 per cent confidence level.

### **HM Cnc's ephemeris**

As was explained above in the case of V407 Vul, in order to calculate the uncertainties in phase due to the ephemeris we need to know the covariance terms of the ephemeris. Therefore we applied the same method as before and digitised and fitted the data of Figure 7 of Strohmayer (2005). We obtained the same fit coefficients as Strohmayer (2005) so our digitisation does not cause loss of information; in this case no ROSAT

$t$	$\delta t$
49257.539963	0.000132
50002.756944	0.000132
50203.620631	0.000066
50533.184874	0.000132
50731.445156	0.000066
50912.313875	0.000132
52688.834853	0.000066
52957.531428	0.000066
53100.143737	0.000066
53274.922783	0.000066

Table A.2: Data adapted from Ramsay et al. (2006a).  $t$  is time of the sharp rise to maximum in different observations of V407 Vul. We also give the error of the time ( $\delta t$ ).

$t_0$ (TDB)	53009.889943753
$\phi_0$	0.0003(14)
$\nu$ (Hz)	0.00311013824(10)
$\dot{\nu}$ (Hz s $^{-1}$ )	3.63(0.04) $\times 10^{-16}$
$r(\phi_0, \nu)$	-0.48041115
$r(\phi_0, \dot{\nu})$	-0.61096603
$r(\nu, \dot{\nu})$	0.94898169

Table A.3: Ephemeris of HM Cnc derived from Figure 7 of Strohmayer (2005). The uncertainties of the parameters are given within brackets. We also give the correlation coefficients for the fitted parameters.

data were involved. We also obtain the covariance terms. Our fitted parameters are given in Table A.3. We show the phase residuals after subtracting a constant frequency model ( $\nu_0 = 0.0031101279743869$  Hz) in the bottom panel of Figure A.1 and we also give the times off the middle of the off phase in Table A.4. We applied an  $F$ -ratio test to the HM Cnc data. This time there were 69 points and we obtained a  $\chi^2$  of 54.9 for the parabolic fit and 10380 for the linear fit. This gives an  $F$ -ratio of 186, significant at the 99.99 per cent confidence level.

The correct value of the  $F$ -ratio using equation (5.2) is 12413 which is highly significant.

$t$	$\delta t$
52225.344624	0.000032
52225.344641	0.000032
52225.344646	0.000032
52225.344614	0.000031
52225.344651	0.000033
52225.344600	0.000033
52225.344641	0.000031
52225.344608	0.000032
52225.526984	0.000030
52225.527002	0.000033
52225.526972	0.000032
52225.526998	0.000034
52225.526939	0.000031
52225.527010	0.000034
52225.526972	0.000032
52225.526990	0.000031
53009.942053	0.000032
53009.942023	0.000032
53009.942099	0.000034
53009.942112	0.000035
53009.942129	0.000043
53009.942009	0.000036
53009.942004	0.000036
53009.942037	0.000034
53009.942058	0.000034
53010.124436	0.000035
53010.124392	0.000037
53010.124431	0.000043
53010.124378	0.000033
53010.124334	0.000032
53010.124393	0.000032
53012.305146	0.000050
53012.305120	0.000049
53012.305062	0.000043
53012.305131	0.000039
53012.305138	0.000037
53012.305116	0.000036
53012.305161	0.000043
53012.305086	0.000044

Table A.4: Data adapted from Strohmayer (2005).  $t$  is time of the middle of the off phase in different observations of HM Cnc.  $\delta t$  is the error of the time.

$t$	$\delta t$
53023.033906	0.000034
53023.033884	0.000037
53023.033964	0.000035
53023.033923	0.000032
53023.033938	0.000034
53023.033947	0.000034
53023.033900	0.000035
53062.663072	0.000032
53062.663061	0.000038
53062.663162	0.000036
53062.663137	0.000038
53062.663220	0.000042
53062.663117	0.000037
53062.663138	0.000042
53062.663119	0.000041
53138.832728	0.000038
53138.832708	0.000036
53139.015047	0.000031
53139.015100	0.000036
53139.015071	0.000035
53139.015051	0.000032
53139.015058	0.000034
53139.015069	0.000033
53331.165432	0.000033
53331.165471	0.000034
53331.165476	0.000037
53331.165569	0.000044
53331.165491	0.000043
53331.165472	0.000045
53331.165494	0.000043

Table A.4: continued

### Uncertainties on phases from the ephemerides

To calculate the uncertainties in the absolute phases due the uncertainties in the ephemeris we used the relation:

$$\begin{aligned}\sigma_{\phi}^2 &= \sigma_{\phi_0}^2 + (t - t_0)^2 \sigma_{\nu}^2 + (t - t_0)^4 \sigma_{\dot{\nu}}^2 / 4 + \\ &\quad 2(t - t_0) C_{\phi_0 \nu} + (t - t_0)^3 C_{\nu \dot{\nu}} + (t - t_0)^2 C_{\dot{\nu} \phi_0}\end{aligned}\quad (\text{A.1})$$

where  $C_{XY}$  is the covariance of  $X$  and  $Y$  and can be written  $C_{XY} = \sigma_X \sigma_Y r(X, Y)$ . We give the correlation coefficients  $r(X, Y)$  in Table A.1 and Table A.3.

For the phase difference between two epochs  $\Delta\phi = \phi(t_2) - \phi(t_1)$  one cannot simply combine in quadrature the uncertainties on the absolute phases at each epoch because the same coefficients are used in each case. (This is most easily seen by considering the case of two identical epochs for which the uncertainty in the phase difference must be zero.) Instead one must use the following relation:

$$\begin{aligned}\sigma_{\Delta\phi}^2 &= (t_2 - t_1)^2 \sigma_{\nu}^2 + [(t_2 - t_0)^2 - (t_1 - t_0)^2]^2 \sigma_{\dot{\nu}}^2 / 4 + \\ &\quad (t_2 - t_1)[(t_2 - t_0)^2 - (t_1 - t_0)^2] C_{\nu \dot{\nu}}.\end{aligned}\quad (\text{A.2})$$

We used this to calculate the uncertainties on the phase differences in sections 5.3.2 and 5.3.4.

## Appendix B

# Normalisation of the simulated light curves

### B.1 Introduction

This appendix explains the correct normalisation of our simulated light curves. The light curves are generated from a power spectrum  $P(f)$  according to Timmer & Koenig's (1995) method which uses the inverse Fourier transform. And we desire that the Lomb-Scargle periodogram of the simulated light curves match the normalisation of the initial power spectrum. Due to the properties of the  $FT$  and  $FT^{-1}$  this would be a simple procedure if we only had to account for the difference in normalisation between the LSP and the PSD. The problem is that want to generate a light curve sampled onto a finer and longer grid which later is interpolated to the real observing times. This is necessary so that we can account for red noise leak and spurious periodicities that might appear with our sampling times. In our calculation we will start by assuming that we want to compute the PSD instead of the LSP as we also did in the case of the white noise.

## B.2 Normalisation

We imagine a power spectrum characterised by a spectrum  $P(f)$ . We start by generating artificial data from this by the following procedure. On a series of  $N'$  regularly spaced frequencies we generate complex numbers

$$S'_{k'} = X'_{k'} + iY'_{k'}, \quad (\text{B.1})$$

where  $X'_{k'}$  and  $Y'_{k'}$  are independent Gaussian random variables with variance  $= P'_{k'} = P(\Delta f' k')$  where  $\Delta f'$  is the frequency spacing. The dashes refer to the finely spaced arrays used to generate the artificial data which will be interpolated onto coarse undashed arrays. The finely spaced artificial fluxes are generated according to

$$y'_{n'} = \alpha \sum_{k'} S'_{k'} e^{i2\pi n' k' / N'}, \quad (\text{B.2})$$

where the sum is from 0 to  $N' - 1$  as it will be for all dashed indices and  $\alpha$  is a normalising factor which will be set by requiring the final power spectrum to match that input. We then convert these to a continuous function of time using

$$y(t) = \sum_{n'} y'_{n'} g(t - n' \Delta t'), \quad (\text{B.3})$$

where  $\Delta t'$  is the temporal spacing of the fine array which obeys the usual Nyquist criterion

$$\Delta f' \Delta t' = 1/2N', \quad (\text{B.4})$$

and  $g(t)$  is an interpolating function. Sampling onto the final output grid, which I assume to be coarser but still uniformly sampled gives

$$y_n = y(n\Delta t), \quad (\text{B.5})$$

$$= \sum_{n'} y'_{n'} g(n\Delta t - n' \Delta t'), \quad (\text{B.6})$$

$$= \alpha \sum_{n'} \sum_{k'} S'_{k'} e^{i2\pi n' k' / N'} g(n\Delta t - n' \Delta t'), \quad (\text{B.7})$$

where  $\Delta t \geq \Delta t'$  is the spacing of the coarse grid and also  $N\Delta t \leq N'\Delta t'$  so that the fine grid more than spans the coarse one.

I now assume that the FT is calculated according to

$$Y_k = \sum_n y_n e^{-i2\pi nk/N}, \quad (\text{B.8})$$

$$= \alpha \sum_n \sum_{n'} \sum_{k'} S'_{k'} e^{i2\pi n' k'/N'} e^{-i2\pi nk/N} g(n\Delta t - n'\Delta t'). \quad (\text{B.9})$$

and that the power spectrum estimate is obtained from taking the squared modulus of this:

$$\hat{P}_k = Y_k Y_k^*. \quad (\text{B.10})$$

The value of  $\alpha$  is set by requiring that  $\langle \hat{P}_k \rangle = P(\Delta f k) = P_k$ , where

$$\Delta f \Delta t = 1/2N. \quad (\text{B.11})$$

Therefore

$$P_k = \alpha^2 \sum_n \sum_{n'} \sum_{k'} \sum_m \sum_{m'} \sum_{l'} \langle S'_{k'} S'^*_{l'} \rangle e^{i2\pi n' k'/N'} e^{-i2\pi nk/N} e^{-i2\pi m' l'/N'} e^{i2\pi mk/N} \times g(n\Delta t - n'\Delta t') g(m\Delta t - m'\Delta t'). \quad (\text{B.12})$$

Given the way in which the spectral components were generated (Eq. B.1), the term in angle brackets is easily shown to be

$$\langle S'_{k'} S'^*_{l'} \rangle = 2P'_{k'} \delta_{k',l'}, \quad (\text{B.13})$$

thus

$$P_k = 2\alpha^2 \sum_n \sum_{n'} \sum_{k'} \sum_m \sum_{m'} P'_{k'} e^{i2\pi n' k'/N'} e^{-i2\pi nk/N} e^{-i2\pi m' k'/N'} e^{i2\pi mk/N} \times g(n\Delta t - n'\Delta t') g(m\Delta t - m'\Delta t'). \quad (\text{B.14})$$

The sums over the  $n'$  and  $m'$  can be factored into sums over the interpolating function times the exponentials with the corresponding indices, e.g.

$$\sum_{n'} g(n\Delta t - n'\Delta t') e^{i2\pi n' k'/N'}. \quad (\text{B.15})$$

This can be written as

$$e^{i2\pi f t_n} \int g(t) s(t) e^{-i2\pi f t} dt, \quad (\text{B.16})$$

where

$$s(t) = \sum_{n'} \delta(t - t_n + t'_{n'}), \quad (\text{B.17})$$

$$t_n = n\Delta t, \quad (\text{B.18})$$

$$t'_{n'} = n'\Delta t', \quad (\text{B.19})$$

$$f = \frac{k'}{N'\Delta t'}. \quad (\text{B.20})$$

The integral is the FT of the product of two functions which equals the convolution of the FTs of the two functions separately,  $G(f)$  and  $S(f)$ . From the sampling theorem  $G(f) = \Delta t'$  for  $-1/2\Delta t' < f < 1/2\Delta t'$ , 0 otherwise. The FT of the sampling function  $s(t)$  is given by

$$S(f) = e^{-i2\pi f t_n} \sum_{n'} e^{i2\pi f n' \Delta t'}. \quad (\text{B.21})$$

The sum in this equation reaches a sharp peak for  $f\Delta t' = m'$ , an integer, i.e. for a series of regularly spaced frequencies given by

$$f'_{k'} = \frac{k'}{\Delta t'} = k'\Delta f', \quad (\text{B.22})$$

the usual frequencies of DFTs. Moving away from any of these peaks, the sum first reaches zero for a change in frequency  $\delta f' = 1/N'\Delta t' \ll \Delta f'$ . Indeed in the limit of  $N' \rightarrow \infty$ , then the sum becomes a series of delta functions. Convolution with  $G(f)$  blurs these peaks out by  $\pm\Delta f'/2$  giving a constant. We just need to evaluate this constant.

We do so by integration over a frequency range  $f'_{k'} - \Delta f'/2$  to  $f'_{k'} + \Delta f'/2$ , i.e. exactly straddling a peak to evaluate the strength of its near-delta function. From Eq. B.21 we get

$$\int_{f'_{k'} - \Delta f'/2}^{f'_{k'} + \Delta f'/2} S(f) df = e^{-i2\pi f'_{k'} t_n} \sum_{n'} \frac{\sin \pi(n' - \Delta f' t_n)}{\pi(n' - \Delta f' t_n)}. \quad (\text{B.23})$$

If we assume that  $\Delta t = p\Delta t'$  where  $p$  is an integer  $\geq 1$ , then the only non-zero term is when  $n\Delta t = n'\Delta t'$  giving

$$\exp\left(i2\pi \frac{k'n\Delta t}{N'\Delta t'}\right). \quad (\text{B.24})$$

We are left with

$$P_k = 2\alpha^2 \sum_n \sum_{k'} \sum_m P'_{k'} e^{i2\pi k'n\Delta t/N'\Delta t'} e^{-i2\pi nk/N} e^{-i2\pi k'm\Delta t/N'\Delta t'} e^{i2\pi mk/N}. \quad (\text{B.25})$$

The sums over  $n$  and  $m$  now factor, with that over  $n$  looking like:

$$\sum_n \exp\left[i2\pi n\left(\frac{k'\Delta t}{N'\Delta t'} - \frac{k}{N}\right)\right], \quad (\text{B.26})$$

while that over  $m$  is the complex conjugate of this. The two factors combine to make a real quantity equal to

$$F'_{k'} = \left(\frac{\sin \pi x}{\sin \pi x/N}\right)^2, \quad (\text{B.27})$$

where

$$x = \frac{N\Delta t}{N'\Delta t'} k' - k. \quad (\text{B.28})$$

When  $x = 0$ ,  $F'_{k'} = N^2$  and it drops zero when  $x = 1$  corresponding to a change in  $k'$  of

$$\Delta k' = \frac{N'\Delta t'}{N\Delta t} = \frac{\Delta f}{\Delta f'}, \quad (\text{B.29})$$

which equals the ratio of time bases of the fine and coarsely sampled arrays, or equivalently the ratio of the natural frequency spacings. The  $F'_{k'}$  are hence only significant over a short interval and thus we can assume that the  $P'_{k'}$  are approximately constant over the interval of significant  $F'_{k'}$ . One then finds that

$$P_k = 2\alpha^2 N^2 \frac{N'\Delta t'}{N\Delta t} P_k, \quad (\text{B.30})$$

where I have used the relation

$$P_k = P(\Delta fk) = P(\Delta f'k') = P'_{k'}. \quad (\text{B.31})$$

We therefore require that

$$\alpha^2 = \frac{\Delta t}{N' \Delta t'} \frac{1}{2N}. \quad (\text{B.32})$$

Finally we assume that the our data is evenly spaced in time the relation of equation 3.24 holds. Therefore to compensate for the fact that we use the LSP instead of the PSD the normalisation constant B defined by equation 6.1 becomes:

$$B^2 = \frac{\alpha^2 N \bar{h}^2}{2\Delta t} = \left[ \frac{\bar{h}}{2} \right]^2 \frac{1}{\Delta t' N'} \quad (\text{B.33})$$

which is equivalent to equation 6.2.

# Bibliography

Aerts, C., Jeffery, C. S., Fontaine, G., et al. 2006, MNRAS, 367, 1317

Andronov, I. L., Ostrova, N. I., & Burwitz, V. 2005, in Astronomical Society of the Pacific Conference Series, Vol. 335, The Light-Time Effect in Astrophysics: Causes and cures of the O-C diagram, ed. C. Sterken, 229

Andronov, N., Pinsonneault, M., & Sills, A. 2003, ApJ, 582, 358

Balbus, S. A. 2003, ARA&A, 41, 555

Balbus, S. A. & Hawley, J. F. 1991, ApJ, 376, 214

Balbus, S. A., Hawley, J. F., & Stone, J. M. 1996, ApJ, 467, 76

Baptista, R. & Bortoletto, A. 2004, AJ, 128, 411

Baptista, R., Bortoletto, A., & Harlaftis, E. T. 2002, MNRAS, 335, 665

Baptista, R., Steiner, J. E., & Cieslinski, D. 1994, ApJ, 433, 332

Barrett, P., O'Donoghue, D., & Warner, B. 1988, MNRAS, 233, 759

Barros, S. C. C., Marsh, T. R., Dhillon, V. S., et al. 2007, MNRAS, 374, 1334

Barros, S. C. C., Marsh, T. R., Groot, P., et al. 2005, MNRAS, 357, 1306

Baskill, D. S., Wheatley, P. J., & Osborne, J. P. 2005, MNRAS, 357, 626

- Bath, G. T., Edwards, A. C., & Mantle, V. J. 1983a, in *Astrophysics and Space Science Library*, Vol. 101, *Astrophysics and Space Science Library*, ed. M. Livio & G. Shaviv, 55–66
- Bath, G. T., Edwards, A. C., & Mantle, V. J. 1983b, *MNRAS*, 205, 171
- Beard, S. M., Vick, A. J. A., Atkinson, D., et al. 2002, in *Presented at the Society of Photo-Optical Instrumentation Engineers (SPIE) Conference, Vol. 4848, Advanced Telescope and Instrumentation Control Software II*. Edited by Lewis, Hilton. *Proceedings of the SPIE*, Volume 4848, pp. 218-229 (2002)., ed. H. Lewis, 218–229
- Beardmore, A. P., Mukai, K., Norton, A. J., Osborne, J. P., & Hellier, C. 1998, *MNRAS*, 297, 337
- Belloni, T. & Hasinger, G. 1990, *A&A*, 227, L33
- Belloni, T., Verbunt, F., Beuermann, K., et al. 1991, *A&A*, 246, L44
- Bildsten, L., Townsley, D. M., Deloye, C. J., & Nelemans, G. 2006, *ApJ*, 640, 466
- Bitner, M. A., Robinson, E. L., & Behr, B. B. 2007, *ApJ*, 662, 564
- Bopp, B. W. & Moffett, T. J. 1973, *ApJ*, 185, 239
- Bracewell, R. N. 1986, *The Fourier transform and its applications* (McGraw-Hill ; Singapore :McGraw-Hill Book Co , 1986. 2nd ed.)
- Bragaglia, A., Renzini, A., & Bergeron, P. 1995, *ApJ*, 443, 735
- Brinkworth, C. S., Marsh, T. R., Dhillon, V. S., & Knigge, C. 2006, *MNRAS*, 365, 287
- Brocksopp, C., Bandyopadhyay, R. M., & Fender, R. P. 2004, *New Astronomy*, 9, 249
- Bruch, A. 1992, *A&A*, 266, 237
- Bruch, A. 1996, *A&A*, 312, 97

- Bruch, A. 2000, A&A, 359, 998
- Bruch, A. & Duschl, W. J. 1993, A&A, 275, 219
- Bruch, A. & Grutter, M. 1997, Acta Astronomica, 47, 307
- Buckley, D. A. H., O'Donoghue, D., Kilkenny, D., Stobie, R. S., & Remillard, R. A. 1992, MNRAS, 258, 285
- Burn, H. & Kuperus, M. 1988, A&A, 192, 165
- Burwitz, V. & Reinsch, K. 2001, AIP Conf. Proc. 599: X-ray Astronomy: Stellar End-points, AGN, and the Diffuse X-ray Background, 599, 522
- Carrington, R. C. 1859, MNRAS, 20, 13
- Casares, J., Charles, P. A., & Naylor, T. 1992, Nature, 355, 614
- Chaty, S., Haswell, C. A., Malzac, J., et al. 2003, MNRAS, 346, 689
- Churazov, E., Gilfanov, M., & Revnivtsev, M. 2001, MNRAS, 321, 759
- Clarke, J. T., Ballester, G. E., Trauger, J., et al. 1996, Science, 274, 404
- Crawford, J. A. & Kraft, R. P. 1956, ApJ, 123, 44
- Cropper, M. 1988, MNRAS, 231, 597
- Cropper, M. 1990, Space Science Reviews, 54, 195
- Cropper, M., Harrop-Allin, M. K., Mason, K. O., et al. 1998, MNRAS, 293, L57
- Cropper, M., Ramsay, G., Wu, K., & Hakala, P. 2004, in ASP Conf. Ser. 315: IAU Colloq. 190: Magnetic Cataclysmic Variables, ed. S. Vrielmann & M. Cropper, 324
- Dall'Osso, S., Israel, G. L., & Stella, L. 2006a, A&A, 447, 785

- Dall'Osso, S., Israel, G. L., & Stella, L. 2006b, ArXiv Astrophysics e-prints
- D'Antona, F., Ventura, P., Burderi, L., & Teodorescu, A. 2006, ApJ, 653, 1429
- Davies, S. R. 1990, MNRAS, 244, 93
- Davies, S. R. 1991, MNRAS, 251, 64P
- de Kool, M. 1992, A&A, 261, 188
- Deeming, T. J. 1975, ApSS, 36, 137
- Deeter, J. E. 1984, ApJ, 281, 482
- Deeter, J. E. & Boynton, P. E. 1982, ApJ, 261, 337
- Deloye, C. J. & Taam, R. E. 2006, ApJL, 649, L99
- Dhillon, V. & Marsh, T. 2001, New Astronomy Review, 45, 91
- Dhillon, V. S., Marsh, T. R., Hulleman, F., et al. 2005, MNRAS, 363, 609
- Dhillon, V. S., Marsh, T. R., & Littlefair, S. P. 2006, MNRAS, 372, 209
- Dhillon, V. S., Marsh, T. R., Stevenson, M. J., et al. 2007, MNRAS, 378, 825
- di Matteo, T., Celotti, A., & Fabian, A. C. 1999, MNRAS, 304, 809
- Done, C., Madejski, G. M., Mushotzky, R. F., et al. 1992, ApJ, 400, 138
- Dove, J. B., Wilms, J., & Begelman, M. C. 1997, ApJ, 487, 747
- Dravins, D., Lindegren, L., Mezey, E., & Young, A. T. 1998, PASP, 110, 610
- Duquennoy, A. & Mayor, M. 1991, Astron. Astrophys., 248, 485
- Duschl, W. J. & Tscharnuter, W. M. 1991, A&A, 241, 153
- Edelson, R. A. & Krolik, J. H. 1988, ApJ, 333, 646

- Eggleton, P. P. 1976, in IAU Symposium, Vol. 73, Structure and Evolution of Close Binary Systems, ed. P. Eggleton, S. Mitton, & J. Whelan, 209
- Eggleton, P. P. 1983, ApJ, 268, 368
- Elsworth, Y. & James, J. F. 1986, MNRAS, 220, 895
- Elsworth, Y. P. & James, J. F. 1982, MNRAS, 198, 889
- Eracleous, M. & Horne, K. 1996, ApJ, 471, 427
- Espaillat, C., Patterson, J., Warner, B., & Woudt, P. 2005, PASP, 117, 189
- Euchner, F., Reinsch, K., Jordan, S., Beuermann, K., & Gänsicke, B. T. 2005, A&A, 442, 651
- Evans, P. A., Hellier, C., Ramsay, G., & Cropper, M. 2004, MNRAS, 349, 715
- Fabian, A. C., Guilbert, P. W., Motch, C., et al. 1982, A&A, 111, L9
- Feline, W. J., Dhillon, V. S., Marsh, T. R., & Brinkworth, C. S. 2004, MNRAS, 355, 1
- Fender, R. P. 2001, MNRAS, 322, 31
- Fender, R. P., Belloni, T. M., & Gallo, E. 2004, MNRAS, 355, 1105
- Fender, R. P., Gallo, E., & Jonker, P. G. 2003, MNRAS, 343, L99
- Ferland, G. J., Pepper, G. H., Langer, S. H., et al. 1982, ApJL, 262, L53
- Flannery, B. P. 1975, MNRAS, 170, 325
- Foster, G. 1996, AJ, 112, 1709
- Frescura, F. A. M., Engelbrecht, C. A., & Frank, B. S. 2007, ArXiv e-prints, 706
- Friend, M. T., Martin, J. S., Connon-Smith, R., & Jones, D. H. P. 1990, MNRAS, 246, 654

- Fritz, T. & Bruch, A. 1998, A&A, 332, 586
- Galeev, A. A., Rosner, R., & Vaiana, G. S. 1979, ApJ, 229, 318
- Gallo, E., Fender, R. P., Miller-Jones, J. C. A., et al. 2006, MNRAS, 370, 1351
- Gänsicke, B. T., Hagen, H.-J., Kube, J., et al. 2002, in Astronomical Society of the Pacific Conference Series, Vol. 261, The Physics of Cataclysmic Variables and Related Objects, ed. B. T. Gänsicke, K. Beuermann, & K. Reinsch, 623
- Gilliland, R. L. 1982, ApJ, 263, 302
- Gray, D. F. 1992, The observation and analysis of stellar photospheres (Cambridge ; New York : Cambridge University Press, 1992. 2nd ed.)
- Greiner, J., Tovmassian, G., Orio, M., et al. 2001, A&A, 376, 1031
- Groot, P. J., Rutten, R. G. M., & van Paradijs, J. 2004, A&A, 417, 283
- Grossmann, A., Kronland-Martinet, R., & Morlet, J. 1986, Reading and Understanding Continuous Wavelet Transforms (Springer-Verlage , 1989, pp. 2-20)
- Hōshi, R. 1979, Progress of Theoretical Physics, 61, 1307
- Haardt, F. & Maraschi, L. 1993, ApJ, 413, 507
- Haisch, B., Strong, K. T., & Rodono, M. 1991, ARA&A, 29, 275
- Hakala, P., Ramsay, G., & Byckling, K. 2004, MNRAS, 353, 453
- Hakala, P., Ramsay, G., Wu, K., et al. 2003, MNRAS, 343, L10
- Halbwachs, J., Mayor, M., Udry, S., & Arenou, F. 2003, Astron. Astrophys., 397, 159
- Hameury, J.-M., King, A. R., & Lasota, J.-P. 1986, MNRAS, 218, 695

- Harris, F. J. 1978, in Institute of Electrical and Electronics Engineers, Inc. Conference, Vol. 66, Proc. IEEE, Volume 66, p. 51-83, 51–83
- Hasinger, G. & van der Klis, M. 1989, A&A, 225, 79
- Hasinger, G., van der Klis, M., Ebisawa, K., Dotani, T., & Mitsuda, K. 1990, A&A, 235, 131
- Haswell, C. A. 1996, in IAU Symposium, Vol. 165, Compact Stars in Binaries, ed. J. van Paradijs, E. P. J. van den Heuvel, & E. Kuulkers, 351
- Hawley, J. F. & Balbus, S. A. 2002, ApJ, 573, 738
- Hawley, J. F., Balbus, S. A., & Winters, W. F. 1999, ApJ, 518, 394
- Hellier, C. 1993, MNRAS, 265, L35
- Hellier, C. 2001, Cataclysmic Variable Stars (Cataclysmic Variable Stars, Springer, 2001)
- Hellier, C., Mason, K. O., & Cropper, M. 1989, MNRAS, 237, 39P
- Hodgson, R. 1859, MNRAS, 20, 15
- Hollander, A., Kraakman, H., & van Paradijs, J. 1993, A&AS, 101, 87
- Honeycutt, R. K. & Kafka, S. 2004, AJ, 128, 1279
- Horne, J. H. & Baliunas, S. L. 1986a, ApJ, 302, 757
- Horne, J. H. & Baliunas, S. L. 1986b, ApJ, 302, 757
- Horne, K. 1985, MNRAS, 213, 129
- Horne, K. & Stiening, R. F. 1985, MNRAS, 216, 933
- Howell, S. B. 2000, Handbook of CCD Astronomy (Handbook of CCD astronomy / Steve B. Howell. Cambridge, U.K. ; New York : Cambridge University Press, c2000. (Cambridge observing handbooks for research astronomers ; 2))

- Howell, S. B., Nelson, L. A., & Rappaport, S. 2001, ApJ, 550, 897
- Howell, S. B., Rappaport, S., & Politano, M. 1997, MNRAS, 287, 929
- Hua, X.-M. & Titarchuk, L. 1995, ApJ, 449, 188
- Huang, S.-S. 1966, Annales d'Astrophysique, 29, 331
- Hynes, R. I., Charles, P. A., Casares, J., et al. 2003, MNRAS, 340, 447
- Hynes, R. I., Haswell, C. A., Shrader, C. R., et al. 1998, MNRAS, 300, 64
- Iben, I. J. & Livio, M. 1993, PASP, 105, 1373
- Iben, I. J. & Tutukov, A. V. 1991, ApJ, 370, 615
- Iben, I. J. & Tutukov, A. V. 1993, ApJ, 418, 343
- Israel, G. L., Covino, S., Dall'Osso, S., et al. 2004, Memorie della Societa Astronomica Italiana Supplement, 5, 148
- Israel, G. L., Covino, S., Stella, L., et al. 2003, ApJ, 598, 492
- Israel, G. L., Hummel, W., Covino, S., et al. 2002, A&A, 386, L13
- Israel, G. L., Panzera, M. R., Campana, S., et al. 1999, A&A, 349, L1
- Jeffery, C. S., Dhillon, V. S., Marsh, T. R., & Ramachandran, B. 2004, MNRAS, 352, 699
- Kanbach, G., Straubmeier, C., Spruit, H. C., & Belloni, T. 2001, Nature, 414, 180
- Kato, T., Ishioka, R., & Uemura, M. 2002, PASJ, 54, 1033
- Kato, T. & Starkey, D. R. 2002, Informational Bulletin on Variable Stars, 5358, 1
- Kato, T. & Uemura, M. 2001, Informational Bulletin on Variable Stars, 5077, 1

- Kawaguchi, T., Mineshige, S., Machida, M., Matsumoto, R., & Shibata, K. 2000, PASJ, 52, L1
- King, A. R. 1988, QJRAS, 29, 1
- King, A. R., Pringle, J. E., West, R. G., & Livio, M. 2004, MNRAS, 348, 111
- King, A. R., Schenker, K., & Hameury, J. M. 2002, MNRAS, 335, 513
- King, A. R. & Williams, G. A. 1985, MNRAS, 215, 1P
- Kolb, U. 1993, A&A, 271, 149
- Kolb, U. & Baraffe, I. 1999, MNRAS, 309, 1034
- Kolb, U. & Ritter, H. 1992, A&A, 254, 213
- Kozhevnikov, V. P. 2007, MNRAS, 378, 955
- Kraft, R. P., Mathews, J., & Greenstein, J. L. 1962, ApJ, 136, 312
- Krzemiński, W. & Smak, J. 1971, Acta Astronomica, 21, 133
- Kunkel, W. 1967, AJ, 72, 810
- Lamb, F. K., Pethick, C. J., & Pines, D. 1973, ApJ, 184, 271
- Landau, L. D. & Lifshitz, E. M. 1958, The classical theory of fields (Course of theoretical physics - Pergamon International Library of Science, Technology, Engineering and Social Studies, Oxford: Pergamon Press, 1958)
- Leahy, D. A., Darbro, W., Elsner, R. F., et al. 1983, ApJ, 266, 160
- Littlefair, S. P., Dhillon, V. S., Marsh, T. R., et al. 2006, Science, 314, 1578
- Livio, M., Pringle, J. E., & King, A. R. 2003, ApJ, 593, 184

- Lomb, N. R. 1976, ApSS, 39, 447
- Lubow, S. H. & Shu, F. H. 1975, ApJ, 198, 383
- Lyne, A. G., Jordan, C. A., & Roberts, M. E. 2005, Monthly ephemeris, Jodrell Bank  
Crab Pulsar Timing Results., Tech. rep., Jodrell Bank Observation, University of  
Manchester
- Maccarone, T. J. & Coppi, P. S. 2002, MNRAS, 336, 817
- Maccarone, T. J., Coppi, P. S., & Poutanen, J. 2000, ApJL, 537, L107
- Mahasena, P., Inoue, H., & Ishida, M. 2001, in Astronomical Society of the Pacific Con-  
ference Series, Vol. 251, New Century of X-ray Astronomy, ed. H. Inoue & H. Kunieda,  
384
- Malzac, J., Belloni, T., Spruit, H. C., & Kanbach, G. 2003, A&A, 407, 335
- Malzac, J., Belloni, T., Spruit, H. C., & Kanbach, G. 2004, Nuclear Physics B Proceed-  
ings Supplements, 132, 400
- Markoff, S., Falcke, H., & Fender, R. 2001, A&A, 372, L25
- Marsh, T. R. & Duck, S. R. 1996, New Astronomy, 1, 97
- Marsh, T. R. & Nelemans, G. 2005, MNRAS, 363, 581
- Marsh, T. R., Nelemans, G., & Steeghs, D. 2004, MNRAS, 350, 113
- Marsh, T. R. & Steeghs, D. 2002, MNRAS, 331, L7
- Martens, P. C. H. & Kuin, N. P. M. 1989, SoPh, 122, 263
- Mathioudakis, M., Bloomfield, D. S., Jess, D. B., Dhillon, V. S., & Marsh, T. R. 2006,  
A&A, 456, 323

- Mathioudakis, M. & Doyle, J. G. 1990, A&A, 232, 114
- Mauche, C. W. 2004, ApJ, 610, 422
- Maxted, P. F. L., Marsh, T. R., Morales-Rueda, L., et al. 2004, MNRAS, 355, 1143
- McClintock, J. E., Haswell, C. A., Garcia, M. R., et al. 2001, ApJ, 555, 477
- McClintock, J. E., Narayan, R., Garcia, M. R., et al. 2003, ApJ, 593, 435
- McGowan, K. E., Priedhorsky, W. C., & Trudolyubov, S. P. 2004, ApJ, 601, 1100
- Merloni, A., Di Matteo, T., & Fabian, A. C. 2000, MNRAS, 318, L15
- Mestel, L. 1968, MNRAS, 138, 359
- Meyer, F. & Meyer-Hofmeister, E. 1981, A&A, 104, L10
- Meyer, F. & Meyer-Hofmeister, E. 1994, A&A, 288, 175
- Miyamoto, S., Kimura, K., Kitamoto, S., Dotani, T., & Ebisawa, K. 1991, ApJ, 383, 784
- Miyamoto, S. & Kitamoto, S. 1989, Nature, 342, 773
- Moffat, A. F. J. 1969, A&A, 3, 455
- Motch, C., Haberl, F., Guillout, P., et al. 1996, A&A, 307, 459
- Motch, C., Ilovaisky, S. A., & Chevalier, C. 1982, A&A, 109, L1
- Muñoz-Darias, T., Martínez-Pais, I. G., Casares, J., et al. 2006, Advances in Space Research, 38, 2762
- Narayan, R., McClintock, J. E., & Yi, I. 1996, ApJ, 457, 821
- Naylor, T. 1998, MNRAS, 296, 339

- Nelemans, G., Portegies Zwart, S. F., Verbunt, F., & Yungelson, L. R. 2001a, A&A, 368, 939
- Nelemans, G., Yungelson, L. R., & Portegies Zwart, S. F. 2001b, A&A, 375, 890
- North, R. C., Marsh, T. R., Kolb, U., Dhillon, V. S., & Moran, C. K. J. 2002, MNRAS, 337, 1215
- Norton, A. J., Haswell, C. A., & Wynn, G. A. 2004, A&A, 419, 1025
- Nowak, M. A. 1995, PASP, 107, 1207
- Nowak, M. A., Vaughan, B. A., Wilms, J., Dove, J. B., & Begelman, M. C. 1999, ApJ, 510, 874
- Oke, J. B. & Gunn, J. E. 1983, ApJ, 266, 713
- Oliveira, A. S. & Steiner, J. E. 2004, MNRAS, 351, 685
- Osaki, Y. 1974, PASJ, 26, 429
- Osaki, Y. 1989, PASJ, 41, 1005
- Paczynski, B. 1967, Acta Astronomica, 17, 287
- Paczynski, B. 1976, in IAU Symposium, Vol. 73, Structure and Evolution of Close Binary Systems, ed. P. Eggleton, S. Mitton, & J. Whelan, 75
- Paczynski, B. 1981, Acta Astronomica, 31, 1
- Paczynski, B. & Sienkiewicz, R. 1981, ApJL, 248, L27
- Paczynski, B. & Sienkiewicz, R. 1983, ApJ, 268, 825
- Panek, R. J. 1980, ApJ, 241, 1077
- Papadakis, I. E. & Lawrence, A. 1993, MNRAS, 261, 612

- Patterson, J. 1981, ApJ, 45, 517
- Patterson, J. 1984, ApJS, 54, 443
- Patterson, J. 1994, PASP, 106, 209
- Patterson, J., Kemp, J., Harvey, D. A., et al. 2005, PASP, 117, 1204
- Patterson, J., Kemp, J., Richman, H. R., et al. 1998, PASP, 110, 415
- Patterson, J., Patino, R., Thorstensen, J. R., et al. 1996, AJ, 111, 2422
- Pickles, A. J. 1998, PASP, 110, 863
- Podsiadlowski, P., Han, Z., & Rappaport, S. 2003, MNRAS, 340, 1214
- Politano, M. 1996, ApJ, 465, 338
- Poole, T., Mason, K. O., Ramsay, G., Drew, J. E., & Smith, R. C. 2003, MNRAS, 340, 499
- Poutanen, J. & Fabian, A. C. 1999, MNRAS, 306, L31
- Poutanen, J., Svensson, R., & Stern, B. 1997, in ESA Special Publication, Vol. 382, The Transparent Universe, ed. C. Winkler, T. J.-L. Courvoisier, & P. Durouchoux, 401
- Press, W. H. 1978, Comments Astrophys., 7, 103
- Press, W. H. & Rybicki, G. B. 1989, ApJ, 338, 277
- Press, W. H., Teukolsky, S. A., Vetterling, W. T., & Flannery, B. P. 1992, Numerical recipes in C. The art of scientific computing (Cambridge: University Press, —c1992, 2nd ed.)
- Priedhorsky, W., Garmire, G. P., Rothschild, R., et al. 1979, ApJ, 233, 350

- Pringle, J. E. 1981, ARA&A, 19, 137
- Prinja, R. K., Knigge, C., Witherick, D. K., Long, K. S., & Brammer, G. 2004, MNRAS, 355, 137
- Ramsay, G. 2007, ArXiv e-prints, 711
- Ramsay, G., Brocksopp, C., Wu, K., Slee, B., & Saxton, C. J. 2007, MNRAS, 382, 461
- Ramsay, G., Cropper, M., & Hakala, P. 2006a, MNRAS, 367, L62
- Ramsay, G., Cropper, M., Wu, K., Mason, K. O., & Hakala, P. 2000, MNRAS, 311, 75
- Ramsay, G. & Hakala, P. 2005, MNRAS, 360, 314
- Ramsay, G., Hakala, P., & Cropper, M. 2002a, MNRAS, 332, L7
- Ramsay, G., Napiwotzki, R., Hakala, P., & Lehto, H. 2006b, MNRAS, 371, 957
- Ramsay, G., Wu, K., Cropper, M., et al. 2002b, MNRAS, 333, 575
- Rappaport, S., Verbunt, F., & Joss, P. C. 1983, ApJ, 275, 713
- Reiners, A. 2007, ArXiv e-prints, 710
- Reinsch, K., Burwitz, V., & Schwarz, R. 2004, in Revista Mexicana de Astronomia y Astrofisica Conference Series, ed. G. Tovmassian & E. Sion, 122–123
- Revnivtsev, M., Gilfanov, M., & Churazov, E. 2000, A&A, 363, 1013
- Reynolds, M. T., Callanan, P. J., & Filippenko, A. V. 2007, MNRAS, 374, 657
- Ritter, H. & Burkert, A. 1986, A&A, 158, 161
- Robinson, E. L., Barker, E. S., Cochran, A. L., Cochran, W. D., & Nather, R. E. 1981, ApJ, 251, 611

- Robinson, E. L., Shetrone, M. D., & Africano, J. L. 1991, AJ, 102, 1176
- Rodono, M. 1986, The atmospheres of M dwarfs: Observations (NASA, Washington, The M-Type Stars p 409-453 (SEE N88-11592 02-90)), 409–453
- Rodríguez-Gil, P., Casares, J., Martínez-Pais, I. G., Hakala, P., & Steeghs, D. 2001, ApJL, 548, L49
- Roques, F., Doressoundiram, A., Dhillon, V., et al. 2006, AJ, 132, 819
- Rutten, R. G. M., van Paradijs, J., & Tinbergen, J. 1992, A&A, 260, 213
- Savonije, G. J., de Kool, M., & van den Heuvel, E. P. J. 1986, A&A, 155, 51
- Scargle, J. D. 1982, ApJ, 263, 835
- Schlegel, D. J., Finkbeiner, D. P., & Davis, M. 1998, ApJ, 500, 525
- Schmidt, G. D., Ferrario, L., Wickramasinghe, D. T., & Smith, P. S. 2001, ApJ, 553, 823
- Schmidt, G. D., Szkody, P., Smith, P. S., et al. 1996, ApJ, 473, 483
- Schreiber, M. R. & Gänsicke, B. T. 2003, A&A, 406, 305
- Schwarzenberg-Czerny, A. 1998a, MNRAS, 301, 831
- Schwarzenberg-Czerny, A. 1998b, MNRAS, 301, 831
- Schwope, A. D. 1995, in Reviews in Modern Astronomy, Vol. 8, Reviews in Modern Astronomy, ed. G. Klare, 125–146
- Scott, D. M., Finger, M. H., & Wilson, C. A. 2003, MNRAS, 344, 412
- Shafter, A. W. 1983a, PhD thesis, AA(California Univ., Los Angeles.)
- Shafter, A. W. 1983b, ApJ, 267, 222

- Shafter, A. W. 1985, AJ, 90, 643
- Shahbaz, T., Dhillon, V. S., Marsh, T. R., et al. 2005, MNRAS, 362, 975
- Shahbaz, T., Dhillon, V. S., Marsh, T. R., et al. 2003, MNRAS, 346, 1116
- Shakura, N. I. & Syunyaev, R. A. 1973, A&A, 24, 337
- Shu, F. H. 1976, in IAU Symposium, Vol. 73, Structure and Evolution of Close Binary Systems, ed. P. Eggleton, S. Mitton, & J. Whelan, 253
- Sion, E. M., Godon, P., Cheng, F., & Szkody, P. 2007, AJ, 134, 886
- Sion, E. M., Solheim, J.-E., Szkody, P., Gaensicke, B. T., & Howell, S. B. 2006, ApJL, 636, L125
- Smak, J. 1983, ApJ, 272, 234
- Smak, J. 1995, Acta Astronomica, 45, 259
- Smith, A. J., Haswell, C. A., Murray, J. R., Truss, M. R., & Foulkes, S. B. 2007, MNRAS, 378, 785
- Smith, J. A., Tucker, D. L., Kent, S., et al. 2002, AJ, 123, 2121
- Solheim, J.-E. & Yungelson, L. R. 2005, in Astronomical Society of the Pacific Conference Series, Vol. 334, 14th European Workshop on White Dwarfs, ed. D. Koester & S. Moehler, 387
- Spruit, H. C. & Ritter, H. 1983, A&A, 124, 267
- Steeghs, D., Marsh, T. R., Barros, S. C. C., et al. 2006, ApJ, 649, 382
- Stellingwerf, R. F. 1978, ApJ, 224, 953
- Stevenson, M. J. 2004, PhD thesis, University of Sheffield, UK

- Stockman, H. S., Schmidt, G. D., Liebert, J., & Holberg, J. B. 1994, *ApJ*, 430, 323
- Strohmayer, T. E. 2002, *ApJ*, 581, 577
- Strohmayer, T. E. 2003, *ApJL*, 593, L39
- Strohmayer, T. E. 2004, *ApJ*, 610, 416
- Strohmayer, T. E. 2005, *ApJ*, 627, 920
- Strohmayer, T. E., Zhang, W., Swank, J. H., & Lapidus, I. 1998, *ApJL*, 503, L147
- Strong, K. T., Benz, A. O., Dennis, B. R., et al. 1984, *SoPh*, 91, 325
- Szatmary, K., Vinko, J., & Gal, J. 1994, *A&AS*, 108, 377
- Szkody, P., Silber, A., Hoard, D. W., et al. 1995, *ApJL*, 455, L43
- Taam, R. E. & Spruit, H. C. 1989, *ApJ*, 345, 972
- Tapia, S. 1977, *ApJL*, 212, L125
- Taylor, C. J., Thorstensen, J. R., & Patterson, J. 1999, *PASP*, 111, 184
- Taylor, C. J., Thorstensen, J. R., Patterson, J., et al. 1998, *PASP*, 110, 1148
- Timmer, J. & Koenig, M. 1995, *A&A*, 300, 707
- Tomsick, J. A., Kalemci, E., & Kaaret, P. 2004, *ApJ*, 601, 439
- Tovmassian, H. M., Zalinian, V. P., Silant'ev, N. A., Cardona, O., & Chavez, M. 2003, *A&A*, 399, 647
- Uemura, M., Kato, T., Ishioka, R., et al. 2004, *PASJ*, 56, 823
- Uttley, P., McHardy, I. M., & Papadakis, I. E. 2002, *MNRAS*, 332, 231

- van der Klis, M. 1988, in Timing Neutron Stars, eds. H. Ogelman and E.P.J. van den Heuvel. NATO ASI Series C, Vol. 262, p. 27-70. Dordrecht: Kluwer, 1988., 27–70
- van der Klis, M. 1995, in The Lives of the Neutron Stars. Proceedings of the NATO Advanced Study Institute on the Lives of the Neutron Stars, held in Kemer, Turkey, August 29-September 12, 1993. Editor(s), M.A. Alpar, U. Kiziloglu, J. van Paradijs; Publisher, Kluwer Academic, Dordrecht, The Netherlands, Boston, Massachusetts, 1995. LC #: QB843.N4 L583 1993. ISBN #: 0-7923-324-6-6., p.301, ed. M. A. Alpar, U. Kiziloglu, & J. van Paradijs, 301
- van der Klis, M. 1997, in Statistical Challenges in Modern Astronomy II, ed. G. J. Babu & E. D. Feigelson, 321
- van der Klis, M. 2006, Rapid X-ray Variability (Compact stellar X-ray sources), 39–112
- van der Klis, M., Hasinger, G., Stella, L., et al. 1987, ApJL, 319, L13
- van Paradijs, J. & McClintock, J. E. 1995, in X-ray binaries, p. 58 - 125, 58–125
- Vande Putte, D., Smith, R. C., Hawkins, N. A., & Martin, J. S. 2003, MNRAS, 342, 151
- Vaughan, S. 2005, A&A, 431, 391
- Verbunt, F. & Rappaport, S. 1988, ApJ, 332, 193
- Verbunt, F. & Zwaan, C. 1981, Astron. Astrophys., 100, L7
- Verbunt, F. & Zwaan, C. 1981, A&A, 100, L7
- Vogt, N. 1982, ApJ, 252, 653
- Wahlgren, G. M., Wing, R. F., Kaitchuck, R. H., et al. 1985, in Bulletin of the American Astronomical Society, Vol. 17, Bulletin of the American Astronomical Society, 599

- Warner, B. 1974, MNRAS, 168, 235
- Warner, B. 1995, Cambridge Astrophysics Series, 28
- Warner, B. 2004, PASP, 116, 115
- Warner, B. & Cropper, M. 1983, MNRAS, 203, 909
- Warner, B. & Nather, R. E. 1971, MNRAS, 152, 219
- Warner, B. & Wickramasinghe, D. T. 1991, MNRAS, 248, 370
- Warner, B. & Woudt, P. A. 2002, MNRAS, 335, 84
- Webbink, R. F. 1984, ApJ, 277, 355
- Whitehurst, R. 1988, MNRAS, 232, 35
- Wickramasinghe, D. T. & Ferrario, L. 2000, PASP, 112, 873
- Wijnands, R. A. D., van der Klis, M., Psaltis, D., et al. 1996, ApJL, 469, L5
- Willem, B., Kolb, U., Sandquist, E. L., Taam, R. E., & Dubus, G. 2005, ApJ, 635, 1263
- Williams, G. 2003, PASP, 115, 618
- Wilms, J., Nowak, M. A., Pottschmidt, K., et al. 2001, MNRAS, 320, 327
- Wood, J. & Crawford, C. S. 1986, MNRAS, 222, 645
- Wood, J., Horne, K., Berriman, G., et al. 1986, MNRAS, 219, 629
- Wu, K., Cropper, M., Ramsay, G., & Sekiguchi, K. 2002, MNRAS, 331, 221
- Wynn, G. A. 2000, New Astronomy Review, 44, 75
- Wynn, G. A., King, A. R., & Horne, K. 1997, MNRAS, 286, 436

- Yonehara, A., Mineshige, S., & Welsh, W. F. 1997, ApJ, 486, 388
- Young, A. T. 1967, AJ, 72, 747
- Zahn, J.-P. 1977, A&A, 57, 383
- Zamanov, R., Boer, M., Le Coroller, H., & Panov, K. 2006, Informational Bulletin on Variable Stars, 5733, 1
- Zurita, C., Casares, J., & Shahbaz, T. 2003, ApJ, 582, 369
- Zurita, C., Casares, J., Shahbaz, T., et al. 2002, MNRAS, 333, 791